LBNL-46128



# Quantitative Characterization of the Protein Contents of the Exocrine Pancreatic Acinar Cell by Soft X-Ray Microscopy and Advanced Digital Imaging Methods

Billy W. Loo, Jr.
Ph.D. Thesis

Department of Bioengineering
University of California, Berkeley

and

Materials Sciences Division
Ernest Orlando Lawrence Berkeley National Laboratory
University of California
Berkeley, CA 94720

June 2000

This work was supported by the Director, Office of Science, Office of Basic Energy Sciences, and the Office of Biological and Environmental Research, of the U.S. Department of Energy under Contract No. DE-AC03-76SF00098.

## DISCLAIMER

# Quantitative characterization of the protein contents of the exocrine pancreatic acinar cell by soft x-ray microscopy and advanced digital imaging methods

by

**Billy W. Loo, Jr.**

DISSERTATION

Submitted in partial satisfaction of the requirements for the degree of

DOCTOR OF PHILOSOPHY

in

**Bioengineering**

in the

GRADUATE DIVISIONS

of the

UNIVERSITY OF CALIFORNIA SAN FRANCISCO

and

UNIVERSITY OF CALIFORNIA BERKELEY

# Quantitative Characterization of the Protein Contents of the Exocrine Pancreatic Acinar Cell by Soft X-Ray Microscopy and Advanced Digital Imaging Methods



by

Billy W. Loo, Jr.

## Acknowledgments

The work described in this manuscript, undertaken while I was a doctoral student in Bioengineering at the University of California, San Francisco and Berkeley campuses, and a medical student at the University of California, Davis, spanned a period of 11 years and was performed at two national laboratories and three university campuses. An undertaking of this size and duration cannot be the work solely of an individual. Many people in myriad ways have helped me to complete this project, and to develop as a scientist and a human being. I thank them sincerely, and feel privileged to count them as mentors, colleagues, and friends. I apologize in advance for the unintentional omissions I undoubtedly will make.

First, I thank God for leading me to this work as a part of His plan for my life, for upholding me through these years when often the end appeared continually beyond reach, and for strengthening me when the unavoidable obstacles, frustrations, and pressures came. Many times, to accomplish the objective seemed humanly impossible. I see in retrospect that it was indeed.

I thank my thesis committee chair and mentor Stephen S. Rothman for giving me an opportunity when I needed it, for giving me the leeway to explore my ideas and interests, and for his vision and his insights into science and the scientific method. I thank my thesis and qualifying exam committee members David T. Attwood, Bruce H. Hasegawa, H.K. "Bernie" Huang, and Harold Lecar and my qualifying examination chair Stephen L. Lehman for their guidance, support, help, and forbearance. I thank the late Werner

Meyer-Ilse for his generosity with resources when few were available to me, and for the time we spent sharing ideas, scientific discussions, and friendship. He is much missed.

My family has been an incredible source of love, encouragement, understanding, and sanity. My wife Elise Y. Tung Loo has been a wonderful blessing in my life. She has made the difficult times easier, supported me emotionally, spiritually, and materially, provided me with a beautiful, energetic son (William Ethan "Tiger"), and even helped me with technical aspects of my thesis work. I thank my father Billy W. Loo for sharing his wisdom with me, for teaching me to be independent, and for his confidence in me, and my mother Lamae Loo for just being my "mom." I thank my parents-in-law Lee Hong Tung and Ngai Lai Li for their tremendous help in taking care of my family through stressful times.

Many other individuals have been of critical help to me in this work, for which I am most grateful. I mention them here according to the institution at which I originally worked with them, though their individual affiliations are more diverse and in some cases have since changed.

At the University of California, Berkeley, and the Ernest Orlando Lawrence Berkeley National Laboratory: Steven G. Adams, Erik H. Anderson, Mary Helen Barcellos-Hoff, Phillip J. Batson, Rolf H. Behrsing, Edward W. "Wes" Bethel, John T. Brown, Daniel E. Callahan, Luis A. Curtis, René Delano, Gregory P. Denbeaux, Tony T. Freeman, Sharon Fujimura, Raymond Z. Fuzesy, Robert M. Glaeser, Kenneth A. Goldberg, Kaarin K. Goncz, Eric M. Gullikson, George Harp, Everett H. Harvey, John M. Heck, Adam P. Hitchcock, Catherine A. Hong, Malcolm R. Howells, Nasif N. Iskander, Lotti Jochum,

Melvin P. Klein, Carolyn A. Larabell, Jesse Lee, Keith Leslie, William T. Lin, Stephen J. Lockett, William H. Love, Angelic Lucero, Hector Medecki, Mario M. Moronne, Bahram Parvin, Daniel M. Pinkas, Jos Polman, Shradda A. Ravani, Paula Sicurello, Joachim Stohr, Ron E. Tackaberry, Ray Thatcher, Charmaine V. Toy, Hsien-Chen Tseng, James H. Underwood, Ryohei Urata, Dimitri N. "Ed" Voronin, William L. Worthington.

At the State University of New York, Stony Brook, and the Brookhaven National Laboratory: Harald Ade, Sid Bhargava, Katherine S. Conkling, Pete Davis, Chris J. Jacobsen, Darrel D. Joel, Janos Kirz, Steve Lindaas, Ian McNulty, Menno Oversluizen, Mark L. Rivers, David Sayre, Shawn Williams.

At the University of California, San Francisco: David A. Agard, J. Keenan Brown, Je-Wei Chen, Nusi P. Dekker, Brenda Gee, Ira D. Goldfine, James Grendell, Dieter Gruenert, Mats G.L. Gustafsson, Debra Harris, David Hoogstrate, Karla Kruse, Shyh-Liang "Andrew" Lou, Betty A. Maddux, Wallace F. Marshall, Bonnie J. McClintock, Joseph A. Regezi, Ilse M. Sauerwald, Alan Simmons, Kent Soohoo, Rujapong "Joe" Sukhabote, Steven Wong.

At the University of California, Davis: Robert Cardiff, Stephen DiMauro, Aaron J. Lee, Ernest Lewis, Stanley Meizel, Jerold Theis, Kenneth O. Turner, Donal Walsh.

At the Lawrence Livermore National Laboratory: Dino R. Ciarlo.

At Genteric Company: Theresa Hashim.

I am grateful for financial support from Associated Western Universities, the National Institutes of Health, the Regents of the University of California, the University of California, Davis, and the California Medical Education and Research Foundation.

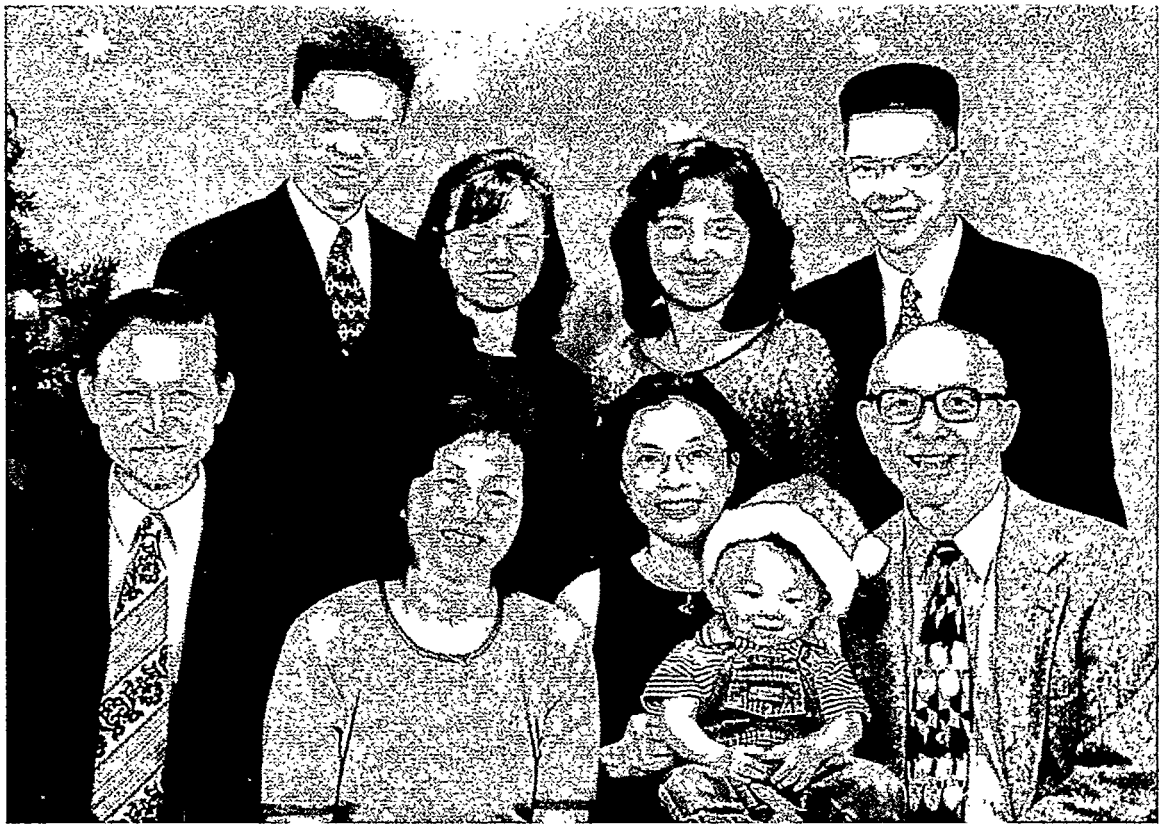

*Back row*: David and Blenda Loo (left), Bill and Elise Loo (right)
*Front row*: Lee Hong Tung and Ngai Lai Li (left), Billy (Sr.) and Lamae Loo, with William Ethan "Tiger" Loo (right)

## Sources of published chapters

This dissertation contains as several of its chapters materials reprinted from a number of published sources. These are listed below.

Chapter 2: Loo, B.W., Jr. & Rothman, S.S. (1995) High resolution microscopic imaging with x-rays: technology and application to the biological sciences. *Proceedings of WESCON'95, San Francisco, California, November 7-9, 1995*, pp. 668-672. IEEE.

Chapter 4: Loo, B.W., Jr., Brown, J.K. & Rothman, S.S. (1995) X-ray microtomography: three-dimensional reconstruction methods for x-ray microscopy of biological samples. *Three-Dimensional Microscopy: Image Acquisition and Processing II, San Jose, California, February 9-10, 1995.* (ed. by T. Wilson and C.J. Cogswell), Proceedings SPIE Vol. 2412, pp. 196-209.

Chapter 5: Loo, B.W., Jr., Williams, S., Lin, W.T., Love, W.H., Meizel, S. & Rothman, S.S. (1992) High resolution x-ray stereomicroscopy: true three-dimensional imaging of biological samples. *Soft X-Ray Microscopy, San Diego, CA, USA, July 19-21, 1992*, Proceedings SPIE Vol. 1741, pp. 393-401.

Chapter 6: Loo, B.W., Jr., Meyer-Ilse, W. & Rothman, S.S. (2000) Automatic image acquisition, calibration, and montage assembly for biological x-ray microscopy. *Journal of Microscopy*. **197**, 185-201.

Chapter 7: Loo, B.W., Jr., Parvin, B. & Rothman, S.S. (1996) Two- and three-dimensional segmentation for measurement of particles in the analysis of microscopic digital images of biological samples. *Three-Dimensional Microscopy: Image Acquisition*

*and Processing III, San Jose, California, January 30 - February 1, 1996.* (ed. by C.J. Cogswell, G.S. Kino, and T. Wilson), Proceedings SPIE Vol. 2655, pp. 209-215.

Chapter 8: Loo, B.W., Jr., Sauerwald, I.M., Hitchcock, A.P. & Rothman, S.S. (in press) A new sample preparation method for soft x-ray microscopy: nitrogen-based contrast and radiation tolerance properties of glycol methacrylate embedded and sectioned tissue. *Journal of Microscopy.*

Chapter 3 was written as a class project for Engineering 210 at the University of California, Berkeley (instructor Prof. D.T. Attwood) in 1994. Chapter 9 is being prepared for publication as a paper in a peer-reviewed journal.

## Abstract

The study of the exocrine pancreatic acinar cell has been central to the development of models of many cellular processes, especially of protein transport and secretion. Traditional methods used to examine this system have provided a wealth of qualitative information from which mechanistic models have been inferred. However they have lacked the ability to make quantitative measurements, particularly of the distribution of protein in the cell, information critical for grounding of models in terms of magnitude and relative significance. This dissertation describes the development and application of new tools that were used to measure the protein content of the major intracellular compartments in the acinar cell, particularly the zymogen granule. Soft x-ray microscopy permits image formation with high resolution and contrast determined by the underlying protein content of tissue rather than staining avidity. A sample preparation method compatible with x-ray microscopy was developed and its properties evaluated. Automatic computerized methods were developed to acquire, calibrate, and analyze large volumes of x-ray microscopic images of exocrine pancreatic tissue sections. Statistics were compiled on the protein density of several organelles, and on the protein density, size, and spatial distribution of tens of thousands of zymogen granules. The results of these measurements, and how they compare to predictions of different models of protein transport, are discussed.

## Table of Contents

## List of Tables

## List of Figures/Illustrations

# Chapter 1. Introduction

The focus of the work that led to this dissertation has been the quantitative characterization of the protein contents of the acinar cell of the exocrine pancreas, in the hope that proposed models of protein secretion could be evaluated in light of that information and their predictions tested. As discussed in some detail in the following chapters, this cellular system has long been studied and models of the processes involved in its main function, protein transport and secretion, have served as prototypes of models for many other cellular functions in many other cell types. The classical model of protein transport is based on now traditional methods that have allowed the description of ultrastructural morphology, specific biochemical identification and localization, and many other qualitative aspects of the cell (Palade, 1975; Rothman, 1975). However, quantitative measurements such as the determination of protein content at the level of individual subcellular structures have not been possible, except in bulk on components isolated and purified from their source tissue.

My colleague and predecessor Kaarin K. Goncz performed the first measurements of the protein content of individual subcellular organelles, zymogen granules, isolated from pancreatic tissue (Goncz, 1994). The work described in this manuscript, which I undertook with the help of many collaborators, is an extension of these measurements to a variety of intracellular organelles within their source tissue rather than in isolation. A large part of this effort was devoted to the development of new tools and technology that made these measurements possible, particularly soft x-ray microscopy and automated digital image processing and analysis. In this context a number of significant milestones were achieved. These include the dynamic imaging of initially living cells, three-

dimensional stereoscopic imaging, the imaging of sections of embedded whole soft tissues, and dual energy nitrogen-edge imaging, all firsts in high-resolution soft x-ray microscopy (Rothman *et al.*, 1992; Loo *et al.*, 1992b; Loo *et al.*, in press).

I took several approaches to studying the biological problem before settling on the one that proved the most fruitful in the end. Initially, I concentrated on dynamic studies of isolated whole cells, alive and suspended in an aqueous medium, with the intent of capturing the stimulated secretion events as they happened in the x-ray microscope. This work, covered briefly in some of the following chapters, met with some success, but also many technical challenges, including the difficulties of preparing isolated cells reliably, designing a sample handling system capable of manipulating these cells and their microenvironment, and protecting cells from the damaging effects of high-dose ionizing radiation. Because of the thickness of the cells, it also required the development of three-dimensional imaging methods in x-ray microscopy, which were nonexistent at the time (the early work in that area is described in Chapters 4 and 5).

Ultimately, much more rapid progress was made in developing a method of preparing sections of whole pancreatic tissue that had very favorable properties in an x-ray microscope. It was convenient and effectively solved many problems including those of sample handling, radiation damage, and sample thickness. Also, since the cells were not isolated, their organization in the tissue was preserved. However, dynamic studies were not possible in this system. Instead a statistical approach was taken to test predictions of how protein should be distributed in various intracellular compartments, especially the zymogen granule, under different mechanistic models. This required the compilation of statistics on large populations of organelles and large data sets, and therefore the

development of automated computerized methods for acquiring, calibrating, and analyzing the data. This experiment, which has turned out to be the largest x-ray microscopic study to date, and the computerized methods developed to help perform it are described in the later chapters.

Nearly all of the following chapters have been separately published or accepted for publication as conference proceedings articles or in peer-reviewed journals. As such, they span a range in time of the entire lifetime of the project so far, representing different stages of its development. They have been organized into three sections as follows.

Section 1 (Chapters 2 to 5) deals with the method of biological soft x-ray microscopy. Chapter 2 (Loo & Rothman, 1995) is an overview of biological x-ray microscopy, describing its unique features, relevance to biology, and enabling technologies. Chapters 3 and 4 discuss contrast theory in x-ray microscopy and such related issues as resolution, dose, and wavelength selection. Chapter 3 (Loo, 1994) focuses on the two-dimensional imaging case while Chapter 4 (Loo *et al.*, 1995) addresses three-dimensional imaging. Chapter 5 (Loo *et al.*, 1992a) presents some experimental proofs of principle, including three-dimensional imaging by stereomicroscopy and dynamic imaging of initially living cells.

Section 2 (Chapters 6 & 7) describes the automated methods developed to perform the biological experiment. Chapter 6 (Loo *et al.*, 2000) covers automatic acquisition and calibration of x-ray microscopic images as well as their assembly into large-field montages. Chapter 7 (Loo *et al.*, 1996) covers automatic image segmentation to identify and measure large numbers of zymogen granules in images of pancreatic tissue.

Section 3 (Chapters 8 & 9) describes the quantitative characterization of biological tissues by x-ray microscopy. Chapter 8 (Loo *et al.*, in press) describes the sample preparation method used, the radiation tolerance properties of the sample, and measurements of the distribution of its protein and plastic embedding medium components. Chapter 9 (Loo & Rothman, in preparation) presents the results of the experiment, quantitatively characterizing the distribution of protein in different compartments of the acinar cell, and its implications for models of protein transport.

## References


Goncz, K.K. (1994) A comprehensive study of the physical properties of isolated zymogen granules using scanning transmission x-ray microscopy. Graduate Group in Biophysics. University of California, Berkeley.

Loo, B.W., Jr. (1994) Density resolution and dose relationships in soft x-ray microscopy. Class project for Engineering 210, (instructor D.T. Attwood). University of California, Berkeley.

Loo, B.W., Jr., Brown, J.K. & Rothman, S.S. (1995) X-ray microtomography: three-dimensional reconstruction methods for x-ray microscopy of biological samples. Three-Dimensional Microscopy: Image Acquisition and Processing II, San Jose, California, February 9-10, 1995. (ed. by T. Wilson and C.J. Cogswell), Proceedings SPIE Vol. 2412, pp. 196-209.

Loo, B.W., Jr., Meyer-Ilse, W. & Rothman, S.S. (2000) Automatic image acquisition, calibration, and montage assembly for biological x-ray microscopy. Journal of Microscopy. **197**, 185-201.

Loo, B.W., Jr., Parvin, B. & Rothman, S.S. (1996) Two- and three-dimensional segmentation for measurement of particles in the analysis of microscopic digital images of biological samples. Three-Dimensional Microscopy: Image Acquisition and Processing III, San Jose, California, January 30 - February 1, 1996. (ed. by C.J. Cogswell, G.S. Kino, and T. Wilson), Proceedings SPIE Vol. 2655, pp. 209-215.

Loo, B.W., Jr. & Rothman, S.S. (1995) High resolution microscopic imaging with x-rays: technology and application to the biological sciences. Proceedings of WESCON'95, San Francisco, California, November 7-9, 1995, pp. 668-672. IEEE.

Loo, B.W., Jr. & Rothman, S.S. (in preparation) Quantitative characterization of the protein contents of the acinar cell of the exocrine pancreas by x-ray microscopy. .

Loo, B.W., Jr., Sauerwald, I.M., Hitchcock, A.P. & Rothman, S.S. (in press) A new sample preparation method for soft x-ray microscopy: nitrogen-based contrast and radiation tolerance properties of glycol methacrylate embedded and sectioned tissue. Journal of Microscopy.

Loo, B.W., Jr., Williams, S., Lin, W.T., Love, W.H., Meizel, S. & Rothman, S.S. (1992a) High resolution x-ray stereomicroscopy: true three-dimensional imaging of biological samples. Soft X-Ray Microscopy, San Diego, CA, USA, July 19-21, 1992, Proceedings SPIE Vol. 1741, pp. 393-401.

Loo, B.W., Jr., Williams, S., Meizel, S. & Rothman, S.S. (1992b) X-ray stereomicroscopy: high resolution 3-D imaging of human spermatozoa in aqueous suspension with natural contrast. Journal of Microscopy. **166**, RP5-RP6.

Palade, G. (1975) Intracellular aspects of the process of protein synthesis. Science. **189**, 347-358.

Rothman, S.S. (1975) Protein transport by the pancreas. Science. **190**, 747-753.

Rothman, S.S., Goncz, K.K. & Loo, B.W., Jr. (1992) Following protein transport with the high resolution x-ray microscope. X-Ray Microscopy III: Proceedings of the Third International Conference, London, September 3-7, 1990. (ed. by A.G. Michette, G.R. Morrison, and C.J. Buckley), pp. 373-383. Springer-Verlag, Berlin.

# Section 1: X-ray microscopy — overview, theoretical considerations, and proofs of principle

# Chapter 2. High resolution microscopic imaging with x-rays: technology and application to the biological sciences

## Introduction

Ever since the invention of the visible light microscope, there has been a quest for ever sharper views of microscopic biological structure. Even before the advent of electron microscopy, it was recognized that the short wavelengths of x-rays could in principle allow high resolution imaging. But only in the last decade or so have technological advances made the original promise of biological x-ray microscopy realizable (Rudolph *et al.*, 1984; Howells *et al.*, 1991). These advances include the development of sources, optics, and detectors for the low energy x-rays ("soft" x-rays) best suited for imaging cellular structure.

Modern x-ray microscopy (XM) is a versatile tool that offers several modes of operation and a variety of contrast mechanisms. Some of these may be viewed simply as high resolution extensions of existing visible light methods, while others are unique to x-rays, allowing new views of biological samples.

XM fills a special niche between visible light microscopy (VLM) and electron microscopy (EM): it combines resolution beyond VLM, currently 30 to 50 nm, with penetration depth much greater than EM, up to several micrometers of water and organic material. Thus it can be used to image whole cells in an aqueous environment, in a near native state, potentially even living. In addition, it is capable of quantitative, element specific mapping with high sensitivity.

Finally, XM benefits from the same kinds of digital imaging technologies as have numerous other modern microscopies. X-ray micrographs are digitized as part of the imaging process because of the electronic detectors used, producing quantitative representations of signal strength. Digital image processing can then be used to perform automated feature detection and measurement, correction of optical blurring, and tomographic reconstruction of three-dimensional structure.

**X-ray technologies**

Most of this century has seen the development of x-ray microscopy languish behind visible light and electron methods: unlike the case of microscopies using these other forms of radiation, there has until recently been no adequate way to produce, focus, and detect soft x-rays. The coming together of new technologies in these areas have now made XM a practical biological instrument.

Synchrotron accelerators are used as high brightness sources of x-rays (Attwood *et al.*, 1985). In such an accelerator, a beam of electrons traveling at near light speed emits synchrotron radiation at x-ray wavelengths as it travels a ring shaped path. Precisely manufactured reflective diffraction gratings can be used to disperse the radiation according to wavelength, allowing the selection of monochromatic x-rays of the desired wavelength. In addition, inserting a straight section into the ring with a periodic magnetic structure called an undulator produces a laser-like x-ray beam with a high degree of spatial coherence, a prerequisite for scanning microscopy. Thus wavelength-tunable sources with varying degrees of coherence to meet the needs of the desired application are now available for microscopy.

Because soft x-rays are strongly attenuated by any substantial thickness of most materials, lenses that work by refraction cannot be used. Fresnel zone plates, diffractive optical elements consisting of alternating opaque and transmissive circular zones, act as lenses with a resolution determined by the size of their features, with smaller sizes corresponding to higher resolution (Anderson, 1989). Microelectronic fabrication methods are used to produce zone plates with feature dimensions currently as small as 30 nm, or about ten times the wavelength of the x-rays, and with approximately the same resolution. The ability to fabricate small features continues to improve, and along with it resolution. A full field imaging microscope analogous to a conventional visible light microscope can be built using zone plates as condenser and objective lenses. Alternatively, a single zone plate lens can be used to focus a coherent beam to a fine point, for use as a scanning probe.

Detectors sensitive to soft x-rays now exist that combine high detection efficiency and low noise with a linear response to x-ray intensity over a large dynamic range (Wilhein *et al.*, 1994). The result is a signal quality limited essentially only by photon counting statistics. The area detector of choice for imaging microscopes is a back-side thinned and illuminated charge coupled device (CCD) camera. For point by point scanning, the typical detectors are a gas proportional counter or an avalanche photodiode.

**Imaging with x-rays**

Contrast between features of interest and the surrounding background is critical to any form of microscopy. For most kinds of microscopy, some kind of staining is required

to produce the necessary contrast. Many of the numerous staining protocols that have been developed over the years for both VLM and EM are useful for XM as well.

Heavy metal stains such as those used for EM attenuate x-rays much more strongly than organic material, and can serve as contrast agents for XM as well (Balhorn *et al.*, 1992). Because of the greater penetration depth of x-rays, XM can be used for high resolution imaging when the extensive sample preparation required for EM such as dehydration, embedding, and sectioning is undesirable.

Immunolabeling has become a staple of modern microscopy because of the molecular specificity it affords. Heavy metals and fluorescent probes attached to antibodies specific to molecules of interest have been used as contrast agents for EM and VLM, respectively. As mentioned, the heavy metal probes work with XM on the basis of x-ray attenuation. It is also possible to use the finely focused x-ray probe of a scanning x-ray microscope to excite visible light luminescence in fluorescent probes, and thereby do immunofluorescence microscopy at XM resolutions (Jacobsen *et al.*, 1993; Irtel von Brenndorff *et al.*, 1994).

**Unique features**

What makes XM unique is the ability to do quantitative imaging with practically no sample preparation other than isolation of the cells or other biological structures from their source (Rothman *et al.*, 1992). Not even fixation or staining is required unless especially desirable for a specific application. Figure 2-1 illustrates the strength of attenuation of x-rays by protein and water with respect to x-ray energy (Henke *et al.*, 1993). In the energy range between the inner shell electron binding energies for carbon

and oxygen (x-ray wavelengths 44Å and 23Å, respectively), the difference in attenuation between protein (or any carbon and nitrogen containing molecule) and water provides a natural contrast mechanism based solely on constituents already present in the sample. This soft x-ray energy range is known as the "water window." The mass of the sample can be computed readily on a pixel by pixel basis from the intensity of x-ray transmission through the sample.

In the authors' own work, we are interested in changes in protein content within the secretory vesicles of pancreatic acinar cells at various stages of secretion (Goncz & Rothman, 1992; Goncz *et al.*, 1995). XM has been central to our ability to make these measurements. Figure 2-2 shows a transmission x-ray micrograph of a pancreatic acinar cell containing dense secretory vesicles, with darker or more absorptive structures corresponding to greater protein mass. In general, quantitation of the protein as well as other contents of intact intracellular compartments, be they vesicles or endoplasmic reticulum or Golgi apparatus, is done poorly if at all by other methods.

In addition, the sharp transition in the attenuation coefficient at the absorption edge for a particular element permits the use of dual energy imaging for quantitative mapping of that element with high sensitivity. The water window contains absorption edges for several biologically interesting elements, including among others, carbon, nitrogen, calcium, and potassium. For example, XM has been used for calcium mapping in bone (Kenney *et al.*, 1985; Jacobsen *et al.*, 1987).

## Digital imaging

The images formed in x-ray microscopes are recorded electronically and stored directly as digital data. This greatly facilitates image measurement and analysis. It also allows the application of the large suite of advanced digital imaging tools, both existing and under development, to XM.

In order to make statistically meaningful measurements on the physical properties of biological systems, which typically have a great variance, it is necessary to analyze large volumes of data. Practicality demands that such measurements be automated. For example, to approach the secretion problem, we are developing computer algorithms to automatically recognize and compile population statistics on secretory granules within pancreatic cells (Loo *et al.*, 1996). Figure 2-3 demonstrates this process, showing the cell from Figure 2-2 with its granules highlighted by the recognition algorithm, and the histogram of granule sizes for the cell. To perform the equivalent task manually on a large number of cells would be prohibitive.

Computerized reconstruction methods can be used to correct a number of artifacts that are introduced by the imaging process. One such artifact is image blurring due to the finite aperture of the lens (Jacobsen *et al.*, 1991). Another is the projection of three-dimensional structure onto two-dimensional images. As in the case of medical x-ray tomography, a large number of projections made at different view angles can be used to reconstruct the three-dimensional sample structure by computerized tomography (Loo *et al.*, 1992b; Loo *et al.*, 1992a; Loo *et al.*, 1995). This should be applicable to XM in both transmission and x-ray stimulated luminescence modes. Efforts are currently under way

at a number of x-ray microscopy facilities to implement the hardware for sample rotation for tomography.

**Future directions**

The basic instrumentation technologies of x-ray microscopy have been improving continually. Progress in optics fabrication and detector technology will result in higher resolution, a larger range of usable x-ray energies, and reduced imaging time and radiation dose. Increased computerized control of the microscopes will lead to automated imaging and higher sample throughput.

However, the greatest room for growth in XM is in the area of sample handling technology and its incorporation into microscope designs. Depending on the needs of particular applications, temperature controlled sample stages, including cryogenic stages, environmental sample chambers for the injection of hormones and nutrients, rotational stages for three-dimensional imaging, and a large variety of others are being or will be developed, as will new contrast modes and staining protocols specifically designed for XM.

X-ray microscopy has now reached the level of maturity in which the biological experiment is the ultimate driving force behind the technology.

## Figures

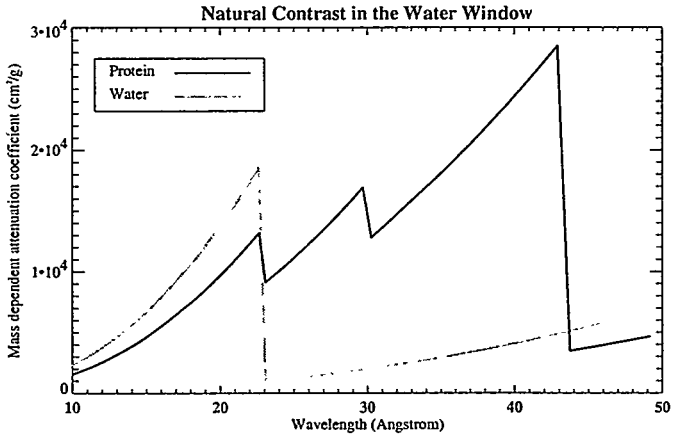


**Figure 2-1**

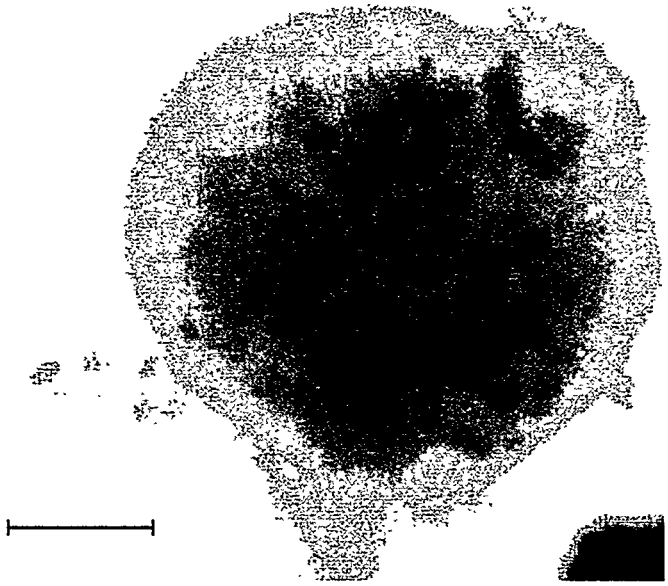

**Figure 2-2**

Isolated pancreatic acinar cell containing zymogen granules. Cell is in water, unfixed and unstained. Scale bar is 5 micrometers.

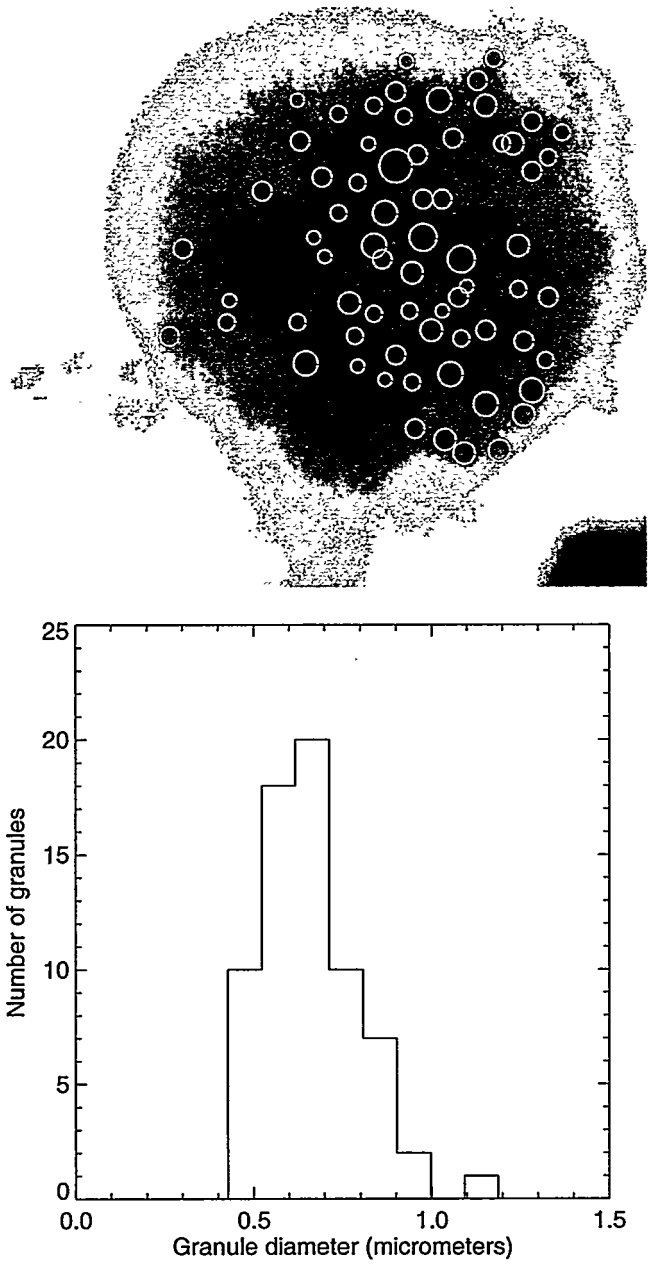


**Figure 2-3**
Automated recognition and compilation of statistics on zymogen granules by the computer.

## References


Anderson, E.H. (1989) Fabrication technology and applications of zone plates. *X-Ray/EUV Optics for Astronomy and Microscopy, San Diego, California, August 7-11, 1989.* (ed. by R.B. Hoover), Proceedings SPIE Vol. 1160, pp. 1-10.

Attwood, D.T., Halbach, K. & Kim, K.J. (1985) Tunable coherent x-rays. *Science.* **228**, 1265-1272.

Balhorn, R., Corzett, M., Allen, M.J., Lee, C., Barbee, T.W., Jr., Koch, J.A., MacGowan, B.J., Matthews, D.L., Mrowka, S.J., Trebes, J.E., McNulty, I., Da Silva, L.B., Gray, J.W., Anderson, E.H., Kern, D. & Attwood, D.T., Jr. (1992) Application of x-rays to the analysis of DNA packaging in mammalian sperm. *Soft X-Ray Microscopy, San Diego, CA, USA, July 19-21, 1992.* (ed. by C. Jacobsen and J.E. Trebes), Proceedings SPIE Vol. 1741, pp. 374-385.

Goncz, K.K., Behrsing, R. & Rothman, S.S. (1995) The protein content and morphogenesis of zymogen granules. *Cell and Tissue Research.* **280**, 519-530.

Goncz, K.K. & Rothman, S.S. (1992) Protein flux across the membrane of single secretion granules. *Biochimica et Biophysica Acta.* **1109**, 7-16.

Henke, B.L., Gullikson, E.M. & Davis, J.C. (1993) X-ray interactions: photoabsorption, scattering, transmission, and reflection at E=50-30000 eV, Z=1-92. *Atomic Data and Nuclear Data Tables.* **54**, 181-342.

Howells, M.R., Kirz, J. & Sayre, D. (1991) X-ray microscopes. *Scientific American.* **264**, 42-48.

Irtel von Brenndorff, A., Moronne, M.M., Larabell, C., Selvin, P. & Meyer-Ilse, W. (1994) Soft x-ray stimulated high resolution luminescence microscopy. *X-Ray Microscopy IV: Proceedings of the Fourth International Conference, Chernogolovka, Russia, September 20-24, 1993.* (ed. by V.V. Aristov and A.I. Erko). Bogorodskii Pechatnik, Chernogolovka.

Jacobsen, C., Kenney, J.M., Kirz, J., Rosser, R.J., Cinotti, F., Rarback, H. & Pine, J. (1987) Quantitative imaging and microanalysis with a scanning soft x-ray microscope. *Physics in Medicine and Biology*. **32**, 431-437.

Jacobsen, C., Lindaas, S., Williams, S. & Zhang, X. (1993) Scanning luminescence x-ray microscopy: imaging fluorescence dyes at suboptical resolution. *Journal of Microscopy*. **172**, 121-129.

Jacobsen, C., Williams, S., Anderson, E., Browne, M.T., Buckley, C.J., Kern, D., Kirz, J., Rivers, M. & Zhang, X. (1991) Diffraction-limited imaging in a scanning transmission x-ray microscope. *Optics Communications*. **86**, 351-364.

Kenney, J.M., Jacobsen, C., Kirz, J., Rarback, H., Cinotti, F., Thomlinson, W., Rosser, R. & Schidlovsky, G. (1985) Absorption microanalysis with a scanning soft x-ray microscope: mapping the distribution of calcium in bone. *Journal of Microscopy*. **138**, 321-328.

Loo, B.W., Jr., Brown, J.K. & Rothman, S.S. (1995) X-ray microtomography: three-dimensional reconstruction methods for x-ray microscopy of biological samples. *Three-Dimensional Microscopy: Image Acquisition and Processing II, San Jose, California, February 9-10, 1995*. (ed. by T. Wilson and C.J. Cogswell), Proceedings SPIE Vol. 2412, pp. 196-209.

Loo, B.W., Jr., Parvin, B. & Rothman, S.S. (1996) Two- and three-dimensional segmentation for measurement of particles in the analysis of microscopic digital images of biological samples. *Three-Dimensional Microscopy: Image Acquisition and Processing III, San Jose, California, January 30 - February 1, 1996*. (ed. by C.J. Cogswell, G.S. Kino, and T. Wilson), Proceedings SPIE Vol. 2655, pp. 209-215.

Loo, B.W., Jr., Williams, S., Lin, W.T., Love, W.H., Meizel, S. & Rothman, S.S. (1992a) High resolution x-ray stereomicroscopy: true three-dimensional imaging of biological samples. *Soft X-Ray Microscopy, San Diego, CA, USA, July 19-21, 1992*, Proceedings SPIE Vol. 1741, pp. 393-401.

Loo, B.W., Jr., Williams, S., Meizel, S. & Rothman, S.S. (1992b) X-ray stereomicroscopy: high resolution 3-D imaging of human spermatozoa in aqueous suspension with natural contrast. *Journal of Microscopy*. **166**, RP5-RP6.

Rothman, S.S., Goncz, K.K. & Loo, B.W., Jr. (1992) Following protein transport with the high resolution x-ray microscope. *X-Ray Microscopy III: Proceedings of the Third International Conference, London, September 3-7, 1990.* (ed. by A.G. Michette, G.R. Morrison, and C.J. Buckley), pp. 373-383. Springer-Verlag, Berlin.

Rudolph, D., Niemann, B., Schmahl, G. & Christ, O. (1984) The Göttingen x-ray microscope and x-ray microscopy experiments at the BESSY storage ring. *X-Ray Microscopy: Proceedings of the International Symposium, Göttingen, September 14-16, 1983.* (ed. by G. Schmahl and D. Rudolph). Springer-Verlag, Berlin.

Wilhein, T., Rothweiler, D., Tusche, A., Scholze, F. & Meyer-Ilse, W. (1994) Thinned, back-illuminated CCDs for x-ray microscopy. *X-Ray Microscopy IV: Proceedings of the Fourth International Conference, Chernogolovka, Russia, September 20-24, 1993.* (ed. by V.V. Aristov and A.I. Erko), pp. 470-474. Bogorodskii Pechatnik, Chernogolovka.

## Chapter 3. Density resolution and dose relationships in soft x-ray microscopy

### Introduction

Soft x-ray microscopy has some unique features that make it attractive for imaging biological samples: 1. Short wavelength — it is possible to achieve higher resolution than with visible light; 2. Good penetration through air, water, and organic material — it is possible to image whole cells (up to 10 μm thick) in "natural" environment; 3. Element specific contrast — it is possible to image without stains; 4. Quantitative densitometry (especially in absorption contrast mode).

Soft x-rays have enough energy to cause ionizations — radiation damage is an important consideration. To measure a given feature, what dose must be applied, and on what factors does it depend?

### The Rose model of feature detectability

Let us consider the problem of detecting a weak signal against a noisy background. Following a well-known argument by Rose (Rose, 1973), we take the mean background intensity to be I, with a standard deviation $\sigma_I$. The feature we wish to detect differs on average from the background by ΔI. In order to detect the feature, we require that the signal deviate from the background by at least k standard deviations. In other words, the relationship describing the detectability threshold is:

$$\Delta I = k\sigma_I \tag{1}$$

Dividing both sides by I, and defining contrast $C = \Delta I/I$, and signal to noise ratio $SNR = I/\sigma_I$, we have:

$$k = C \times SNR. \tag{2}$$

According to Rose, for the human visual system, k must be at least 5 for a feature to be detectable. This is known as the Rose criterion.

**Application to x-ray microscopy**

We consider the case of absorption contrast. The derivation is similar to one by Howells (Howells, 1990; Howells, 1992). The relationship describing transmission of x-rays through a material is Beer's Law:

$$N = N_0 \, e^{-\rho_a \mu} \tag{3}$$

where N is the mean number of photons transmitted for $N_0$ incident photons, $\rho_a$ is the plane-projected density (mass per unit area, or areal density) of the material, and $\mu$ is its mass dependent absorption coefficient, which depends on photon energy.

As an example of a biological sample, the material we consider is protein in water. Our sample model is the following: we wish to measure a difference in protein areal density of $\Delta\rho_a$ on a background of protein of density $\rho_a$. We can consider $\Delta\rho_a$ to be the desired density resolution. Furthermore, the sample is immersed in a water layer of thickness $t_w$. We make the approximation that to first order, the protein is completely solvated and displaces a negligible amount of water, *i.e.*, the water is of uniform density ($\rho_w = 1$ g/cm$^3$) throughout the sample. We also assume that the only source of noise is Poisson

counting statistics, so that if our background signal is N counts per area element, then $\sigma_N = \sqrt{N}$.

First, we derive an expression for contrast. Differentiating equation (3) we have:

$$\frac{dN}{d\rho_a} = -\mu N \tag{4}$$

so that for small $\Delta\rho_a$:

$$C = \frac{\Delta N}{N} \approx -\mu \Delta\rho_a \tag{5}$$

Substituting into equations (2) and (3), and noting that the Beer's Law expression must now account for transmission through both protein and water, with $\rho_w$, $t_w$, and $\mu_w$ representing density, thickness, and absorption coefficient for water, we have:

$$k = \mu \Delta\rho_a \sqrt{N} = \mu \Delta\rho_a \sqrt{N_0 e^{-(\rho_a \mu + \rho_w t_w \mu_w)}} \tag{6}$$

We now consider the dose absorbed by protein directly, and the dose to the surrounding water. Dose to water is important since free radical species from water radiolysis can damage biological macromolecules.

Dose is defined as energy absorbed per unit mass, and is proportional to the photon energy and the number of absorbed photons, and inversely proportional to feature area. To calculate the number of photons absorbed by protein, $N_{P,abs}$, we must take into account that the surrounding water partially shields the protein, and introduce a geometry dependent shielding factor, $\gamma$, to give:

$$N_{P,abs} = N_0\,(1 - e^{-\rho_a \mu})\, e^{-\gamma(\rho_w t_w \mu_w)} \tag{7}$$

Solving for $N_0$ in equation (6) and substituting, the direct dose to protein is:

$$D_P = \frac{h\upsilon \times N_{P,abs}}{A\,\rho_a} = \frac{h\upsilon}{A\,\rho_a}\left(\frac{k}{\mu\,\Delta\rho_a}\right)^2 (e^{\rho_a \mu} - 1)\, e^{\rho_w t_w \mu_w (1-\gamma)} \tag{8}$$

where A is the feature area. In the limit of very low background density ($\rho_a \approx 0$), equation (8) reduces to:

$$D_P \approx \frac{h\upsilon}{A\mu}\left(\frac{k}{\Delta\rho_a}\right)^2 e^{\rho_w t_w \mu_w (1-\gamma)} \tag{9}$$

which has lost its dependence on $\rho_a$. Following similar reasoning, the dose to the surrounding water is:

$$D_W = \frac{h\upsilon}{A\rho_w t_w}\left(\frac{k}{\mu\,\Delta\rho_a}\right)^2 (e^{\rho_w t_w \mu_w} - 1)\, e^{\rho_a \mu (1-\gamma')} \tag{10}$$

Note that if water shields the protein completely, *i.e.*, photons must pass through the entire water layer before reaching the protein, then $\gamma = 1$ and $\gamma' = 0$, and *vice versa*.

**Simulation and Results**

The figures to follow demonstrate the above relationships when applied to a cell phantom. The parameters of the phantom are as follows:

1. Cell: elliptical cylinder of protein, with width 5 μm and major and minor diameters of 5 and 4 μm, and density 0.12 g/cm$^3$ ($4.8\times10^{-5}$ g/cm$^2$ at peak).

2. Granules: 1 μm cubes of protein with density 0.30 g/cm$^3$ ($3.0\times10^{-5}$ g/cm$^2$).

3. Aggregates: 400 Å cubes of protein inside granules with areal densities of $3.0\times10^{-6}$, $6.0\times10^{-6}$, $7.5\times10^{-6}$, and $9.0\times10^{-6}$ g/cm$^2$, corresponding respectively to 10, 20, 25, and 30 per cent of the granule areal density.

4. Fibers: 566 Å wide bars of protein inside the cell with density 0.30 g/cm$^3$ ($1.76\times10^{-6}$ g/cm$^2$).

5. Pixel size is 200 Å. Areal densities are summed where features superimpose.

Figure 3-1 shows mass absorption coefficients, dose to protein, and dose to water as functions of photon energy. For these plots, dose is determined according to the Rose criterion of detectability ($k = 5$) for the protein aggregates (400×400 Å area, various values of $\Delta\rho_a$) in the thickest part of the cell ($\rho_a = 7.80\times10^{-5}$ g/cm$^2$). As a reasonable guess, we assume a value of 0.5 for both $\gamma$ and $\gamma'$. The difference between the absorption coefficients of protein and water in the spectral range between the K-shell absorption edges of carbon and oxygen (the "water window") account for the ability to do absorption contrast imaging. Here, protein is taken roughly to have the composition $C_{3.13}H_{4.98}O_{1.01}N_{0.85}S_{0.03}$.

In Figures 3-1b and 3-1c, the optimal photon energy is the one for which the threshold dose is the lowest. They demonstrate the following relationships: decreasing

$\Delta\rho_a$ shifts the required dose up; decreasing the background ($\rho_a = 5.77$ g/cm$^2$) shifts the optimal energy to the lower energy end of the water window; increasing the shielding of protein by water ($\gamma = 0.75$, $\gamma' = 0.25$) lowers the optimal energy for dose to protein, but increases it for dose to water.

Figure 3-2a shows the density map for the phantom. Figure 3-2b shows the transmission probability maps for the phantom at wavelengths of 29.7 Å (417.5 eV) and 23.1 Å (536.7 eV), corresponding to the best and worst energies, respectively, within the water window for detecting the $6.0\times10^{-6}$ g/cm$^2$ aggregate in the thickest part of the cell. Figure 3-2c shows the same images with the display rewindowed for maximum contrast in the region of interest.

Figures 3-3a to 3-3c show the maps of photon counts for these two wavelengths when the dose is $7.29\times10^5$, $5.30\times10^5$, and $2.33\times10^5$ Gray, corresponding respectively to k = 5 at 23.1 Å, k = 5 at 29.7 Å, and k = 5 at 29.7 Å for the densest aggregate. Figure 3-4 shows the same images rewindowed for maximum contrast. Finally, Figure 3-5 shows the corresponding line plots through the features of interest, superimposed and displaced for comparison to the noise-free case.

As can be seen in the figures, the difference between the best and worst energies is not great — usually within a factor of 2 — and not strongly sensitive to the background density and distribution geometry. Also, k = 5 seems to be a relatively conservative threshold criterion. The doses in this example are quite high, but typically, small differences in volume density add up to greater differences in areal density than modeled here, and the features of interest usually have structure over an area of more than a few pixels

(*e.g.*, the fibers appear readily detectable even though k is quite small over a 400 Å wide area). These factors would tend to decrease the dose required.

## Conclusions

For absorption contrast, the best photon energies from the perspective of the contrast to dose ratio are in the water window. Within the water window, differences are not great — other experimental factors (or breakdowns in assumptions) may have a stronger influence on choice of photon energy. Such factors include sample thickness and depth of focus, and optical and detective quantum efficiency. The recommendation based on the simulations here is: for thin samples (< 3 μm) use a wavelength of around 36 Å or 344 eV (between C & N absorption edges); for thick samples (< 10 μm) use a wavelength of around 24 Å or 517 eV (close to O absorption edge).

## Figures

Fig. 1a: Mass absorption coefficients for protein and water

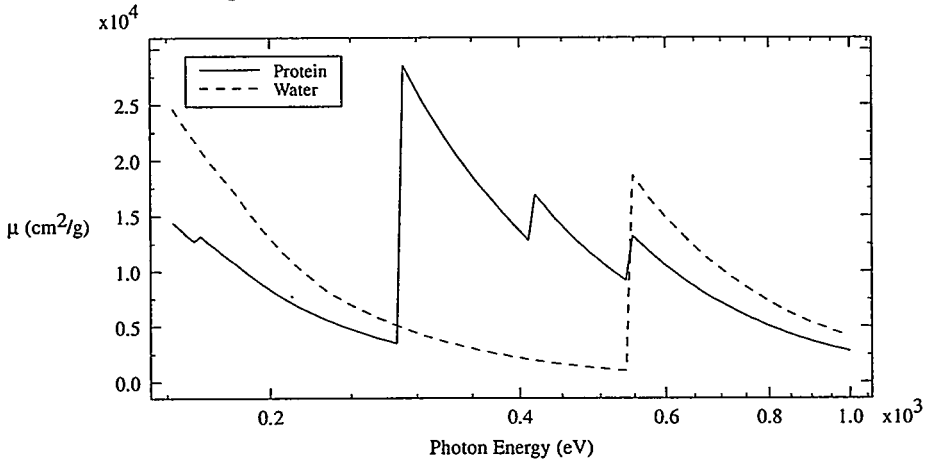


Fig. 1b: Direct dose to protein (400 Å resolution, k=5)

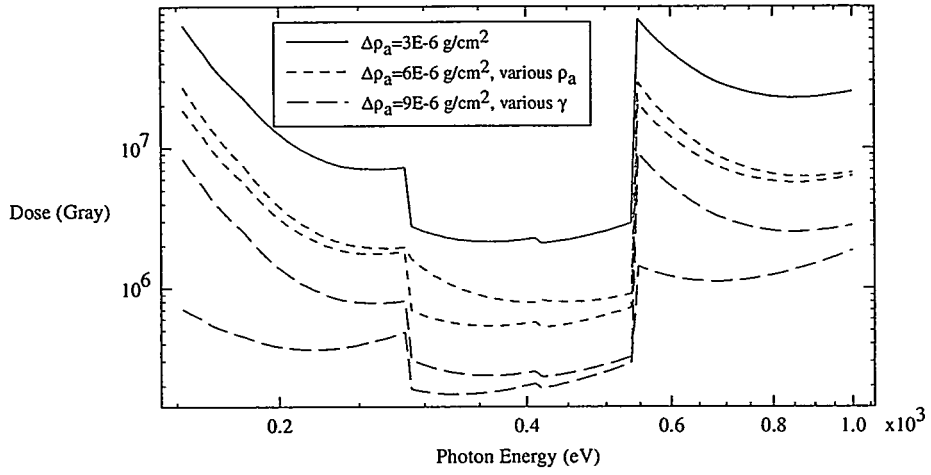


Fig. 1c: Dose to water (400 Å resolution, k=5)

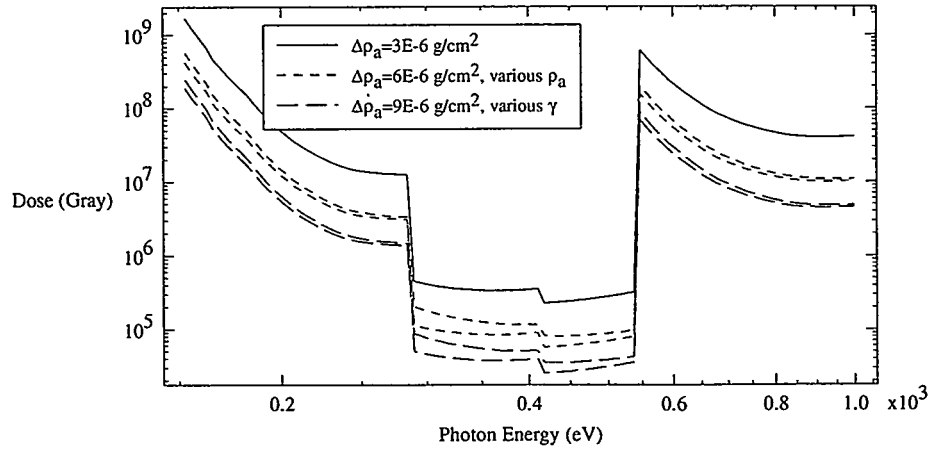


**Figure 3-1**

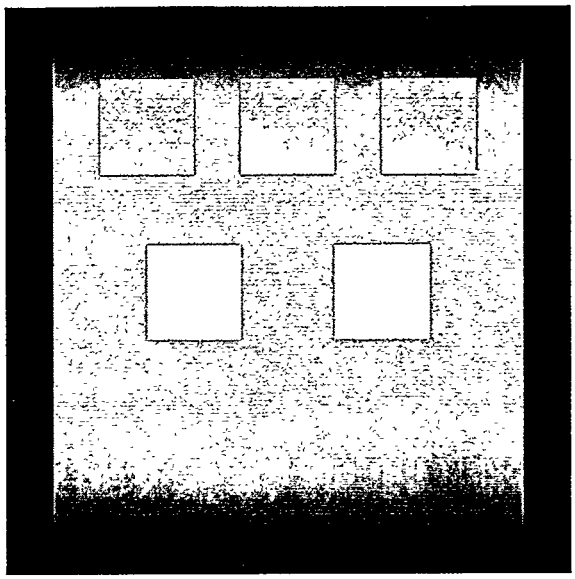

2a

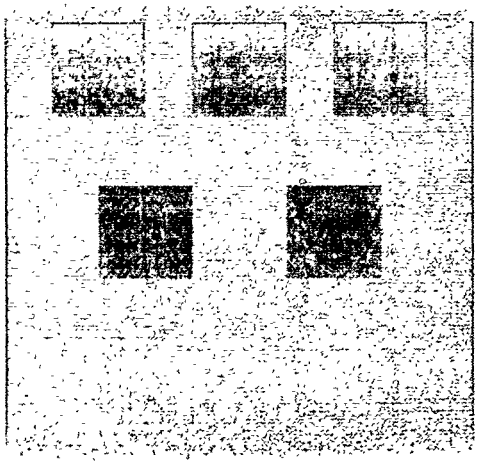

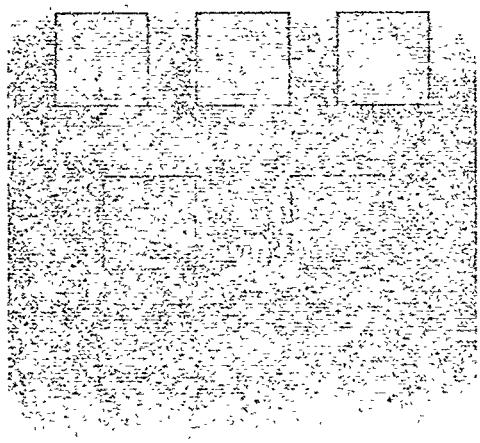

2b

2c

**Figure 3-2**

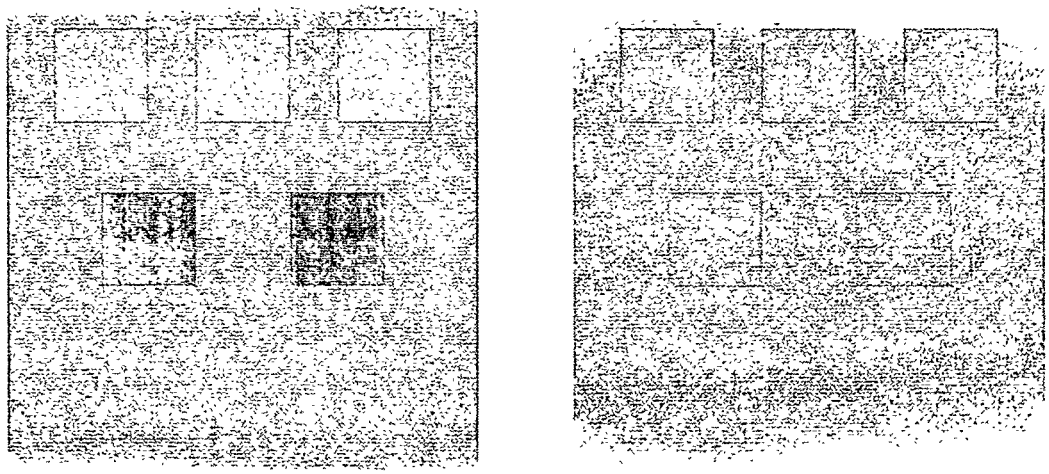

3a

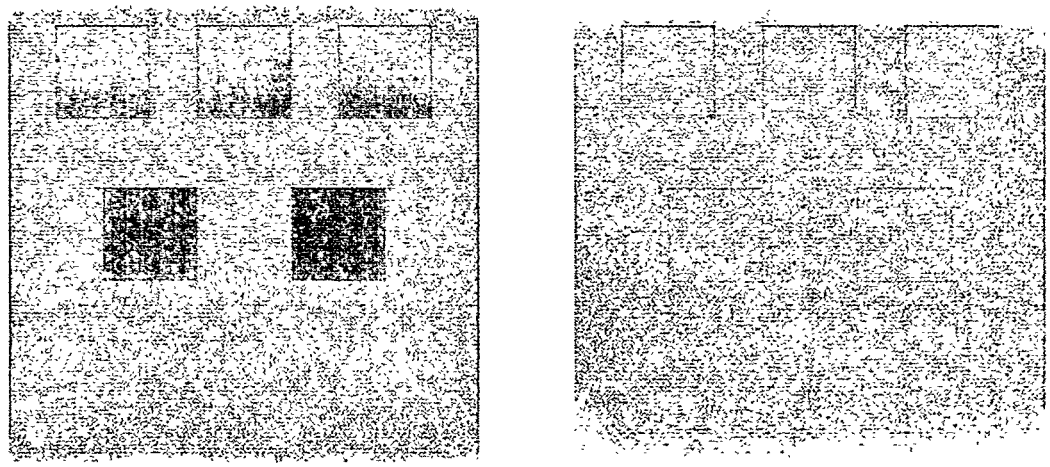

3b

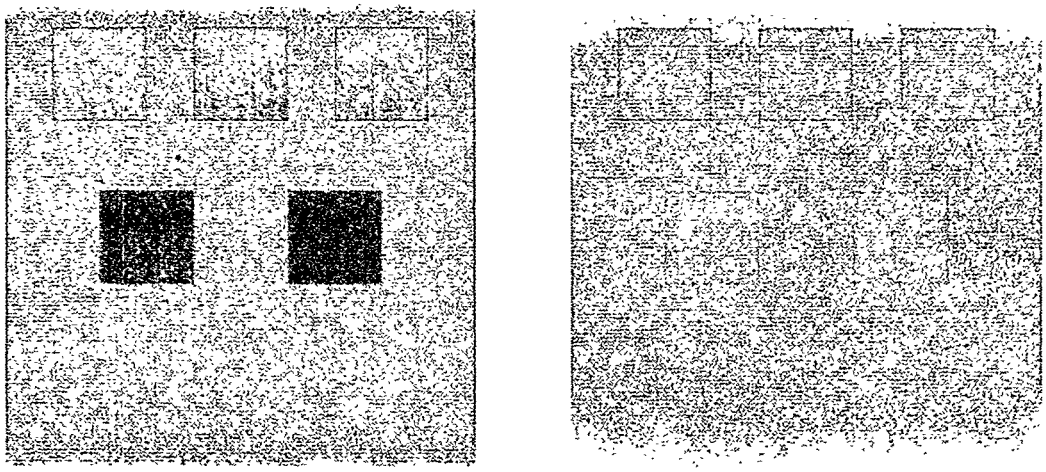

3c

**Figure 3-3**

4a

4b

4c

**Figure 3-4**

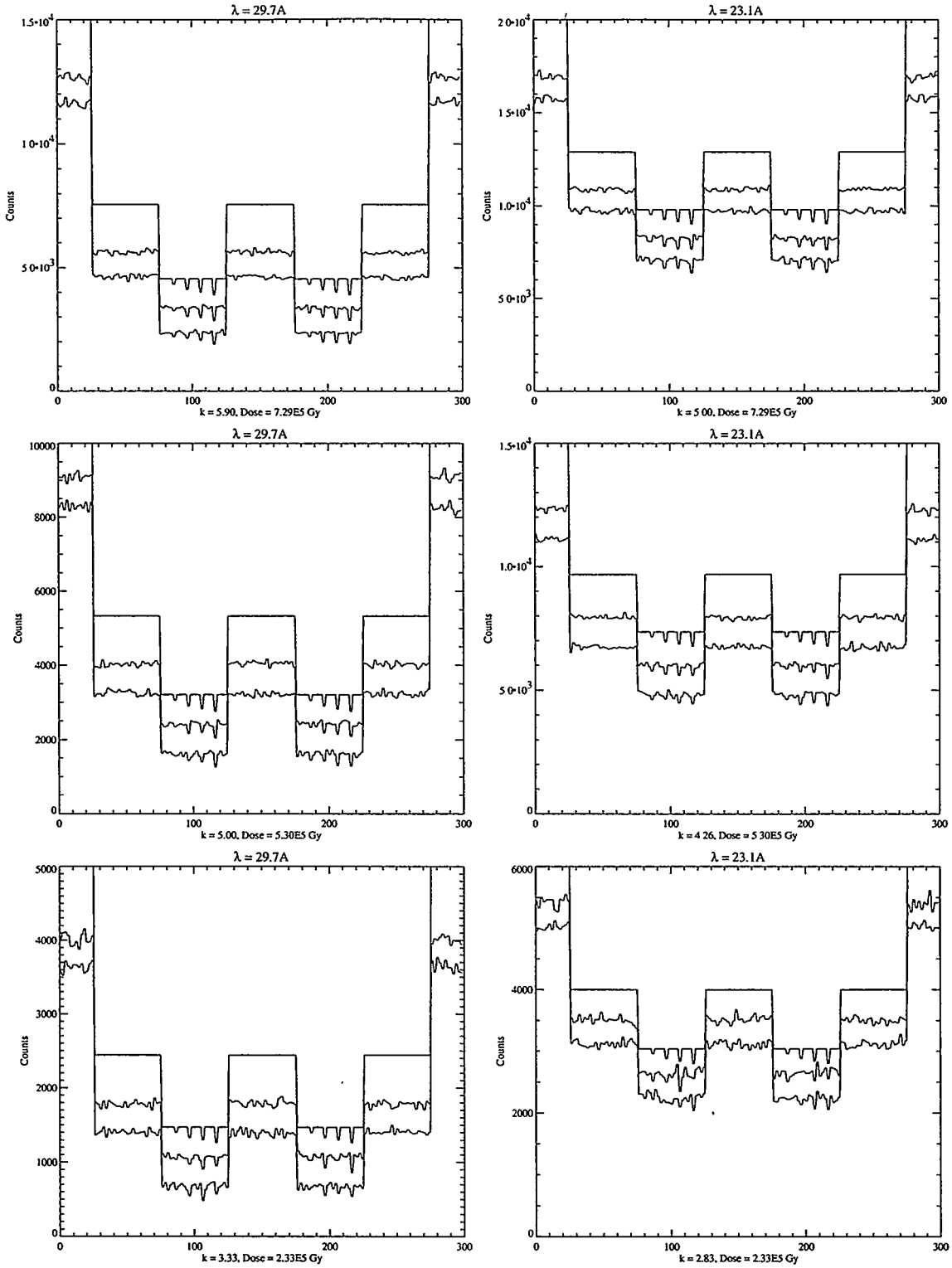
λ = 29.7A
Counts
k = 5.90, Dose = 7.29E5 Gy
λ = 23.1A
Counts
k = 5.00, Dose = 7.29E5 Gy
λ = 29.7A
Counts
k = 5.00, Dose = 5.30E5 Gy
λ = 23.1A
Counts
k = 4.26, Dose = 5.30E5 Gy
λ = 29.7A
Counts
k = 3.33, Dose = 2.33E5 Gy
λ = 23.1A
Counts
k = 2.83, Dose = 2.33E5 Gy

**Figure 3-5**

## References

Howells, M.R. (1990) Soft x-ray imaging for the life sciences. *Synchrotron Radiation and Biophysics.* (ed. S. Hasnain), Halsted Press. New York.

Howells, M.R. (1992) Contrast mechanisms in x-ray microscopy. *X-Ray Microscopy III.*

Rose, A. (1973) Chap. 1 and 2 in *Vision: human and electronic*, Plenum Press. New York.

## Chapter 4. X-ray microtomography: three-dimensional reconstruction methods for x-ray microscopy of biological samples


### Abstract

Biological soft x-ray microscopy using x-ray optics and synchrotron sources has made possible quantitative, element-specific imaging of whole cells in aqueous media at significantly higher resolutions than those of conventional visible light methods. Tomographic reconstruction has been proposed as a means to realize the full potential of the method for viewing thick objects whose structures would otherwise be superimposed in single view projections. The authors present an iterative tomographic reconstruction algorithm, using a regularized weighted least squares objective function, accelerated with the conjugate gradient approach, and modified for the problem of transmission tomography with correction of blurring by an instrumental point spread function. The non-negativity constraint is implemented using a preconditioner. We show by computer simulations that reconstructions that meet realistic and acceptable goals for spatial and density resolution should be achievable at doses compatible with the structural integrity of biological samples at the specified resolution.


### Introduction

*Motivation:*

Our desire to develop novel imaging methods complementary to existing ones was motivated originally by our study of mechanisms of cellular protein transport and secretion in the exocrine cell of the pancreas (Goncz & Rothman, 1992; Goncz *et al.*,

1995). In particular, the problem required the ability to determine quantitatively the protein content and distribution within an intracellular compartment, the roughly spherical zymogen granules of the pancreatic acinar cell, and to measure changes in these parameters with the physiological state. The advent of x-ray microscopy made it possible to make these measurements in the zymogen granule. Clearly however, such a method would have much broader utility if it could be applied to organelles with finer or more complicated 3-D structure, and which are difficult to isolate intact, such as endoplasmic reticulum or Golgi apparatus. Indeed, there appear to be no existing methods to measure protein content within such compartments.

In addition to the protein content, a question of interest is the 3-D topology of intracellular compartments. Recently, high resolution scanning electron microscopy has been used to reveal features of intracellular structure that appear to challenge traditional views, demonstrating direct communications between the endoplasmic reticulum and Golgi apparatus, and between adjacent Golgi cisternae (Tanaka & Fukudome, 1991; Tanaka *et al.*, 1986). While the SEM technique is capable of very high resolution, on the order of a few nanometers, it can only visualize surfaces, and therefore requires fracturing the cell and removing all the non-membrane matrix components. Also, foreground objects obscure the view of background structures, so that the determination of topology is incomplete. A complementary transmission method could in principle overcome some of these limitations, while allowing in addition the measurement of intra- and intercompartmental contents.

*Advantages of soft x-ray illumination for biological microimaging:*

The recent technologies of microfabricated diffractive optics and synchrotron radiation sources have made it possible to build practical x-ray microscopes that realize the theoretical advantages of soft x-ray illumination that had been understood for about a century previously (Howells *et al.*, 1991). The achievable resolution is in principle limited by the wavelength of the radiation to about 2 - 4 nm, though currently it is limited by the ability to manufacture lenses with sufficiently fine structure to about 30 - 50 nm, or about 5 - 7 times better than conventional visible light resolutions. Also, the attenuation length of x-rays in organic material and water is significantly longer than that of electrons, on the order of several micrometers, allowing the imaging of whole cells in an aqueous environment without sectioning. In these ways, x-ray microscopy fills a niche between visible light and electron microscopies.

One aspect unique to the x-ray method is the mode of interaction between the x-ray photons and the material examined. At these photon energies, the primary interaction is inner shell absorption of the photons by the typically low Z atoms of biological material (Howells *et al.*, 1991). Figure 4-1 shows the mass dependent attenuation coefficients of protein and water as a function of wavelength. In protein, the K shell absorption edges due to carbon (44 Å), nitrogen (31 Å), and oxygen (23 Å) are clearly demonstrated. Thus in the energy window between the carbon and oxygen absorption edges, known as the "water window," protein absorbs x-rays much more strongly than does water, providing a "natural" contrast in the absence of stains. It is therefore possible to make element-specific densitometric measurements of cells on a pixel by pixel basis.

*Advantages and potential difficulties unique to soft x-ray microtomography:*

X-ray microscopy is a transmission technique, so that all components in the cell are simultaneously visible. However, particularly for thick objects, any single view is a superposition of structures from many planes within the object, making interpretation difficult. Tomography is a method for recovering depth information from projections of an object taken at many different view angles. The particular case of soft x-ray microtomography (XMT) has a number of aspects which distinguish it from computerized tomography in medical x-ray imaging (MCT).

First, each image formed in the x-ray microscope is approximately a true parallel projection of object structure, which is the simplest case to handle, whereas medical x-ray tomography is typically a fan beam problem. This comes about for the following reason. The numerical aperture of the zone plate lens is given by (Anderson, 1989):

$$NA = \lambda / 2\,\delta \tag{1}$$

where $\delta$ is the outermost zone width of the lens, so that the depth of focus is given by:

$$\Delta f = \pm \lambda / 2\,NA^2 = \pm 2\,\delta^2 / \lambda \tag{2}$$

For typical zone plates and wavelengths, this turns out to be several micrometers, or around the thickness of an average cell. Because of this, XMT is the method of choice for recovering 3-D information in soft x-ray imaging, as opposed to the optical sectioning methods used in visible light microscopy. It should also be noted then that for tomography, the depth of focus of the optics should be matched to the sample thickness,

so that thicker samples require the use either of lower resolution lenses or shorter wavelength radiation, with concomitantly greater depth of focus.

Second, XMT does not suffer from two important artifacts associated with MCT: beam hardening and scattering. The high spectral brightness of synchrotron sources makes it possible to illuminate the sample with monochromatized light, which is required to eliminate chromatic aberration for the highest resolution. Therefore, the effective attenuation coefficients do not vary with position in the sample as they do with MCT. Also, the principal process in the attenuation of soft x-rays is absorption by photoelectric effect with minimal scattering (Henke *et al.*, 1993), so there is no loss of contrast due to detection of scattered light.

On the other hand, XMT reconstruction must deal with some potential difficulties not normally encountered, or at least not treated, in the medical case. The first arises from the fact that the zone plate lenses have finite numerical aperture, so that the microscopic images are blurred by a spatially invariant point spread function (PSF). The PSF of a perfect zone plate is an Airy pattern, with the radius to the first null (equivalent to the Rayleigh resolution) given by (Anderson, 1989):

$$r = 1.22\ \delta \tag{3}$$

This blurring results in decreased contrast, which worsens as $\delta$ becomes larger. Measurements indicate that the performance of current zone plates is close to diffraction limited (Jacobsen *et al.*, 1991; Meyer-Ilse *et al.*, 1992), so equation (3) is a reasonable estimate of the degree of blurring. While there are a number of sources of blurring in MCT, they are typically not corrected for, except in special cases.

The doses required for XMT are much higher than for MCT. This is because for similar signal levels, similar numbers of photons must be deposited into a mass many orders of magnitude smaller. Therefore, the attempt must be made in XMT to use the minimum level of counting statistics required to detect features of the targeted size and density contrast.

Finally, because of the difficulty mechanically to mount free standing samples about the size of a cell, a sample holder must usually be used which can interfere with the full range of rotation. In such cases, reconstructions would suffer from limited angle artifacts.

## Tomographic reconstruction

*Defining a "realistic" problem:*

Figure 4-2 shows the digital phantom used for all the reconstructions presented here. While it is intended to model a cell with several subcellular organelles, as mentioned above, the actual densities within the various compartments are unknown. Indeed our objective is to determine them. The values used in this model are based in part on measurements on 2-D x-ray micrographs of cells imaged by the authors (Rothman *et al.*, 1992), which apply best to the coarser structures. The phantom is therefore best regarded simply as a tool for investigating the classes of objects that can be measured by the method.

The phantom represents a slice containing $256 \times 256$ pixels 40 nm on a side and 80 nm thick. The pixel values represent density (expressed in g/cm$^3$) of protein-like organic material. The cell cytoplasm is depicted as a $5 \times 9$ $\mu$m ellipse of density 0.06 g/cm$^3$. The

nucleus is a $3 \times 4$ $\mu$m ellipse with a contrast of 0.04 (*i.e.*, a *difference* of 0.04 g/cm$^3$ between the nucleus and the surrounding cytoplasm). Several circular granules ranging in diameter from 0.48 to 1 $\mu$m and in contrast from 0.06 to 0.19 are on the opposite side of the cell. Within the granules are circular aggregates with a diameter of 0.08 $\mu$m (80 nm) and contrast of either 0.06 or 0.09. Within the nucleus are $0.1 \times 0.2$ or $0.1 \times 0.4$ $\mu$m nucleoli with contrast 0.06 or 0.09. Also included are thin ribbon-like structures of width around 80 nm and a contrast of 0.06, as well as two $0.40 \times 0.76$ $\mu$m mitochondria of contrast 0.06 and internal contrast 0.03 and 0.05. The cell is assumed to be embedded in a 5 $\mu$m thick layer of water of essentially infinite extent that has a uniform density of 1.0 g/cm$^3$, including in the region occupied by the cell.

The problem which we address is to detect with statistical significance the 80 nm aggregates of contrast 0.09 g/cm$^3$ within the granules, without the use of exogenous contrast agents or sectioning, and using x-ray wavelengths within the water window only. The problem is "realistic" in that it is technically the simplest. In terms of parameters such as object size, aqueous environment, *etc.*, this is an experiment that could in principle be performed at any of the existing synchrotron x-ray microscope facilities given an appropriate rotating sample stage, and perhaps a cryogenic sample stage for minimizing radiation sensitivity. In fact, the authors have previously acquired x-ray stereo image pairs of cells as a demonstration of the technical feasibility of tomographic imaging (Loo *et al.*, 1992a; Loo *et al.*, 1992b). Moreover, from the standpoint of the reconstruction problem, this represents a worst case scenario in that no measures either to enhance contrast and resolution or to reduce the required dose are assumed here. Some potential measures towards these ends are described below in the discussion.

*Description of the algorithm:*

We propose the use of iterative reconstruction algorithms for three reasons: they are less sensitive to noise than the usual Fourier inversion methods used in medical CT, which is an issue because of the need to use the minimum acceptable illumination; they have superior performance on limited angle problems, in which there is a large null space in the frequency domain; and they allow easily the incorporation of constraints on the solution space, which can be important since there is typically no unique solution to the reconstruction problem. The details of the algorithm used here are given in the Appendix.

The weighted least squares objective function, equivalent to the chi-squared statistic for normally distributed random variables, is an attractive one to use because its gradient can be easily expressed analytically even when complexities such as blurring by a PSF or the transformation between density and transmission data are folded into the problem. It also has a well understood statistical interpretation since for normally distributed random variables, the minimizer of the chi-squared statistic is the maximum likelihood solution. And while photon counts are Poisson distributed random variables, the count rates for imaging are typically sufficiently high that they approach an approximately normal distribution.

A highly efficient algorithm for the minimization of many functions is the conjugate gradient algorithm (Press *et al.*, 1992). The algorithm is most efficient if the objective function is a quadratic surface, so that the distance to the minimum along any line is easy to compute. However, in the case of transmission tomography, the step size to the minimum cannot be expressed in closed form because of the non-linear (exponential)

relationship between object density and transmitted intensity. Our approach is to compute an approximate distance to the line minimum by linearizing the exponential function in a way that becomes increasingly valid as the minimum is approached, and improving on the approximation by making a few computationally inexpensive iterations on each line minimization (see Appendix). The solution space is constrained by a regularizer, and by non-negativity. The non-negativity constraint is implemented using a preconditioner by an approach similar to one described by Kaufman (1993), with the modifications mentioned above.

*Description of simulations:*

1. Imaging parameters.

Table 1 shows the imaging parameters that were modeled in these simulations. The choice of this wavelength / zone plate combination is based primarily on the need to match the depth of focus to the sample thickness. The whole sample should remain in focus throughout its range of rotation. In order to maximize resolution for a given depth of focus, we choose a short wavelength within the water window. This might seem to be counterproductive since the sample contrast is also the lowest around this wavelength (see Figure 4-1). However, because of the exponential falloff of intensity with depth in the sample, the dose distribution is highly uneven for thick samples, with very high doses on the side of the sample facing the beam. Shorter wavelength radiation with longer attenuation length spreads the dose more evenly across the sample thickness. The contrast to dose ratio is therefore actually optimal at this wavelength.

| Imaging Parameters | | |
|---|---|---|
| • Wavelength: | $\lambda = 24$ Å | (E = 517 eV) |
| • Zone plate: | $\delta = 80$ nm | (outermost zone width) |
| • Rayleigh resolution: | $r = 98$ nm | |
| • Depth of focus: | $\Delta f = \pm 5.33\ \mu m$ | (10.67 $\mu$m total) |
| • Attenuation coefficients at this wavelength: | | |
| | $\mu_{protein}$ = 10060.0 $cm^2/g$ | |
| | $\mu_{water}$ = 1114.9 $cm^2/g$ | |

Table 4-1

2. Estimation of required illumination.

We consider now the amount of illumination required to detect our target feature. A theorem by Hegerl & Hoppe (1976) states that the total number of absorbed photons required to detect a particular voxel in a 3-D reconstruction is the same as the number required to detect the same voxel in a single 2-D projection. This implies that we can estimate the necessary exposure intensity by calculating how many photon counts would be required to detect our target feature in a single projection, then use that number divided by the number of views as the exposure intensity for each view in the tomographic data set. The validity of the Hegerl-Hoppe theorem has been borne out by recent simulations by McEwen *et al.* (1995), as well as by the simulations presented here.

We first calculate the illumination required to detect, in one projection, an isolated 80 nm cylinder of 0.09 g/cm$^3$ protein against a uniform background. The problem is illustrated in Figure 4-3. Detection, according to Rose's criterion for feature detectability (Rose, 1973), requires that the reduction of transmission by the object relative to the background be at least five times the noise amplitude on the background, or for Poisson distributed random variables:

$$\Delta I \geq 5 \cdot \sigma_I = 5 \cdot \sqrt{I} \tag{4}$$

where I is the mean number of photons transmitted through the background. Attenuation of photons by the target material follows Beer's law (Henke *et al.*, 1993), so:

$$\Delta I = I \cdot \left(1 - e^{-\rho\mu t}\right) \tag{5}$$

where ρ is the density of the target material, $\mu$ is its mass dependent attenuation coefficient, and t is its thickness. Solving for I in (4) and (5), the Hegerl-Hoppe theorem predicts that to detect our feature, the number of photons transmitted through the background, per pixel, per view, should be:

$$I = \frac{1}{N} \cdot \left( \frac{5}{1 - e^{-\rho\mu t}} \right)^2 \tag{6}$$

where N is the number of angular views. For the imaging parameters above, this works out to $I = 4.7998 \times 10^5 / N$.

However, as can be seen in Figure 4-3, the actual background in which the target feature must be detected in various projections through the phantom is at between 40 - 60% transmission, so that the above prediction should be about doubled. Moreover, there are two sources of blurring that reduce contrast and for which illumination must be increased to compensate. First of all, the backprojection operation implicit in the tomographic reconstruction process involves convolution of the true object density map with a 1/r blurring kernel (Jain, 1989; Herman, 1980). We find that an intensity of about 1.6 times the predicted requirement results in satisfactory correction of this factor (see results section). In addition, there is the blurring due to the instrumental point spread function, which for the zone plate selected results in a 32 percent decrease in the contrast

of the target feature. Again, approximately doubling the intensity compensates for this so that the illumination used for these simulations is about 3.2 times that predicted by the Hegerl-Hoppe theorem for the case of the feature within a cell.

3. Generation of simulated data sets.

To avoid square pixel artifacts when generating simulated measurements of transmitted counts, the phantom was constructed on a $1024 \times 1024$ grid. The projection step used to compute the ray sums at the various view angles (the sinogram) was performed on the oversized phantom. All the angular views were evenly spaced, with an angular spacing of 0.8955°, and with various restrictions on the tilting range. The density sinogram was then converted to a transmission sinogram, on which the blurring step was performed by convolving each row of the sinogram, corresponding to one angular view, with the blurring kernel. The blurring kernel was constructed by taking the appropriate 2-D Airy pattern point spread function for the lens, and projecting it onto a line. Using this 1-D line spread function allowed us to simplify the problem by dealing with the reconstruction of a single slice, rather than the entire volume, which was appropriate for the purpose of this study. Rigorous treatment of the 3-D reconstruction problem would require taking into account the cross-talk between slices caused by the blurring. The blurred sinogram was then subsampled by averaging, so that the final number of ray projections per view was 256. A sample transmission sinogram is shown in Figure 4-4.

| Data for reconstruction: | Angular range: | N | I |
|---|---|---|---|
| R90 | -90° to +90° | 201 | 3880 |
| R90U/D | -90° to +90° | 201 | 7760 |
| R80 | -80° to +80° | 179 | 4356 |
| R80U/D | -80° to +80° | 179 | 8712 |
| R70 | -70° to +70° | 156 | 5000 |
| R70U/D | -70° to +70° | 156 | 10000 |
| R60 | -60° to +60° | 134 | 5820 |
| R60U/D | -60° to +60° | 134 | 11640 |

Table 4-2

Finally, each pixel in the transmission sinograms was replaced by a sample from a Poisson random distribution with mean equal to the mean number of transmitted counts for that pixel. The mean number of transmitted counts through the background region, *i.e.*, the water layer, in each view was computed according to equation (6), with the adjustments described above. Note that because the x-ray path length changes with view angle, the incident intensity was adjusted for each angular view to produce the required transmission through the background region. Table 2 summarizes the data sets generated for the various reconstructions. The reconstructions are named according to the range of tilt (±60° to ±90°), and whether the reconstruction was done with correction for PSF blurring by deconvolution (D), was uncorrected for blurring (U), or was done from data that was not blurred by a PSF (angular range designation only). The U and D reconstructions were done from the same data sets. The unblurred data sets were generated with half the counting statistics of the blurred data sets. For the blurred data sets, the total number of detected counts across all the views is about $3 \times 10^8$ counts.

## Results of simulations

*Criteria for evaluation:*

The reconstructions were evaluated using three figures of merit: visual quality, quality of a line profile through features of interest, and normalized mean squared error (NMSE) with respect to the phantom, which is given by:

$$NMSE = \frac{\sum_i (r_i - p_i)^2}{\sum_i p_i^2} \tag{7}$$

where the $r_i$ are the reconstructed pixel values, and the $p_i$ are the phantom pixel values. Figure 4-5 shows the position on the reconstructions at which the line profiles are measured. The right hand aggregate of the doublet is the one with 0.09 g/cm$^3$ contrast.

*Effect of restricted tilt range:*

Figure 4-6 shows reconstructions with various restrictions on the range of sample rotation, with deconvolution of the PSF. Visually, the gross structure appears intact in all of the reconstructions, though in the reconstruction restricted to ±60°, the lower "mitochondrion" is basically obscured. Interestingly, some of the small features remain surprisingly sharp despite the restricted angular range. The NMSE of the ±70° reconstruction is about twice as large as for the reconstruction with the full range of rotation, but still small at about 4%. On the whole, it appears from these simulations that restriction of the range of tilt to ±70° still produces acceptable reconstructions.

*Performance of the deconvolution algorithm:*

Figure 4-7 compares a reconstruction from an unblurred data set with one from a blurred data set, corrected by deconvolution. Both were done with the full range of rotation, but the measurement data for R90D had double the photon counts of the one for R90, as indicated in table 2. As stated above, the target features in R90 are satisfactorily resolved with about 1.6 times the required illumination predicted by equation (6), while R90D is comparable in quality visually with about 3.2 times the predicted threshold. The line profiles for both reconstructions appear quite good, with the peaks corresponding to target features sharply defined. In fact, even the features with a contrast of 0.06 g/cm3 are well defined in the line profiles, though technically they may not meet the rather stringent Rose criterion. Evaluated by NMSE, R90D is actually slightly better than R90, even though visually it appears slightly less sharp than R90. This may be because the higher statistics in R90D result in less noise in the broad, uniform features, as seen in the line profiles.

Figure 4-8 compares two reconstructions from the same data set, one uncorrected for blurring due to the PSF, and the other corrected by deconvolution. The range of view angles is ±70°. Visually, there is a noticeable difference in sharpness between the two reconstructions. The difference between the line profiles around the peaks corresponding to the target features bears this out. However, because of the restriction in angular range, even the corrected reconstruction does not resolve features as well as in the case of no angular restriction. Finally, the deconvolution reduces the NMSE by a significant fraction. The relative improvement afforded by deconvolution is more pronounced with greater restriction in the range of angular views.

Figure 4-8 compares two reconstructions from the same data set, one uncorrected for blurring due to the PSF, and the other corrected by deconvolution. The range of view angles is ±70°. Visually, there is a noticeable difference in sharpness between the two reconstructions. The difference between the line profiles around the peaks corresponding to the target features bears this out. However, because of the restriction in angular range, even the corrected reconstruction does not resolve features as well as in the case of no angular restriction. Finally, the deconvolution reduces the NMSE by a significant fraction. The relative improvement afforded by deconvolution is more pronounced with greater restriction in the range of angular views.

**Discussion**

*Radiation dose:*

Dose is defined as energy absorbed per unit mass and is measured in Gray (J/g). The left graph in Figure 4-9a is a surface plot of the dose as a function of position within the sample for reconstructions R70U/D. For each voxel, the dose was calculated by dividing the total energy absorbed in the voxel during the data collection process by the total mass within the voxel. A sharp falloff can be seen from the side of beam entry to the side of beam exit. As stated above, the incident x-ray intensity was adjusted for each angular view to produce the required transmission through the water layer.

The average dose within the region occupied by the cell is $9.3 \times 10^6$ Gray, with the range extending from a minimum of $3.3 \times 10^6$ to a maximum of $2.0 \times 10^7$ Gray. Figure 4-9b shows the histogram of the dose, demonstrating this wide variance about the mean. These numbers must be evaluated in the context of what dose can be tolerated before the

mass distribution of the sample is significantly altered on the size scale of the desired resolution. There are a number of estimates of what should be considered the threshold dose. In electron microscopy of frozen, hydrated samples, the "critical dose" that can be tolerated before sample deterioration at the 10 nm resolution level becomes significant is an electron dose of around $10^8$ Gray (Glaeser, 1975; Glaeser, 1995). In x-ray crystallography of frozen, hydrated protein crystals, calculations and recent measurements at synchrotron facilities indicate that an x-ray dose of $2 - 5 \times 10^7$ Gray can be tolerated before the diffraction pattern is lost (Henderson, 1990). These numbers very likely underestimate the critical dose for the tomography problem described here: they indicate that in frozen samples, atomic positions remain sufficiently well organized to produce diffraction patterns at up to $2 \times 10^7$ Gray, whereas for the XMT problem, we require only that the carbon and nitrogen atoms that were originally in an 80 nm voxel remain in that voxel throughout the data collection, regardless of state of their chemical bonds.

However, even using $2 \times 10^7$ Gray as the worst case critical dose, we see that the reconstruction problem is solved with on average a factor of 2 lower dose than this threshold, and a factor of 10 lower than the critical dose for electron microscopy at a higher resolution. Moreover, the right hand graph of Figure 4-9a shows how the situation could be further improved by exposing the sample from both sides, with concomitant redistribution of the dose. In practice, this could be accomplished by flipping the sample 180° after one side has been exposed, and should be relatively simple to implement in the sample holders used at existing x-ray microscope facilities. The restriction on angular range would remain the same, as would the average dose, but as illustrated in the figure,

and in the histogram of Figure 4-9b, nearly all the voxels would receive close to the average dose, with very few receiving the more extreme doses that approach the threshold.

*Approaches to improving the performance of XMT:*

So far, we have concentrated on the problem of making quantitative 3-D protein densitometric measurements on thick samples. The choice of imaging parameters required to meet our goals places constraints on the achievable resolution. If however the goal is high resolution determination of 3-D topology or localization of specific molecular species, it is possible to trade the ability to make quantitative mass measurements in favor of potentially much higher resolution. This can be accomplished by staining the sample with contrast agents such as metals, with or without conjugation to specific antibodies (Balhorn *et al.*, 1992). Improved resolution follows in a number of ways. Because the contrast is no longer based on protein-water absorption differences, wavelengths shorter than those in the water window can be used, where there is still significant contrast between the metal, and water and organic material. For the same depth of focus, shorter wavelength allows the use of higher resolution lenses. Finally, at sufficiently short wavelengths, the attenuation coefficients of the sample are lower than they are in the water window, so signal intensity is higher for the same dose, allowing detection of smaller features. One variation that seems particularly promising is using lanthanide metals as the contrast, and detecting the x-ray induced visible light luminescence: the luminescence of these probes is resistant to bleaching up to very high doses, and the resolution of the method is determined by the x-ray probe size rather than the wavelength of the detected light (Jacobsen *et al.*, 1993; Irtel von Brenndorff *et al.*,

1994). In addition to the above mentioned advantages, detecting an emission signal makes the reconstruction problem linear, and therefore easier to solve.

If we insist on being able to do quantitative densitometry at higher resolution, there are still options. Primarily, this could be accomplished by reducing the sample thickness. The reduction in the required depth of focus would allow the use of higher resolution lenses. The reduced overall attenuation by the sample would allow the detection of the same feature at a lower level of illumination and dose, or for the same dose would allow the detection of smaller features. Some cells, such as cultured cells, are naturally thin (about 1 - 2 $\mu$m thick). For thick samples, one possibility would be to make frozen thick sections of about 1 - 2 $\mu$m thickness, which should still be thick enough to preserve much of the interesting 3-D structure of convoluted objects like the endoplasmic reticulum or Golgi complex. This would also open the possibility of imaging sections from whole tissue that would otherwise be impractical to image with soft x-rays.

## Conclusions

The results of the simulated x-ray microtomographic reconstructions presented here indicate that even in a worst case scenario from a reconstruction and feature detection standpoint, it should be possible to detect interesting features in 3-D at high resolution within the constraints imposed by radiation dose. Furthermore, from a methodological perspective, XMT of biological samples should be within the technological reach of existing x-ray microscopy facilities. Finally, a number of methods can in principle be employed to extend the range of utility of XMT to a broad spectrum of biological problems.

**Acknowledgments**

The authors thank the following individuals for their assistance and helpful discussions: David T. Attwood, Robert M. Glaeser, Everett H. Harvey, Bruce Hasegawa, Malcolm R. Howells, Nasif N. Iskander, Lotti Jochum, Hector Medecki, Werner Meyer-Ilse, Ron E. Tackaberry.

BWL gratefully acknowledges support under a fellowship from Associated Western Universities, Inc., and a National Institutes of Health training grant to the UCSF/UCB Bioengineering Graduate Group. JKB gratefully acknowledges the support of the Whitaker Foundation.

All the reconstruction software was written in the IDL image processing language from Research Systems, Inc., Boulder, CO, USA, except for the projection/backprojection engine, which was written in C. All figures were produced using IDL.

## Appendix

The reconstruction problem can be formulated in vector notation as follows: let **x** be a vector containing an estimate of the true object densities, where each element of **x** represents the value of one pixel in the reconstruction. Let the matrix **A** be the projection operator, which transforms **x** to its sinogram, **s**. $\mathbf{A}^T$ would then be the backprojection operator. Let **t** be the transmission sinogram of **x**, and let the matrix **H** be the operation that convolves **t** with the PSF to produce the blurred transmission sinogram, **c**. $\mathbf{H}^T$ would then be the operator that performs cross-correlation with the PSF. The case of no blurring, when the PSF is a delta function, is represented by $\mathbf{H} = \mathbf{I}$, the identity matrix. Let **b** be the measured blurred transmission sinogram, and let **W** be the diagonal matrix whose elements along the diagonal are the inverse of the estimated variance of the measurements $b_i$. Let **d** be the difference between **c** and **b**. The preceding definitions are summarized by:

$$\begin{aligned} &\mathbf{s} = \mathbf{A} \cdot \mathbf{x} \\ &\mathbf{t} = I_0 \exp(-\mathbf{s}) \\ &\mathbf{c} = \mathbf{H} \cdot \mathbf{t} \\ &\mathbf{d} = \mathbf{c} - \mathbf{b} \\ &\mathbf{W} : W_{ii} = b_i, W_{i \neq j} = 0 \end{aligned} \tag{A1}$$

where $I_0$ is the transmitted counts through the background. Then the objective of the algorithm is to minimize the function:

$$F(\mathbf{x}) = \left|\mathbf{W}^{1/2} \cdot \mathbf{d}\right|^2 + r\left|\mathbf{B} \cdot \mathbf{x}\right|^2 = \mathbf{d}^T \cdot \mathbf{W} \cdot \mathbf{d} + r\mathbf{x}^T \cdot \mathbf{B}^T \cdot \mathbf{B} \cdot \mathbf{x} \tag{A2}$$

The second term in the objective function is known as a regularization term. In the absence of a unique solution to the weighted least squares problem, the secondary function can be used to bias the solution according to some criterion. In this case, **B** is a high pass filtering operation, so that by minimizing F, we choose a solution that is biased towards having weaker high frequency Fourier components. For these reconstructions, the frequency space filter implemented by B was:

$$B(\omega) = (\omega / \omega_0)^n \tag{A3}$$

where $\omega_0$ is the Nyquist critical frequency. The parameters $r$ and $n$ can be used to choose the strength of regularization.

Given the ability to compute the gradient of F, and the distance $\lambda$ from any point $\mathbf{x}_0$ to the minimum along a direction **v**, the conjugate gradient algorithm can be used to construct a set of N conjugate directions $\mathbf{v}_i$, where N is the number of elements of **x**. Successive line minimizations over this set of directions leads to the overall minimum of the function if it is a quadratic surface (Press *et al.*, 1992). The algorithm is also useful for minimizing functions involving nonlinear operators that are approximately quadratic near their minima, as is this objective function. The algorithm works iteratively, starting with an initial guess $\mathbf{x}_0$, as follows:

$$
\begin{aligned}
&1.\ \mathbf{g}_0 = \nabla F(\mathbf{x}_0) \\
&2.\ \mathbf{v}_0 = -\mathbf{g}_0 \\
&\text{Begin iteration :} \\
&3.\ \lambda = \text{distance to minimum along } \mathbf{v}_i \\
&4.\ \mathbf{x}_{i+1} = \mathbf{x}_i + \lambda \mathbf{v}_i \\
&5.\ \mathbf{g}_{i+1} = \nabla F(\mathbf{x}_{i+1}) \\
&6.\ \gamma = \frac{\mathbf{g}_{i+1}^T \cdot \mathbf{g}_{i+1}}{\mathbf{g}_i^T \cdot \mathbf{g}_i} \\
&7.\ \mathbf{v}_{i+1} = \gamma \mathbf{v}_i - \mathbf{g}_{i+1}
\end{aligned}
\tag{A4}
$$

where $i$ is the iteration index. For this objective function, the gradient is given by:

$$
\begin{aligned}
&\nabla F(\mathbf{x}) = -2\mathbf{A}^T \cdot \mathbf{T} \cdot \mathbf{H}^T \cdot \mathbf{W} \cdot \mathbf{d} + 2r\mathbf{B}^T \cdot \mathbf{B} \cdot \mathbf{x} \\
&\mathbf{T} : T_{ii} = t_i, T_{i \neq j} = 0
\end{aligned}
\tag{A5}
$$

Because the objective function and gradient incorporate the effect of the PSF, this algorithm will lead to its correction.

Step 3 of the algorithm is the most difficult to implement because of the nonlinearity of the exponential function required for computing the transmission. The problem is to minimize $F(\mathbf{x}_0 + \lambda\, \mathbf{v})$ with respect to $\lambda$, and we define:

$$
\begin{aligned}
&\mathbf{s}_{\mathbf{x}_0 + \lambda \mathbf{v}} = \mathbf{A} \cdot \mathbf{x}_0 + \lambda \mathbf{A} \cdot \mathbf{v} = \mathbf{s}_0 + \lambda \mathbf{s}' \\
&\mathbf{t}_{\mathbf{x}_0 + \lambda \mathbf{v}} = \exp(-\mathbf{s}_0 - \lambda \mathbf{s}') = \mathbf{T}_0 \cdot \exp(-\lambda \mathbf{s}') \\
&F(\mathbf{x}_0 + \lambda \mathbf{v}) = \left| \mathbf{W}^{1/2} \cdot \left[ \mathbf{H} \cdot \mathbf{T}_0 \cdot \exp(-\lambda \mathbf{s}') - \mathbf{b} \right] \right|^2 + r \left| \mathbf{B} \cdot (\mathbf{x}_0 + \lambda \mathbf{v}) \right|^2 \\
&\mathbf{T}_0 : T_{0,ii} = t_{0,i}, T_{0,i \neq j} = 0; \mathbf{t}_0 = I_0 \exp(-\mathbf{s}_0)
\end{aligned}
\tag{A6}
$$

The problem can be linearized at this point by making the approximation:

$$
\exp(-\lambda \mathbf{s}') \approx \mathbf{1} - \lambda \mathbf{s}' \tag{A7}
$$

which is a valid approximation when $\lambda s'$ is small, *i.e.*, when $\mathbf{x}_0$ is close to the line minimum. With this approximation, it is possible to solve $dF/d\lambda = 0$ for $\lambda$ to yield:

$$\lambda = \frac{\mathbf{d}^T \cdot \mathbf{W} \cdot \mathbf{q} + r\mathbf{x}_0^T \cdot \mathbf{B}^T \cdot \mathbf{B} \cdot \mathbf{v}}{\mathbf{q}^T \cdot \mathbf{W} \cdot \mathbf{q} + r\mathbf{v}^T \cdot \mathbf{B}^T \cdot \mathbf{B} \cdot \mathbf{v}} \qquad \text{(A8)}$$
$$\mathbf{q} = \mathbf{H} \cdot \mathbf{T}_0 \cdot \mathbf{A} \cdot \mathbf{v}$$

The line minimum can then be reached iteratively by evaluating $\lambda$ a few times, each time updating **x**, **s**, **t**, **c**, **d**, and **q**. Since **v** and **s**′ do not change during these iterations, there are no expensive **A** operations to compute, and the process is computationally efficient. In practice, 3 - 4 iterations usually result in a very good approximation, as measured by the dot product of the search direction with the local gradient at the supposed minimum. A problem can arise, however, if the regularization is too strong, since the goal of minimizing the regularization term eventually conflicts with that of minimizing the chi-squared statistic, and the linear approximation no longer holds.

Finally, it is possible to rescale the problem for faster convergence and implement a non-negativity constraint by solving the preconditioned form of the problem (Kaufman, 1993). This is accomplished simply by modifying the following steps of the above algorithm:

$$3'.\ \lambda = \text{distance along } \mathbf{v}_i \text{ to minimum or constraint, whichever is smaller}$$
$$6'.\ \gamma = \frac{\mathbf{g}_{i+1}^T \cdot \mathbf{P} \cdot \mathbf{g}_{i+1}}{\mathbf{g}_i^T \cdot \mathbf{P} \cdot \mathbf{g}_i} \qquad \text{(A9)}$$
$$7'.\ \mathbf{v}_{i+1} = \gamma \mathbf{v}_i - \mathbf{P} \cdot \mathbf{g}_{i+1}$$

where **P** is a diagonal matrix that is reset each time the constraint is hit to contain the current elements of **x** along its diagonal. This algorithm is equivalent to the normal conjugate gradient algorithm applied to the function F(**y**), where $\mathbf{y} = \mathbf{P}^{-1/2} \cdot \mathbf{x}$, and **A** and **B** are replaced respectively by $\mathbf{A} \cdot \mathbf{P}^{1/2}$ and $\mathbf{B} \cdot \mathbf{P}^{1/2}$. This has the effect of rescaling the problem so that high object values that are far from the starting guess are "reeled in" while the low values which are close to the constraint are slowed from hitting it.

For all the reconstructions presented here, the initial guess for **x** was **0**, and the initial value of **P** was an elliptical pattern of value 1, 10 pixels larger than the cell in each dimension, and zero outside the ellipse. This caused the pixels outside of the ellipse, which was known to be outside the region of support of the object, to remain at zero throughout the iterations.

## Figures

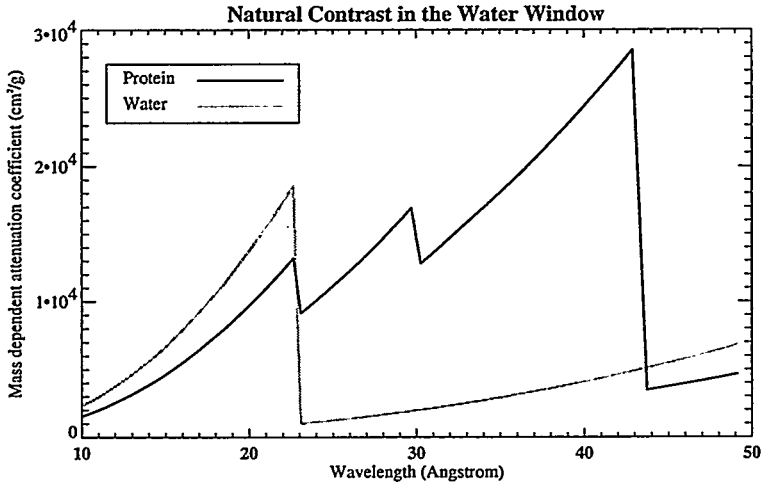


**Figure 4-1**

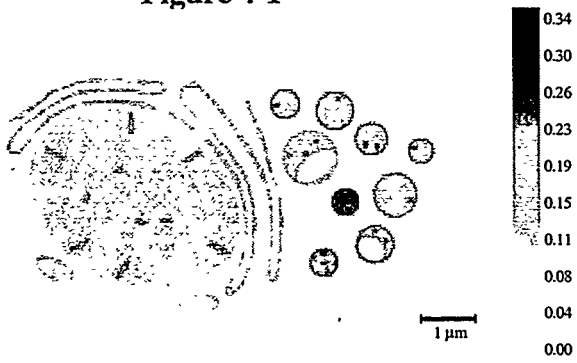


**Figure 4-2**

Digital phantom of a biological cell

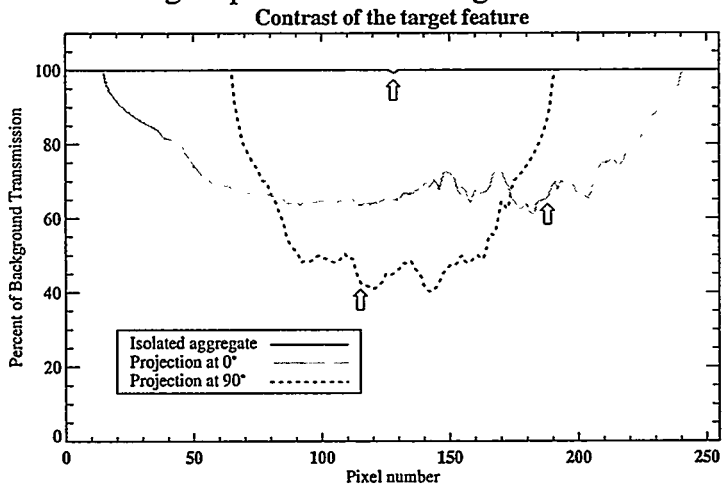


**Figure 4-3**

Arrows indicate projected position of target feature in isolation, and within the phantom.

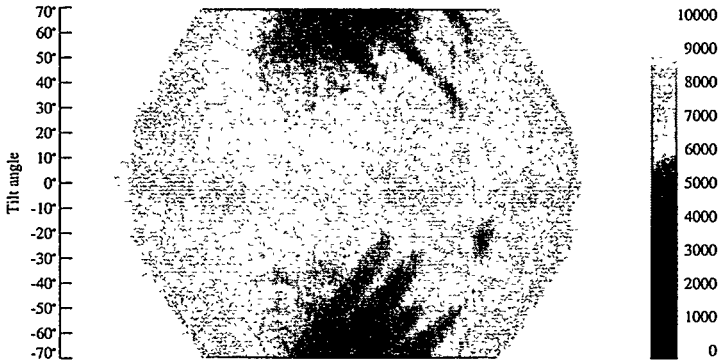


**Figure 4-4**
Simulated measurement data (transmitted counts) for angular range [-70°, +70°]

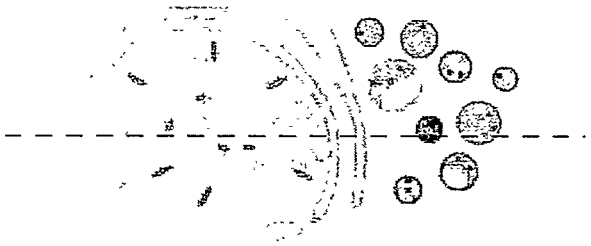

**Figure 4-5**
Dashed line indicates position at which line profiles are measured

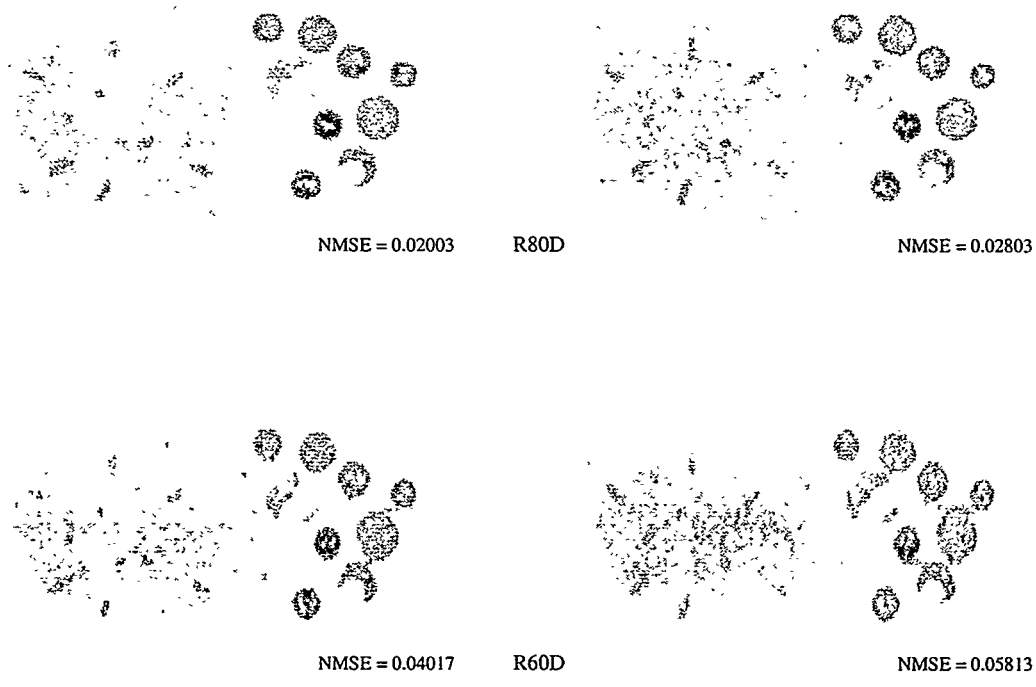


**Figure 4-6**
Tomographic reconstructions with various restrictions on range of view angles

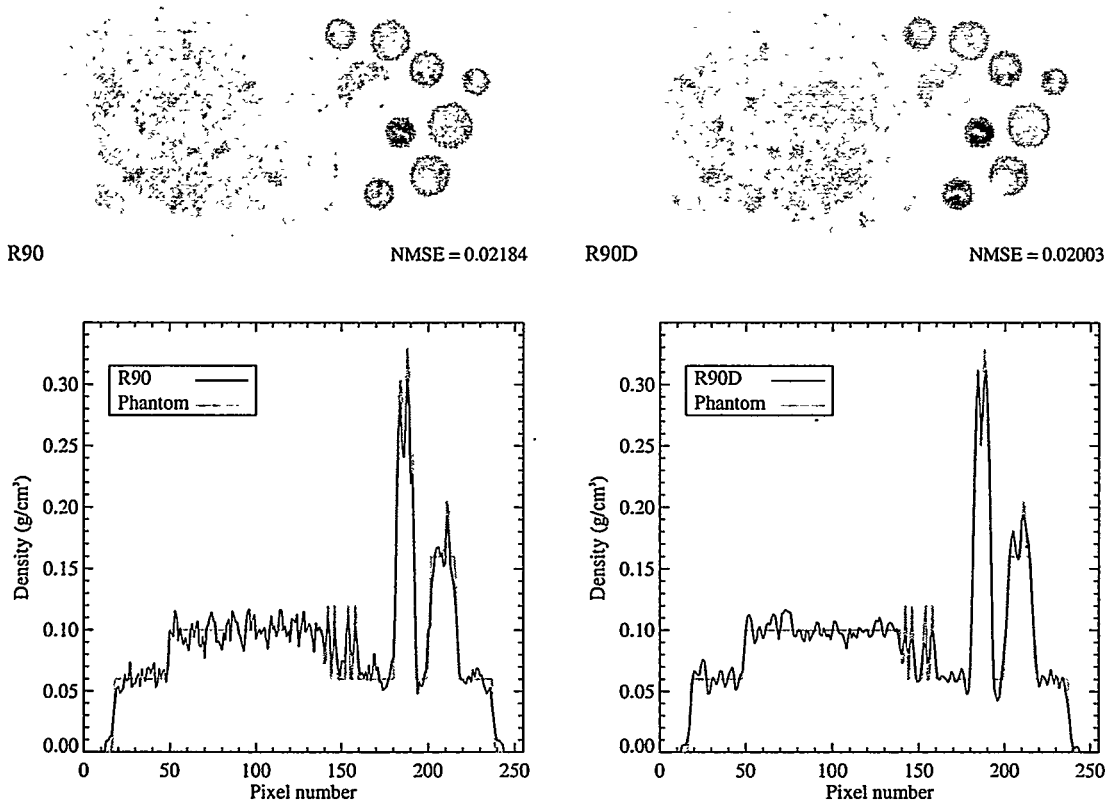


**Figure 4-7**

Comparison of reconstruction with no blurring by a PSF (R90) to reconstruction with PSF blurring corrected by deconvolution (R90D). R90 was done with half the dose of R90D.

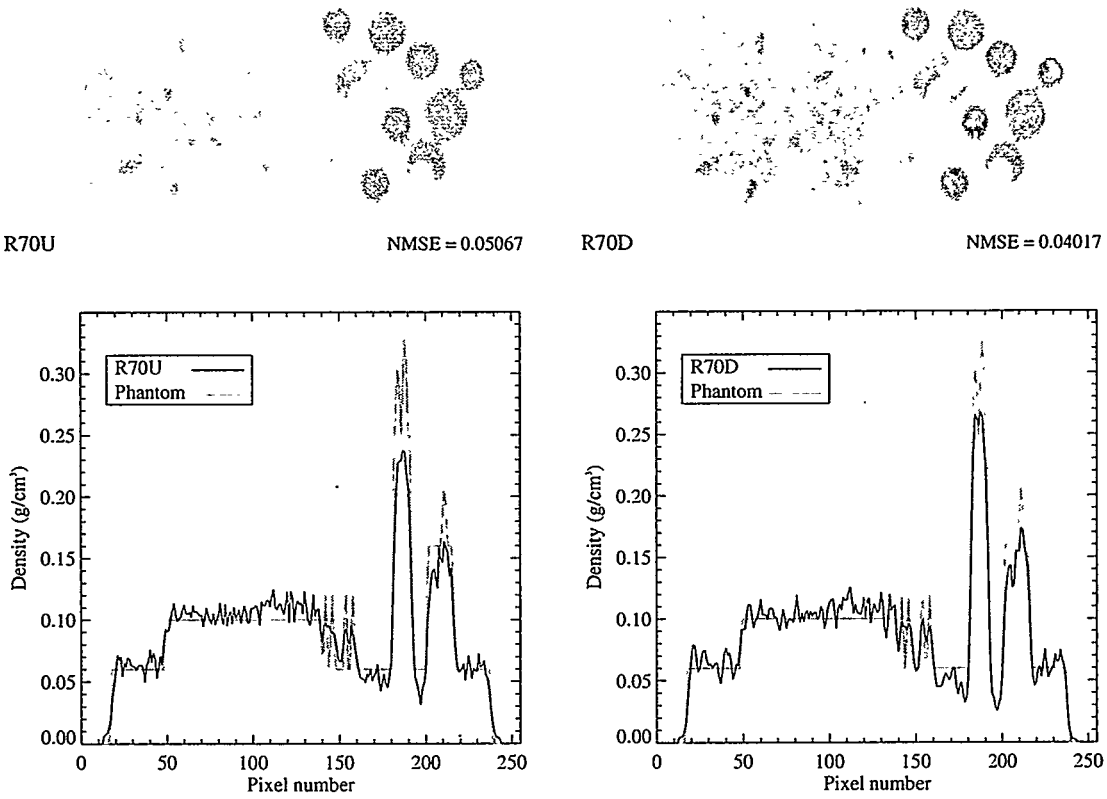


**Figure 4-8**

Comparison of reconstruction uncorrected for blurring (R70U) to reconstruction with PSF blurring corrected by deconvolution (R70D). Both reconstructions were done using the same data set.

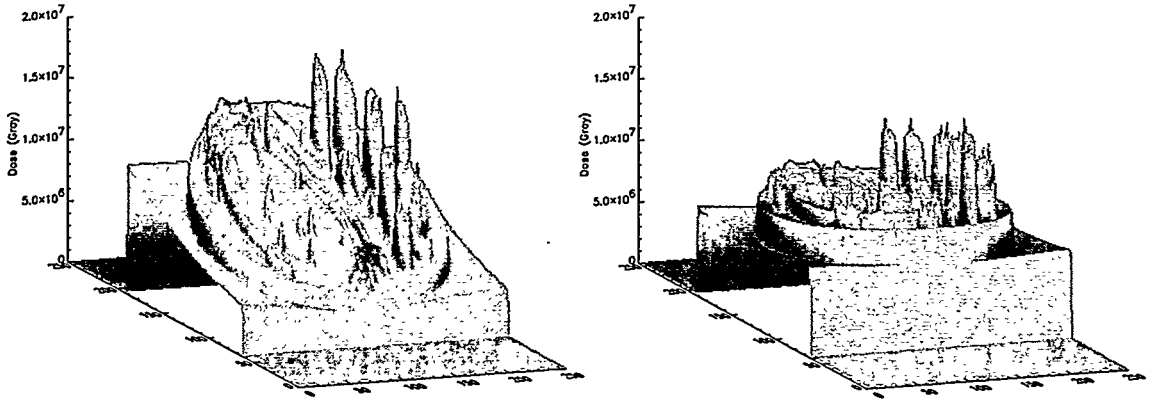


**Figure 4-9a**

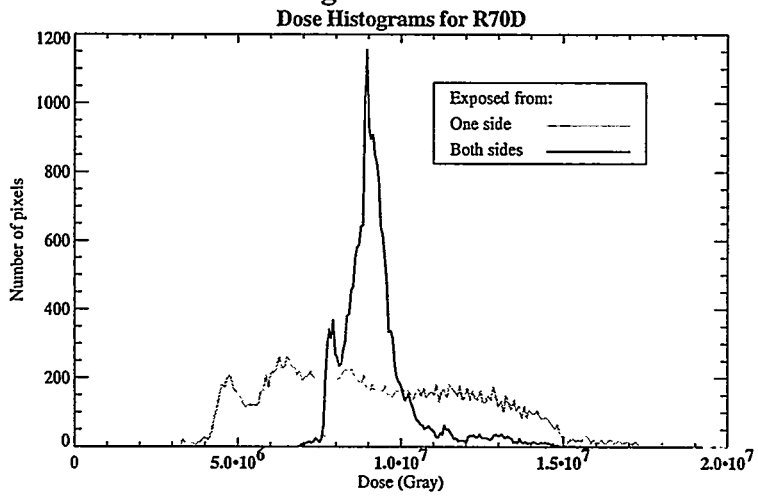


**Figure 4-9b**

## References


Anderson, E.H. (1989) Fabrication technology and applications of zone plates. *X-Ray/EUV Optics for Astronomy and Microscopy, San Diego, California, August 7-11, 1989.* (ed. by R.B. Hoover), Proceedings SPIE Vol. 1160, pp. 1-10.

Balhorn, R., Corzett, M., Allen, M.J., Lee, C., Barbee, T.W., Jr., Koch, J.A., MacGowan, B.J., Matthews, D.L., Mrowka, S.J., Trebes, J.E., McNulty, I., Da Silva, L.B., Gray, J.W., Anderson, E.H., Kern, D. & Attwood, D.T., Jr. (1992) Application of x-rays to the analysis of DNA packaging in mammalian sperm. *Soft X-Ray Microscopy, San Diego, CA, USA, July 19-21, 1992.* (ed. by C. Jacobsen and J.E. Trebes), Proceedings SPIE Vol. 1741, pp. 374-385.

Glaeser, R.M. (1975) Radiation damage and biological electron microscopy. Chap. 12 in *Physical Aspects of Electron Microscopy and Microbeam Analysis.* (eds. B.M. Siegel and D.R. Beaman), Wiley. New York.

Glaeser, R.M. (1995) Ernest Orlando Lawrence Berkeley National Laboratory. Personal communication.

Goncz, K.K., Behrsing, R. & Rothman, S.S. (1995) The protein content and morphogenesis of zymogen granules. *Cell and Tissue Research.* **280**, 519-530.

Goncz, K.K. & Rothman, S.S. (1992) Protein flux across the membrane of single secretion granules. *Biochimica et Biophysica Acta.* **1109**, 7-16.

Hegerl, R. & Hoppe, W. (1976) Influence of electron noise on three-dimensional image reconstruction. *Zeitschrift fur Naturforschung A (Astrophysik, Physik und Physikalische Chemie).* **314**, 1717-1721.

Henderson, R. (1990) Cryo-Protection of Protein Crystals Against Radiation Damage in Electron and X-Ray Diffraction. *Proceedings of the Royal Society of London Series B-Biological Sciences.* **241**, 6-8.

Henke, B.L., Gullikson, E.M. & Davis, J.C. (1993) X-ray interactions: photoabsorption, scattering, transmission, and reflection at E=50-30000 eV, Z=1-92. *Atomic Data and Nuclear Data Tables*. **54**, 181-342.

Herman, G.T. (1980) *Image reconstruction from projections: the fundamentals of computerized tomography*. Academic Press, San Francisco.

Howells, M.R., Kirz, J. & Sayre, D. (1991) X-ray microscopes. *Scientific American*. **264**, 42-48.

Irtel von Brenndorff, A., Moronne, M.M., Larabell, C., Selvin, P. & Meyer-Ilse, W. (1994) Soft x-ray stimulated high resolution luminescence microscopy. *X-Ray Microscopy IV: Proceedings of the Fourth International Conference, Chernogolovka, Russia, September 20-24, 1993*. (ed. by V.V. Aristov and A.I. Erko). Bogorodskii Pechatnik, Chernogolovka.

Jacobsen, C., Lindaas, S., Williams, S. & Zhang, X. (1993) Scanning luminescence x-ray microscopy: imaging fluorescence dyes at suboptical resolution. *Journal of Microscopy*. **172**, 121-129.

Jacobsen, C., Williams, S., Anderson, E., Browne, M.T., Buckley, C.J., Kern, D., Kirz, J., Rivers, M. & Zhang, X. (1991) Diffraction-limited imaging in a scanning transmission x-ray microscope. *Optics Communications*. **86**, 351-364.

Jain, A.K. (1989) Chap. 10 in *Fundamentals of digital image processing*, Prentice Hall. Englewood Cliffs.

Kaufman, L. (1993) Maximum likelihood, least squares, and penalized least squares for PET. *IEEE Transactions on Medical Imaging*. **12**, 200-214.

Loo, B.W., Jr., Williams, S., Lin, W.T., Love, W.H., Meizel, S. & Rothman, S.S. (1992a) High resolution x-ray stereomicroscopy: true three-dimensional imaging of biological samples. *Soft X-Ray Microscopy, San Diego, CA, USA, July 19-21, 1992*, Proceedings SPIE Vol. 1741, pp. 393-401.

Loo, B.W., Jr., Williams, S., Meizel, S. & Rothman, S.S. (1992b) X-ray stereomicroscopy: high resolution 3-D imaging of human spermatozoa in aqueous suspension with natural contrast. *Journal of Microscopy*. **166**, RP5-RP6.

McEwen, B.F., Downing, K.H. & Glaeser, R.M. (1995) The relevance of dose-fractionation in tomography of radiation-sensitive specimens. *Ultramicroscopy*. **60**, 357-373.

Meyer-Ilse, W., Guttmann, P., Thieme, J., Rudolph, D., Schmahl, G., Anderson, E., Batson, P., Attwood, D., Iskander, N. & Kern, D. (1992) Experimental characterization of zone plates for high resolution x-ray microscopy. *X-Ray Microscopy III: Proceedings of the Third International Conference, London, September 3-7, 1990.* (ed. by A.G. Michette, G.R. Morrison, and C.J. Buckley), pp. 284-289. Springer-Verlag, Berlin.

Press, W.H., Teukolsky, S.A., Vetterling, W.T. & Flannery, B.P. (1992) Chap. 2.7 and 10.6 in *Numerical Recipes in C: the Art of Scientific Computing*. 2nd edition, Cambridge University Press. Cambridge.

Rose, A. (1973) Chap. 1 and 2 in *Vision: human and electronic*, Plenum Press. New York.

Rothman, S.S., Goncz, K.K. & Loo, B.W., Jr. (1992) Following protein transport with the high resolution x-ray microscope. *X-Ray Microscopy III: Proceedings of the Third International Conference, London, September 3-7, 1990.* (ed. by A.G. Michette, G.R. Morrison, and C.J. Buckley), pp. 373-383. Springer-Verlag, Berlin.

Tanaka, K. & Fukudome, H. (1991) Three-dimensional organization of the Golgi complex observed by scanning electron microscopy. *Journal of Electron Microscopy Technique*. **17**, 15-23.

Tanaka, K., Mitsushima, A., Fukudome, H. & Kashima, Y. (1986) Three-dimensional architecture of the Golgi complex observed by high resolution scanning electron microscopy. *Journal of Submicroscopic Cytology*. **18**, 1-9.

# Chapter 5. High-resolution x-ray stereomicroscopy: true three-dimensional imaging of biological samples

## Summary

X-ray microscopy has the potential to become a powerful tool for the study of biological samples, allowing the imaging of intact cells and subcellular organelles in an aqueous environment at resolutions previously achievable only by electron microscopy. The ability to examine a relatively thick sample raises the issue of superposition of objects from multiple planes within the sample, making difficult the interpretation of conventional, orthogonally projected images. This paper describes our early attempts at developing three-dimensional methods for x-ray microimaging (Loo *et al.*, 1992): the first to use x-ray optics, and to our knowledge, the first demonstrating sub-visible resolutions and natural contrast. These studies were performed using the scanning transmission x-ray microscope (STXM) at the National Synchrotron Light Source, Brookhaven National Laboratory.

## Introduction

Soft x-rays have a number of advantages over visible light and electrons as a source of illumination for biological microscopy. Because of their short wavelengths (typically 25 to 36 Å) compared to visible light, and the development of high resolution diffractive zone plate optics, diffraction limited imaging is possible (Jacobsen *et al.*, 1991) with resolutions currently three to five times better than possible with visible light microscopy (50 to 70 nm *vs.* 200 to 250 nm). In addition, x-rays penetrate both water and organic material much more efficiently than do electrons, allowing the imaging of whole cells

without the need for sectioning. Table 1 gives some examples of attenuation length and transmission of x-rays through water and biological samples we have examined. Imaging times of approximately one minute with counting statistics of greater than 100 counts per pixel in the darkest part of the image are readily achievable, with improvements of up to an order of magnitude anticipated in the immediate future. Finally, imaging with x-rays offers "natural contrast." Because organic molecules absorb x-rays much more strongly than the surrounding water in the wavelength range between the oxygen and carbon K shell absorption edges (the "water window"), stains are unnecessary (Figure 5-1). These advantages give rise to the concept of "physiological imaging"—the imaging of whole (intact) cells and subcellular organelles, unmodified except by separation from their source tissue, in an aqueous, physiological environment. The implication of this is that we can image cells that, at least at the beginning of the experiment, are still functional. And depending on the damage caused by the imaging process (*e.g.*, by radiation exposure) and the sensitivity of the process under study to that damage, we may be able to acquire dynamic information about biological samples.

| |
|---|
| **Examples of attenuation lengths in water:** |
| 3.1 μm at λ = 36.4 Å — 20% transmission at 5 μm thickness |
| 8.1 μm at λ = 25.0 Å — 29% transmission at 10 μm thickness |
| **Transmission through selected biological samples:** |
| Pancreatic zymogen granules (1 to 2 μm thick) — 60 to 95% transmission |
| Human spermatozoa (2 to 5 μm thick) — 35 to 75% transmission |
| Pancreatic acinar cells (7 to 15 μm thick) — 3 to 61% transmission |
| (Range from most opaque to most transparent regions of object) |

Table 5-1

The ability to image intact specimens, while clearly desirable, gives rise to the following problem: the image of a thick object comprises a superposition of elements

from multiple planes within the object. Such images, especially of objects with complex internal architecture or processes involving changes in three-dimensional spatial relationships, can be difficult to interpret. To illustrate, Figure 5-2 demonstrates how a single view may be inadequate to interpret the image of a dynamic cellular process.

The approach to recovering the information lost by superposition is different for visible light and x-ray methods. High resolution visible light optics have a high numerical aperture and short depth of focus comparable to their lateral resolution ($\Delta f \approx d \approx \lambda$). Thus three dimensional reconstruction is accomplished by physical or optical sectioning. X-ray optics on the other hand have a low numerical aperture and long depth of focus ($\Delta f > d > \lambda$). An x-ray image therefore approximates a parallel projection of the object onto a plane, a condition ideal for stereoscopy and tomography.

For these studies, a multiple angle viewing stage was designed and fabricated at Lawrence Berkeley Laboratory for use with the STXM (Figure 5-3). The stage allows a maximum rotation of plus and minus 30 degree currently, and translation of the sample along two axes for positioning of objects to be imaged on the axis of rotation. From the figure, "depth resolution" can be expressed as $\Delta z = d/\sin\theta$, where d is the lateral resolution of the microscope.

**Results**

Three samples were imaged: rat spermatozoa, human spermatozoa, and rat pancreatic zymogen granules. The imaging parameters and conditions are summarized in Table 2. The following images (Plates 5-1 through 5-5) demonstrate the ability of the method to

meet a number of the goals biological microscopists have for x-ray microscopy—resolution significantly beyond that of visible light methods, the ability to image biological samples in a near-physiological state, and three-dimensional imaging.

Imaging Parameters and Conditions

| | |
|---|---|
| • Wavelength: | $\lambda = 36.4$ Å |
| • Zone plate: | $\delta = 60$ nm (outer zone width) |
| • Rayleigh resolution: | $d = 73$ nm |
| • Pixel size: | 9 to 48 nm |
| • "Depth resolution:" | $\Delta z = 0.42$ μm for $\theta = 10°$ |
| • Depth of focus: | $\Delta f = 4.8$ μm for $\lambda = 36.4$ Å |
| • Contrast: | Due to carbon content—No stains |
| • Sample conditions: | *Unsectioned & suspended in aqueous medium* |

Table 5-2

## Conclusion

Future directions in this work include improving both the lateral and depth resolution of the method. As finer optics are developed, we will benefit from them. Also, larger optics with the current resolutions would improve the working distance and allow sample tilting through a larger range of angles. Extending the range of angles can also be accomplished simply by refining the design of the multi-angle viewing stage to accommodate more effectively the limited spatial confines of the STXM. Given the ability to image at multiple angles, the next logical step would be to attempt microtomography using computerized reconstruction techniques.

Finally, shortening the image acquisition time for stereoscopy should open the possibility of "four-dimensional" imaging, with both spatial and time resolution. In previous work (Rothman *et al.*, 1992) we demonstrated the ability to observe time-resolved changes within a single object with two-dimensional imaging. Specifically, we

were able to measure both the position and mass of individual zymogen granules as these parameters changed with time within an intact pancreatic cell undergoing osmotic swelling in the absence of hormonal stimulation (Plate 5-6). Extending the current work to these studies might allow observation of the secretory process in a stimulated cell in a more direct manner than possible with other methods.

**Acknowledgments**

The authors would like to thank the following people for their valuable contributions to this work.

At Lawrence Berkeley Laboratory: Center for X-Ray Optics—Erik H. Anderson, David T. Attwood, Phillip J. Batson, René Delano, Eric M. Gullikson, Nasif N. Iskander, Keith Leslie, Ron E. Tackaberry, Charmaine V. Toy, James H. Underwood; Life Sciences Division—Hsien-Chen Tseng; Mechanical Engineering Technology Department—Luis A. Curtis, Tony T. Freeman, George Harp, Dimitri N. (Ed) Voronin, William L. Worthington; Advanced Light Source Experimental Systems Group—Malcolm R. Howells. Engineering Science Department—Billy W. Loo, Sr.; Information and Computing Sciences Division—Edward W. (Wes) Bethel; Photography Services Department—Steven G. Adams; Physics Department—Raymond Z. Fuzesy.

At the University of California, Berkeley: Graduate Group in Biophysics—Kaarin K. Goncz.

At the University of California, Davis, School of Medicine: Department of Cell Biology and Human Anatomy—Kenneth O. Turner; Department of Medical Microbiology and Immunology—Jerold Theis.

At the State University of New York, Stony Brook: Department of Physics—Pete Davis, Janos Kirz.

At Lawrence Livermore National Laboratory: Dino Ciarlo.

At the University of Chicago: Mark L. Rivers.

This work was supported by U.S. Department of Energy Contract No. DE-AC03-76SF00098, National Science Foundation Grant No. DIR-9005893 and National Institutes of Health Grant No. HD-23098.

## Figure captions

**Figure 5-1.** Mass dependent absorption coefficients of protein and water in the x-ray wavelength region known as the "water window.'

**Figure 5-2.** Schematic depiction of the process of exocytosis, the generally proposed mechanism of cellular secretion in which secretory granules migrate to the periphery of the cell, fuse with the plasma membrane, and release their contents to the exterior. The top and bottom sequences illustrate this process as it might appear in the same cell if viewed from two different angles 90 degrees apart. A single view might yield a very different interpretation than the two taken together. For example, the bottom sequence viewed alone suggests a totally intracellular process, with no gross movement.

**Figure 5-3.** Schematic representation of the sample tilting mechanism and the concept of "depth resolution" in stereoscopy.

## Figures

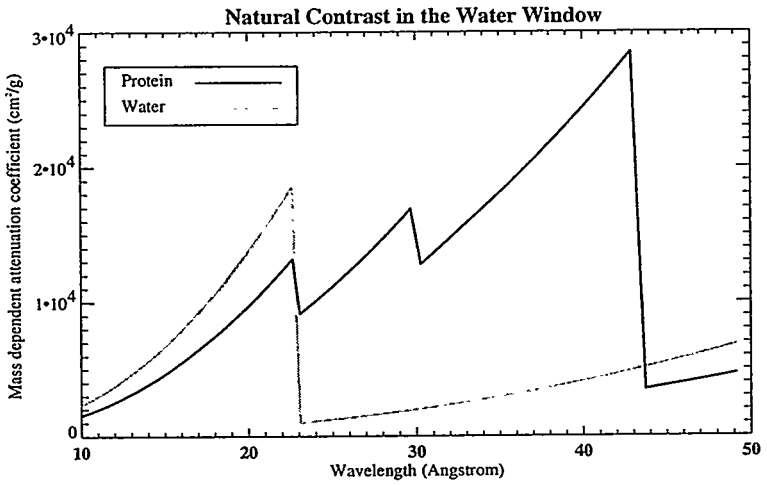


Figure 5-1

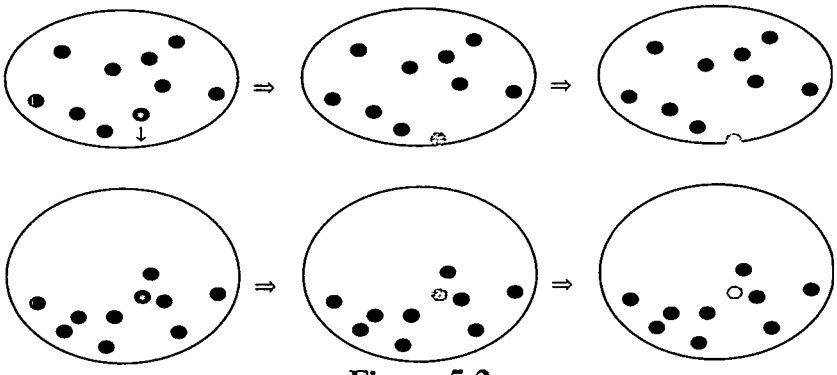

Figure 5-2

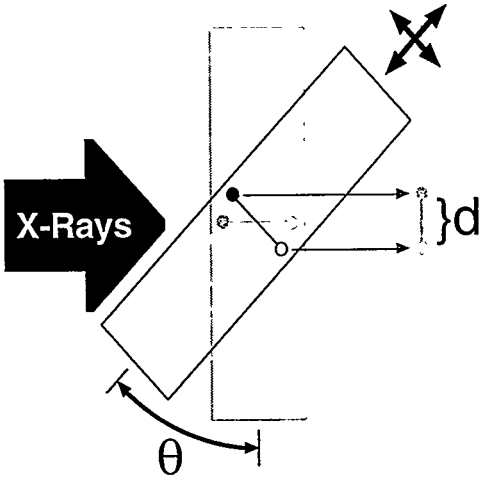


Figure 5-3

## Micrograph captions

**Plate 5-1.** Surface plot of the head, neck, and part of the tail of a rat spermatozoon, in which sample absorptivity is represented as "height" to appreciate better certain features. Part of the tail of another cell overlaps with the head. This image demonstrates the ability to detect density variations within the head region and the fine structure of the tail in the absence of stains. The axonemal complex of the tail, a feature less than 0.1 μm wide, is visualized clearly even in the unsectioned cell as a line of increased absorptivity in the center of the tail. It is important to note that while this type of representation gives the impression of depth, it contains no true three-dimensional spatial information. Imaging parameters: 500 x 200 pixels, 40 nm pixel size, 60 nm zone plate.

**Plate 5-2.** Human spermatozoon: head, mid-piece, and principal piece of tail. Apparent in this image are the density variations in the head, and the structure in the mid-piece region of the tail. Also, there is a clear demarcation between the mid-piece of the tail, which contains the mitochondrial sheath, and the principal piece. The increased density in the posterior part of the head is a consistent feature in x-ray and phase contrast visible light micrographs of these objects, but absent in transmission electron micrographs. This suggests that it may represent a structure seen only in unsectioned cells, perhaps the post-acrosomal sheath. Imaging parameters: 300 x 360 pixels, 30 nm pixel size, 60 nm zone plate.

**Plate 5-3.** Human spermatozoon: head, mid-piece of tail, and cytoplasmic droplet. Part of a tail from another cell overlaps with the head. This image demonstrates the ability to

resolve the turns of the helical mitochondrial sheath (the "bumps" indicated by the arrows), structures that previously could be resolved only by electron microscopy. Also seen is a cytoplasmic droplet (C), a remnant of the cell's maturation process. Imaging parameters: 360 x 150 pixels, 30 nm pixel size, 60 nm zone plate. From Loo *et al.* (1992).

**Plate 5-4.** Stereo image pair of human spermatozoa. This image shows two cells, with the tail of one wrapped around the head of the other. The "depth resolution" is 0.4 $\mu$m. The most striking feature is the ability to trace the looping path of the tail in three-dimensional space. Some internal structure is apparent in the head and mid-piece regions. Ultimately the goal of the method is to be able to distinguish clearly the intracellular architecture of the cell in three dimensions. The ability to detect density variations with good contrast within the cell suggests that this should be readily achievable with improvements in lateral and depth resolutions. Imaging parameters: 350 x 260 pixels, 50 nm pixel size, 60 nm zone plate, 20° angle separation. From Loo *et al.* (1992).

**Plate 5-5.** Stereo image pair of a secretory (zymogen) granule isolated from rat pancreas. At less than 1 $\mu$m diameter, the zymogen granule (upper left part of field) is the smallest object we have imaged. "Depth resolution" is 0.8 $\mu$m. Three-dimensional intragranular structure is difficult to appreciate, but the spatial relationship of the granule to other objects in the field (debris) is clear. Imaging parameters: 400 x 400 pixels, 9 nm pixel size, 60 nm zone plate, 10° angle separation.

**Plate 5-6.** Time-lapse sequence of rat pancreatic acinar cell. These images, taken approximately seven minutes apart, are of the same cell as it undergoes osmotic swelling, possibly as a result of exposure to x-rays. Between frames 2 and 3, the cell loses half of its mass as it lyses. The dark objects within the cell are zymogen granules. Most significantly, it is possible to follow individual granules through time (for example, the group of granules in the upper right region of the cell) until they are lost (frame 4). In addition, it is possible to determine changes in the mass of the granules. With the shorter imaging times now achievable, it should be possible to follow in a quantitative fashion the secretory process of the cell in response to hormonal stimulation with both time and depth resolution—"four-dimensional" imaging. Imaging parameters: 256 x 256 pixels, 95 nm pixel size, 70 nm zone plate. From Rothman *et al.* (1992).

**Micrographs:**

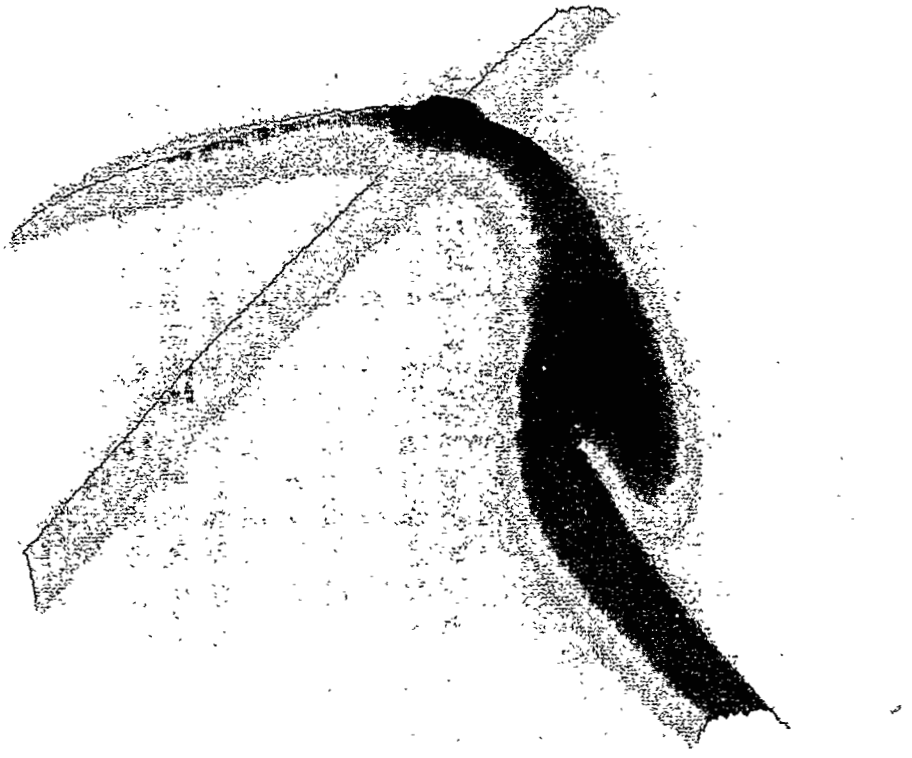

**Plate 5-1**

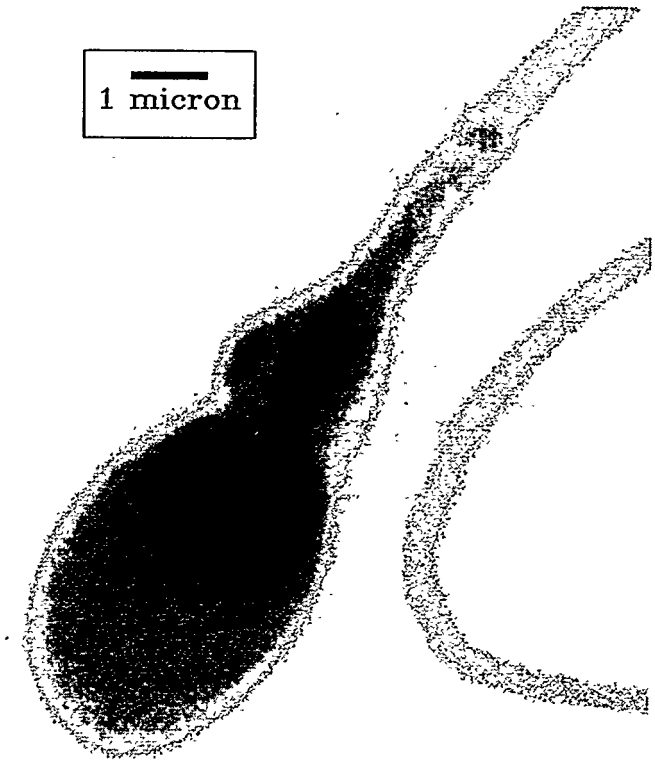


**Plate 5-2**

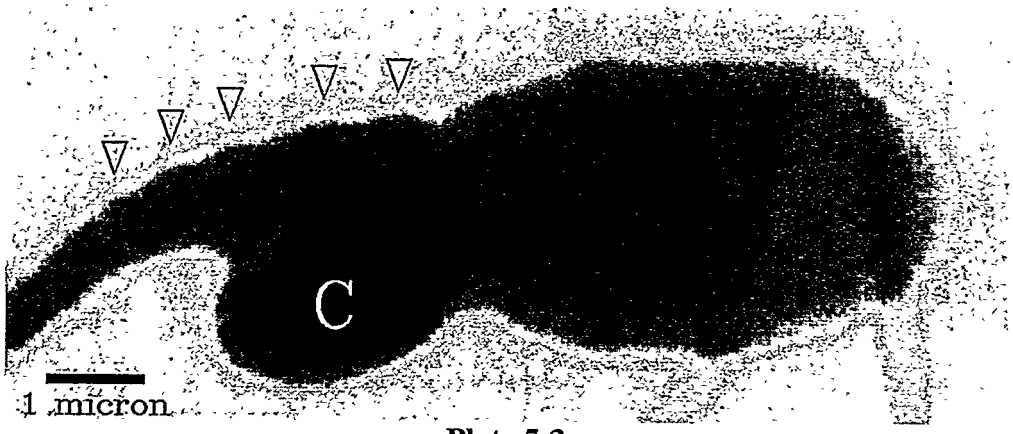


**Plate 5-3**

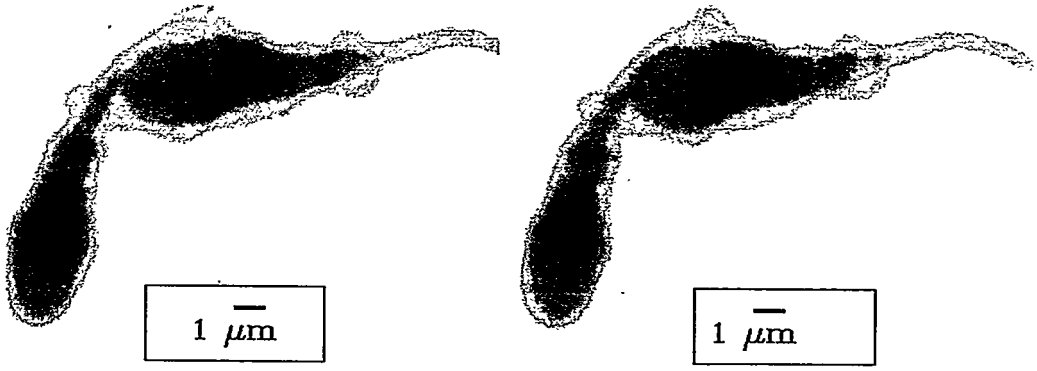


**Plate 5-4**

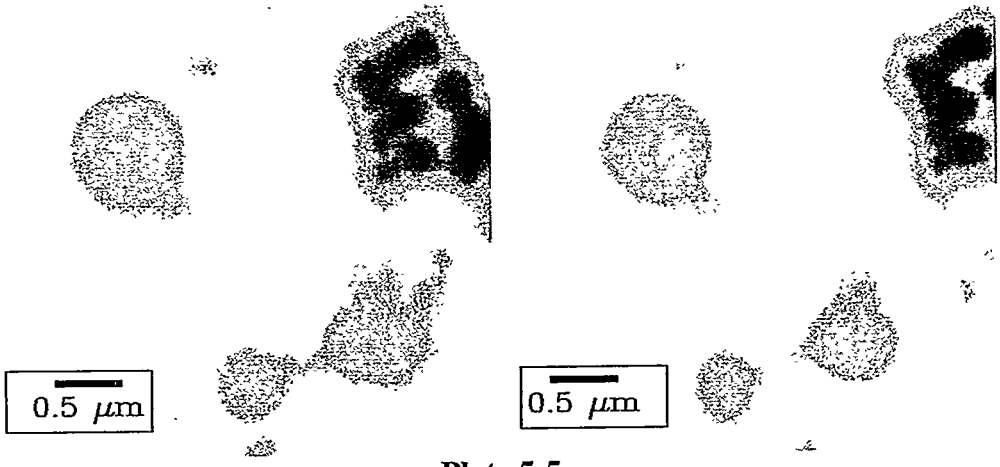


**Plate 5-5**

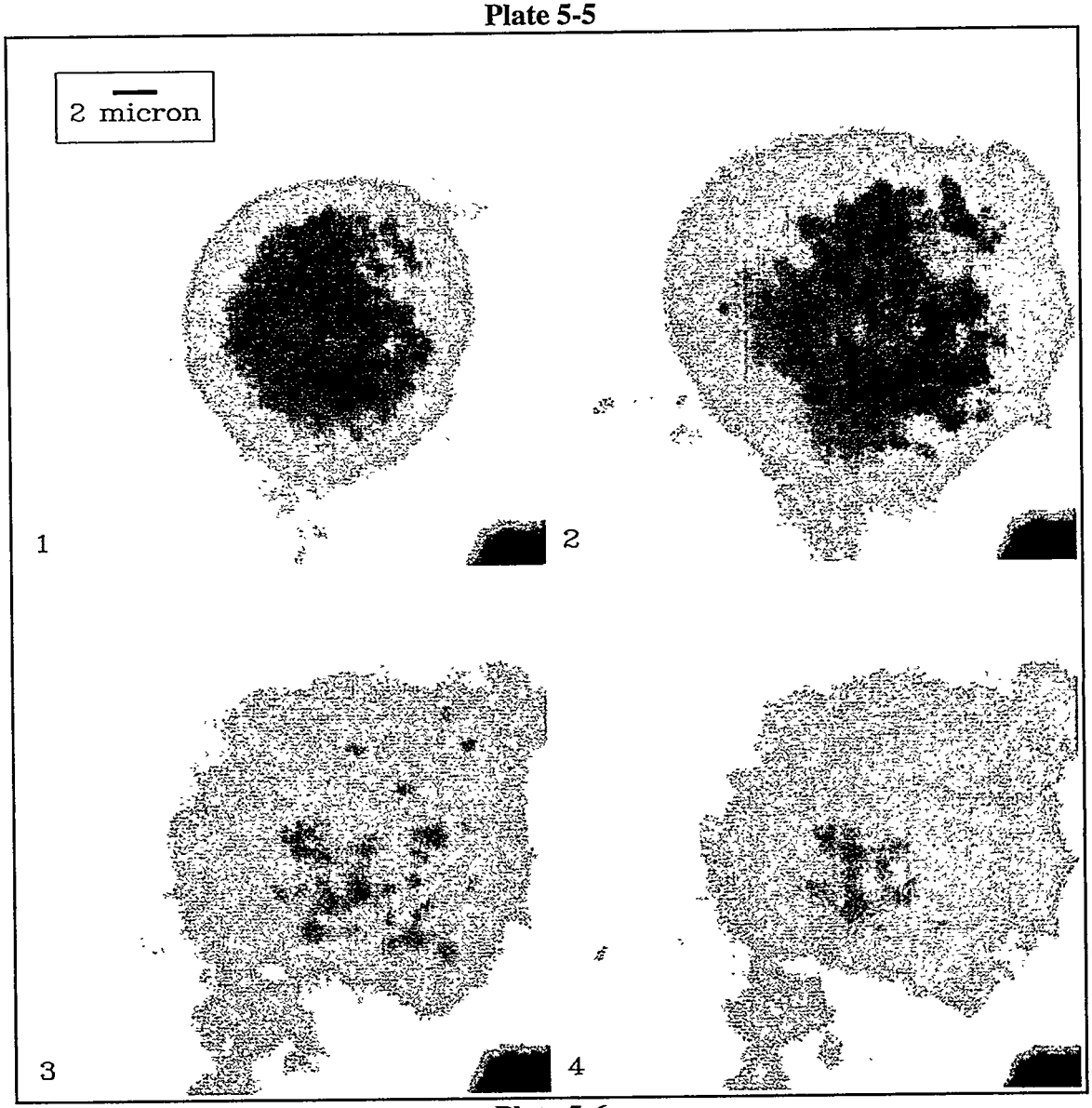


**Plate 5-6**

## References

Jacobsen, C., Williams, S., Anderson, E., Browne, M.T., Buckley, C.J., Kern, D., Kirz, J., Rivers, M. & Zhang, X. (1991) Diffraction-limited imaging in a scanning transmission x-ray microscope. *Optics Communications*. **86**, 351-364.

Loo, B.W., Jr., Williams, S., Meizel, S. & Rothman, S.S. (1992) X-ray stereomicroscopy: high resolution 3-D imaging of human spermatozoa in aqueous suspension with natural contrast. *Journal of Microscopy*. **166**, RP5-RP6.

Rothman, S.S., Goncz, K.K. & Loo, B.W., Jr. (1992) Following protein transport with the high resolution x-ray microscope. *X-Ray Microscopy III: Proceedings of the Third International Conference, London, September 3-7, 1990.* (ed. by A.G. Michette, G.R. Morrison, and C.J. Buckley), pp. 373-383. Springer-Verlag, Berlin.

# Section 2: Automatic acquisition, calibration, and analysis of biological x-ray microscopic images

# Chapter 6. Automatic image acquisition, calibration, and montage assembly for biological x-ray microscopy


## Summary

We describe a system for the automatic acquisition and processing of digital images in a high-resolution x-ray microscope, including the formation of large-field high-resolution image montages. A computer-controlled sample positioning stage provides approximate coordinates for each high-resolution subimage. Individual subimages are corrected to compensate for time-varying, nonuniform illumination and CCD-related artifacts. They are then automatically assembled into a montage. The montage assembly algorithm is designed to use the overlap between each subimage and multiple neighbors to improve performance of the registration step and the fidelity of the result. This is accomplished by explicit use of recorded stage positions, optimized ordering of subimage insertion, and registration of subimages to the developing montage. Using this procedure registration errors are below the resolution limit of the microscope (43 nanometers). The image produced is a seamless, large-field montage at full resolution, assembled automatically without human intervention. Beyond this, it is also an accurate x-ray transmission map that allows the quantitative measurement of anatomical and chemical features of the sample. Applying these tools to a biological problem, we have conducted the largest x-ray microscopic study to-date.


## Introduction

X-ray microscopy has some unique and attractive features as a tool for biological imaging (Schmahl *et al.*, 1980; Rothman *et al.*, 1990; Kirz *et al.*, 1995). Among the most

important are high contrast due to the natural constituent molecules in cells and tissues, and significantly higher resolution than visible light microscopy. In an x-ray microscope, low energy x-rays (with wavelengths ranging from 2 to 4 nm in this work) illuminate a sample, and an image is formed from the transmitted photons. Materials absorb these "soft" x-rays in a manner highly dependent on their elemental and chemical composition (Henke *et al.*, 1993). This "natural contrast" permits quantitative measurement of the distribution of intrinsic cellular components (*e.g.*, carbon, nitrogen, protein, DNA) without stains. In addition, the relatively high penetration of soft x-rays (up to several micrometers) allows imaging of a wide range of samples from standard embedded tissue sections of various thickness to whole cells in their native state (*e.g.*, in aqueous media). High-resolution imaging is made possible by microfabricated diffractive optical elements that are used as lenses, called zone plates (Anderson & Kern, 1992; Schmahl *et al.*, 1996), whose fine feature size allows imaging with 43 nanometer (nm) resolution in the microscope used here (Heck *et al.*, 1999). This is five times the maximum resolution of a standard visible light microscope.

In recent years, the development of high quality zone plate lenses as well as the availability of high brightness sources of x-rays, in the form of synchrotron radiation facilities, has allowed the building of a number of practical x-ray microscopes (Thieme *et al.*, 1998) that are only now beginning to yield biological results. At this early stage in its maturation, much work is needed to make the x-ray microscope a useful tool for routine research in biology and to exploit its features fully. To achieve this goal, development is required in three areas: microscope instrumentation, sample preparation, and digital image acquisition and processing. This paper deals primarily with the last of these. In it

we describe how we acquire image data and obtain accurate quantitative information from them, and how we extend the high resolution of the method over large fields of view. As a practical matter, the methods must be automatic to allow for the processing of large numbers of samples encompassing large fields of view.

Quantitative imaging requires characterizing the properties and inherent sources of error of each component of the microscope system. Two in particular concern us here. The synchrotron source has a time-varying intensity and pattern of illumination for which we must compensate, and the charge-coupled device (CCD) camera used for image recording introduces artifacts, such as dark current and nonuniform pixel response. Though methods for correcting CCD-related artifacts are standard and well documented in the literature (*e.g.*, Krivanek & Mooney, 1993), here we describe our particular approach and the issues specific to our system.

To take advantage of the high resolution of the x-ray microscope, we must use high magnification, and consequently sacrifice field of view. This tradeoff is found in almost all forms of microscopy regardless of the wavelength of illumination (electrons, x-rays, or visible light), particularly in full-field imaging. This applies even to many forms of scanning microscopy, since scanning stages often have a smaller range of motion as the step size becomes finer. As a result, it has been difficult to undertake projects that require sampling large areas at high resolution, for example studying samples with both small and large scale features, or survey and screening studies. One solution to this problem is to build large-field composite images from many smaller high-resolution subimages, a process variously referred to as montaging, mosaicking, field stitching, or tiling. Automatic montage assembly for various kinds of photography and videography has been

extensively developed in computer vision and graphics (*e.g.*, Dani & Chaudhuri, 1995; Davis, 1998). Similar methods have been applied to microscopic imaging, including the assembly of huge montages in electron microscopy (Vogt *et al.*, 1996), and three-dimensional montages in visible light microscopy (Turner *et al.*, 1997). A number of commercial implementations are also available. Below we describe the system we have designed for automatically acquiring digital images and assembling large-field montages of arbitrary size at the full resolution of the x-ray microscope, and we demonstrate its application to biological samples.

## Methods

*The x-ray microscope:*

We used a digital x-ray microscope, called XM-1 (Meyer-Ilse *et al.*, 1995; Meyer-Ilse *et al.*, 1998), at the Advanced Light Source (ALS) synchrotron radiation facility at Lawrence Berkeley National Laboratory (LBNL). XM-1 is a conventional-type, or full-field imaging, transmission microscope. A condenser zone plate demagnifies the incoherent light source (a bending magnet on the ALS) onto the sample, and an objective zone plate images the sample onto an image detector. Two components of the microscope, the image detector and the sample stage, have a particular impact on calibrating images and assembling large-field montages.

The image detector is a charge-coupled device (CCD) camera, thinned and back-illuminated for high efficiency detection of soft x-rays (Wilhein *et al.*, 1994). The CCD chip has a 1024 by 1024 array of 24 micrometer (μm) pixels. The field of view of XM-1 in its most heavily used configuration is a circular area approximately 10 μm in diameter,

and at 2,400 times magnification (the one most often used) this field, projected to the image plane, matches the width of the CCD. The corresponding pixel size in the image is 10 nm. Often, we use subsampling by binning CCD pixels together to reduce the exposure time and data storage requirements. At 2 times binning, or a 20 nm pixel size, the Nyquist sampling criterion is still met for 40 nm resolution. When total field size is a more important consideration than raw resolution, 4 times binning can be used. The digital data from the CCD is read directly into a computer, which facilitates subsequent processing.

The sample positioning system, developed at LBNL, has a unique design, with two separate sample stages, one each in the x-ray microscope (XM), and an external visible light microscope (VLM). Stage position readout is accomplished using Heidenhain optical encoder scales in 3 orthogonal directions on each stage, with readout increments of 20 nm. A magnetic kinematic mounting system allows mounting and unmounting of the sample on and off a stage with a reproducibility comparable to the resolution of the microscope, in the tens of nanometers. The three-dimensional coordinate systems of the two stages are related to each other by a matrix transformation incorporating the relative offset, rotation, and skew between them. The correspondence between positions in the two stages is accurate to less than 2 μm in the object plane, and about 1 μm along the optic axis, or approximately the depth of focus of both the VLM (with a 0.6 NA objective lens) and the XM. Thus, using this system it is possible to select and focus on sample areas of interest entirely within the VLM. Sample exposure to x-rays is thereby limited to the final image recording, minimizing dose. This is a critical consideration for dose-sensitive samples. The sample stage coordinates at which each image is acquired are

recorded and saved with the image data, and then used in the montage assembly process as estimates of subimage position.

*Acquisition of high-resolution subimages in XM-1:*

When acquiring subimages for montage assembly, the center and total width of the area of interest are recorded using the graphical interface of the microscope control software. A rectangular grid of equally spaced subimage positions is then computed to cover the region. For circular subimage fields, this pattern of coverage is not ideal, because in order to have sufficient overlap between neighboring subimages along the diagonals, there is more overlap than necessary between horizontal and vertical neighbors. An equidistant triangular pattern of coverage would be optimal, and should be relatively easy to implement. The grid spacing is typically between 5 to 6 μm, depending on the subimage field diameter (usually about 8 μm), giving 0.5 to 2 μm (or 25 to 100 pixels in the case of 2 times binning) of maximum overlap between neighboring subimages.

Under computer control, the sample stage is sequentially moved to each of the preselected subimage positions and the sample is exposed. The current in the synchrotron storage ring continuously decreases with time, resulting in decreased source intensity. Thus, when acquiring each subimage, the ring current is read, and exposure time adjusted automatically to compensate. The exposure, or product of ring current and exposure time measured in milliampere-seconds (mAs), is kept approximately constant across all subimages. At regular intervals in the subimage acquisition sequence, preselected empty areas on the sample window containing no sample features are exposed to provide

background images to be used for field inhomogeneity correction (described below). The entire process, except for user selection of the region of interest and background areas, and the initial selection of the exposure level, is automated.

*Corrections applied to individual subimages:*

1. Dark current correction.

The major sources of signal in the CCD camera are charge generated by image forming x-ray photons, and dark current. Dark current in a CCD pixel is due to the accumulation of thermally generated charge carriers over the integration time, and is highly dependent on temperature (Dereniak & Crowe, 1984). The temperature of the CCD chip is maintained at -50 degrees Celsius by a thermoelectric cooler to keep dark current at an acceptable level. We modeled dark current signal in each pixel as an affine linear function of integration (exposure) time that is additive to the photon-produced signal. In addition there is an intensity offset that is added to the signal by the camera readout electronics to prevent readout noise from generating negative intensity values.

Dark current images are collected for camera calibration on a periodic basis by acquiring images with no light on the camera. Multiple dark current images are acquired at each of several different exposure times and several different camera binning factors. Linear regression is performed on a pixel by pixel basis, giving a slope and offset of dark current versus exposure time for each pixel. Most of the offset component is due to the above mentioned intensity baseline offset. Figure 6-1a is an image of the dark current slope in the CCD camera. From these measurements, "bad" pixels are identified. These are pixels that saturate due to dark current within a specified exposure time, or have slope

or offset different from the mean of the array by more than a specified tolerance (typically 10 standard deviations), or are unresponsive as demonstrated by a zero variance over multiple exposures. Between 0.4 to 0.9 per cent of the image pixels are bad, depending on the binning factor, with the higher proportion occurring with more binning. The dark current slope and offset, and the bad pixels, are recorded in a calibration file for each binning factor.

Each subimage is corrected for dark current by subtracting a corresponding calculated dark current image, *i.e.*, the offset plus the slope times the exposure time of the subimage. This is in principle a photometrically accurate correction. This is different from the standard procedure of subtracting a single acquired dark image with the same exposure time as the subimage, and has the theoretical advantage that it does not add the small amount of noise due to statistical variations in dark current signal and readout noise.

To illustrate the small magnitude of the dark current contribution, the signal intensity due to x-ray photons in a background image that is saturated to about 60 per cent of the camera's dynamic range in about 12 seconds (Figure 6-1b) is approximately 1,200 times greater than the dark current signal in that exposure time. A significant increase in dark current was noted once, which led to the discovery that the CCD chip had lost contact with the thermoelectric cooler. The problem resolved as soon as this was corrected. We have also noted a very slow but measurable increase in dark current with x-ray exposure over the lifetime of the instrument, presumably due to radiation damage. This can be seen to some extent in Figure 6-1a in the pattern of dark current slope, since some parts of the chip were much more heavily exposed than others during the initial alignment of optical components in the microscope.

2. Region of support selection and exposure normalization.

The field of view in each subimage is circular and therefore does not fill the entire square CCD pixel array. An iris in front of the camera is used to block off areas outside the field of view, and can be adjusted to exclude scattered light that is more intense at the periphery of the field. The information containing area of the images, or region of support, which is the same for all images with the same camera iris setting, is identified interactively. The remainder of the pixels are masked off by setting them to a value of zero (see Figure 6-1c). A typical region of support has a diameter of about 8 μm in the sample plane.

As described above, the exposure time is automatically adjusted to compensate for decreasing beam intensity over time. Any remaining differences in exposure between subimages are balanced by dividing each subimage by its measured exposure (in mAs).

3. Field inhomogeneity correction.

The image field may be inhomogeneous because of nonuniform illumination and nonuniform pixel response or sensitivity to light. Both factors cause differing rates of signal accumulation between pixels and cannot be isolated from each other. However we can simultaneously compensate for all sources of inhomogeneity that cause such a multiplicative effect by dividing each sample image by a background image. Additive phenomena, such as scattered light that reaches the camera, are not properly corrected by this means. A background image is an image of an area on the sample holder that contains no sample features. In a perfect system, such an image should have uniform intensity across the field. Any inhomogeneity is due to artifacts. Figure 6-1b shows a

background image acquired in XM-1. Some of the patterns on the image are due to debris or dirt on the CCD camera that obstruct some pixels and thereby decrease their sensitivity to x-rays by absorbing part of the signal.

If the pattern of illumination were constant with time, it would be possible to use the standard procedure of normalizing all images to a single background image formed by averaging several exposures with no sample in the beam. However we have found that during the course of a long subimage acquisition sequence, the background pattern changes smoothly with time, possibly due to a drift in the position of the ALS beam or components in the optical path (see Figure 6-5). Therefore background images must be acquired at multiple time points throughout the subimage acquisition sequence. At each of these times, several empty areas on the sample window are imaged. They are averaged together to reduce the effect of photon shot noise, and the effect of dirt or other features that are inadvertently captured within any of the background images. To minimize further the effect of extraneous features, the sample stage is moved to an out-of-focus plane to blur them. Finally, if any noticeable effects due to blemishes in the background image remain, the pixels can be identified interactively and replaced by the average of the corresponding pixels from the other background images acquired at the same time.

Because background images are collected throughout the subimage collection sequence, each subimage is bracketed in time by two background images. The acquisition time of every subimage and background image is recorded with the image data. This allows the generation of a time interpolated background image for each subimage, by performing a pixel by pixel linear interpolation between the bracketing background images.

Each background image is subjected to the same dark current correction, region of support masking, and exposure normalization as described for the individual subimages. Each subimage is then corrected by division by its corresponding background image. As seen in Figure 6-1d, the corrected image shows only the true sample structure, with a homogeneous background response. Despite these corrections, we occasionally found a small amount of additional intensity, particularly near the edges of the field of view, probably due to an additive signal such as scattered light in the microscope system. This is usually only noticeable in an assembled montage, where it appears as a small intensity mismatch at the borders of neighboring subimages (see Figure 6-6).

*Assembling subimages into a large-field montage:*

After the individual subimages are corrected, they are inserted into the montage. The goal is to register each subimage accurately with the target region in the montage into which it is to be inserted. We assume that magnification and rotation are constant over all subimages, and that registration can be accomplished solely by translation. As shown, the quality of the resulting registration reinforces the validity of this assumption in our system. The ability to register any two images with one another improves as the feature overlap between them increases. The montage assembly algorithm attempts to maximize feature overlap between any subimage and its target area in the montage. The recorded sample stage positions are used at multiple steps in the process.

First, a subimage adjacency table is generated, identifying which subimages neighbor which, based on their stage positions and the subimage field size defined by the region of support mask, as described above. The dimensions of the entire montage are similarly

calculated, and the subimage closest to the center of the field is identified. Starting with the centermost subimage, an optimized insertion order is determined as follows: the adjacency table is used to organize subimages into sequential generations of neighbors, the first generation being the immediate neighbors of the centermost subimage, the next being their neighbors, and so on. Subimages within each generation are sorted in order of their distance from the centermost subimage, again based on their stage positions.

Next, an empty image array is created with the dimensions of the full montage, with a small margin added to accommodate possible errors in the stage positions. A correspondence is calculated between the pixel positions in the montage and the stage positions. The centermost subimage is then inserted into the appropriate position in the montage. As each subsequent subimage is inserted, the correspondence between pixel and stage positions allows identification of the target area of the developing montage into which it will be inserted. This target area contains contributions from the parts of previously inserted subimages that overlap with the current one. It is extracted from the montage, and used as a reference image to which the current subimage is registered. The amount of translation or shift that must be applied to the subimage to register it to the reference region is calculated. The subimage is then inserted into the montage at a position appropriately shifted relative to its corresponding stage position.

This approach has a number of advantages. It saves on computation because each subimage is registered only once (with a corresponding reference region from the developing montage) rather than pairwise with each of its neighbors. Also, because reference regions contain data from more than one previously registered subimage, there is much more feature overlap with the subimage to be inserted than there would be if

registration were performed pairwise between individual subimages. Figure 6-2a shows a subimage, and the reference region from the developing montage to which it is registered.

The registration step itself is a form of generalized correlation operation (Knapp & Carter, 1976; Azaria & Hertz, 1984) with the addition of a non-linear processing step. The non-linear processing step, a gradient magnitude operation, is performed first on the subimage and its reference image. This highlights the features in the images, producing a bright signal at object edges, and a dark signal in the relatively uniform areas in the background and in the interior of objects. Figure 6-2b shows the gradient magnitude images of the subimage and reference image in Figure 6-2a. The result is a sharpening of the peak produced by the subsequent correlation step (Figure 6-2 insets). We used a Sobel gradient operator, which performs well in the presence of typical noise levels, to compute the gradients of each subimage and its reference image.

Then a filtered cross-correlation operation is performed on the gradient magnitude images to determine by what amount the subimage should be shifted relative to its reference image and therefore its recorded stage position. Each cross-correlation is computed over a range of shifts corresponding to zero plus and minus 0.6 μm with respect to the stage position for the subimage being inserted. This accommodates the largest anticipated shift based on the accuracy of stage position readout, plus a safety margin. A difference of Gaussians bandpass filter is applied to the cross-correlation image to sharpen peaks while suppressing noise. The position of the highest peak in the filtered cross-correlation image is used to determine the shift to apply. Figure 6-2c demonstrates that the peak position is unaffected by the addition of a substantial amount of artificial Gaussian noise. In this example, the standard deviation of the noise was

chosen to be two-thirds the difference in intensity between the bars and spaces of the test structure (signal to noise ratio, SNR, of 1.5), far more than typical for this kind of imaging.

The subimage is then inserted into the montage at its shifted coordinates. Figure 6-3a shows a registered set of gradient magnitude subimages. Their corresponding cross-correlation images are in Figure 6-3b. While all the cross-correlation images are scaled to comparable brightness in the display, the range of the peak correlation intensities spans nearly four orders of magnitude. With very few exceptions, even at the lowest end of the range, the peaks are prominent enough to identify the appropriate shift uniquely.

Each pixel value in the areas of overlap between adjacent subimages is computed as the average of all the subimage pixels contributing to it. This increases the signal to noise ratio in the areas of overlap, and minimizes wasted radiation exposure to any part of the sample in the sense that all of the exposure goes towards improving image quality. A completed montage of thin gold structures used as high-resolution test objects is in Figure 6-4c.

Finally, as mentioned above, despite all the corrections there is occasionally a noticeable intensity mismatch in the montage at subimage borders, due to some uncorrected factor such as scattered light. Without knowing the nature of the source of the artifact, it is not possible to correct for it. However, its appearance can be minimized by blending subimages into the mosaic. Rather than doing a straight average in the overlapping areas, a weighted average is used, with the weights for each subimage tapering smoothly to zero near its border. Figure 6-6 shows the effect of this blending.

This is, of course, not a true correction, but still it is helpful in minimizing the impact of the artifact on subsequent image analysis or processing, such as automated image segmentation (Loo *et al.*, 1996).

## Results

*Microfabricated resolution test objects:*

We evaluated the performance of our image acquisition and processing system on real microscope images taken of two thin gold structures microfabricated for the purpose of testing microscope resolution. The two structures, each with a diameter of 47 μm, together spanning a region 94 μm across, have features down to approximately 40 nm in dimension. Figure 6-4c is a montage of the full field of view containing both test structures, a composite of 200 subimages. The insets are magnified views of the central portions containing the finest features, demonstrating the full resolution of the microscope. The pixel size is 20 nm.

The performance of the registration can be assessed by comparing high-detail areas in the montage to the original subimages containing the same features. Figure 6-4a shows two original subimages from the central regions of the test structures. No degradation in resolution is discernable in the corresponding areas of the montage, despite overlap from several subimages, indicating registration errors smaller than the resolution limit of the microscope. In addition, as mentioned above, the corresponding montage areas have better signal to noise because of the contribution of signal from multiple subimages.

Because of the montage assembly algorithm's essentially perfect registration performance, at least on high contrast structures such as the resolution test objects, we found that it could be used to aid in a number of microscope diagnostics. In comparing the recorded stage positions of the subimages of the test objects to their adjusted positions, we found a nonrandom pattern of discrepancy. These were determined to be due to a 1.8 per cent error in the microscope magnification, corresponding to a 2.8 cm error in the sample to CCD distance (over a total of 1.56 m), and a 0.39 degree rotation between the CCD camera and the sample stage. No skew between the sample stage axes was identified. These errors are easily compensated for by a simple matrix transformation. A small random mismatch remained due to the limited precision of the optical encoder readout. Initially, we found the mean error in the determination of position to be substantially worse than expected based on the manufacturer's specified tolerance of 30 nm in the encoder readout. The problem was traced at least in part to an incorrect voltage offset in the optical encoders. After correction of this problem the mean position determination error, or the distance between each recorded stage position of a subimage and its true position, was 90 nm with a standard deviation of 50 nm. However, because the direction of the error is random, the mutual misregistration between any two adjacent subimages is somewhat larger at about 110 nm on average, with a standard deviation of 60 nm, sufficient to cause substantial degradation of the resolution without correction as seen in Figure 6-4b. This information can be used to set a limit on the maximum shift to calculate in the registration step.

*Biological samples:*

Applying the techniques to a biological problem (Rothman *et al.*, 1992; Loo *et al.*, 1996), we set out to measure the population statistics on the size, protein mass, and number of zymogen granules in pancreatic exocrine tissue. A quantitative morphometry problem such as this requires measurement of large samples to obtain a statistically meaningful estimate of these population parameters. In addition, it requires imaging large fields of view, because zymogen granules are distributed very unevenly, usually being clustered around ductal structures in the tissue.

Figure 6-7 is a montage of 400 subimages of a plastic embedded tissue section of rat pancreas, nominally 0.75 μm thick. The sample is unstained, and at the imaging wavelength used (2.4 nm) the contrast in such a plastic embedded sample is based primarily on the nitrogen content of the tissue, effectively providing a density map of protein and nucleic acid. The total field of view is 110 μm across, or about 2,700 by 2,700 pixels at 40 nm pixel size. The pancreatic cells are arranged in cluster-like units called acini, surrounding a duct system that conveys secreted material eventually to the gut. At their apical end, adjacent to the duct, the cells are packed with dense, sphere-like zymogen granules. Supporting structures are seen, such as red blood cell carrying capillaries, as are other intracellular organelles, such as mitochondria. The magnified view in Figure 6-7b demonstrates additional fine structure, including patterns of linear lucencies well beyond the ability of visible light microscopes to resolve. These may represent endoplasmic reticulum cisternae oriented perpendicular to the plane of sectioning, but whatever their identity they indicate the high resolution of the method.

The zymogen granules, often under one micrometer in size, are beyond the ability of the standard visible light microscope to measure and count accurately. Nor is there a direct way to quantify their protein content in either the visible light or electron microscopes. With its combination of high resolution and natural contrast, x-ray microscopy, in particular, large-field x-ray microscopy, can make all of the desired measurements on zymogen granules (size, number, and protein content), and is to the best of our knowledge the only tool available at present to do so. Nearly 100 such montages were assembled in this study, requiring the acquisition of nearly 27,000 subimages, making it the largest x-ray microscopic study to-date. The biological results will be published in a separate paper.

**Discussion**

We have developed digital imaging methods to help realize and enhance key strengths of x-ray microscopy, in particular high natural contrast permitting quantitative measurements, and high resolution. Quantitative x-ray imaging can only be accomplished by accounting for and correcting several instrument-related sources of error. To this end we have characterized the components of our system and shown how photometrically accurate images can be produced. We have also developed a method for acquiring images that retains the high resolution of x-ray microscopy while allowing an arbitrarily large field of view.

Though parts are similar to methods found in the literature, the montage assembly algorithm presented has a number of distinguishing features. In particular, it makes explicit use of recorded sample stage positions to estimate the overall size of the montage

field and the distance between subimages, to generate a subimage adjacency table, to compute coordinates for extracting target regions from the developing montage, and to calculate the required size of the cross-correlation arrays. It also determines an optimized subimage insertion order based on the adjacency table and the distance of subimages from the center of the developing montage. These two features provide dependable performance with arbitrary subimage acquisition order and adjacency pattern. That is to say, no assumptions are required about the spatial or temporal organization of the subimages. The algorithm will assemble the montage from all subimages that have a pathway of connectivity with a specified subimage, or the centermost one by default. Registering subimages with extracted target regions of the developing montage also affords certain advantages. First, it is more robust, because any neighbors of a particular subimage that have already been inserted contribute to its reference image, increasing the amount of feature overlap. It is also more computationally efficient since registration is performed on each subimage only once. Moreover, the approximate insertion position and the maximum shift are already known from the stage position, reducing the search space, and therefore computation. An optimization similar to the latter is achieved in some other published algorithms using a multi-resolution pyramid approach (Dani & Chaudhuri, 1995; Vogt *et al.*, 1996). However, these still require pairwise cross-correlation operations between each subimage and multiple neighbors.

As for the registration step itself, many methods have been devised for mutually aligning images (*e.g.*, Brown, 1992). Ours can be considered a hybrid of the two main approaches, *i.e.*, signal processing/statistical analysis and computer vision/image understanding. The first is represented by generalized correlation methods, in particular

maximum likelihood estimation (Knapp & Carter, 1976; Eversole & Nasburg, 1983). This method can be thought of (Knapp & Carter, 1976) as filtered cross-correlation in which two filters are applied. One is a whitening filter to deconvolve the signal autocorrelation from the delta function representing the image shift, and is generally high pass in nature for real-world images (Pratt, 1974). The other is a signal to noise ratio filter to suppress frequencies with high noise power, and is generally low pass in nature. Overall, the combined filters have bandpass characteristics. The statistical nature of the signal and noise components of the images must be known, estimated, or assumed in order to determine the exact filter weights. Instead of attempting to estimate optimal filter parameters, we have simply chosen a generic bandpass filter (the difference of Gaussians) that we have found to work well on our images. In addition, the derivation of the optimal estimate generally assumes a large region of overlap between the signals or images. However when assembling montages in microscopy, an attempt is generally made to overlap the subimage fields by a narrow margin, especially when minimal sample exposure is desired, as in fluorescence microscopy because of bleaching, and electron and x-ray microscopies because of radiation damage. In this case, the intersection between the regions of support of the search and reference images changes substantially with displacement, producing a slowly varying intensity background in the correlation image that can overwhelm the true peak (see Figure 6-2). Here, filtering with the difference of Gaussians, which tapers to zero weight at zero frequency, has the additional advantage that it suppresses this low frequency intensity background.

The second approach consists of a wide variety of nonlinear operations that are designed to extract features from the images to be registered. The correspondence

between these features can then be determined. For example, Turner *et al.* (1997) identify specific landmarks such as cell nuclei in the subimages by image segmentation, and register corresponding ones. This approach can give highly accurate registration. However, it requires that the segmented features be well distributed in the regions of overlap between subimages. In addition, segmentation algorithms tend not to be generalizable to all kinds of samples. We have found that the gradient magnitude operator, a step down from true image segmentation, is a simple, general, and reliable means of emphasizing features for registration in images. While it might be expected to perform poorly in the presence of noise due to its high pass nature, this does not seem to be a problem even when noise levels are much higher than we have observed (see Figure 6-2c).

There are weaknesses common to many montage assembly algorithms, including the one described here. If for some reason one of the subimages is incorrectly registered, it can affect the positioning in the montage of subsequently inserted subimages. This can happen under certain unfavorable conditions, for example if the area of overlap between a subimage and previously inserted subimages is relatively featureless, or contains only features that are periodic or have parallel edges. In such cases the cross-correlation would have an ambiguous or non-unique peak. Alternatively, features in the overlapping areas might change between exposures. Exposure induced changes in the sample are frequently seen in biological electron microscopy. They can also be seen with certain samples in the x-ray microscope, particularly hydrated biological samples, though we have not noticed it in the samples we have used. This problem is a complicated one, and might be addressed

by applying some kind of warping transform designed to compensate for beam induced artifact.

The first problem, accumulated errors due to ambiguous registration, appears more tractable however. Though the optimum registration may be ambiguous between a subimage and previously inserted subimages, it might be better between it and later subimages. Thus one solution might be to optimize the insertion order further by dynamic reordering. If, during the registration step, the cross-correlation peak for a subimage is smaller than some significance threshold, such as a certain number of standard deviations above the mean value of the cross-correlation image, the subimage can be moved to a later position in the insertion list, such as in the next generation of neighbors. Then by the time it is inserted, more of its neighbors will have contributed to its target area in the montage, increasing the chance of an unambiguous match. Another strategy, at somewhat increased computational expense, might be to perform global optimization of registration across all the subimages. In this scheme, pairwise cross-correlations would be precomputed between all neighboring subimages. The positions of all the subimages would then be shifted simultaneously so as to maximize the sum of all the cross-correlations, possibly by an iterative algorithm. In this way, the shift applied to any subimage would be most strongly influenced by its position relative to the neighboring subimages with which it shares the most features, regardless of the order of insertion. A similar idea is described by Davis (1998).

An unexpected realization of montage assembly was that the method could be used to calibrate microscopes. Indeed, this may well be one of the most sensitive means available to detect small errors in magnification, rotational misalignment between the detector and

sample stage, and sample stage skew. Finally, automating some of the last remaining steps still requiring human interaction, such as background region selection, blemish identification in background images, initial exposure selection, and subimage region of support masking, can be accomplished entirely in software, and would involve relatively simple computer vision algorithms. Automatic sample focussing (in the VLM) could also be implemented, and would require the addition of a motorized VLM focussing stage.

The major accomplishments of this work, in addition to the high quality images that were produced, were the methods we adapted and developed to obtain photometrically accurate x-ray images that allow quantitative measurements of cellular structures, and to explore large fields of view at the maximum resolution of the microscope. These capabilities were indispensable for the studies we hoped to undertake. In particular, we planned to make quantitative estimates, the first of their kind, of the protein mass of individual zymogen granules *in situ*, to establish how that mass varies among these objects, and to extrapolate such measurements, as well as parameters such as size and number, to the population as a whole. Aside from its particular biological interest, such a capability would illustrate the utility of x-ray microscopy for ultrastructural research, particularly when there is a desire to obtain quantitative information about the chemical contents of an object. The use of automation and montage assembly techniques makes it possible to overcome a major shortcoming of x-ray microscopy as a practical tool for biological research to this point — the inability to examine a sample of sufficient size to provide fully realized generalizations about the material under study.

**Acknowledgements**

We wish to thank our colleagues at the Center for X-Ray Optics and the Advanced Light Source at Lawrence Berkeley National Laboratory, and at the University of California, San Francisco, Berkeley, and Davis for their help in this work. In particular, the following people have made critical contributions, for which we are grateful: Erik H. Anderson, David T. Attwood, Rolf H. Behrsing, John T. Brown, Everett H. Harvey, John M. Heck, Aaron J. Lee, Jesse Lee, Hector Medecki, Jos Polman, Ilse M. Sauerwald, Hsien-Chen Tseng, Elise Y. Tung-Loo, Ryohei Urata.

BWL gratefully acknowledges the support of a National Institutes of Health training grant to the UCSF/UCB Bioengineering Graduate Group, a Laboratory Graduate fellowship from Associated Western Universities, Inc., and a fellowship from the Regents of the University of California. The XM-1 project and the ALS are supported by the U.S. Department of Energy, Office of Basic Energy Sciences and Office of Biological and Environmental Research, and the Laboratory Directed Research and Development Program of the E. O. Lawrence Berkeley National Laboratory, under the Department of Energy contract No. DE-AC03-76SF00098.

We would like to dedicate this paper to the memory of our friend, colleague, and co-author, Werner Meyer-Ilse (1954-1999). Dr. Meyer-Ilse was the principal scientist responsible for the development of the XM-1 transmission soft x-ray microscope at Lawrence Berkeley National Laboratory used in this study. The microscope was his passion, and he was intimately involved in every aspect of its design, implementation, operation, and maintenance. He died on July 14, 1999 from injuries sustained in an

automobile accident while visiting his native Germany. Werner had a rare combination of integrity, charity, brilliance, and professionalism, and he will be sorely missed.

## Figure captions

**Figure 6-1**: Corrections applied to individual subimages. **1a**, an image of CCD dark current slope. Some areas of the chip accumulate dark current signal faster than others, possibly due to radiation damage from heavy hard x-ray exposure during the initial alignment of microscope optics. **1b**, a background image obtained by exposing a sample free area of the sample holder, demonstrating inhomogeneous intensity due to nonuniformity in illumination and pixel sensitivity. **1c**, an uncorrected subimage of part of a pancreatic acinar cell. The region of support, or information containing area, of the image has been identified, and pixels outside this region have been set to a value of zero. **1d**, the corrected subimage, after subtraction of dark current signal and normalization to the background image. The background response is now uniform, and true sample features are clearly seen, including the cell nucleus (*N*) and nucleolus (*n*), and several zymogen granules (*z*).

**Figure 6-2**: Subimage registration. As each subimage (**2a**, left) is inserted into the montage, it is registered with respect to a reference image extracted from its target area in the developing montage (**2a**, right). The reference image contains contributions from more than one previously inserted subimage, increasing feature overlap and the performance of the registration. The registration step itself is a filtered cross-correlation operation applied to the gradient magnitude images (**2b**) of the subimage and its reference image. The inset images show the results of cross-correlation between each of the subimage/reference pairs. Using the gradient magnitude operation results in a significantly sharper correlation peak. The top of

each inset pair is the direct cross-correlation, while the bottom is the filtered cross-correlation. Filtering enhances the peak, and suppresses the slowly varying intensity background caused by the small amount of overlap between the images. **2c**, the same as **2b**, but with a large amount of artificial noise added to the source images. Despite the significant degradation of the gradient magnitude images, the correlation peak is still distinct and its position is unchanged.

**Figure 6-3**: Cross-correlation registration. **3a**, a set of registered gradient magnitude images. The numbers indicate the temporal order of subimage acquisition. **3b**, the corresponding cross-correlation arrays between subimages and their reference images, in order of insertion sequence. Subimage 46, the centermost subimage, was inserted first (so cross-correlation is not performed on it). It is followed by the rest in an optimized sequence determined by the montage assembly algorithm. The position of the cross-correlation peak indicates the amount of shift required for proper registration. The crosses indicate the origin of the cross-correlation arrays, corresponding to zero shift. Subimages 11 and 90 have almost featureless areas of overlap with subimages inserted before them, and therefore have ambiguous cross-correlation peaks. However, subimages with even minimal features in their overlap areas (*e.g.*, 1, 2, 10, 81, and 91) still have distinct peaks, demonstrating the robustness of the method. The range of the peak intensities shown here spans nearly four orders of magnitude.

**Figure 6-4**: Performance of registration on microfabricated gold structures, with finest feature dimensions of about 40 nm. **4a**, two individual high-resolution subimages from the central parts, containing the finest features, of each of the structures. Such

images have been used to measure the resolution of the microscope, determined to be 43 nm. The pixel size is 20 nm. **4b**, corresponding parts of the montage assembled using only the recorded stage positions, without registration by cross-correlation. The stage position determination errors are sufficient to degrade the resolution significantly. Arrows indicate some fine features in overlap regions that are blurred due to misregistration. **4c**, the full montage of both gold structures, registered using the montage assembly algorithm. It spans an area of about 104 by 94 μm (5,200 by 4,700 pixels at 20 nm pixel size). Inset images show the same central areas. Full resolution is preserved when compared to the individual subimages (**4a**), which demonstrates essentially perfect registration.

**Figure 6-5**: Effect of time varying pattern of illumination. The pattern of illumination changes gradually with time, due to drift of either the synchrotron source or microscope optics. In this montage of pancreatic tissue, 400 subimages, collected over about 3 hours, are each normalized to background images acquired just before the beginning of the sequence (starting at the upper right corner). This results in a significant intensity gradient across the montage, and mismatched intensities at subimage borders. When each subimage is normalized to a time interpolated background image, constructed from multiple background images acquired throughout the sequence, a proper correction is obtained (see Figure **6-7**).

**Figure 6-6**: Blending. When subimages are inserted into the montage, the areas of overlap are constructed by averaging pixel values from the contributing subimages (top). Despite the corrections that have been applied, some residual uncorrected factor, possibly scattered light, sometimes causes an intensity mismatch at the

subimage borders (arrows). Blending can be performed (bottom) by using a weighted average in the overlapping areas, with weights that taper near the subimage borders. The result is seamless, which facilitates subsequent image analysis.

**Figure 6-7**: High-resolution, large-field montage of a pancreatic tissue section. **7a**, the full montage of 400 subimages, spanning 110 by 110 μm (about 2,700 by 2,700 pixels at 40 nm pixel size). The exocrine (acinar) cells of the pancreas are arranged in clusters called acini (*A*). Throughout the tissue are capillaries (*c*), some of which are sectioned at the level of the capillary endothelial cell nucleus. Red blood cells (*r*) are also seen. Several intracellular organelles are demonstrated in this view, including cell nuclei (*N*), mitochondria (*m*), and numerous dense, round zymogen granules (*zg*) that store digestive enzymes prior to their secretion into the gut, clustered at the apical end of the acinar cells. **7b**, full resolution view of the acinus in the center of **7a**. Again the nucleus (*N*), nucleolus (*n*), mitochondrion (*m*), and zymogen granule (*z*) are demonstrated, but now in more detail. Patterns of fine linear lucencies are also visible in the basolateral region of some cells. These may represent endoplasmic reticulum cisternae that are oriented perpendicular to the plane of sectioning (*er*).

## Figures

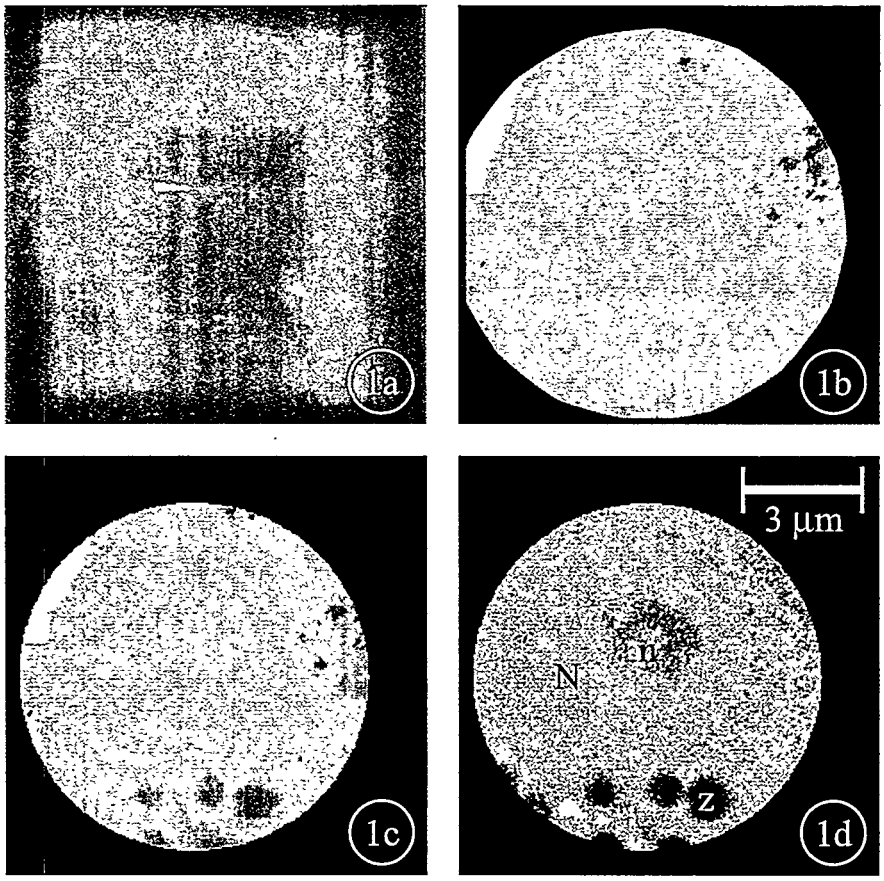


**Figure 6-1**

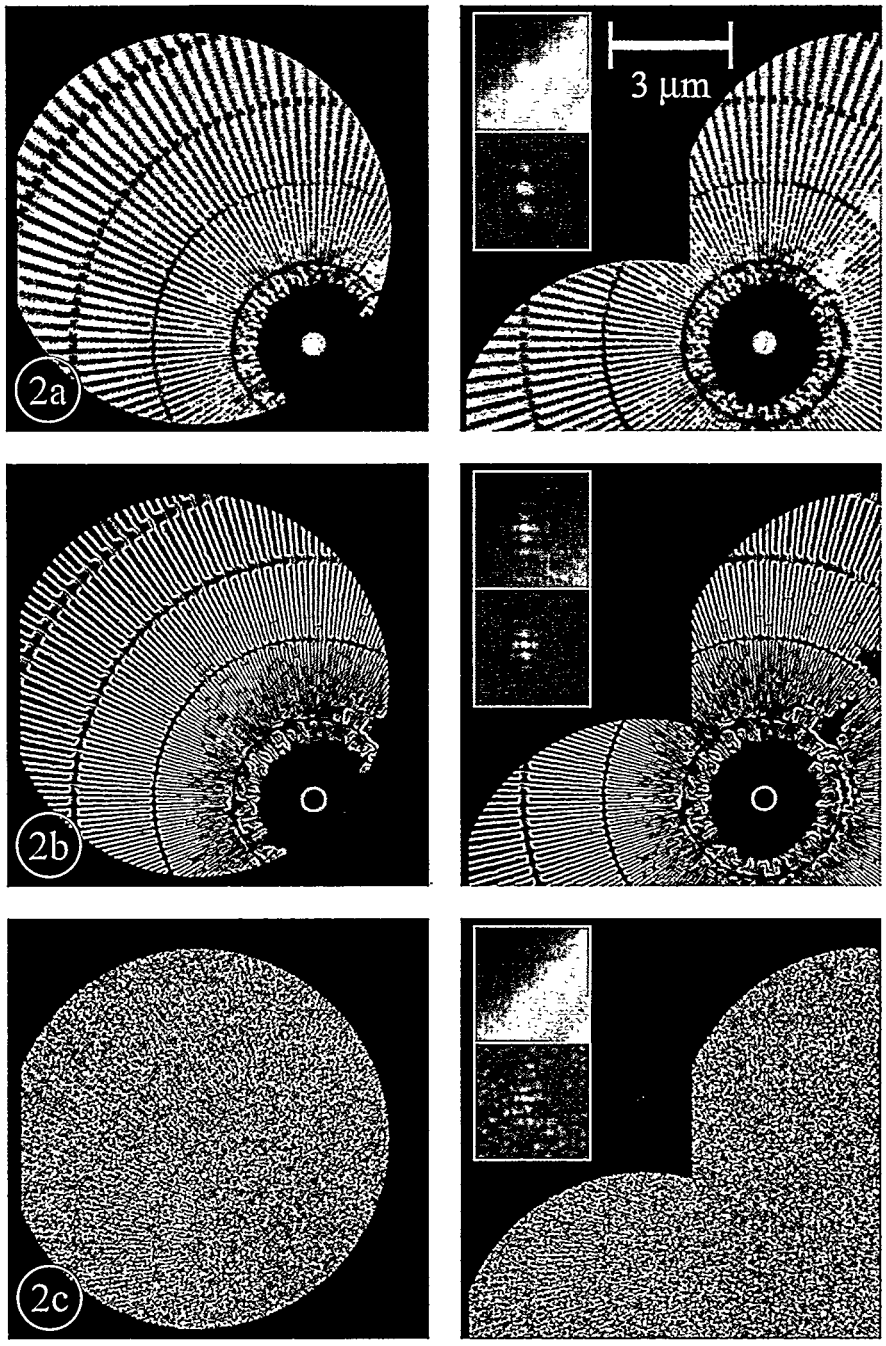


**Figure 6-2**

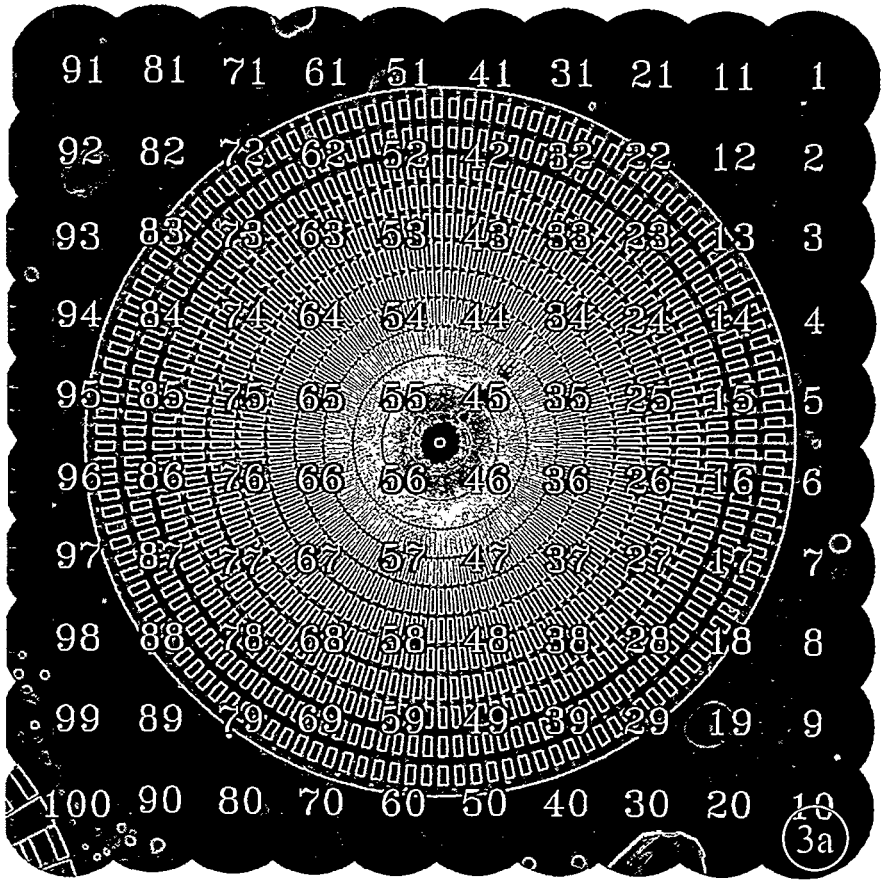
91 81 71 61 51 41 31 21 11 1
92 82 72 62 52 42 32 22 12 2
93 83 73 63 53 43 33 23 13 3
94 84 74 64 54 44 34 24 14 4
95 85 75 65 55 45 35 25 15 5
96 86 76 66 56 46 36 26 16 6
97 87 77 67 57 47 37 27 17 7
98 88 78 68 58 48 38 28 18 8
99 89 79 69 59 49 39 29 19 9
100 90 80 70 60 50 40 30 20 10
3a

**Figure 6-3a**

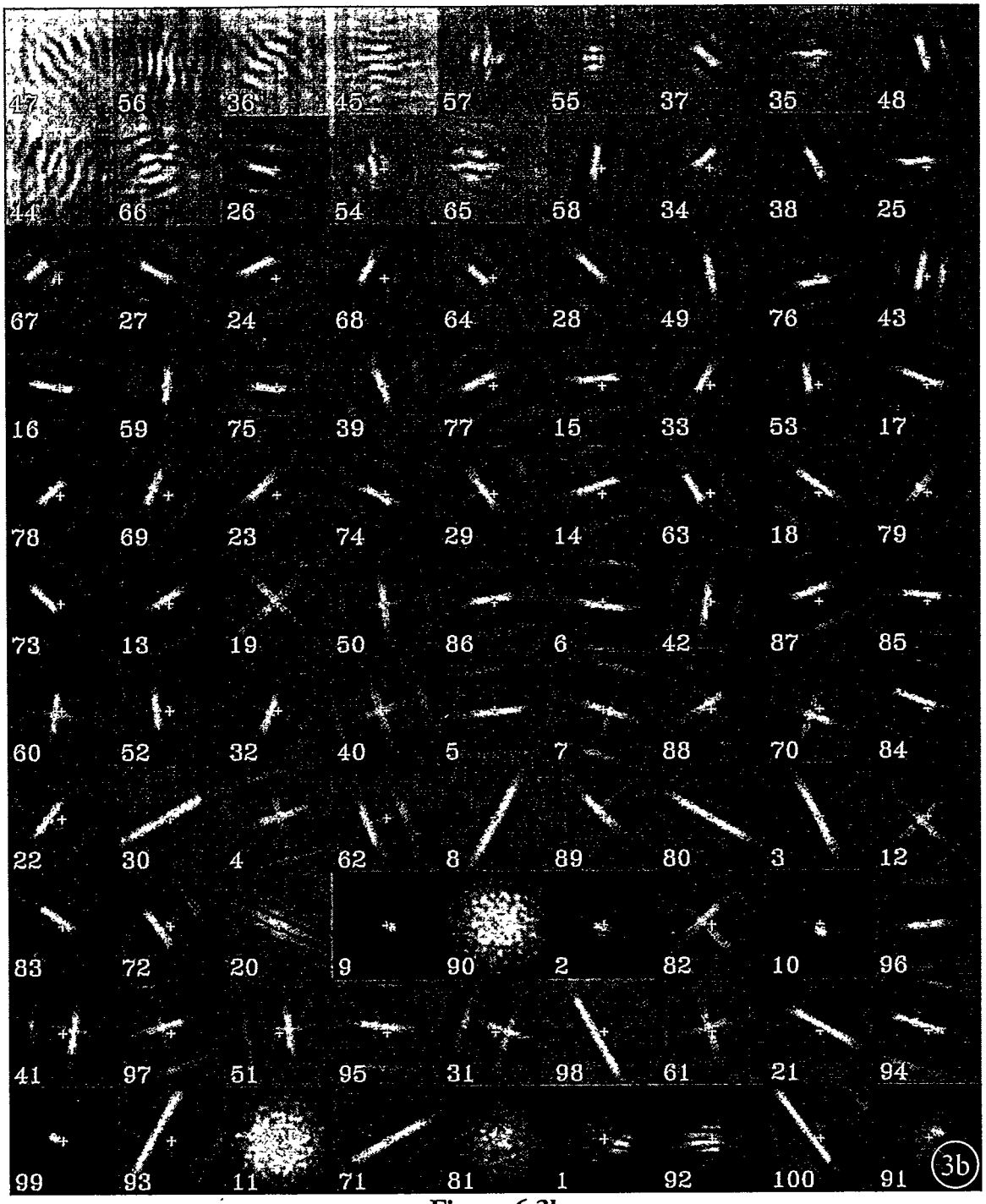
47 56 36 45 57 55 37 35 48
44 66 26 54 65 58 34 38 25
67 27 24 68 64 28 49 76 43
16 59 75 39 77 15 33 53 17
78 69 23 74 29 14 63 18 79
73 13 19 50 86 6 42 87 85
60 52 32 40 5 7 88 70 84
22 30 4 62 8 89 80 3 12
83 72 20 9 90 2 82 10 96
41 97 51 95 31 98 61 21 94
99 93 11 71 81 1 92 100 91
3b

**Figure 6-3b**

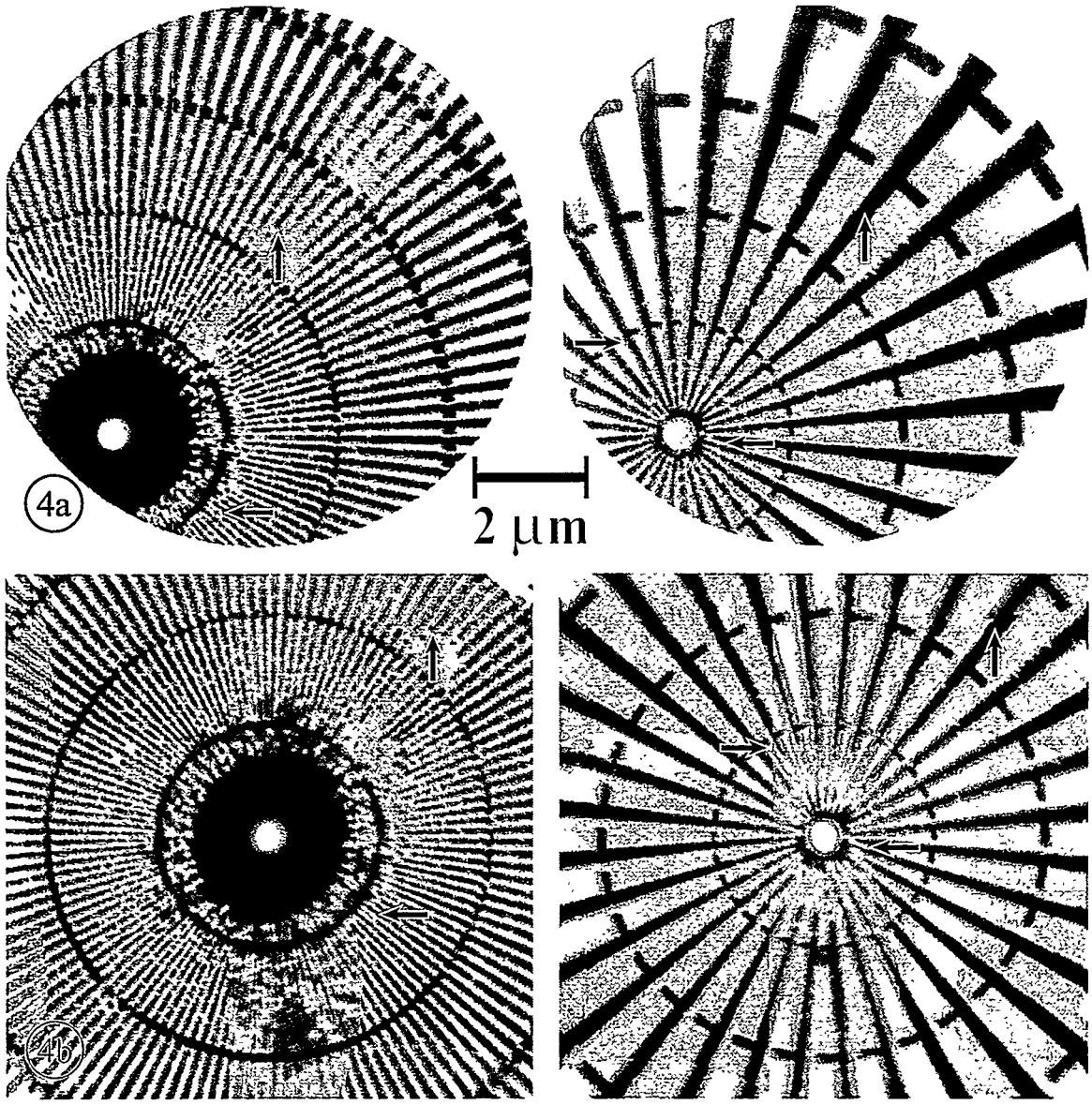


**Figure 6-4a, 6-4b**

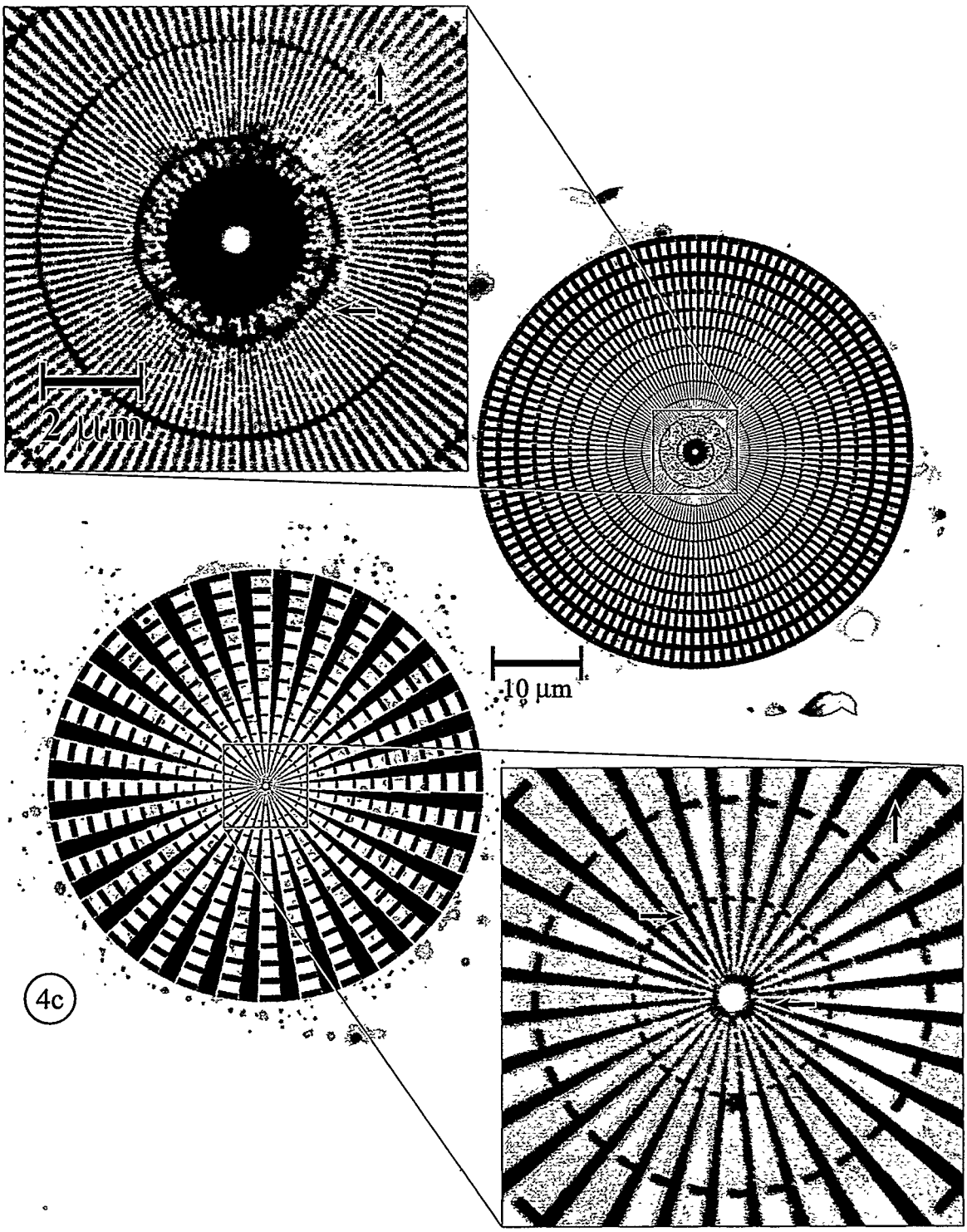


**Figure 6-4c**

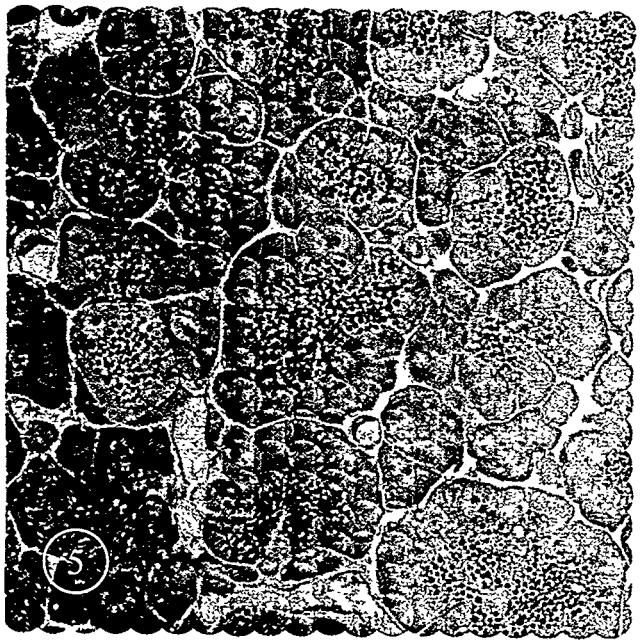

**Figure 6-5**

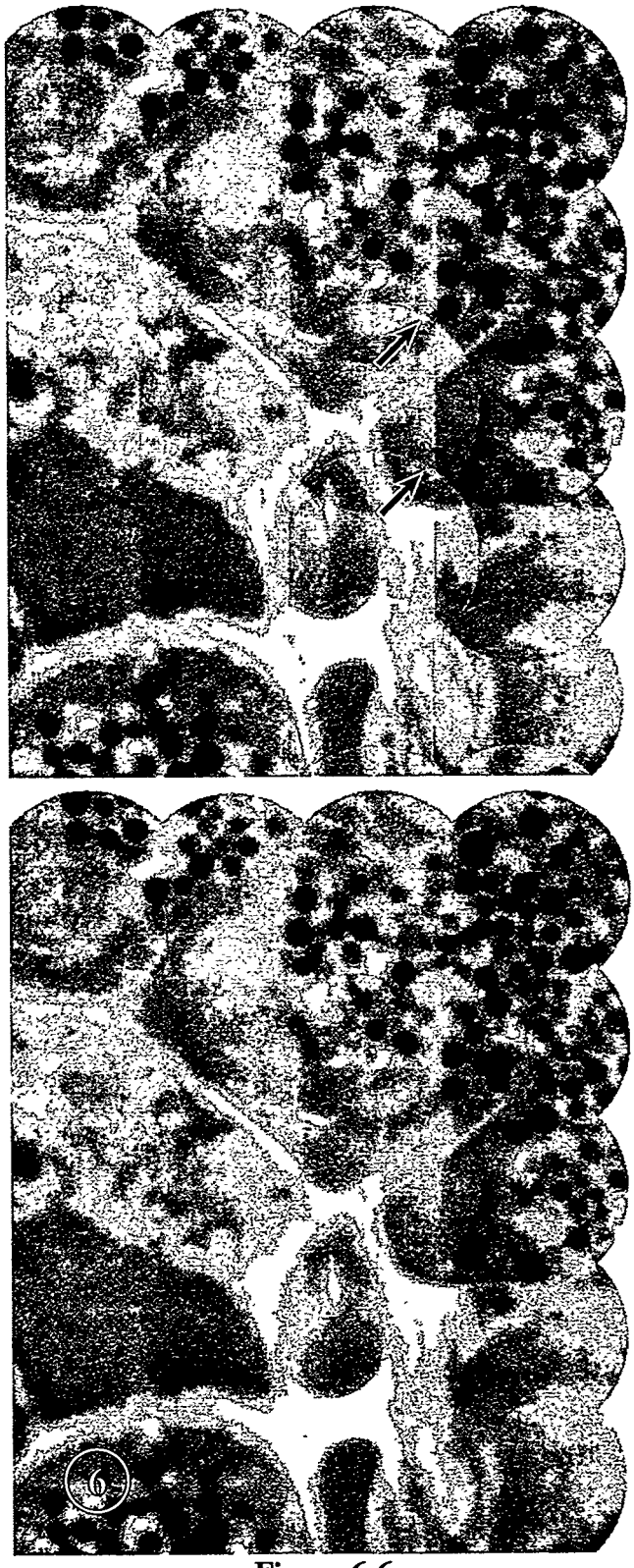

**Figure 6-6**

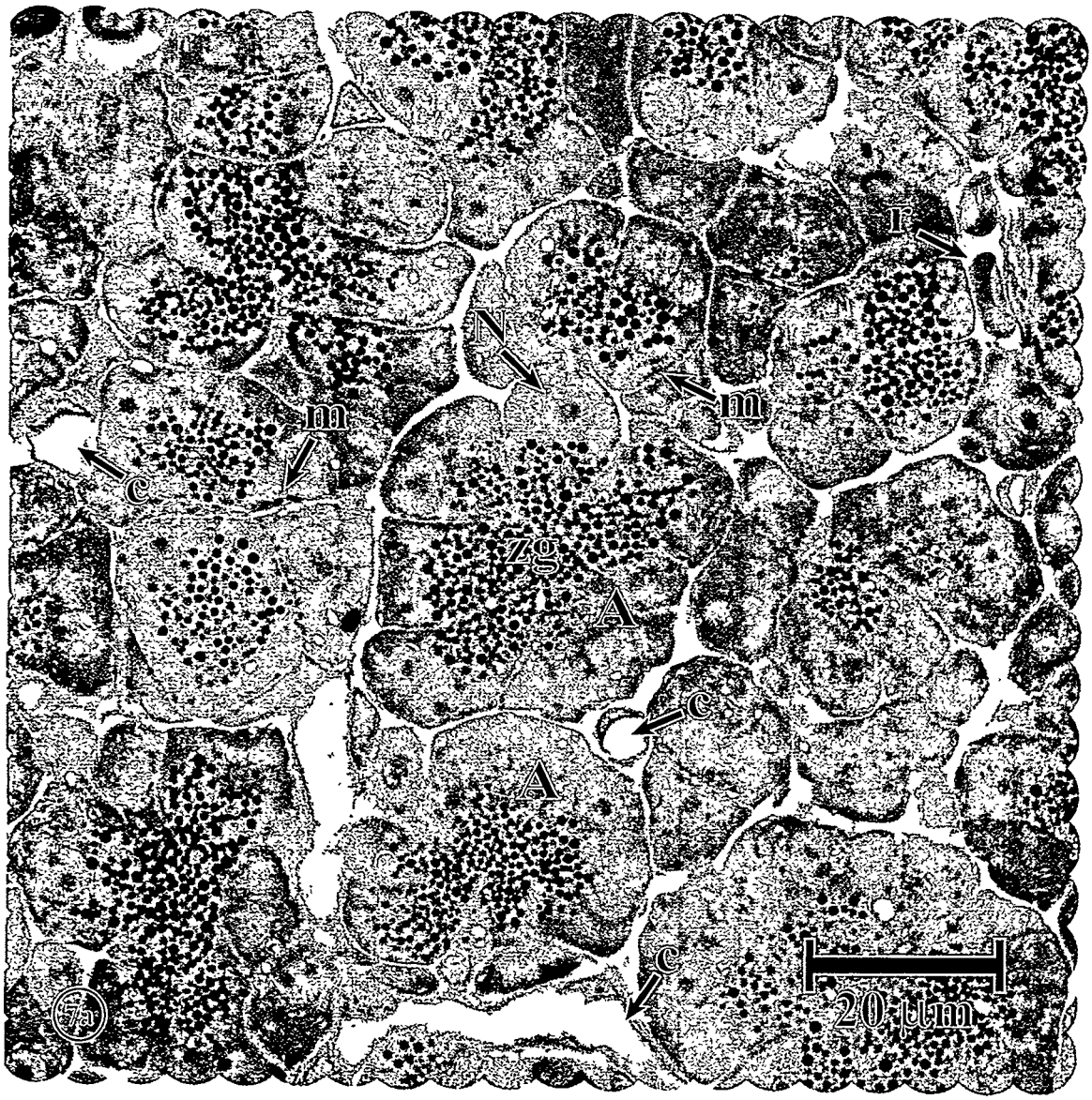


**Figure 6-7a**

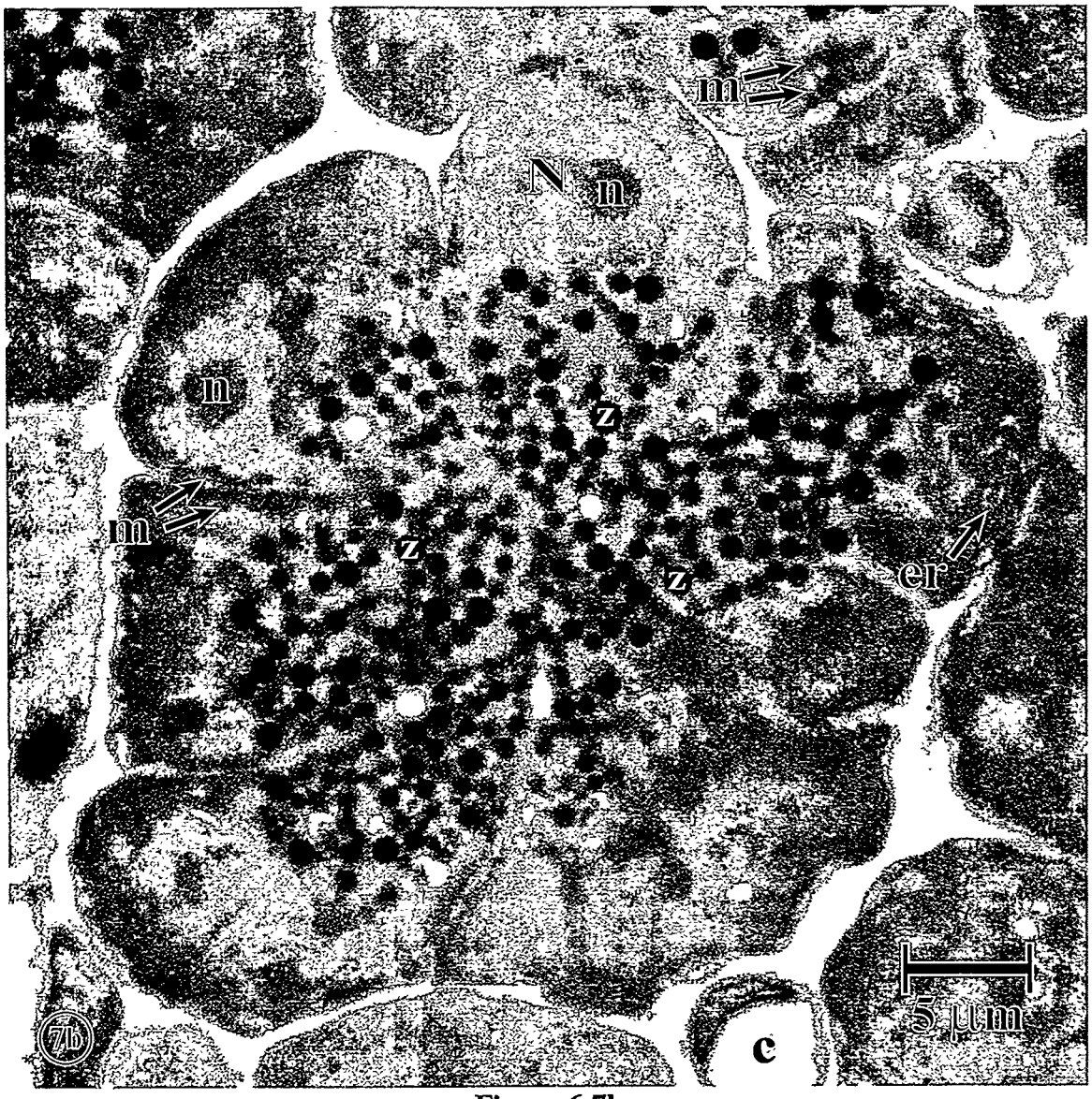


**Figure 6-7b**

## References


Anderson, E.H. & Kern, D. (1992) Nanofabrication of zone plates for x-ray microscopy. *X-Ray Microscopy III: Proceedings of the Third International Conference, London, September 3-7, 1990.* (eds. A.G. Michette, G.R. Morrison, and C.J. Buckley), pp. 75-78. Springer-Verlag, Berlin.

Azaria, M. & Hertz, D. (1984) Time delay estimation by generalized cross correlation methods. *IEEE Transactions on Acoustics, Speech and Signal Processing*. **ASSP-32**, 280-285.

Brown, L.G. (1992) A survey of image registration techniques. *ACM Computing Surveys*. **24**, 325-376.

Dani, P. & Chaudhuri, S. (1995) Automated assembling of images: image montage preparation. *Pattern Recognition*. **28**, 431-445.

Davis, J. (1998) Mosaics of scenes with moving objects. *Proceedings of the 1998 IEEE Computer Society Conference on Computer Vision and Pattern Recognition, Santa Barbara, California*, pp. 354-360. IEEE Computer Society, Los Alamitos.

Dereniak, E.L. & Crowe, D.G. (1984) *Optical radiation detectors*. John Wiley & Sons, New York.

Eversole, W.L. & Nasburg, R.E. (1983) Maximum likelihood estimation for image registration. *Applications of Digital Image Processing VI, San Diego, California, August 23-26, 1983*. (ed. A.G. Tescher), Proceedings SPIE Vol. 432, pp. 190-194.

Heck, J.M., Attwood, D.T., Meyer-Ilse, W. & Anderson, E.H. (1999) Resolution determination in x-ray microscopy: an analysis of the effects of partial coherence and illumination spectrum. *Journal of X-Ray Science and Technology*. **8**, 95-104.

Henke, B.L., Gullikson, E.M. & Davis, J.C. (1993) X-ray interactions: photoabsorption, scattering, transmission, and reflection at E=50-30000 eV, Z=1-92. *Atomic Data and Nuclear Data Tables*. **54**, 181-342.

Kirz, J., Jacobsen, C. & Howells, M. (1995) Soft x-ray microscopes and their biological applications. *Quarterly Reviews of Biophysics*. **28**, 33-130.

Knapp, C.H. & Carter, G.C. (1976) The generalized correlation method for estimation of time delay. *IEEE Transactions on Acoustics, Speech and Signal Processing*. **ASSP-24**, 320-327.

Krivanek, O.L. & Mooney, P.E. (1993) Applications of slow-scan CCD cameras in transmission electron microscopy. *Ultramicroscopy*. **49**, 95-108.

Loo, B.W., Jr., Parvin, B. & Rothman, S.S. (1996) Two- and three-dimensional segmentation for measurement of particles in the analysis of microscopic digital images of biological samples. *Three-Dimensional Microscopy: Image Acquisition and Processing III, San Jose, California, January 30 - February 1, 1996*. (eds. C.J. Cogswell, G.S. Kino, and T. Wilson), Proceedings SPIE Vol. 2655, pp. 209-215.

Meyer-Ilse, W., Medecki, H., Brown, J.T., Heck, J.M., Anderson, E.H., Stead, A., Ford, T., Balhorn, R., Petersen, C., Magowan, C. & Attwood, D.T. (1998) X-ray microscopy in Berkeley. *X-Ray Microscopy and Spectromicroscopy: Proceedings of the Fifth International Conference, Würzburg, August 19-23, 1996*. (eds. J. Thieme, G. Schmahl, D. Rudolph, and E. Umbach), pp. I-1 to I-12. Springer, Berlin.

Meyer-Ilse, W., Medecki, H., Jochum, L., Anderson, E., Attwood, D., Magowan, C., Balhorn, R., Moronne, M., Rudolph, D. & Schmahl, G. (1995) New high-resolution zone-plate microscope at Beamline 6.1 of the ALS. *Synchrotron Radiation News*. **8**, 29-33.

Pratt, W.K. (1974) Correlation techniques of image registration. *IEEE Transactions on Aerospace and Electronic Systems*. **AES-10**, 353-358.

Rothman, S., Anderson, E., Attwood, D., Batson, P., Buckley, C., Goncz, K., Howells, M., Jacobsen, C., Kern, D., Kirz, J., Rarback, H., Rivers, M., Shu, D., Tackaberry, R. &

Turek, S. (1990) Soft x-ray microscopy in biology and medicine: status and prospects. *Physica Scripta*. **T31**, 18-22.

Rothman, S.S., Goncz, K.K. & Loo, B.W., Jr. (1992) Following protein transport with the high resolution x-ray microscope. *X-Ray Microscopy III: Proceedings of the Third International Conference, London, September 3-7, 1990.* (eds. A.G. Michette, G.R. Morrison, and C.J. Buckley), pp. 373-383. Springer-Verlag, Berlin.

Schmahl, G., Rudolph, D., Niemann, B. & Christ, O. (1980) Zone-plate x-ray microscopy. *Quarterly Reviews of Biophysics*. **13**, 297-315.

Schmahl, G., Rudolph, D., Schneider, G., Thieme, J., Schliebe, T., Kaulich, B. & Hettwer, M. (1996) Diffraction optics for x-ray imaging. *Microelectronic Engineering*. **32**, 351-367.

Thieme, J., Schmahl, G., Rudolph, D. & Umbach, E., Editors (1998) *X-Ray Microscopy and Spectromicroscopy: Proceedings of the Fifth International Conference, Würzburg, August 19-23, 1996*. Springer, Berlin.

Turner, J.N., Ancin, H., Becker, D.E., Szarowski, D.H., Holmes, M., O'Connor, N., Wang, M., Holmes, T. & Roysam, B. (1997) Automated image analysis technologies for biological 3D light microscopy. *International Journal of Imaging Systems and Technology*. **8**, 240-254.

Vogt, R.C., Trenkle, J.M. & Harmon, L.A. (1996) Mosaic construction, processing, and review of very large electron micrograph composites. *Applications of Digital Image Processing XIX, Denver, Colorado, August 7-9, 1996.* (ed. A.G. Tescher), Proceedings SPIE Vol. 2847, pp. 2-15.

Wilhein, T., Rothweiler, D., Tusche, A., Scholze, F. & Meyer-Ilse, W. (1994) Thinned, back-illuminated CCDs for x-ray microscopy. *X-Ray Microscopy IV: Proceedings of the Fourth International Conference, Chernogolovka, Russia, September 20-24, 1993.* (eds. V.V. Aristov and A.I. Erko). Bogorodskii Pechatnik, Chernogolovka.

# Chapter 7. Two- and three-dimensional segmentation for measurement of particles in the analysis of microscopic digital images of biological samples


## Abstract

The authors present a Hough transform based image segmentation algorithm for automated detection, counting, and measurement of particles in two- and three-dimensional microscopic digital image data sets. The algorithm has proven to be both sensitive and specific for the particles of interest, even in the presence of noise and blurring. We apply the algorithm to the problem of automated compilation of population statistics on the size and mass of zymogen granules in pancreatic acinar cells. We present results describing the performance of the algorithm on digital phantoms, and image data from conventional fluorescence and confocal microscopes.


## Motivation

We have been studying mechanisms of cellular secretion in the exocrine cell of the pancreas (Goncz & Rothman, 1992; Goncz *et al.*, 1995). The pancreatic acinar cell contains a densely populated zone of vesicles which store enzymes used for digestion (Figure 7-1). These roughly spherical vesicles, called zymogen granules, have a diameter of about one micrometer. Our studies require a compilation of statistics on granule size, number, and content, and how these population parameters change with different physiological states (*e.g.*, stimulated versus unstimulated).

Clearly, manual segmentation of sufficiently large granule populations to do the analysis would be subjective, error prone, and prohibitively tedious. Our goal is to

develop a computer aided segmentation protocol that is sensitive, accurate, and totally automated except for an initial setting of segmentation parameters.

**Description of the algorithm**

Hough transform based segmentation is a type of matched filtering method that is particularly useful for finding parametrically described shapes (Ballard & Brown, 1982). The Hough transform maps shapes in image space into peaks in the parameter space. It performs robustly against breaks in the outlines of the target shapes, such as those produced by noise in the image. Our implementation is a variant in which the gradient direction information is used for increased efficiency and performance.

In the 2-D case, we search for positions and sizes of disc shaped objects in a three-dimensional parameter space (position in x and y coordinates, and diameter). The 3-D segmentation protocol (for finding spherical objects) is directly analogous to the 2-D one: the same procedures are followed in building and searching a 4-D parameter space (position in x, y, and z coordinates, and diameter). The transform is computed in three steps, illustrated in Figure 7-2. First, edge elements are located by thresholding the gradient magnitude image, which is computed using a Sobel gradient approximation.

Second, an accumulator array is constructed in parameter space. Each edge element in image space "votes" for the cell in the accumulator array corresponding to the hypothesized center of a circle assuming the edge element lies on a circle object. The gradient direction information is used at this step: the vote count of the cell in the accumulator array, corresponding to a position of distance one radius along the gradient direction from the edge element, is incremented when searching for bright objects against

a dark background (as in fluorescence images). A step along the opposite direction is used when searching for dark objects. The third dimension of the accumulator array is built up by repeating this process for a range of diameters.

Finally, the accumulator array is searched for peaks stronger than a threshold intensity. For computational efficiency, we first search for the positions of the disc centers by projecting the diameter dimension of the accumulator array onto the x-y parameter space and performing a 2-D search for peaks. Then we search the local 3-D regions of the array surrounding the center positions to find the diameters. This is significantly faster than searching the entire 3-D volume at once. If any of the hypothesized objects overlap, the ones with weaker peaks in the accumulator array are rejected.

In the current implementation, the only parameters to adjust are the threshold levels for the gradient magnitude and the peaks in the accumulator array. Others might be considered as well, for example, allowing edge elements to have different numbers of votes depending on edge strength. The parameters are set once for each class of images to be segmented: they are tuned for optimal performance on a few images, then applied uniformly to all other images of the same type.

**Performance on digital phantoms**

The performance of the algorithm was evaluated by testing it on a set of digital phantoms designed to model the real objects of interest, zymogen granules (see Figure 7-3). The zymogen granules were modeled as non-overlapping elliptical objects of uniform intensity within each object. The position, eccentricity, and axis orientation of each object

was random. The intensity and diameter were normal random variables with means and standard deviations approximating measured values from real images. The objects were embedded in a uniform background simulating the background intensity in images of the real objects. The phantom images were blurred to simulate the blurring due to the finite numerical aperture of the microscope objective lens. A stationary Gaussian noise was added, with noise magnitude sufficient to make the phantom images visibly noisier than the real image data.

After an initial tuning of thresholds for the segmentation procedure, ten such phantoms were generated and tested with the segmentation algorithm. Table 1 summarizes the performance of the algorithm on these phantoms. The errors are calculated as reference (or phantom) values minus measured (or hypothesized) values, so that a positive error occurs when the measured value is too small and a negative one when the measured value is too large. The exception is the error in position, which is calculated as the distance between the reference and measured positions. The reference intensities are taken from the blurred phantom image, since it would be unfair to require any algorithm to determine unblurred values. A possible way to deal with this problem is addressed in the Discussion.

| | | | | |
|---|---|---|---|---|
| Total number of objects: | 1,700 | | | |
| True positive identifications: | 1,682 | (99% sensitivity) | | |
| False negative identifications: | 18 | | | |
| False positive identifications: | 0 | (100% specificity) | | |
| Mean error in diameter: | 2.57 | ± | 1.37 | pixels |
| Mean error in position: | 0.218 | ± | 0.457 | pixels |
| Mean error in intensity: | -56.8 | ± | 32.1 | (12 bit digital intensity) |
| Mean error in intensity (size corrected): | 9.61 | ± | 36.0 | (12 bit digital intensity) |
| Mean intensity of true positives: | 1071 | ± | 151 | (12 bit digital intensity) |
| Mean intensity of false negatives: | 755 | ± | 93 | (12 bit digital intensity) |
| Mean diameter of true positives: | 15.37 | ± | 2.63 | pixels |
| Mean diameter of false negatives: | 15.00 | ± | 3.58 | pixels |

**Table 7-1**

Performance of the segmentation algorithm on digital phantoms. Statistics are given as mean ± standard deviation.

It can be seen that both the sensitivity and specificity of the segmentation are high. It is also possible to trade off between sensitivity and specificity by setting the thresholds accordingly. For example, by lowering the thresholds, more real objects can be detected at the risk of detecting nonexistent objects that are an artifact of noise.

The error in position is sub-pixel. However, the measured diameters of the objects are too small, as can be seen in Figure 7-3E. At the same time, the measured intensities are too high. In fact, these errors are highly correlated (not shown), and are both related to the optical blurring, which results in a smaller apparent size, and therefore an extraction of intensity values from the central, brightest region of the blurred objects. Because the error in size measurement is uncorrelated with all other parameters (*i.e.*, object diameter, eccentricity, and intensity) (not shown), it is appropriate to correct the measured diameters by adding 2.57, the mean error value, to each diameter measurement. This effectively removes the error in the intensity measurement as well (see table).

One might expect the algorithm to be biased against lower intensity and smaller objects, since weaker edges and smaller circumference (fewer edge elements) both result

in smaller peaks in the accumulator array. From the table, comparing the reference values of true positives with false negatives shows that there is a bias against lower intensity objects, but not against smaller objects.

**Segmentation on real image data**

Using the same threshold settings as for the phantoms, the segmentation algorithm was applied to a real image of zymogen granules in a tissue section from rat pancreas. The tissue section was treated with a fluorescence histochemical method relatively specific for zymogen granule proteins, and imaged in an epifluorescence microscope equipped with a charge-coupled device digital camera, producing a 2-D image. The image dimensions are $256 \times 256$ pixels, 0.04 μm/pixel, and 12 bit dynamic range for intensity. Figure 7-4 shows the original image, and the hypothesized object locations and sizes generated by the segmentation algorithm. Judging by eye, the algorithm seems to have found almost all of the objects actually present, while not producing false positive identifications. Again, the thresholds can be set for this class of images to balance better sensitivity with specificity.

The objective of developing the segmentation method is to compile relevant population statistics on zymogen granules. Figure 7-5 shows the measured distribution of granule sizes and intensities (not corrected for possible errors in size). In the actual experiment, these measurements will be made and compared for tissue sections collected under a set of different physiological states, such as time points following the addition of a secretory stimulant.

The 3-D segmentation algorithm was tested on a 3-D confocal image stack of zymogen granules in a fluorescence histochemically treated tissue section from pancreas. The image dimensions were $128 \times 128 \times 16$, 0.05 μm/pixel in X and Y, and 0.10 μm step size in Z. The intensities are in numbers of photons. Figure 7-6 shows the result of the segmentation. Many of the objects that appear to be false negative identifications are actually hypotheses that were rejected because the center of the objects lay outside the stack in Z, so the sensitivity is comparable to the 2-D case despite the much lower signal intensity of the confocal method. The higher relative sensitivity of the 3-D segmentation arises from the fact that there are many more edge elements on a spherical shell than on a circular outline to contribute to the peak in parameter space. Figure 7-7 shows the measured population statistics. The diameter measurements of the 2-D and 3-D segmentation procedures correspond well.

**Discussion**

This initial study demonstrates that a Hough transform based segmentation approach should be able to meet the experimental objective described for studying the secretion problem in pancreatic cells.

A number of additional strategies conceivably should improve the performance of the method. In this study we made no attempt to pre- or post-process the images or segmentation data. Image preprocessing could improve the efficiency of the segmentation procedure, as well as remove some of its biases. For example, noise suppression (*e.g.*, by median filtering or wavelet transform compression) should eliminate many false edge elements and thus reduce the computation in building the accumulator array. The bias

against faint objects might be reduced by an adaptive smoothing procedure, which would effectively strengthen their edges. It should possible, with knowledge about the aberrations produced by the imaging process, to reconstruct the unblurred object shapes and intensities by deconvolution (Agard *et al.*, 1989), improving the accuracy of the values measured by segmentation. Postprocessing of the segmentation data, such as shape refinement to account for the fact that the objects are not perfect circular discs or spheres, should improve the accuracy of volume and intensity measurements.

These methods should also be directly extensible to dynamic problems, such as tracking granule motion through time in two and three dimensions.

**Acknowledgments**

The authors thank the following individuals for their assistance and helpful discussions: David T. Attwood, Kenneth A. Goldberg, Everett H. Harvey, Center for X-Ray Optics, LBNL; Daniel E. Callahan, Life Sciences Microscope Resource, LBNL; Mary Helen Barcellos-Hoff, Mario M. Moronne, Shraddha A. Ravani, Life Sciences Division, LBNL; Nussi Dekker, Bonnie McClintock, Joseph Regezi, Oral Pathology Laboratory, UCSF.

Histological tissue processing was done by the Oral Pathology Laboratory at the University of California, San Francisco. Microscopy was done using the facilities of the Life Sciences Microscope Resource at Lawrence Berkeley National Lab. Image processing was done using the computing facilities of the Center for X-Ray Optics at Lawrence Berkeley National Lab. All the segmentation software was written in the IDL

image processing language from Research Systems, Inc., Boulder, CO, USA. All figures were produced using IDL.

BWL gratefully acknowledges support under a fellowship from Associated Western Universities, Inc., and a Regents Fellowship from the University of California, San Francisco.

**Figure captions**

**Figure 7-1**: Left, hematoxylin and eosin stained section of pancreatic tissue; refractile objects in central region surrounding the ductal space are zymogen granules. Right, higher magnification fluorescence image of the zymogen granule containing region of a pancreatic tissue section.

**Figure 7-2**: Left, sample image to be segmented for disc shaped objects. Center, gradient magnitude image, demonstrating edges. Right, the slice from the accumulator array in parameter space for diameter = 25 pixels. The complete accumulator array is a 3-D stack in which each slice corresponds to a different diameter.

**Figure 7-3**: A, sample digital phantom. B, phantom with blur and noise added. C, gradient magnitude image of B. D, accumulator array, projected onto x-y parameter space. E&F, outlines indicating hypothesized object locations and sizes, drawn on original and noisy, blurred phantom images, respectively.

**Figure 7-4**: Left, original image. Right, outlines of hypothesized objects drawn on original image.

**Figure 7-5**: Histograms showing measured population statistics of zymogen granules in a section of pancreatic tissue.

**Figure 7-6**: Selected X-Y, X-Z, and Y-Z slices from a 3-D volume of pancreatic tissue imaged with a confocal fluorescence microscope. Left, outlines of hypothesized

objects are superimposed on original image. Right, original image. Step size in Z is twice the X-Y pixel size.

**Figure 7-7**: Histograms showing measured population statistics of zymogen granules imaged with a 3-D confocal microscope.

## Figures

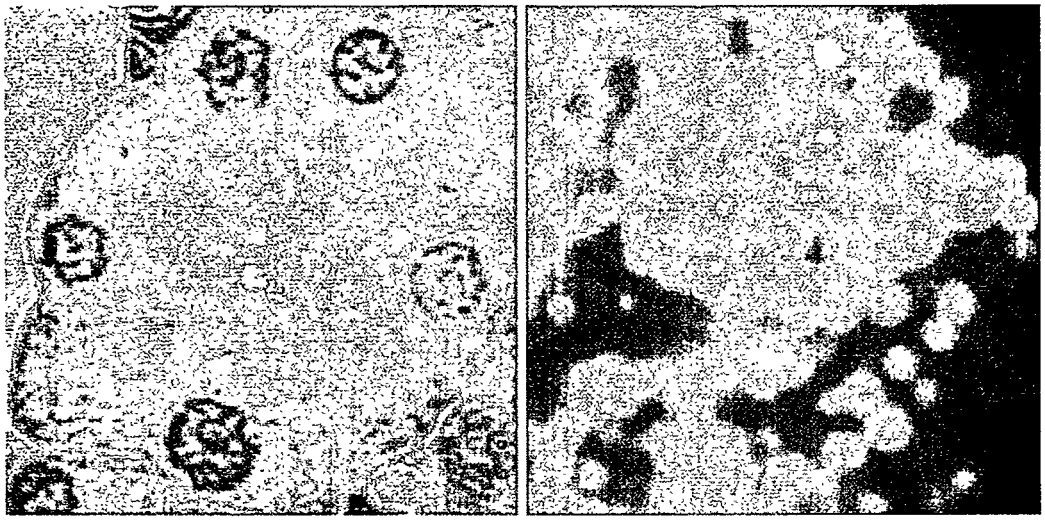

Figure 7-1

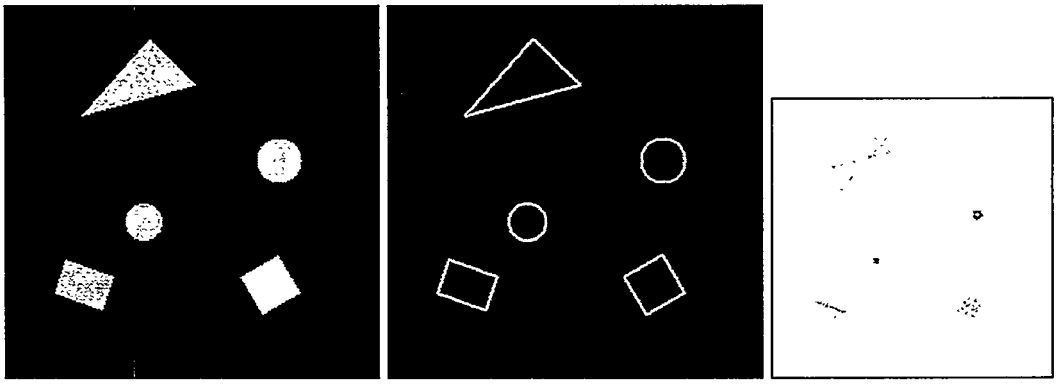

Figure 7-2

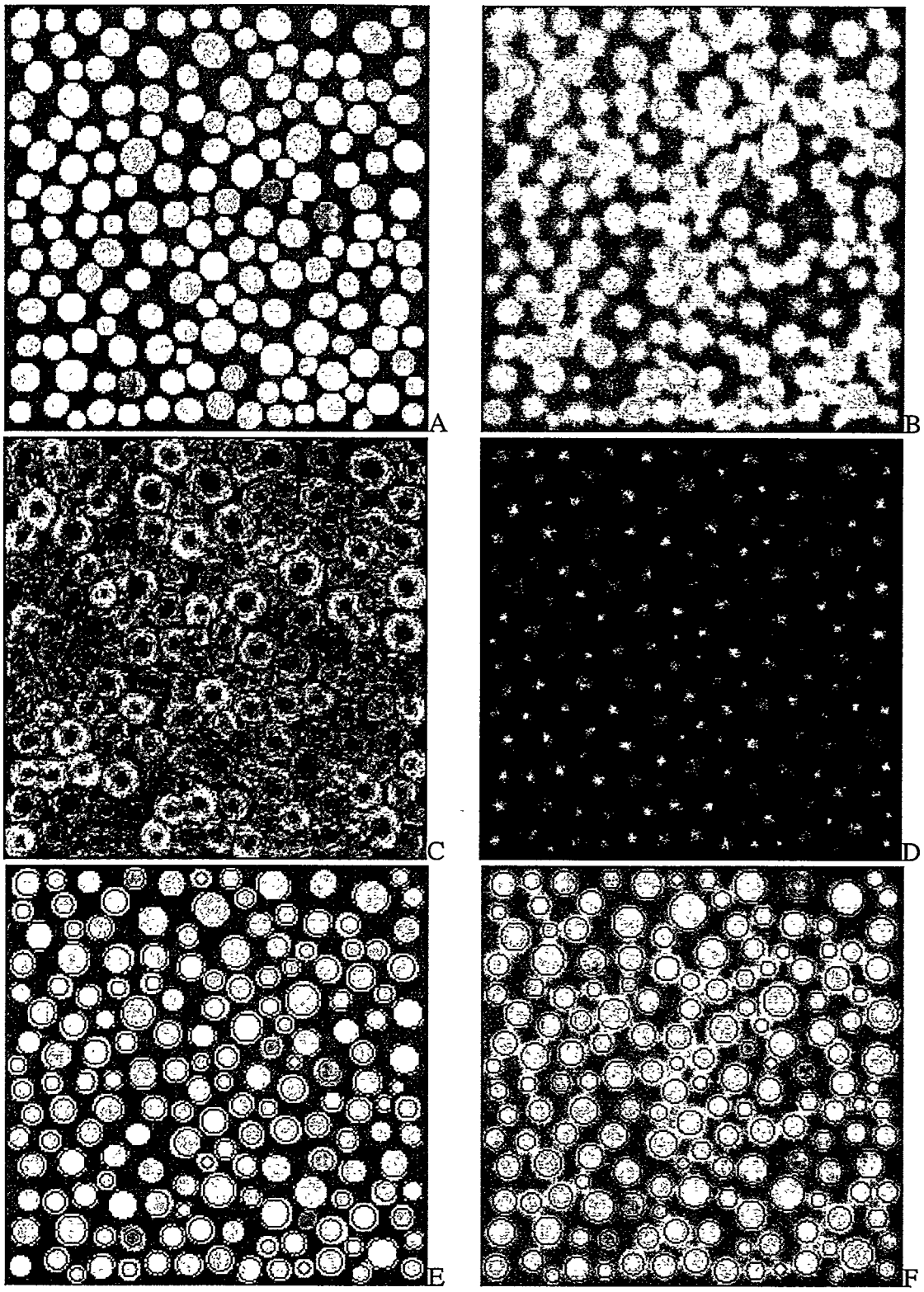


**Figure 7-3**

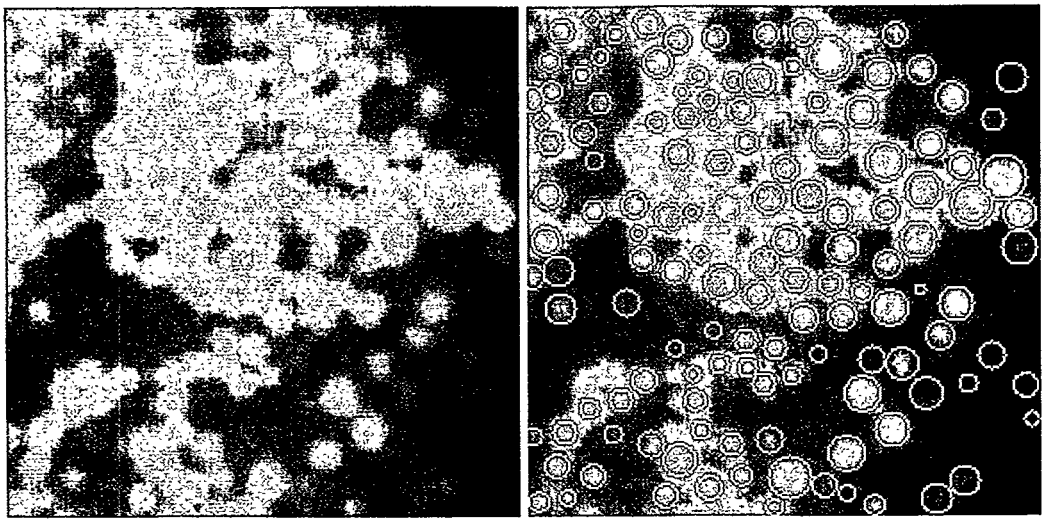

Figure 7-4

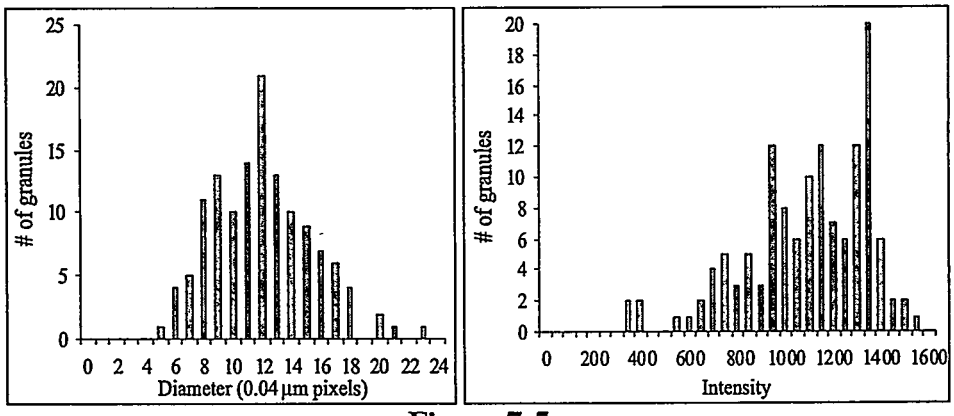


Figure 7-5

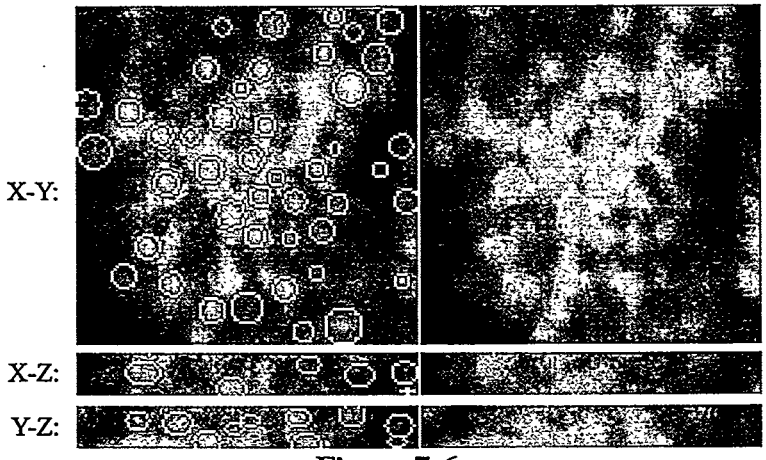


Figure 7-6

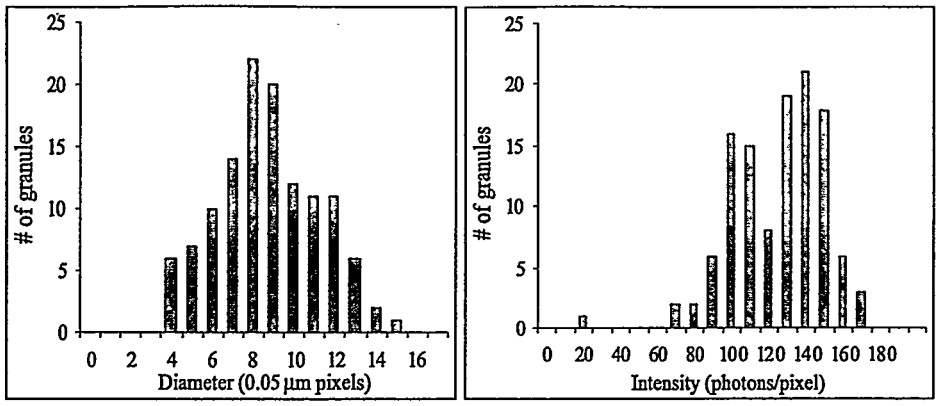
# of granules
Diameter (0.05 µm pixels)
# of granules
Intensity (photons/pixel)

**Figure 7-7**

## References

Agard, D.A., Hiraoka, Y., Shaw, P. & Sedat, J.W. (1989) Fluorescence microscopy in three dimensions. *Methods in Cell Biology*. **30**, 353-377.

Ballard, D.H. & Brown, C.M. (1982) *Computer vision*. Prentice-Hall, Englewood Cliffs, N.J.

Goncz, K.K., Behrsing, R. & Rothman, S.S. (1995) The protein content and morphogenesis of zymogen granules. *Cell and Tissue Research*. **280**, 519-530.

Goncz, K.K. & Rothman, S.S. (1992) Protein flux across the membrane of single secretion granules. *Biochimica et Biophysica Acta*. **1109**, 7-16.

## Section 3: Quantitative characterization of pancreatic tissue sections and the protein contents of the acinar cell

# Chapter 8. A new sample preparation method for soft x-ray microscopy: nitrogen-based contrast and radiation tolerance properties of glycol methacrylate-embedded and sectioned tissue

## Summary

We describe the preparation of a biological tissue for imaging in a transmission soft x-ray microscope. Sections of exocrine pancreas embedded in glycol methacrylate polymer, an embedding medium widely used in visible light and electron microscopy, were examined. Contrast was based primarily on the nitrogen content of the tissue, and dual-wavelength imaging at the nitrogen K-shell absorption edge was used to map the distribution and provide quantitative densitometry of both the protein and embedding matrix components of the sample. The measurements were calibrated by obtaining the absorption spectrum of protein near the nitrogen edge. The contrast was consistent and reproducible, making possible the first large-scale x-ray microscopic study on sections of plastic-embedded soft tissue. At radiation doses of up to $10^8$ Gray, much more than required for routine imaging, no distortion and little mass loss were observed. This sample preparation method should permit routine imaging of tissues in x-ray microscopes, previously a difficult task, as well as multi-modal imaging (using visible light, x-ray, electron, and scanned probe microscopies) on the same sample.

## Introduction

Sample preparation technologies have been a cornerstone of traditional biological microscopy. Electron microscopy of biological samples would not have been possible without the development of myriad methods for fixing, embedding, sectioning, and

staining or otherwise labeling cells and tissues. Likewise, biological visible light microscopy derives much, perhaps most, of its utility from such methods, even though in principle it can and has been used to image living samples subjected to minimal preparation. This ability to image samples in a more natural state is shared, and in a few aspects surpassed, by a relatively new form of microscopy that uses soft x-rays for illumination and x-ray optics for image formation (Schmahl *et al.*, 1980; Rothman *et al.*, 1990; Kirz *et al.*, 1995). Soft x-rays (typically of wavelength between 2 and 5 nanometers) interact with matter to produce high contrast biological images based solely on intrinsic components rather than stains. By appropriate selection of illuminating wavelengths this contrast can be both element and chemical specific (Kenney *et al.*, 1985; Zhang *et al.*, 1996; Buckley *et al.*, 1998). Modern x-ray lenses, in the form of microfabricated diffractive optical elements called zone plates (Anderson & Kern, 1992), allow this to be accomplished at resolutions of 40 to 50 nanometers currently (Heck *et al.*, 1999), or about 5 times the resolution of visible light microscopes. Compared to electrons, soft x-rays penetrate much thicker samples, up to about ten micrometers, or the full thickness of an unsectioned cell.

Perhaps because of these strengths, most of the work done in biological x-ray microscopy to-date has concentrated on isolated cells and subcellular organelles or cultured cells grown in a single cell layer, often hydrated and sometimes initially living, imaged with little or no prior preparation. Nevertheless, the method stands to benefit greatly from the development of sample preparation techniques analogous to those used in visible light and electron microscopies, just as these other forms of microscopy have benefited. Currently however sample preparation for x-ray microscopy is an immature

field, though a number of sample preparation methods are being developed, including immuno-labeling with silver enhanced gold beads (Meyer-Ilse *et al.*, in press; Larabell *et al.*, in press) and fluorescent probes (Irtel von Brenndorff *et al.*, 1994; Moronne, 1999), and cryogenic freezing (Schneider & Niemann, 1998; Maser *et al.*, 1998; Meyer-Ilse *et al.*, in press).

One notable area of weakness has been the inability to image tissues in the x-ray microscope. Imaging tissues more than a few cell layers deep in any microscope requires sectioning them to a manageable thickness for the type of microscopy being used, because the illuminating radiation has a finite penetrating ability, and because the superposition of features from multiple depth layers in the sample makes structural interpretation difficult. In general, embedding tissue in some form of matrix is needed for sectioning, though with more limitations frozen, hydrated samples can be sectioned as well. Epoxy-embedded and sectioned mineralized samples such as bone, cartilage, and calcified tendon have been imaged with element-specific contrast in an x-ray microscope (Kenney *et al.*, 1985; Buckley *et al.*, 1998). However until recently, attempts to image soft tissues have had little success, apparently due to a lack of image contrast (Jacobsen, 1999; Sicurello, 1999). These attempts have included samples embedded in Epon and Epon/Araldite, with and without removal of the embedding medium before imaging. Nyakatura *et al.* (1988) obtained a single image of a section of rat kidney proximal tubule after removal of the Epon embedding medium by potassium hydroxide treatment. This image demonstrated good contrast and high-resolution features but the results were not reproducible (Meyer-Ilse, 1999).

The problem with these previous attempts stems primarily from the difficulty of obtaining carbon-based contrast in samples consisting of organic materials embedded in a carbon-rich matrix. Recently, the authors and another group (Loo & Rothman, 1997; Khaleque & Buckley, 1998) have demonstrated satisfactory contrast in embedded and sectioned soft tissues. The latter work exploits contrast based on differences between protein and the embedding matrix in their near-edge absorption spectra at the carbon K-shell absorption edge. As discussed below, in the current work we take advantage of nitrogen-based contrast by using wavelengths shorter than the nitrogen K-shell absorption edge.

We describe here a method of embedding and sectioning a soft tissue that demonstrates a number of desirable features in an x-ray microscope, including high natural contrast and radiation tolerance. Glycol methacrylate (GMA, 2-hydroxyethyl methacrylate) polymer is a water-soluble plastic embedding medium used widely in visible light microscopy and, to a somewhat lesser extent, in electron microscopy. Several advantages of GMA embedding have been shown (Cole & Sykes, 1974; Bennett *et al.*, 1976): compared to paraffin, ultrastructural preservation and clarity are improved, tissue distortion is reduced, and thinner sections can be cut, from 0.5 to 3 micrometers routinely (ultrathin sections are also possible), with good uniformity of section thickness (Helander, 1983). Unlike epoxies, acrylic embedding media do not react covalently with tissue molecules, making possible a wide range of histo- and immunochemistry (Bennett *et al.*, 1976; Brinn & Pickett, 1979).

## Methods

*Sample preparation:*

Pancreatic tissue was removed from the rat and fixed after a modification of the method of Ermak & Rothman (1981). Male Sprague-Dawley rats were fasted overnight for 18 to 22 hours. They were anesthetized by inhalation of methoxyflurane (Metofane, Mallinckrodt Veterinary, Inc., Mundelein, IN, U.S.A.), then sacrificed by decapitation and exsanguinated. The pancreas was removed and dissected into small pieces of less than one millimeter in size. Tissue pieces were fixed in 1.5% glutaraldehyde and 1% paraformaldehyde in 0.08 M cacodylate buffer (pH 7.4) at 4° C for approximately 24 hours. They were then transferred to 0.08 M cacodylate buffer without the aldehyde fixatives, and stored at 4° C for up to 21 days prior to embedding.

The embedding method was essentially a routine light microscopic preparation slightly modified from published protocols (Beckstead *et al.*, 1981; Brinn & Pickett, 1979) using the JB-4 embedding kit from Polysciences, Inc. (Warrington, PA, U.S.A.), a formulation of the GMA embedding technique. Tissue pieces were dehydrated by immersion in 70% acetone (diluted with water) for 15 minutes, followed by four exchanges of 100% acetone at 20 minutes each. They were then infiltrated by immersion in a 1:1 mixture of acetone and JB-4 Solution A, primarily consisting of GMA monomer with some of the plasticizer n-butoxyethanol (two exchanges at 30 minutes each), followed by 100% JB-4 Solution A overnight at 4° C under vacuum. All the reagents for the dehydration and infiltration steps were used cold (4° C). Prior to polymerization the tissue pieces were transferred to catalyzed Solution A (0.18 gram catalyst, containing

benzoyl peroxide, per 40 ml Solution A) for one hour. They were then placed in polyethylene block molds with 6 by 8 by 5 millimeter hexagonal wells, covered with freshly prepared polymerizing mixture (40:1 mixture of catalyzed Solution A to Solution B, containing the accelerator N,N-dimethylaniline) and plastic block holders, and allowed to polymerize overnight. Again, these steps were carried out at 4° C, and under vacuum to prevent atmospheric oxygen from inhibiting the polymerization.

The blocks were sectioned with glass knives using a Reichert-Jung (Leica) 2050 Supercut automatic rotary microtome. Sections nominally 0.75 micrometer (μm) thick were cut dry and transferred with forceps to a clean water bath at room temperature where they flattened by surface tension. They were then picked up on sample holders and air dried at room temperature. No mounting medium or coverslip was used, leaving the sample exposed on one side. The sample holder used in this study consisted of a square silicon wafer frame, 100 μm thick and 11 mm wide, supporting a membrane of x-ray transparent silicon nitride 100 nanometers (nm) thick over a 3.5 mm square hole (window) in the center of the wafer. The sample holders were fabricated by lithographic techniques at Lawrence Livermore National Laboratory by Dino R. Ciarlo.

*The x-ray microscope:*

We used a transmission soft x-ray microscope, called XM-1 (Meyer-Ilse *et al.*, 1995; Meyer-Ilse *et al.*, 1998), at the Advanced Light Source (ALS), a high-brightness synchrotron radiation facility at Lawrence Berkeley National Laboratory (LBNL). XM-1 is a conventional-type, or full-field imaging, microscope. Figure 8-1 is a schematic representation of the optical layout. The microscope uses two zone plates as lenses, one

as a condenser that demagnifies the incoherent light source (a bending magnet on the ALS) onto the sample, and the other as an objective that images the sample onto a detector. The detector is a charge-coupled device (CCD) camera, thinned and back-illuminated for high efficiency detection of soft x-rays (Wilhein *et al.*, 1994). The digital output of the camera is read directly into a computer for storage and subsequent processing.

Zone plates have strong axial chromatic aberration (Anderson, 1989). As a result, the condenser zone plate also serves as a monochromator (Niemann *et al.*, 1983), in conjunction with a pinhole just upstream of the sample plane, and provides a spectral resolution ($\lambda / \Delta\lambda$) of 300, or a bandwidth of about 0.01 nm in the wavelength range used. This allows wavelength tuning over the broad emission spectrum of the source. The wavelengths used in this study were 2.4 nm, just below the oxygen K-shell absorption edge in energy (the low absorption side), and 3.1 and 3.0 nm, on either side of the nitrogen K-shell absorption edge.

This x-ray microscope employs a unique sample mounting and positioning system, with two separate sample stages, one each in the x-ray microscope and an external visible light microscope (VLM). The sample mounts reproducibly to either stage via a magnetic kinematic mounting system, and the coordinate systems of the two stages are related by a known correspondence. It is therefore possible to do all sample selection and focussing using the VLM, with no x-ray exposure prior to final imaging.

Images were acquired in one of two modes: single field or montage. The image field size of XM-1 in its standard configuration is a circular area of about 8 to 10 μm

depending on the magnification (usually 2,400 times). To expand the field size an algorithm was developed to assemble large-field image montages from many standard-size subfields (Loo *et al.*, 2000). Most of the images in this study were acquired in this mode.

*Measurement of radiation tolerance:*

Radiation tolerance measurements were performed on a sample prepared as described above at 2.4 nm wavelength (the usual operating wavelength in this instrument). 10 image fields of pancreatic tissue were selected using the VLM and were imaged 2, 4, 6, 8, or 10 times at an exposure level sufficient to produce a good quality image in terms of photon counting statistics. A super-region encompassing the 10 exposed subfields was then selected and imaged by assembling a montage (see Figure 8-3a) to demonstrate any potential change in the exposed areas relative to their surroundings. In addition, several fields in bare GMA plastic portions of the section, containing no pancreatic tissue, were exposed multiple times at 3.0 nm or 3.1 nm wavelength or both, and the change in mass measured. Finally, a large-field montage image was acquired at 2.4 nm wavelength of an area containing smaller fields previously imaged at a very high dose at 3.0 and 3.1 nm wavelength (see Figure 8-6).

*Calculation of dose:*

Dose is absorbed energy per unit mass, measured in Gray (Joules/kilogram). Both the absorbed energy and the mass of the sample are calculated quantities, derived from the measurement of photons detected by the CCD camera. Images are acquired of both the sample and a background region on the sample holder window where no sample is

present. The ratio of these images gives the transmissivity $T$ (fractional energy transmission) of the sample (on a pixel by pixel basis):

$$T = \frac{I}{I_0} \cdot \frac{e_0}{e} \tag{1a}$$

where $I$ is the detected signal intensity through the sample, $I_0$ is the detected intensity through the background region, and $e$ and $e_0$ are the corresponding exposure levels (product of exposure time and synchrotron beam current) at which the images were recorded. $I$ and $I_0$ are corrected for dark current in the CCD detector. The transmissivity is also related to the physical properties of the sample by (Henke *et al.*, 1993):

$$T = \mathrm{Exp}(-\mu\rho_a) \tag{1b}$$

where $\mu$ is the mass dependent absorption coefficient for the sample material, and $\rho_a$ is its areal density (mass per unit area perpendicular to the x-ray beam or optic axis).

Given these relationships, we can determine the quantities of interest. The absorbed energy $A$ (the portion that is not transmitted) is:

$$A = (T^{-1} - 1) \cdot I \cdot Q^{-1} \tag{2}$$

where $Q$ is the light transfer/detection efficiency of all components in the optical path downstream of the sample (see Figure 8-1). The mass $M$ of the sample (per pixel) is given by:

$$M = a\rho_a = -\frac{a}{\mu}\log T \tag{3}$$

where $a$ is the area of a pixel. Dose is then the ratio of $A$ to $M$.

The two quantities that must be known or approximated to calculate the dose from the measured transmissivity $T$ are $\mu$ and $Q$. The mass dependent absorption coefficients ($\mu$) for the elements have been tabulated at wavelengths from 0.04 to 122 nm (Henke *et al.*, 1993). If the relative proportions of elements in a material are known, the composite absorption coefficient for the material can be calculated from the tabulated values. The absolute molecular formula is not required. The composition of GMA polymer was taken to be $C_6H_{10}O_3$ (Bennett *et al.*, 1976), and the composition of protein was taken to be $C_{100}H_{155}N_{27}O_{30}S$. The formula for protein was derived by examining the primary sequences of several proteins (available in the *Entrez* online database from the National Center for Biotechnology Information, National Institutes of Health, http://www.ncbi.nlm.nih.gov) found in the pancreas or mammalian tissues (amylase, trypsinogen, lipase, collagen, and albumin), and taking the average composition assuming no glycosylation. The calculated absorption coefficients for this generic protein formula is within one percent of those of the individual proteins listed above over the wavelength range used, indicating little variation in absorptance from one protein to another.

The light transfer efficiency $Q$ is a product of the transmissivity of the narrow gas-filled gap between the sample and the vacuum window, the transmissivity of two silicon nitride windows (the vacuum window and the support membrane for the objective zone plate) totaling 225 nm in thickness, the diffraction efficiency of the objective zone plate, and the quantum efficiency of the CCD camera. Given the elemental composition and density of a material, its transmissivity can be calculated from the tabulated absorption coefficients and Equation 1b. During imaging, a stream of helium gas (which absorbs x-

rays very weakly) flows around the sample, displacing nearly all of the atmospheric air in its vicinity (which can absorb strongly depending on the wavelength due to its high nitrogen content). Assuming a 99% displacement of air, the helium/air gap transmits over 99% of the x-rays emerging from the sample. The silicon nitride windows together transmit 39, 20, and 40% at wavelengths of 2.4, 3.0, and 3.1 nm, respectively. The calculated (theoretical) diffraction efficiency of the zone plate used in this experiment was 5%, and the actual efficiency was probably about 3%. The quantum efficiency of the same type of CCD as used in this instrument has been measured (Wilhein *et al.*, 1994), and is between 55 and 65% over the wavelength range used. Thus the overall light transfer efficiency was between 0.36 and 0.74%, depending on the wavelength. Not accounted for was absorption due to deposition of a carbon contaminant on the objective zone plate because of poor vacuum at the time of this experiment. The contamination increased gradually with x-ray exposure, and caused an additional variable amount (less than 50%) of absorption over the course of these measurements. Overall, taking these uncertainties into account, the dose estimates presented here are probably accurate to within a factor of 2 to 4, and are probably underestimates.

*Calculation of protein and plastic content:*

Most of the images in this study were acquired at 2.4 nm wavelength, the usual operating wavelength of the XM-1 instrument. In order to calibrate these images for quantitative protein measurements, two sample areas were imaged at wavelengths on both sides of the nitrogen K-shell absorption edge. Let us assume for the moment that the sample consists solely of two materials, $m_1$ and $m_2$, and that at each of two wavelengths,

$\lambda'$ and $\lambda''$, the corresponding absorption coefficients, $\mu_1'$, $\mu_1''$, $\mu_2'$, and $\mu_2''$, are known. Then by Equation 1b:

$$\begin{aligned} \mu_1'\rho_{a,1} + \mu_2'\rho_{a,2} &= -\log T' \\ \mu_1''\rho_{a,1} + \mu_2''\rho_{a,2} &= -\log T'' \end{aligned} \tag{4}$$

Two measurements, $T'$ and $T''$, make it possible to solve for the two unknowns, $\rho_{a,1}$ and $\rho_{a,2}$ (the areal densities of the two component materials), as follows:

$$\rho_{a,1} = \frac{-\mu_2''\log T' + \mu_2'\log T''}{\mu_1'\mu_2'' - \mu_1''\mu_2'} \text{ and } \rho_{a,2} = \frac{\mu_1''\log T' - \mu_1'\log T''}{\mu_1'\mu_2'' - \mu_1''\mu_2'} \tag{5a}$$

or rearranged,

$$\rho_{a,1} = \frac{-\log T' + \left(\frac{\mu_2'}{\mu_2''}\right)\log T''}{\mu_1' - \mu_1''\left(\frac{\mu_2'}{\mu_2''}\right)} \text{ and } \rho_{a,2} = \frac{-\log T' + \left(\frac{\mu_1'}{\mu_1''}\right)\log T''}{\mu_2' - \mu_2''\left(\frac{\mu_1'}{\mu_1''}\right)} \tag{5b}$$

This system of equations is ill-conditioned (*i.e.*, produces an unstable solution) if the absolute value of its determinant $|\mu_1'\mu_2'' - \mu_1''\mu_2'|$ is small. The imaging wavelengths $\lambda'$ and $\lambda''$ should therefore be chosen to maximize this quantity. For example, if they are on either side of an absorption edge of one of the components, *e.g.*, $m_1$, the absorption coefficient $\mu_1$ will have a large change across the edge, with little change in $\mu_2$, resulting in a determinant of large magnitude.

To a good approximation, a soft tissue sample prepared as described above consists entirely of organic molecules such as protein, nucleic acids, lipids, and the plastic

embedding medium. These molecules contain varying proportions of the elements carbon, hydrogen, nitrogen, oxygen, phosphorus, and sulfur. Protein and nucleic acids can be distinguished from the other constituents (the plastic matrix being of greatest concern) by their high nitrogen content (16 to 17% by mass).

As a consequence, we can model the sample as being composed of two components: nitrogen (assigned to $m_1$) and a composite material consisting of the rest of the elements in the sample (assigned to $m_2$). The two chosen wavelengths (3.0 and 3.1 nm) straddle the nitrogen K-shell absorption edge (nominally 3.025 nm). The attenuation coefficients of, *e.g.*, GMA polymer and the non-nitrogenous part of protein, are sufficiently different from each other that we cannot assume a single value for $\mu_2'$ or $\mu_2''$. However, as apparent in Equation 5b, to determine the nitrogen mass only the ratio of $\mu_2'$ to $\mu_2''$ is required, and this ratio is constant to within 0.1% for the materials of interest (GMA polymer, non-nitrogenous parts of protein and DNA, lipids, carbohydrates), with a value of 0.92 for the two given wavelengths. The protein and DNA mass can then be calculated based on their known fractional nitrogen content, and the balance of the mass, if assumed to be due to GMA polymer, can subsequently be calculated given the measured transmissivities by Equation 4.

We applied two additional corrections in our calculations. First, we attempted to account for possible errors due to radiation exposure effects. The two sample areas selected for nitrogen edge imaging in this experiment were the central regions of two pancreatic acini (see Figures 8-5 and 8-6). In order to allow for the correction of possible changes in transmissivity due to radiation induced mass loss, one acinus was imaged at

3.1 nm first followed by 3.0 nm, and the other was imaged in the reverse wavelength order. The first image of each pair (having received no prior radiation dose) could then serve as a control for the second of the other pair. Pixels in three intensity ranges were selected in each of the image pairs corresponding to high protein density (in the middle of the dense zymogen granules), intermediate protein density (in cytoplasmic regions between granules), and low protein density (in the duct lumen). A linear transformation was applied to the transmissivity values in the second image of each pair to make pixel values in each of the intensity categories more similar to those in the corresponding intensity categories in the first image of the opposite pair. Calculations were then performed on the corrected images as described above. Attempting in addition to correct the first image of each pair for the dose deposited in that first exposure using the mass loss curves described below (see Figure 8-4) had a negligible impact on the results.

Second, the wavelengths used were sufficiently close to the nitrogen absorption edge that near-edge effects due to covalent bonding and other environmental factors cause a substantial deviation of the absorption coefficient of nitrogen from its tabulated theoretical values. We estimated the true absorption coefficients by measuring the absorption spectrum of a protein (albumin) near the nitrogen edge as described in the next section. These were the values used for $\mu_1$ in the above relationships to determine the mass of protein and plastic.

*XANES spectrum of albumin, and the determination of the mass dependent absorption coefficient in the nitrogen 1s K-shell region*

Equation 5 above in principle allows the determination of the nitrogen content of a sample given two images acquired using x-ray wavelengths on either side of the nitrogen K-shell absorption edge. Required in these expressions are the mass dependent absorption coefficients at each of the two wavelengths, for each of the two components of the sample's mass: that due to nitrogen, and that due to all other elements in the sample. As already noted, though the absorption coefficients have been tabulated for all the elements over a wide range of wavelengths (Henke *et al.*, 1993), the true coefficient for an element deviates substantially from the tabulated values at wavelengths near its absorption edges. This x-ray absorption near-edge structure (XANES) in the spectrum of an element is strongly influenced by the local environment of the atom, particularly covalent bonds to adjacent atoms. For nitrogen in protein, the amide bond has the greatest influence on the spectrum near the nitrogen edge.

To obtain accurate absorption coefficients for nitrogen in protein, we determined the spectrum of a protein, albumin, near the nitrogen edge, using the scanning transmission x-ray microscope (STXM) on beamline 7.0.1 (an undulator beamline) of the Advanced Light Source at LBNL. We obtained the spectrum near the carbon K-edge as well. In other work, the nitrogen K-shell spectrum of albumin, along with the carbon K-shell spectra of albumin and fibrinogen, are also being used as standards for investigations of the localization of these proteins on polymer surfaces (Hitchcock *et al.*, in press). Similar XANES spectra of proteins and DNA have been measured by others at the nitrogen edge

(Kirtley *et al.*, 1992; Shinohara *et al.*, 1998) and the carbon edge (Zhang *et al.*, 1996), but were not converted to mass dependent absorption coefficients.

The transmissivity of a free standing thin film of albumin was measured at 250 wavelengths from 2.86 to 3.22 nm and 242 wavelengths from 3.82 to 4.46 nm, by normalizing the transmission through albumin to transmission through the surrounding helium atmosphere. The mass dependent absorption coefficient of albumin is directly proportional to the optical density (or minus the logarithm of the transmissivity) thus measured, per Equation 1b. We determined the proportionality constant between them (equivalent to the inverse of areal density) by first assuming that the regions of the spectrum far from the absorption edges coincide with the tabulated theoretical values. The molecular formula for bovine serum albumin is $C_{3071}H_{4826}N_{816}O_{927}S_{40}$, based on its primary structure and assuming no glycosylation (data from the *Entrez* online database, http://www.ncbi.nlm.nih.gov). The theoretical absorption coefficient based on this formula for albumin is plotted in Figure 8-2. For the theoretical spectrum, the edge transition energies were set to 405 eV (for the nitrogen K-edge) and 292 eV (carbon K-edge), which are values estimated by comparing albumin's spectral features with those of amide molecules for which the ionization limits are known (Hitchcock & Mancini, 1994).

We wish to find the proportionality constant $k$ that minimizes the difference $D$ in a least squares sense between the measured and theoretical values at the tail ends of the spectrum:

$$D = \sum_i \left(\mu_{tab,i} - k \cdot OD_i\right)^2 \tag{6}$$

where $\mu_{tab}$ are the tabulated coefficients, $OD$ are the measured optical densities, and $i$ is the index over the 20 data points at each end of the measured spectrum. The value of $k$ that minimizes $D$ is:

$$k = \frac{\sum_i \mu_{tab,i} \cdot OD_i}{\sum_i OD_i^2} \tag{7}$$

The measured spectrum, $\mu_{meas} = k \cdot OD$, is also plotted in Figure 8-2.

At wavelengths near the nitrogen edge, the difference between the measured albumin absorption spectrum and its computed theoretical spectrum (based on its elemental composition) is due to its nitrogen component. The contributions of the nitrogen and non-nitrogen components can be separated as:

$$\mu_{meas} = f_N \mu_N + (1 - f_N)\mu_{other} \tag{8a}$$

where $\mu_{meas}$ is the measured absorption coefficient of albumin as above, $\mu_N$ is absorption coefficient of the nitrogen component, $\mu_{other}$ is the absorption coefficient of the non-nitrogen component, and $f_N$ is the fraction of the molecular weight of albumin due to nitrogen. This gives:

$$\mu_N = \frac{\mu_{meas} - (1 - f_N)\mu_{other}}{f_N} \tag{8b}$$

$f_N$ is 16.5% for albumin. $\mu_{other}$ is taken to be the theoretical values based on the tabulated data for a compound with the formula $C_{3071}H_{4826}O_{927}S_{40}$ (albumin without the nitrogen

component). The actual values for the absorption coefficient of the nitrogen component derived in this way are plotted in Figure 8-2 (inset), along with the tabulated values.

Also indicated in Figure 8-2 are the two wavelengths used in the dual-wavelength imaging portion of this study. The energy scale of the spectra acquired on the STXM was calibrated against the well characterized 3s and 3p Rydberg peaks of nitrogen gas ($N_2$) (Chen *et al.*, 1989), and is accurate to within less than 0.05 eV. However, there was an energy calibration error in XM-1 estimated at approximately 2 eV in energy or 0.015 nm in wavelength, based on comparing transmission data on silicon nitride windows between the two instruments. Thus while the nominal wavelengths used were 3.0 and 3.1 nm, the actual wavelengths were about 3.015 and 3.116 nm. Because the longer of the two wavelengths falls on a steep part of the absorption coefficient curve in Figure 8-2 (inset), the uncertainty in the energy calibration produces an uncertainty in the calculated nitrogen or protein density of up to about 10%. The measured absorption coefficient of nitrogen was $4.7\times10^4$ $cm^2/g$ at 3.015 nm wavelength, and $6.4\times10^3$ $cm^2/g$ at 3.116 nm wavelength. The corresponding tabulated values were $3.05\times10^4$ and $1.26\times10^3$ $cm^2/g$. As can be seen from Equation 5, using the tabulated values would have resulted in calculated nitrogen or protein densities about 40% too high.

## Results and discussion

*Contrast:*

Figure 8-3a is an image montage acquired at 2.4 nm wavelength. It demonstrates unambiguously many structural and ultrastructural features at high resolution. These include capillary endothelial cells (C), numerous pancreatic exocrine cells arranged in

clusters called acini (A), cell nuclei (N), nucleoli (n), mitochondria (m), and zymogen granules (z). In addition, the nucleus of a centroacinar cell (ca) is visible in one of the acini. The contrast evident in this image was consistently achievable for all the samples in this study, which included sections from multiple pancreatic tissue pieces from each of seven animals. Nearly 100 large-field montages like this one were acquired, consisting of nearly 27,000 individual subimages, making this the largest x-ray microscopic study to-date. This work was part of a larger experiment in which we set out to measure the population statistics on size, protein mass, and number of zymogen granules in pancreatic exocrine tissue to evaluate mechanisms of protein transport (Rothman *et al.*, 1992; Loo *et al.*, 1996). The biological results will be published in a separate paper.

A useful image can be recorded only if there is a difference in the absorption of x-rays between sample features, consisting primarily of protein or nucleic acid, and their background, the plastic embedding matrix in this case. Figure 8-2 contains a plot of the mass dependent absorption coefficients of protein and GMA polymer over a range of wavelengths including the carbon, nitrogen, and oxygen K-shell absorption edges. Clearly, at wavelengths between the nitrogen and oxygen edges (including the 2.4 and 3.0 nm wavelengths used in this study) a sample pixel filled with protein would absorb x-rays significantly more strongly than a pixel containing the same mass of plastic. Conversely the same two pixels would be difficult to distinguish if illuminated by x-rays with a wavelength longer than the nitrogen edge or shorter than the oxygen edge. Thus nitrogen content is the main contributor to image contrast.

All previous work on embedded and sectioned soft tissue has been done with x-ray wavelengths longer than that at the nitrogen edge. This probably accounts for much of the

difficulty in obtaining satisfactory contrast. Contrast was nevertheless seen in sections of embedded mineralized tissues probably because unlike soft tissues, which are composed mainly of water (that subsequently is replaced by the embedding material), such tissues are composed primarily of dense material with little water content, and thus give appreciable contrast against the embedding matrix based on density alone. The x-ray microscope that was used for almost all of this earlier work, the Stony Brook scanning transmission x-ray microscope (STXM) at the National Synchrotron Light Source at Brookhaven National Laboratory (Kirz *et al.*, 1995; Maser *et al.*, 1998), has a longer portion of the optical path in air, so that absorption due to atmospheric nitrogen made using shorter wavelengths, like those used in this work, unfavorable (Jacobsen, 1999). On the other hand, in XM-1 the monochromator pinhole and downstream vacuum window are mounted on cones that can be positioned very close to the sample, minimizing the air gap. This helps overcome the problem, and in fact 2.4 nm is the usual operating wavelength of the microscope.

Recently, Khaleque & Buckley (1998) used a wavelength at which the embedding materials have stronger absorptance than protein, producing negative contrast. This is due to near-edge effects at the carbon edge. The ability to use wavelengths shorter than the nitrogen edge (currently being incorporated in the Stony Brook STXM as well) has the advantage of strong contrast due to the high content of nitrogen in protein and nucleic acids and its absence in the plastic.

*Radiation tolerance:*

Indicated on Figure 8-3a are ten subfields that were imaged two to ten times prior to acquisition of the large-field montage. Only in the most heavily exposed (ten times) fields is a change in intensity appreciable visually, and only then because the intensity scale of the display has been adjusted to emphasize the difference. Figure 8-3b shows the central part of each of these areas displayed as a ratio of the first exposure to the last. Darker pixels indicate a greater change in transmissivity. Several features are notable in these images. First, the degree of change in transmissivity (due to mass loss) is dose dependent. Second, it is nonuniform, being greater in areas of lower protein density. Third, despite the mass loss, there is no discernable distortion of the sample after up to ten exposures. Distortion would manifest as misalignment of the edges of features in these ratio images, resulting in ghosting.

Figure 8-4 shows plots of sample mass, expressed as a fraction of the initial mass, versus dose. The mass axis is a log scale. A straight line would be expected if a fixed fractional mass loss were produced by each increment in dose. The data fall on a curve, however, suggesting a biphasic or multiphasic response to dose, with decreasing fractional mass loss per unit dose at higher doses. The fitted curves shown are quadratic functions. The data from the images in Figure 8-3b are plotted as four curves. One results from averaging pixel values over each of the individual exposures. The other three result from partitioning the pixels into three categories: high protein density (in the middle of the dense zymogen granules), intermediate protein density (in cytoplasmic regions outside granules), and low protein density (in extracellular areas). The slope, or extent of mass loss with dose, is least in high protein density areas. The last curve was generated

from data on bare GMA plastic areas exposed multiple times at 3.0 or 3.1 nm wavelength. The slope is similar to that of the low protein density curve at 2.4 nm wavelength. These observations suggest that the GMA component of the sample is significantly more sensitive to radiation than the protein component, and that the dose sensitivity is approximately independent of wavelength (at least for the plastic matrix).

A dose of $1.2\times10^7$ Gray (Gy) produces a 5% mass loss in plain GMA polymer, as do $4.4\times10^7$ Gy and $6.8\times10^7$ Gy in areas of intermediate and high protein density, respectively. In tissue on the whole, it takes $3.5\times10^7$ Gy to produce a 5% mass loss, and even at $10^8$ Gy mass loss is less than 10%. On the other hand, the dose used to form a single image, with all the above-mentioned inefficiencies in the system at the time, was about $10^7$ Gy at 2.4 nm, $5\times10^7$ Gy at 3.0 nm, and $2\times10^7$ Gy at 3.1 nm. Thus the potential mass loss at the nitrogen edge was non-negligible and corrections were needed to compensate for radiation effects, while imaging at 2.4 nm wavelength produced relatively minimal changes.

Figure 8-6 demonstrates the mass loss that occurs with extremely high doses. It is a large field montage (at 2.4 nm wavelength) encompassing two smaller areas that were also imaged earlier in montage mode at both 3.0 and 3.1 nm wavelength. The prior cumulative dose to these areas was about $7\times10^9$ Gy. The fractional mass loss was 19% in high protein density areas, 25% in intermediate protein density areas, and 31% in low protein density areas. Based on the curves in Figure 8-4, these appear to be practically asymptotic values for mass loss. Furthermore, despite the significant mass loss there appears to be no appreciable distortion of basic cellular and tissue architecture.

Although the samples were sufficiently robust to tolerate these doses, minimizing dose is clearly desirable. Even in a single exposure, the doses used were far higher than theoretically required to produce images of equivalent quality. The main reason for this is the low light transfer efficiency of all the components downstream of the sample (significantly less than 1%), the largest loss being in the objective zone plate. Methods are being developed to produce zone plates with significantly better diffraction efficiency. In addition, a much greater reduction in dose is possible using a scanning microscope, in which a single zone plate is used to form an x-ray microprobe that is scanned across the sample. Only the detector is downstream of the sample in this case, and compared to the current work, the required dose should be roughly two orders of magnitude lower.

There was another source of inefficiency in montage mode imaging at the time of this study. The available monochromator pinhole was a 15 μm square hole. Because the monochromator pinhole defines the size of the irradiated area on the sample, a larger area was exposed than fit within the imaged area (the 8 to 10 μm circular field of view). Consequently, most of the subfields imaged in montage mode (except those at the edges of the super-region) received the equivalent of about four exposures (when images of some of their neighboring subfields were acquired) before actually being imaged themselves. Furthermore, by the end of a montage acquisition sequence, most of the imaged area was exposed about nine times. Single field imaging at a spacing greater than the monochromator pinhole size is not affected. A smaller monochromator pinhole has subsequently been installed, allowing montage image acquisition with a dose similar to that in single image mode (in addition to improving spectral resolution).

Finally, as to the mechanism of mass loss with soft x-ray exposure in dry samples such as these, it must involve volatilization or vaporization of the sample. This might happen by reaction with residual atmospheric oxygen not displaced by helium (or ozone produced by its ionization by x-rays). An observation consistent with this hypothesis is that visible light fluorescence (observed in a visible light microscope) increases in an area of formaldehyde-fixed cultured cells after it is imaged in the x-ray microscope (Meyer-Ilse, 1999). Enhancement of fluorescence in formaldehyde-fixed samples by exposure to ozone is a known technique in histochemistry (Chap. 19 in Pearse, 1985). If reaction with atmospheric oxygen is in fact the mechanism of mass loss, it should be possible to prevent or at least reduce mass loss by excluding air around the sample more completely, for example by building a helium filled chamber around the sample stage.

*Distribution of protein and GMA polymer:*

Figure 8-5 shows two image fields in the centers of two acini at both 3.0 and 3.1 nm wavelength (a and b), their calculated nitrogen mass distribution (c), and calculated GMA polymer distribution (d). The high, intermediate, and low protein density regions had average protein areal densities of $6.9\times10^{-5}$, $3.9\times10^{-5}$, and $2.8\times10^{-5}$ g/cm$^2$, respectively, and average GMA polymer areal densities of $-0.1\times10^{-5}$, $2.3\times10^{-5}$, and $2.6\times10^{-5}$ g/cm$^2$, respectively. Based on the transmissivity of pure GMA regions in the sample, the thickness of the section was estimated (as described in the next section) to be 0.51 μm. This allows an estimation of volumetric density (as areal density divided by thickness), yielding high, intermediate, and low average protein densities of 1.36, 0.77, and 0.56 g/cm$^3$, respectively, and corresponding average GMA polymer densities of -0.02, 0.46,

and 0.51 g/cm$^3$. Figure 8-7 is a plot of GMA polymer density versus protein density for each of the nearly 82,000 pixels in these two sample areas. The data fit well to a straight line of negative slope, indicating that each unit of protein excludes a fixed amount of plastic embedding matrix, essentially excluding it completely at the highest protein densities.

The regression line was fitted to points in the main peak of the scatter plot. Also apparent is a second smaller peak falling below the regression line. Spatially, the points in the second peak correspond almost exclusively to pixels in the intraductal space of the imaged acini, where the protein density was the lowest. That it falls below the regression line indicates a proportionally reduced plastic content in these areas, possibly reflecting an increased radiation sensitivity of the plastic component in low protein areas as indicated by the curves in Figure 8-4. Also, 20% of the pixels have a calculated plastic density below zero, which is physically impossible. Though this is partly due to noise in the data, it likely also results at least in part from a systematic overestimation of protein density such as due to uncertainty in the energy calibration of the microscope as described above. A relatively small error in protein density can produce a large proportion of pixels with apparently negative plastic density since the plastic is already nearly excluded from these high protein areas.

The intercepts of the regression line indicate the density of plastic where protein density is zero, and *vice versa*; *i.e.*, the densities of each component uncontaminated by the other. The y-intercept indicates a density for pure GMA of 1.15 g/cm$^3$, compared to the density of bulk GMA polymer of 1.21 g/cm$^3$ (measured independently as described in the next section). The similarity between these values supports the assumption that

section thickness is consistent between the tissue-containing and pure plastic regions of the section, and helps validate the conversion from areal to volumetric density. The x-intercept yields a protein density of 1.34 g/cm$^3$ where the GMA is completely excluded by protein, essentially the same as the average density of protein in the dense centers of the zymogen granules. This is also similar to that of pure protein, about 1.4 g/cm$^3$ (Sober, 1968), and suggests that protein within the granules is in the dehydrated state when the sample is prepared in this fashion.

Moreover, these intragranular protein density measurements are substantially higher than previously measured values for protein concentration in freshly isolated zymogen granules, averaging in the range 250-270 mg/ml with peak values of about 600 mg/ml (Goncz *et al.*, 1995; Ho & Rothman, 1983). The difference is probably related to major differences in sample preparation. For example, tissue shrinkage is a well known artifact of preparative treatments such as the fixation, dehydration, and embedding used in the current work (Hanstede & Gerrits, 1983). This is manifest in measurements of zymogen granule diameter. As measured by x-ray microscopy, granules (also from fasted rats of the same species), unfixed and in aqueous suspension, have an average diameter of 1.08 μm (Goncz *et al.*, 1995), whereas in the current work, average granule diameter in GMA-embedded tissue sections (to be reported in full in a separate paper) is about 0.77 μm, consistent with electron microscopic measurements of granule size in epoxy-embedded tissue sections that have produced values in the range of 0.73-0.85 μm (Ermak & Rothman, 1981; Beaudoin *et al.*, 1984). The 1.4 fold difference in linear dimension (between 1.08 and 0.77 μm), assuming it is symmetric in all dimensions, translates to a 2.8 fold difference in volume, a substantial fraction of the proportional difference of the

measured densities between the two preparations: the dense centers of the zymogen granules in this study have an average density 5 to 5.4 times that of the average and 2.3 times that of the peak density of freshly isolated granules. This illustrates that the expression of tissue shrinkage in planar terms, typical in two-dimensional microscopy, belies the actual magnitude of volumetric shrinkage, which becomes readily apparent only with the tools to measure mass in such a direct fashion. Furthermore, the similarity of the intragranular density measured in the GMA-embedded samples to that of pure protein suggests that the mechanism of shrinkage is related to dehydration of the sample with incomplete replacement of water by the embedding matrix.

Though other investigators have used dual- and multi-wavelength imaging at the carbon K-shell and calcium L-shell absorption edges to obtain contrast and map tissue components (Kenney *et al.*, 1985; Zhang *et al.*, 1996; Buckley *et al.*, 1998), this is the first work to use dual-wavelength imaging at the nitrogen K-shell edge in a high resolution x-ray optical microscope. Using an x-ray contact microradiographic system, Ito *et al.* (1996) were able to obtain spectromicrographs of cultured cells across a large part of the soft x-ray spectrum (including the nitrogen edge) at a resolution comparable to that of a visible light microscope. Nitrogen-based imaging, in addition to taking advantage of the large nitrogen difference between tissue and embedding medium, can also in principle be used to differentiate protein from DNA by exploiting a strong difference between the absorption peaks in their nitrogen near-edge spectra (Kirtley *et al.*, 1992; Shinohara *et al.*, 1998). This has been done at the carbon edge by Zhang *et al.* (1996).

*Section thickness:*

Because of the well-defined relationship between transmission and the areal density of the sample (see Equation 1b), it is possible to determine the thickness of a sample given its density and mass dependent absorption coefficient. Rectangular blocks of polymerized GMA embedding material were machined, measured, and weighed (courtesy of W.A. Bates and W. Meyer-Ilse, Lawrence Berkeley National Laboratory) to determine the density of the plastic: 1.21 g/cm$^3$. The transmission of 7 sections, normalized to the transmission through the silicon nitride support membrane on each of their respective sample holders, was measured at 3 to 6 spots on each section (24 total) in areas containing only the plastic (devoid of tissue) to determine their thickness.

The nominal microtome setting for thickness was 0.75 μm. The actual thickness calculated as described ranged from 0.31 to 0.91 μm over these 7 sections, with an average thickness of 0.56 μm and a standard deviation of 0.23 μm. However, thickness variation *within* sections, as measured by the standard deviation from the respective mean values, was only 0.02 μm. These measurements are consistent with the finding of Helander (1983) that thickness within sections is quite uniform, particularly in the pure plastic component.

## Conclusions

While x-ray microscopic instrumentation has matured in recent years, corresponding sample preparation methods are still in their infancy. This work demonstrates that GMA embedding and sectioning, widely used in other forms of microscopy, is applicable to x-

ray microscopy essentially without modification. This should allow soft x-ray microimaging, with its unique contrast properties, of a wide range of tissues prepared routinely as for other forms of microscopy, including pathology samples. It also offers the opportunity to carry out multi-modal microscopy (including visible light, x-ray, and electron imaging) on a given sample. This could be a powerful approach since the information provided by x-ray microscopy complements that provided by visible light and electron microscopies. In addition, because one surface of the sample can be left exposed, scanned probe microscopy (*e.g.*, atomic force microscopy or scanning tunneling microscopy) can also be performed. For example, we have recently begun measurements to assess more accurately the uniformity of the section thickness by AFM.

As shown, good contrast is obtained between the sample and the embedding medium due the variable nitrogen content of the tissue. This also makes it possible, using two or more imaging wavelengths, to obtain chemically specific contrast near the nitrogen absorption edge. Furthermore one can similarly take advantage of the near-edge absorption structure of any other major elemental constituent in the sample, including carbon, oxygen, and minerals such as calcium (Kirtley *et al.*, 1992; Zhang *et al.*, 1996; Buckley *et al.*, 1998).

The samples demonstrated good radiation tolerance at the doses used for imaging, and with some additional measures to reduce dose and prevent mass loss, a range of powerful x-ray microscopic imaging modes becomes practical. For example, in a typical XM-1 configuration at the time of this study (with its attendant sources of optical inefficiency) it took about $10^7$ Gy to form an image, about three times less than the dose that produced significant (5%) mass loss in GMA-embedded tissue sections. This is also

about the same as the theoretical dose required to do soft x-ray microtomography with 80 nm resolution in all three dimensions (Loo & Rothman, 1995; Loo & Rothman, 1997). Thus quantitative, high-resolution three-dimensional elemental mapping on such samples is possible. Similarly, chemical mapping by spectromicroscopy with high spectral resolution, requiring many exposures at different wavelengths, is feasible. Finally, because these samples are insensitive to radiation induced distortion, they are highly amenable to montage imaging and large-field survey studies of tissue (Loo *et al.*, 2000).

**Acknowledgements**

We wish to thank our colleagues at the Center for X-Ray Optics, Advanced Light Source, and Life Sciences Division at Lawrence Berkeley National Laboratory, at Lawrence Livermore National Laboratory, at the University of California, San Francisco, Berkeley, and Davis, at the State University of New York, Stony Brook, and at Genteric Corporation for their help in this work. We are grateful in particular to the following individuals, who have made critical contributions: David T. Attwood, Mary Helen Barcellos-Hoff, William A. Bates, John T. Brown, Daniel E. Callahan, Je-Wei Chen, Dino R. Ciarlo, Nusi P. Dekker, Gregory P. Denbeaux, Everett H. Harvey, Theresa Hashim, Catherine A. Hong, Malcolm R. Howells, Chris J. Jacobsen, Melvin P. Klein, Carolyn A. Larabell, Aaron J. Lee, Jesse Lee, Betty A. Maddux, Bonnie J. McClintock, Werner Meyer-Ilse, Mario M. Moronne, Daniel M. Pinkas, Jos Polman, Shradda A. Ravani, Joseph A. Regezi, Paula Sicurello, Joachim Stohr, Hsien-Chen Tseng, and Elise Y. Tung-Loo. We especially thank the late Werner Meyer-Ilse and his staff for generously providing the use of and continually improving the XM-1 microscope facility, and for many helpful discussions and comments.

BWL gratefully acknowledges the support of a National Institutes of Health training grant to the UCSF/UCB Bioengineering Graduate Group, a Laboratory Graduate fellowship from Associated Western Universities, Inc., and a fellowship from the Regents of the University of California. The research of APH is funded in part by a strategic project grant from NSERC (Canada). The XM-1 project and the ALS are supported by the U.S. Department of Energy, Office of Basic Energy Sciences and Office of Biological and Environmental Research, and the Laboratory Directed Research and Development Program of the E. O. Lawrence Berkeley National Laboratory, under the Department of Energy contract No. DE-AC03-76SF00098.

## Figure Captions

**Figure 8-1.** Schematic representation of the optical layout of the high-resolution x-ray microscope XM-1. The design is of the conventional, full-field imaging type. The optical elements are in vacuum, and the vacuum windows (one of which serves as a monochromator pinhole) are mounted on cones close to the sample to minimize the air gap surrounding the sample, where the remaining air is largely displaced by a stream of helium gas. The optical efficiency of all elements downstream of the sample (the helium/air gap, vacuum window, zone plate lens and support membrane, and CCD camera) affects the dose required to form an image of a given statistical quality.

**Figure 8-2.** Mass dependent absorption coefficient spectra of a protein (albumin) and glycol methacrylate (GMA). For albumin, both the tabulated theoretical values based on its elemental composition and the measured values near the nitrogen and carbon K-shell absorption edges are plotted. These differ substantially from each other due to near-edge spectral features which are sensitive to molecular structure. In the wavelength window between the oxygen and nitrogen absorption edges, the difference between the absorption coefficients of protein and GMA due to the nitrogen content of protein provides most of the contrast in images acquired at these wavelengths, whereas outside of this wavelength range, their spectra nearly coincide. Dotted lines indicate the wavelengths used in this study. **Inset**, the mass dependent absorption coefficient spectrum of nitrogen in protein derived from the measurements on albumin, compared to the tabulated values.

**Figure 8-3. a**, an image montage acquired at 2.4 nm wavelength of GMA-embedded and sectioned pancreatic tissue, demonstrating many structural and ultrastructural features at high resolution and with strong contrast. Clearly visible are pancreatic exocrine cells arranged in clusters called acini (A), cell nuclei (N), nucleoli (n), mitochondria (m), many protein-rich zymogen granules (zg) surrounding ductal spaces at the center of the acini, capillary endothelial cells (C), and the nucleus of a centroacinar cell (ca) in one of the acini. The total image size is about 2,700×2,700 40 nm pixels, or a little over 100×100 μm in area. The 10 regions marked by squares were each imaged the specified number of times prior to acquiring the large field montage to measure the extent of radiation induced mass loss. Only in the most heavily exposed fields (10 times) is an intensity difference visually appreciable, even with the intensity scale adjusted to emphasize the difference. **b**, the ratio of the first exposure to the last, in the central part of each of the pre-exposed areas in **a**. Areas with the greatest change in transmissivity between the first and last exposures appear the darkest, demonstrating a dose dependent mass loss that is also spatially nonuniform, with greater loss in areas of lower protein density.

**Figure 8-4**. Plots of sample mass remaining versus dose. The data at 2.4 nm wavelength are from the measurements from Figure 8-3. Even at doses of $10^8$ Gy, there is a less than 10% mass loss in tissue as a whole, while the dose to required to form an image of good statistical quality in this study was only about $10^7$ Gy (which because of optical inefficiencies was itself over 100 times greater than the theoretically required dose). The GMA plastic component of the sample appears significantly more

radiation sensitive than the protein component, and this sensitivity is similar across the wavelengths used.

**Figure 8-5**. Dual-wavelength imaging of the central parts of two pancreatic acini. The left column is of acinus 1, and the right is of acinus 2. **a**, the first exposure of each acinus (at 3.1 nm wavelength for acinus 1, and 3.0 nm for acinus 2). **b**, the second exposure (3.0 nm for acinus 1, and 3.1 nm for acinus 2). The two acini were imaged in reverse wavelength sequence from each other to control for possible radiation induced effects, as described in the text. Contrast in the transmission images is much stronger at 3.0 nm than at 3.1 nm, due to increased absorption of the nitrogen-containing tissue components on that side of the nitrogen absorption edge (see Figure **8-2**). **c** and **d**, calculated density maps of the protein and GMA embedding matrix components of the sample, respectively. White represents the highest density, and black the lowest.

**Figure 8-6**. An image montage at 2.4 nm wavelength, demonstrating the effect of extreme radiation dose. The two regions marked by squares surround the areas imaged in Figure **8-5**, and were subsequently exposed to an extreme dose of about $7\times10^9$ Gy prior to the acquisition of this montage. The fractional mass loss in these regions, visible as increased transmitted intensity, ranged from about 20 to 30%, yet despite this there is no appreciable distortion of the basic tissue architecture.

**Figure 8-7**. A plot of GMA polymer density versus protein density for the nearly 82,000 pixels in the areas imaged in Figure **8-5**. The good fit of the data to a straight line suggests that each unit of protein excludes a fixed amount of plastic embedding

matrix. A second smaller peak in the data corresponds spatially to pixels in the low protein intraductal spaces, and falls below the regression line through the main peak, indicating a proportionally lower plastic content in those areas. This might be due to increased sensitivity of the plastic component to radiation in low protein areas, as indicated in Figure **8-4.**

**Figures**

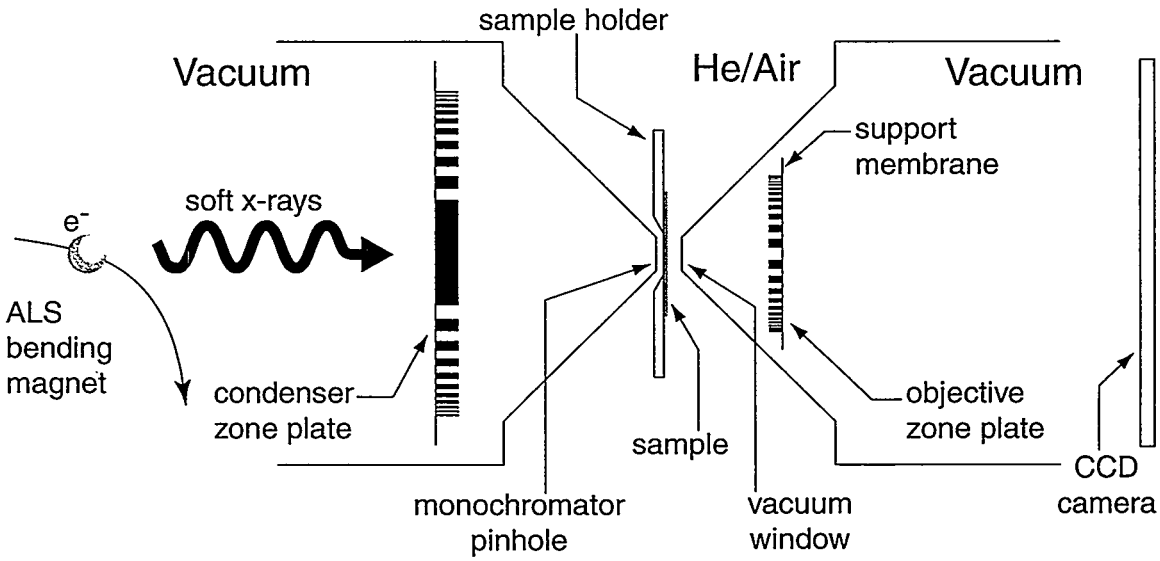


**Figure 8-1**

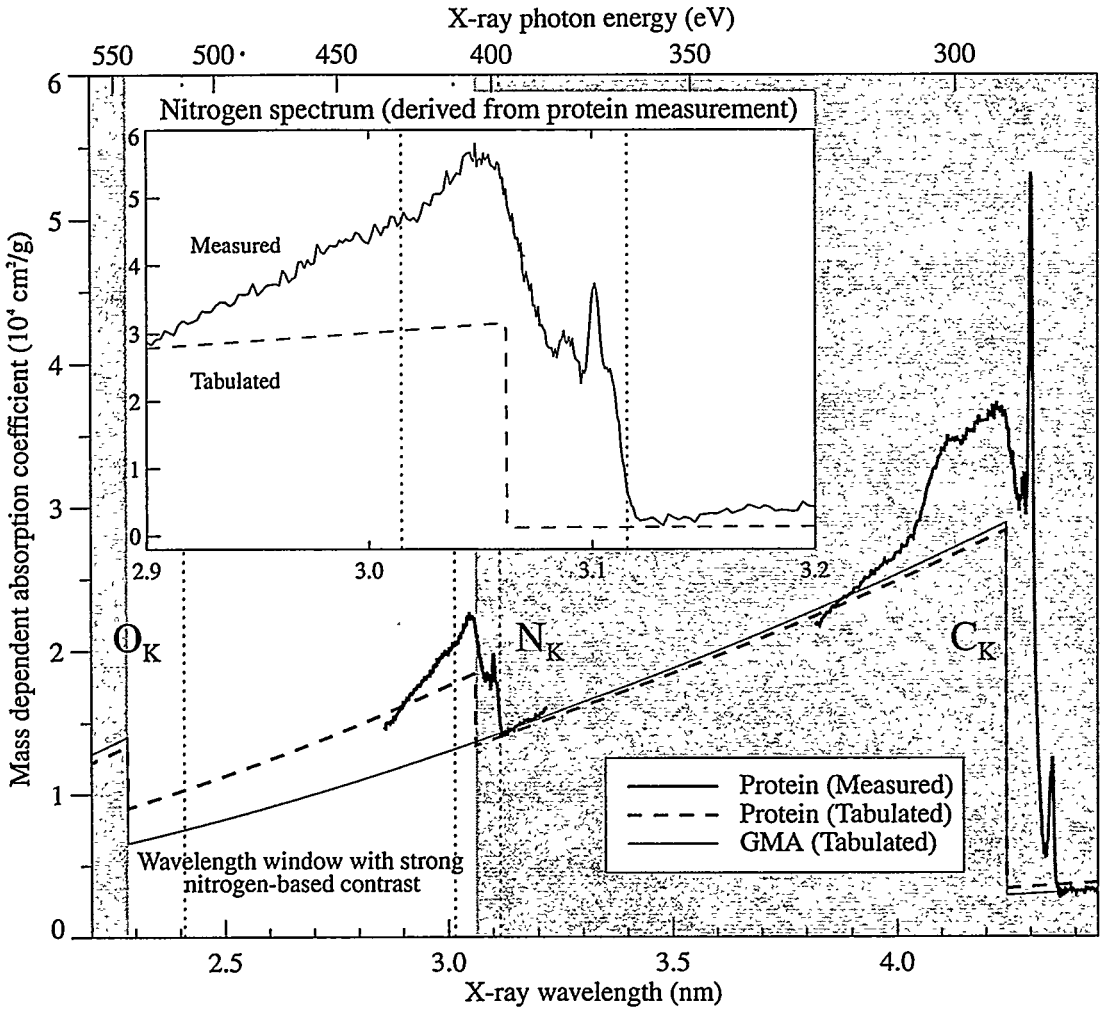
X-ray photon energy (eV)
550
500
450
400
350
300
Nitrogen spectrum (derived from protein measurement)
Measured
Tabulated
2.9
3.0
3.1
3.2
$O_K$
$N_K$
$C_K$
Protein (Measured)
Protein (Tabulated)
GMA (Tabulated)
Wavelength window with strong nitrogen-based contrast
Mass dependent absorption coefficient ($10^4$ cm$^2$/g)
0
1
2
3
4
5
6
2.5
3.0
3.5
4.0
X-ray wavelength (nm)

**Figure 8-2**

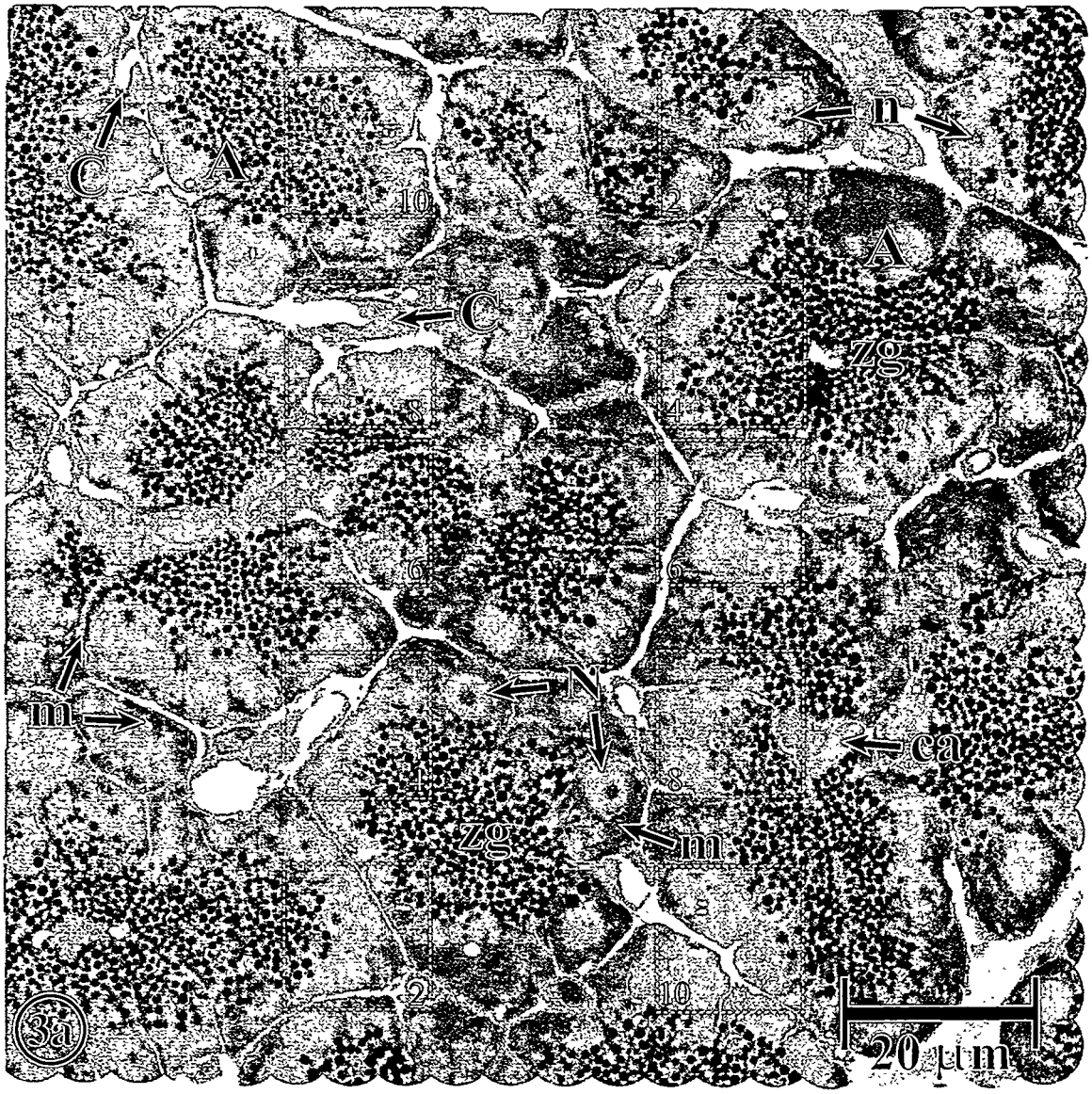


**Figure 8-3a**

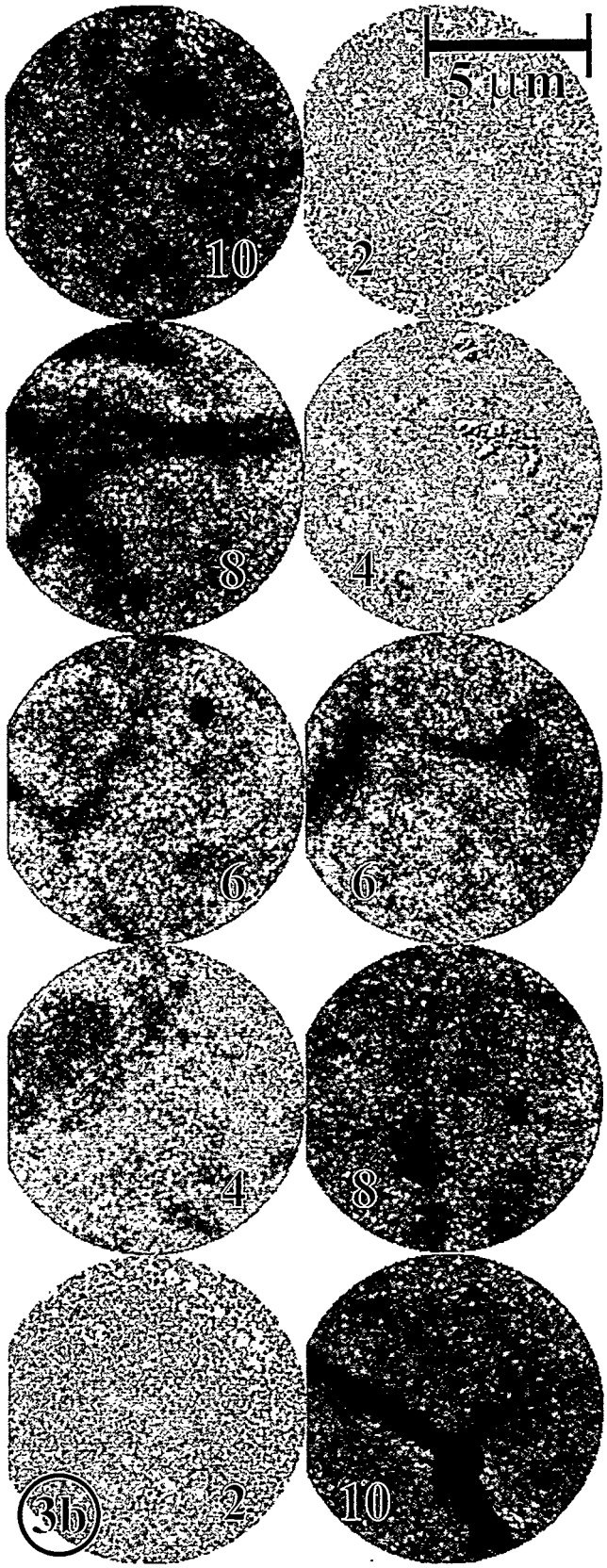


**Figure 8-3b**

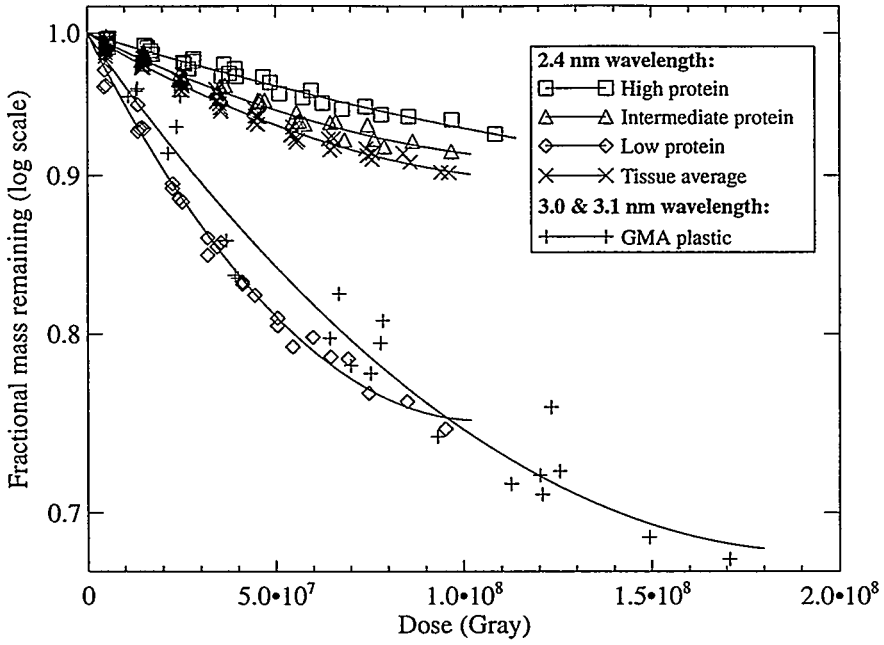
1.0
0.9
0.8
0.7
Fractional mass remaining (log scale)
0
5.0•10^7
1.0•10^8
1.5•10^8
2.0•10^8
Dose (Gray)
2.4 nm wavelength:
High protein
Intermediate protein
Low protein
Tissue average
3.0 & 3.1 nm wavelength:
GMA plastic

**Figure 8-4**

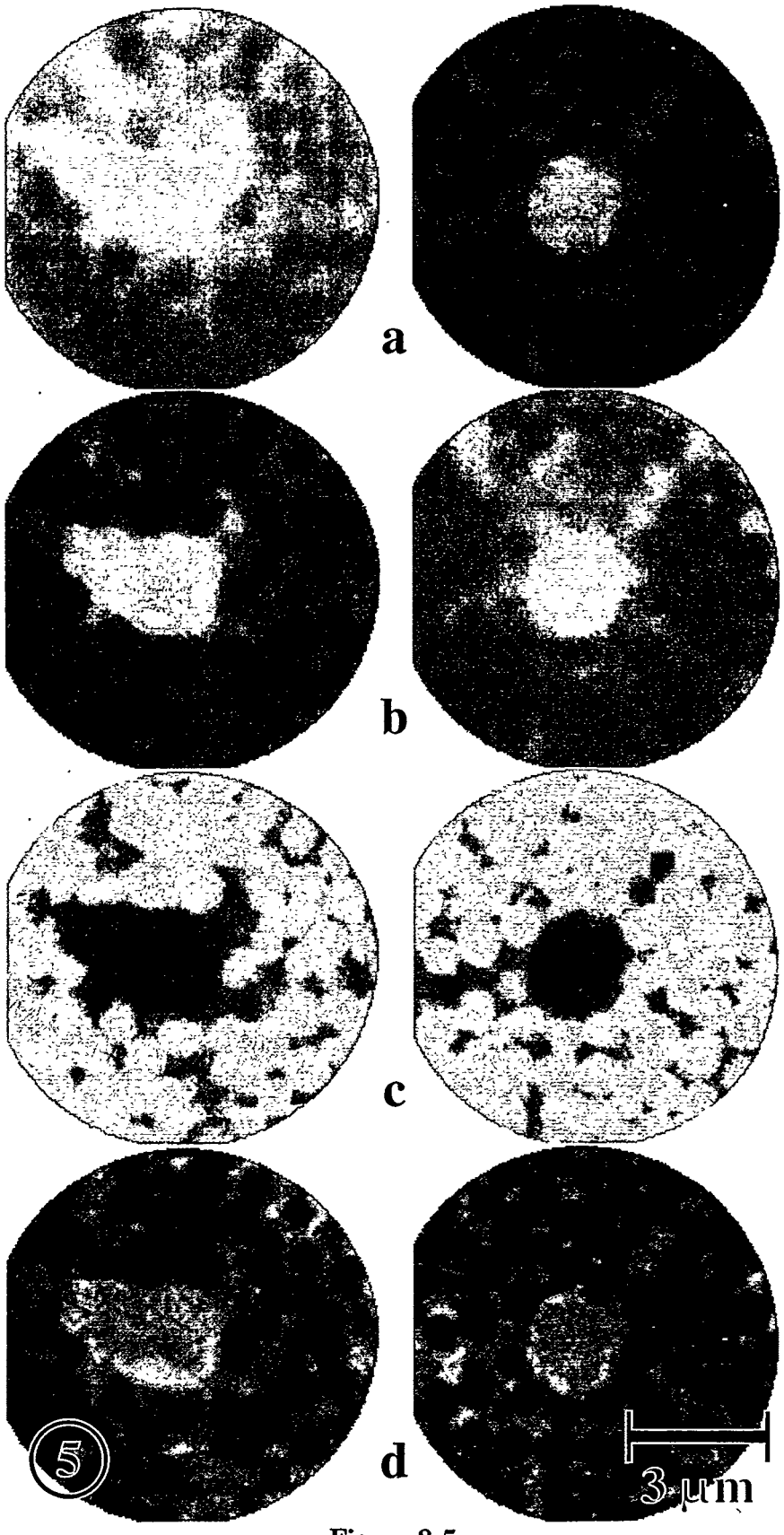


**Figure 8-5**

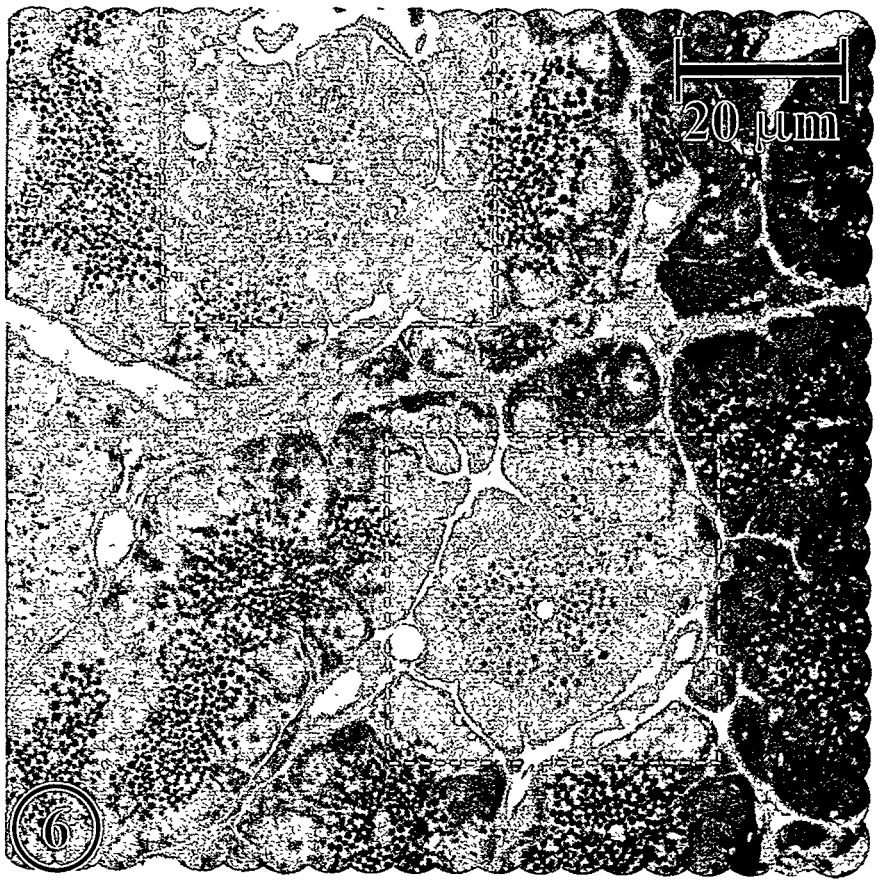


**Figure 8-6**

Distribution of protein and plastic

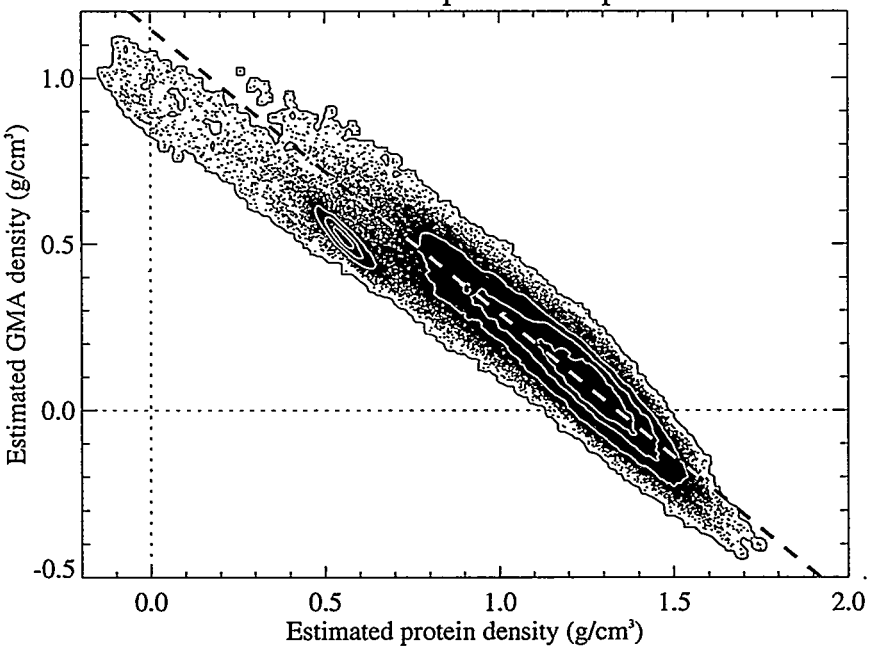


**Figure 8-7**

## References


Anderson, E.H. (1989) Fabrication technology and applications of zone plates. *X-Ray/EUV Optics for Astronomy and Microscopy, San Diego, California, August 7-11, 1989.* (ed. by R.B. Hoover), Proceedings SPIE Vol. 1160, pp. 1-10.

Anderson, E.H. & Kern, D. (1992) Nanofabrication of zone plates for x-ray microscopy. *X-Ray Microscopy III: Proceedings of the Third International Conference, London, September 3-7, 1990.* (ed. by A.G. Michette, G.R. Morrison, and C.J. Buckley), pp. 75-78. Springer-Verlag, Berlin.

Beaudoin, A.R., Grondin, G., Filion, M. & Lord, A. (1984) Secretagogues cause a preferential discharge of large size granules in rat pancreas. *Canadian Journal of Biochemistry and Cell Biology.* **62**, 1288-1292.

Beckstead, J.H., Halverson, P.S., Ries, C.A. & Bainton, D.F. (1981) Enzyme histochemistry and immunohistochemistry on biopsy specimens of pathologic human bone marrow. *Blood.* **57**, 1088-1098.

Bennett, H.S., Wyrick, A.D., Lee, S.W. & McNeil, J.H., Jr. (1976) Science and art in preparing tissues embedded in plastic for light microscopy, with special reference to glycol methacrylate, glass knives and simple stains. *Stain Technology.* **51**, 71-97.

Brinn, N.T. & Pickett, J.P. (1979) Glycol methacrylate for routine, special stains, histochemistry, enzyme histochemistry and immunohistochemistry: a simplified cold method for surgical biopsy tissue. *Journal of Histotechnology.* **2**, 125-130.

Buckley, C.J., Khaleque, N.I., Bellamy, S.J., Robins, M. & Zhang, X. (1998) Mapping the organic and inorganic components of bone. *X-Ray Microscopy and Spectromicroscopy: Proceedings of the Fifth International Conference, Würzburg, August 19-23, 1996.* (ed. by J. Thieme, G. Schmahl, D. Rudolph, and E. Umbach), pp. II-47 to II-55. Springer, Berlin.

Chen, C.T., Ma, Y. & Sette, F. (1989) K-shell photoabsorption of the $N_2$ molecule. *Physical Review A (General Physics).* **40**, 6737-6740.

Cole, M.B., Jr. & Sykes, S.M. (1974) Glycol methacrylate in light microscopy: a routine method for embedding and sectioning animal tissues. *Stain Technology.* **49**, 387-400.

Ermak, T.H. & Rothman, S.S. (1981) Zymogen granules of pancreas decrease in size in response to feeding. *Cell and Tissue Research.* **214**, 51-66.

Goncz, K.K., Behrsing, R. & Rothman, S.S. (1995) The protein content and morphogenesis of zymogen granules. *Cell and Tissue Research.* **280**, 519-530.

Hanstede, J.G. & Gerrits, P.O. (1983) The effects of embedding in water-soluble plastics on the final dimensions of liver sections. *Journal of Microscopy.* **131**, 79-86.

Heck, J.M., Attwood, D.T., Meyer-Ilse, W. & Anderson, E.H. (1999) Resolution determination in x-ray microscopy: an analysis of the effects of partial coherence and illumination spectrum. *Journal of X-Ray Science and Technology.* **8**, 95-104.

Helander, K.G. (1983) Thickness variations within individual paraffin and glycol methacrylate sections. *Journal of Microscopy.* **132**, 223-227.

Henke, B.L., Gullikson, E.M. & Davis, J.C. (1993) X-ray interactions: photoabsorption, scattering, transmission, and reflection at E=50-30000 eV, Z=1-92. *Atomic Data and Nuclear Data Tables.* **54**, 181-342.

Hitchcock, A.P. & Mancini, D.C. (1994) Bibliography and database of inner shell excitation spectra of gas phase atoms and molecules. *Journal of Electron Spectroscopy and Related Phenomena.* **67**, 1-132.

Hitchcock, A.P., Tyliszczak, T., Heng, Y.M., Cornelius, R., Brash, J.L. & Ade, H. (in press) X-ray spectromicroscopy studies of protein-polymer interactions. *X-Ray Microscopy: Proceedings of the VI International Conference on X-ray Microscopy, Berkeley, August 1-6, 1999.* (ed. by W. Meyer-Ilse, T. Warwick, and D.T. Attwood). American Institute of Physics, College Park.

Ho, J.J.L. & Rothman, S.S. (1983) Protein concentration in the pancreatic zymogen granule. *Biochimica et Biophysica Acta.* **755**, 457-466.

Irtel von Brenndorff, A., Moronne, M.M., Larabell, C., Selvin, P. & Meyer-Ilse, W. (1994) Soft x-ray stimulated high resolution luminescence microscopy. *X-Ray Microscopy IV: Proceedings of the Fourth International Conference, Chernogolovka, Russia, September 20-24, 1993.* (ed. by V.V. Aristov and A.I. Erko). Bogorodskii Pechatnik, Chernogolovka.

Ito, A., Shinohara, K., Nakano, H., Matsumura, T. & Kinoshita, K. (1996) Measurement of soft x-ray absorption spectra and elemental analysis in local regions of mammalian cells using an electronic zooming tube. *Journal of Microscopy.* **181**, 54-60.

Jacobsen, C.J. (1999) State University of New York, Stony Brook. Personal communication.

Kenney, J.M., Jacobsen, C., Kirz, J., Rarback, H., Cinotti, F., Thomlinson, W., Rosser, R. & Schidlovsky, G. (1985) Absorption microanalysis with a scanning soft x-ray microscope: mapping the distribution of calcium in bone. *Journal of Microscopy.* **138**, 321-328.

Khaleque, N.I. & Buckley, C.J. (1998) Image contrast in embedded specimens using NEXAFS spectroscopy. *X-Ray Microscopy and Spectromicroscopy: Proceedings of the Fifth International Conference, Würzburg, August 19-23, 1996.* (ed. by J. Thieme, G. Schmahl, D. Rudolph, and E. Umbach), pp. III-95 to III-98. Springer, Berlin.

Kirtley, S.M., Mullins, O.C., Chen, J., van Elp, J., George, S.J., Chen, C.T., O'Halloran, T. & Cramer, S.P. (1992) Nitrogen chemical structure in DNA and related molecules by X-ray absorption spectroscopy. *Biochimica et Biophysica Acta.* **1132**, 249-254.

Kirz, J., Jacobsen, C. & Howells, M. (1995) Soft x-ray microscopes and their biological applications. *Quarterly Reviews of Biophysics.* **28**, 33-130.

Larabell, C.A., Yager, D. & Meyer-Ilse, W. (in press) Localization of proteins and nucleic acids using soft x-ray microscopy. *X-Ray Microscopy: Proceedings of the VI*

*International Conference on X-ray Microscopy, Berkeley, August 1-6, 1999*. (ed. by W. Meyer-Ilse, T. Warwick, and D.T. Attwood). American Institute of Physics, College Park.

Loo, B.W., Jr., Meyer-Ilse, W. & Rothman, S.S. (2000) Automatic image acquisition, calibration, and montage assembly for biological x-ray microscopy. *Journal of Microscopy*. **197**, 185-201.

Loo, B.W., Jr., Parvin, B. & Rothman, S.S. (1996) Two- and three-dimensional segmentation for measurement of particles in the analysis of microscopic digital images of biological samples. *Three-Dimensional Microscopy: Image Acquisition and Processing III, San Jose, California, January 30 - February 1, 1996*. (ed. by C.J. Cogswell, G.S. Kino, and T. Wilson), Proceedings SPIE Vol. 2655, pp. 209-215.

Loo, B.W., Jr. & Rothman, S.S. (1995) High resolution microscopic imaging with x-rays: technology and application to the biological sciences. *Proceedings of WESCON'95, San Francisco, California, November 7-9, 1995*, pp. 668-672. IEEE.

Loo, B.W., Jr. & Rothman, S.S. (1997) High resolution x-ray microtomography of biological samples: requirements and strategies for satisfying them. *Proceedings of the Workshop on High Resolution Computed Microtomography, Ernest Orlando Lawrence Berkeley National Laboratory, University of California, August 12-13, 1996*. (ed. by E. Schlueter and F. Schlacter), pp. 223-262. U.S. Department of Energy.

Maser, J., Jacobsen, C., Kirz, J., Osanna, A., Spector, S., Wang, S. & Warnking, J. (1998) Development of a cryo scanning transmission x-ray microscope at the NSLS. *X-Ray Microscopy and Spectromicroscopy: Proceedings of the Fifth International Conference, Würzburg, August 19-23, 1996*. (ed. by J. Thieme, G. Schmahl, D. Rudolph, and E. Umbach), pp. I-35 to I-44. Springer.

Meyer-Ilse, W. (1999) Ernest Orlando Lawrence Berkeley National Laboratory. Personal communication.

Meyer-Ilse, W., Denbeaux, G., Johnson, L.E., Bates, W., Lucero, A. & Anderson, E. (in press) The high resolution x-ray microscope, XM-1. *X-Ray Microscopy: Proceedings of the VI International Conference on X-ray Microscopy, Berkeley, August 1-6, 1999.* (ed. by W. Meyer-Ilse, T. Warwick, and D.T. Attwood). American Institute of Physics, College Park.

Meyer-Ilse, W., Medecki, H., Brown, J.T., Heck, J.M., Anderson, E.H., Stead, A., Ford, T., Balhorn, R., Petersen, C., Magowan, C. & Attwood, D.T. (1998) X-ray microscopy in Berkeley. *X-Ray Microscopy and Spectromicroscopy: Proceedings of the Fifth International Conference, Würzburg, August 19-23, 1996.* (ed. by J. Thieme, G. Schmahl, D. Rudolph, and E. Umbach), pp. I-1 to I-12. Springer, Berlin.

Meyer-Ilse, W., Medecki, H., Jochum, L., Anderson, E., Attwood, D., Magowan, C., Balhorn, R., Moronne, M., Rudolph, D. & Schmahl, G. (1995) New high-resolution zone-plate microscope at Beamline 6.1 of the ALS. *Synchrotron Radiation News.* **8**, 29-33.

Moronne, M.M. (1999) Development of x-ray excitable luminescent probes for scanning x-ray microscopy. *Ultramicroscopy.* **77**, 23-36.

Niemann, B., Rudolph, D. & Schmahl, G. (1983) The Göttingen x-ray microscopes. *Nuclear Instruments and Methods.* **208**, 367-371.

Nyakatura, G., Meyer-Ilse, W., Guttmann, P., Niemann, B., Rudolph, D., Schmahl, G., Sarafis, V., Hertel, N., Uggerhøj, E., Skriver, E., Nørgaard, J.O.R. & Maunsbach, A.B. (1988) Investigations of biological specimens with the x-ray microscope at BESSY. *X-Ray Microscopy II: Proceedings of the Second International Symposium, Brookhaven, New York, August 31 - September 4, 1987.* (ed. by D. Sayre, M.R. Howells, J. Kirz, and H. Rarback), pp. 365-371. Springer-Verlag, Berlin.

Pearse, A.G.E. (1985) *Histochemistry: Theoretical and Applied.* Fourth edition. Churchill Livingstone, Edinburgh.

Rothman, S., Anderson, E., Attwood, D., Batson, P., Buckley, C., Goncz, K., Howells, M., Jacobsen, C., Kern, D., Kirz, J., Rarback, H., Rivers, M., Shu, D., Tackaberry, R. &

Turek, S. (1990) Soft x-ray microscopy in biology and medicine: status and prospects. *Physica Scripta*. **T31**, 18-22.

Rothman, S.S., Goncz, K.K. & Loo, B.W., Jr. (1992) Following protein transport with the high resolution x-ray microscope. *X-Ray Microscopy III: Proceedings of the Third International Conference, London, September 3-7, 1990*. (ed. by A.G. Michette, G.R. Morrison, and C.J. Buckley), pp. 373-383. Springer-Verlag, Berlin.

Schmahl, G., Rudolph, D., Niemann, B. & Christ, O. (1980) Zone-plate x-ray microscopy. *Quarterly Reviews of Biophysics*. **13**, 297-315.

Schneider, G. & Niemann, B. (1998) Cryo x-ray microscopy experiments with the x-ray microscope at BESSY. *X-Ray Microscopy and Spectromicroscopy: Proceedings of the Fifth International Conference, Würzburg, August 19-23, 1996*. (ed. by J. Thieme, G. Schmahl, D. Rudolph, and E. Umbach), pp. I-25 to I-34. Springer, Berlin.

Shinohara, K., Ito, A. & Kobayashi, K. (1998) Measurement of XANES spectra of biological molecules in the soft x-ray region. *X-Ray Microscopy and Spectromicroscopy: Proceedings of the Fifth International Conference, Würzburg, August 19-23, 1996*. (ed. by J. Thieme, G. Schmahl, D. Rudolph, and E. Umbach), pp. III-157 to III-161. Springer, Berlin.

Sicurello, P. (1999) University of California, Berkeley. Personal communication.

Sober, H.A., Editor (1968) *CRC Handbook of Biochemistry: Selected Data for Molecular Biology*. Chemical Rubber Company, Cleveland.

Wilhein, T., Rothweiler, D., Tusche, A., Scholze, F. & Meyer-Ilse, W. (1994) Thinned, back-illuminated CCDs for x-ray microscopy. *X-Ray Microscopy IV: Proceedings of the Fourth International Conference, Chernogolovka, Russia, September 20-24, 1993*. (ed. by V.V. Aristov and A.I. Erko), pp. 470-474. Bogorodskii Pechatnik, Chernogolovka.

Zhang, X., Balhorn, R., Mazrimas, J. & Kirz, J. (1996) Mapping and measuring DNA to protein ratios in mammalian sperm head by XANES imaging. *Journal of Structural Biology*. **116**, 335-344.

# Chapter 9. Quantitative characterization of the protein contents of the acinar cell of the exocrine pancreas by x-ray microscopy

## Introduction

The acinar cell of the exocrine pancreas, rich with intracellular structure, has been influential in the genesis of the modern perspective of how that structure is related to function (Palade, 1975). Among the methods used to study this cell, electron microscopy has been particularly critical, and has played the central role in identifying and characterizing the structures thought to participate in the cell's main activity, the production and transport of secretory proteins. Based on high resolution electron micrographs, mechanistic inferences have been drawn about how proteins are synthesized and transported within and out of the cell.

However, contrast in conventional forms of microscopy, including both traditional electron and visible light microscopies, is based primarily on the staining characteristics of the tissue rather than its underlying composition, most importantly in this case, it protein contents. Consequently it has not been possible directly to answer important questions about how protein is distributed in different parts of the cell *in situ*, even though such an understanding is necessary to ground models of secretion quantitatively.

We have developed a direct method for making quantitative estimates of protein density within various subcellular compartments in tissue sections, with a relatively new form of microscopy, transmission x-ray microscopy (Schmahl *et al.*, 1980; Rothman *et al.*, 1990; Kirz *et al.*, 1995). The high contrast of this imaging modality is provided by the natural constituents of cells and tissues, in particular its proteins, and hence allows a

quantitative estimation of them. Because of this, along with the high resolution of the method, intermediate between electron and visible light microscopies, the x-ray microscope provides a unique view of biological ultrastructure that is complementary to those provided by these conventional forms of microscopy. To make effective use of this tool for quantitative measurements, we have developed a compatible and convenient sample preparation method, as well as a number of automated digital imaging methods for the acquisition and analysis of volumes of data large enough to obtain meaningful population statistics (Loo *et al.*, 1996; Loo *et al.*, 2000; Loo *et al.*, in press).

We present below both a pictorial survey of the structure and ultrastructure of this tissue as revealed by x-ray microscopy, from high-level tissue architecture to the major intracellular organelles of the acinar cell, and the results of direct measurements of the protein densities of these structures *in situ*. We have focused particular attention on the pancreatic secretion or zymogen granule, and have been able to measure the size and protein density, as well as the spatial distribution within the tissue, of tens of thousands of individual zymogen granules.

## Methods

*Sample preparation:*

We studied pancreatic tissue from male Sprague-Dawley rats. Tissue from seven animals was prepared for viewing in a soft x-ray microscope after the method of Loo *et al.* (in press). Animals were fasted for 18 to 22 hours to maximize the number of zymogen granules present in the cell, and then were anesthetized, sacrificed, the pancreas removed, and small pieces of pancreatic tissue fixed in glutaraldehyde and

paraformaldehyde. The tissue was then embedded in a glycol methacrylate based medium and sectioned. Tissue sections prepared in this way display high contrast, based on the sample's nitrogen content, and robust radiation tolerance in the x-ray microscope (Loo *et al.*, in press).

*Image acquisition:*

All x-ray imaging was done in a transmission soft x-ray microscope, called XM-1 (Meyer-Ilse *et al.*, in press), at the Advanced Light Source (ALS), a high-brightness synchrotron radiation facility at Lawrence Berkeley National Laboratory (LBNL). As described above, this imaging modality was chosen because of its potential to determine the spatial distribution of protein density quantitatively and at high resolution within the tissue.

A number of factors allowed the use of this particular instrument to realize this potential in practice. First, the optical layout of the microscope is such that the sample itself is in air at normal atmospheric pressure, and the x-ray transparent windows that isolate the optics in vacuum can be positioned close to the sample to minimize the air path that the x-rays must traverse. This permits the routine use of an x-ray wavelength (2.4 nm), that would otherwise be absorbed by the nitrogen in air, to probe nitrogen containing molecules in the sample. Second, we calibrated the microscope to compensate for a number of instrument related artifacts, and thus produce photometrically accurate maps of sample transmissivity (Loo *et al.*, 2000). Third, the x-ray microscope sample stage is indexed to a high degree of accuracy to a corresponding sample stage in a visible light microscope, allowing target area selection and focussing to be done entirely in the

VLM before transferring the sample to the XM. We also developed an automated system for acquiring and assembling many adjacent image fields into a large-field montage to extend the field of view of the microscope (Loo *et al.*, 2000). Together, these made it very convenient to select and image large numbers of samples to gather adequate statistics for this study.

*Automated image analysis:*

Having very large data sets does not of itself lead to useful results. Also required is the ability to analyze the data. Particularly with respect to the study of zymogen granules, a means was needed of identifying, measuring, and compiling statistics on the very large number of objects contained in the images that were acquired, and to do so reliably, accurately, and consistently. While a human operator excels at object recognition when the amount of data is relatively small, a machine performs much more uniformly on highly repetitive tasks. We developed an automatic image segmentation algorithm based on the Hough transform to identify and catalogue roughly round objects in images, and tested its performance on digital image phantoms as well as actual microscope images of pancreatic tissue (Loo *et al.*, 1996). In addition zymogen granules in a set of x-ray micrographs of similarly prepared tissue were manually segmented as a standard against which the automatic method could be calibrated. The sensitivity and specificity of the segmentation algorithm for zymogen granules were both found to be greater than 85% compared to this standard. Furthermore, the non-granule features that were misidentified as granules were similarly distributed in size and density to correctly identified granules, so that including them did not introduce significant errors into the population statistics.

The segmentation algorithm was applied to the images acquired in this study to compile the population statistics on zymogen granules presented below (see Figure 9-9a).

*Calculation of sample density:*

Protein and nucleic acid accounts for about 70% of the dry mass of mammalian cells, and nearly all of their nitrogen content (Alberts *et al.*, 1989). At the x-ray wavelength used, 2.4 nm, absorption by nitrogen predominates in determining the contrast between tissue and the plastic embedding medium, and thus the optical density of the sample reflects its protein and nucleic acid content. The source of the nitrogen, whether attributable to protein or nucleic acid, is not distinguishable by the method used in this study. However, protein is by far the larger component of the two (nearly 20% of cell mass as compared to about 1%), and hereafter we use the term "protein density" when referring to the density of the sample's nitrogen containing constituents.

The tissue was modeled as consisting of two components: the protein and the plastic embedding medium. Previously, we used dual wavelength imaging on either side of the nitrogen K-shell absorption edge to determine the density distribution of these two materials in a limited number of samples (Loo *et al.*, in press). The relationship of protein density to plastic density was found to follow a linear function with negative slope. Knowing this slope permits the use of a relatively simple expression to calculate the protein density on a pixel by pixel basis using only a single wavelength for imaging:

$$\rho_{protein} = \frac{OD}{(\mu_{protein} + b \cdot \mu_{plastic}) \cdot t} \qquad (1)$$

where $\rho_{protein}$ is the calculated protein density, $OD$ is the measured optical density, $\mu_{protein}$ and $\mu_{plastic}$ are the mass dependent absorption coefficients for the respective materials at the imaging wavelength, $b$ is the slope of the linear function between protein and plastic densities, and $t$ is the path length through tissue that the x-rays must traverse, or the thickness of the section.

To use this formula a number of factors required correction. Equation 1 assumes that the optical density is calculated as minus the logarithm of the ratio of transmission through tissue to the transmission through a layer of pure plastic embedding medium of the same thickness. When acquiring the images, each image of tissue was normalized to transmission through an area in the same section that contained only the plastic embedding medium presumably having the same thickness. However from the calculated optical densities it became apparent that the assumption of equal thickness did not hold in many cases. Often, tissue containing areas were thinner and consequently transmission through them was too high, yielding zero or negative apparent densities in regions that clearly contained sample material. In addition, previous measurements indicated that the rate of mass loss due to radiation was substantially higher in pure plastic areas than in tissue containing areas (Loo *et al.*, in press). Therefore simply to normalize each image to transmission through empty appearing areas within its own field of view did not provide a reliable means of correction. Finally, to obtain volumetric rather than areal density, section thickness had to be known. At the time of this study it was only possible to obtain independent thickness measurements on a few sections, and those measurements indicated that section thickness not only was significantly different from the nominal

value indicated by the microtome setting, but varied substantially between sections (Loo *et al.*, in press).

We dealt with these uncertainties by the use of multiple internal standards within individual images. First, an image of a large area of a section for which a thickness measurement was available and that appeared to be properly normalized was identified: *viz.*, one that had close to unit transmissivity in areas devoid of tissue compared to the background region in pure plastic, and for which the calculated density values for zymogen granules were consistent with our previously calibrated measurements. In other words, for such an image, Equation 1 could be applied to calculate protein densities without any special assumptions. As such, it was used as the reference against which to calibrate other images. To do this, the assumption was made that the ratio of average densities between various components of the tissue was consistent between samples. Specifically, the ratio between the apparent density of zymogen granules, regions in the nuclear background (containing euchromatin), and regions in cytoplasm (occupied by rough endoplasmic reticulum) were calculated and assumed similar to their ratios (granule to nucleus, granule to cytoplasm, cytoplasm to nucleus) in the reference image. For the zymogen granules, we used the average density of the densest quartile of granules, reasoning that these peak values would more likely be consistent between samples since they approached the physical limits of protein density (Loo *et al.*, in press). Since the logarithmic function translates errors in normalization to offsets in optical density, the correction was applied by adding an appropriate offset to the optical density map in each image such that the differences between these ratios and those in the reference image were minimized. After such a correction, the ratio of sample to reference

optical densities would yield the ratio of their respective section thicknesses, completing the information required to calculate volumetric density. A number of observations supported the assumptions underlying this approach. First, in any of the images, the offset that minimized the difference in one of the ratios tended to be similar to the offset that minimized any of the differences. Second, the standard deviation about the derived mean densities for the various components was small (see Results below). And finally, the derived section thicknesses were roughly correlated with measured thickness in areas of pure plastic in sections for which those measurements were available.

Consistent with our previously reported measurements, the density values determined here were much higher than those measured in samples that were not subjected to the same preparative procedures. Shrinkage of the sample during preparation is sufficient to account for a large part of the difference (Loo *et al.*, in press). The degree of sample shrinkage was estimated by comparing the average diameter of freshly isolated zymogen granules, 1.08 μm (Goncz *et al.*, 1995), to that of the samples used in this study, 0.77 μm (see Results). Because of the cubic relationship between diameter and volume, this apparently small change in diameter translates to volume shrinkage of a factor of about 2.8. In the Results, measurements of protein density (summarized in Table 1) are expressed in terms of the values expected in fresh tissue by dividing the raw values by this factor. One independent assessment of the accuracy of our measurements is in the protein density value of red blood cells. The normal range of hemoglobin concentration in human red blood cells is known to be 0.31 to 0.36 g/cm$^3$, a reasonable estimate of overall protein density in these cells since hemoglobin is the predominant constituent by far. The shrinkage corrected protein density in rat red blood cells based on the x-ray

measurements in this study falls in this range at 0.34 g/cm$^3$. This strengthens our confidence that our estimates of protein density are reasonably accurate despite a number of systematic uncertainties.

## Results

*Overall organization of exocrine pancreatic tissue:*

Figures 9-1 to 9-3 demonstrate the microscopic appearance of exocrine pancreatic tissue as viewed by three different forms of microscopy. The basic cellular unit of the tissue is the acinar cell that stores and secretes the enzymes used in food digestion. These epithelial cells are arranged in units called acini. Each acinus consists of a single layer of acinar cells in a globular or tubular pattern surrounding a central duct, which conveys the secretions into a branching network of ducts that converge into the main duct leading to the intestinal system. The cells forming the intercalated duct extend to the center of the acinus, where they are called centroacinar cells. Also present are supporting structures such as capillary blood vessels containing red blood cells.

Figure 9-1a is a visible light micrograph of pancreatic tissue, plastic embedded, stained, and imaged in transmitted light mode, that demonstrates all of the above described architectural features. Also demonstrated are intracellular structures of the acinar cell, most prominently the nucleus, nucleolus, and numerous zymogen granules filled with secretory enzymes. The acinar cell has a well defined polarity, with zymogen granules aggregating at its apical end near the duct, and the nucleus residing in the relatively granule-free basal region. In hematoxylin and eosin stained tissue viewed by confocal fluorescence visible light microscopy (Figure 9-1b), the zymogen granules

fluoresce intensely, as do the relatively long, rod-shaped mitochondria distributed throughout the cell, otherwise difficult to resolve by conventional visible light microscopy.

Figure 9-2 is a transmission electron micrograph of a pancreatic acinus. The high resolution of the electron microscope as well as heavy metal staining and thin sectioning preparative techniques allow details of the intracellular organelles, particularly their membranous components, to be visualized. Several of the organelles, in particular the nucleus, mitochondrion, and zymogen granule, are now seen to be membrane bound structures. The mitochondria also contain elaborate membranous folds called cristae. Additional structures become discernable as well. The Golgi apparatus appears in section to consist of membranous stacks enclosing cisternae with low electron density. Often spatially associated with the Golgi apparatus are round vesicles of low electron density somewhat larger than zymogen granules, the so-called condensing vacuoles thought to be immature zymogen granules. Essentially the remainder of the space in the cell is occupied by the rough endoplasmic reticulum, appearing in section as closely-spaced, parallel membranous stacks enclosing cisternae of low electron density, and studded on their extracisternal surface with particulate ribosomes. The endoplasmic reticulum tends to be arranged concentrically around the nucleus in the basal region of the cell. These round out the major organelles of the pancreatic acinar cell directly visible by microscopy.

Figures 9-3a-c are x-ray micrographs of pancreatic tissue sections prepared as described above. They demonstrate all of the above mentioned structures at a resolution intermediate between those of the visible light and electron microscopes. That resolution

of about 43 nm (Heck *et al.*, 1999), in addition to the section thickness (substantially thicker than that used in electron microscopy at around 0.6 μm), does not permit direct visualization of membranes as in an electron microscope. However, there are features in these images that based on their location and appearance we hypothesize to correspond to endoplasmic reticulum and Golgi apparatus.

The most distinguishing attribute of the x-ray micrographs is that the contrast is directly related to the protein and nucleic acid content of the tissue structures without stains, since imaging with the x-ray wavelength that was used (2.4 nm) is selective for nitrogen containing compounds. Therefore it has been possible, perhaps for the first time, to make quantitative density measurements of cellular organelles *in situ*. In the following sections, we describe the x-ray microscopic appearance of and report density measurements on the major intracellular organelles of the pancreatic acinar cell, namely: nucleus and nucleolus, mitochondrion, endoplasmic reticulum, Golgi apparatus, and zymogen granule. The density results are summarized in Table 1.

*Nucleus and nucleolus:*

The visual appearance of nuclei in x-ray micrographs as seen in Figure 9-4 is qualitatively very similar to that in visible light and electron micrographs. In cross-section they appear as round structures approximately 5 μm in diameter. Often, acinar cells have two nuclei (Figure 9-4e,f). The nucleus contains material that in VLM and EM (see Figures 9-1a and 9-2) stains with roughly two intensities thought to represent two different states of the nuclear chromatin: darker staining heterochromatin in an inactive condensed state, and lighter staining euchromatin in an active extended state. The

heterochromatin tends to be associated with the edge of the nuclear profile (marginal chromatin) and nucleoli (nucleolar associated chromatin), as well as to form discrete bodies (karyosomes). Similarly, in the x-ray images a more absorbing material, presumably the heterochromatin, is found at the periphery of the nuclei as well as in typically one to three bodies within the nuclei, presumably the nucleolar associated heterochromatin. The remainder of the nuclear space is filled with material, the euchromatin, that is less dense than both the heterochromatin and the material in the surrounding cytoplasmic space occupied by endoplasmic reticulum. Measurements show the euchromatin to have an average corrected density of 0.16 g/cm$^3$, while the nucleoli and associated heterochromatin are about twice as dense with an average density of 0.34 g/cm$^3$.

Exocrine pancreatic tissue appears to have very low mitotic activity. In only one image (Figure 9-4g) have we observed a cell with what appears to be two nuclei, one of which is quiescent and the other of which contains the condensed chromosomes of late prophase. This observation raises the interesting question of the end result of such a division, given that we have never observed cells with more than two nuclei.

*Mitochondrion:*

In x-ray micrographs, mitochondria appear as rod-like structures intermediate in density between the surrounding cytoplasmic space and the dense zymogen granules. Compared with EM, their internal membranous structure is not easily distinguishable because of the lower resolution and greater section thickness. They are typically about 0.3 to 0.4 μm wide and up to several micrometers long, often taking a serpentine path in

and out of the plane of section. Figure 9-5 demonstrates a few of the varied patterns they form within the cell. Frequently, mitochondria lie at borders between cells (Figures 9-5a,b). Occasionally, they appear to form parallel arrays (Figure 9-5d) or clusters (Figure 9-5e). They are also scattered throughout the cell, primarily in the basal region but sometimes at the apical end as well. They have an average density of 0.38 g/cm$^3$, slightly higher than that of the nucleolar regions.

*Endoplasmic reticulum and Golgi apparatus:*

As discussed, the resolution of the x-ray microscope at the time of this study was about 43 nm, whereas the thickness of biological membranes is approximately 5 nm. Thus one would not expect to be able to resolve the individual membranes of structures such as the endoplasmic reticulum (ER) and Golgi apparatus. However, in EM images the cisternal spaces within these organelles often appear several or more times as wide as the membranes themselves, and appear less electron dense than their surroundings. We might therefore expect to be able to visualize these spaces in XM images if they are properly oriented with respect to the plane of sectioning. In fact, we have observed and describe below features we believe probably correspond to these structures.

Frequently in x-ray micrographs we have acquired, a pattern of fine linear lucencies clearly beyond the ability of VLM to resolve can be seen in the basolateral aspect of the cell (Figure 9-6a-d). They typically appear to be arranged concentrically around the nucleus. More often, there is either a subtler reticular appearance (Figure 9-6e,f) or a roughly uniform appearance to the basolateral cytoplasm. At times the lucent gaps are wider (Figure 9-6g), and occasionally certain cells, perhaps damaged by hypoxia or the

trauma of preparation, have an obviously striated pattern of density in that region (Figure 9-6h). Given their appearance and their location in regions of the cell known from EM to be nearly completely occupied by rough endoplasmic reticulum, it is likely these lucencies represent the cisternae of the ER, visible because they happen to be oriented perpendicular to the plane of sectioning. The average density over the ER containing region of the cell is 0.24 $g/cm^3$. As a reference, the average density in the cytoplasm of the very uniform appearing red blood cells is substantially higher at 0.34 $g/cm^3$, the same as that of the nucleolar region in acinar cells. The relatively lower density in the basal cytoplasm of the acinar cell may be a reflection of the low density of the ER cisternal space.

Figure 9-7 contains several examples of roughly round areas of heterogeneous density that is lower than that of the surrounding cytoplasm, situated either adjacent to or within the zymogen granule occupied part of the cell and near the nucleus. Often there are also a few zymogen granules in the middle of the area of decreased density. Again, based on comparisons with EM images, we believe these areas correspond to regions of Golgi apparatus, and perhaps some associated condensing vacuoles. This suggests that like the ER cisternae, Golgi cisternae also have a relatively low protein density. Also, the relatively discrete appearance of these areas gives the impression that the Golgi and condensing vacuoles, rather than being completely separate entities, perhaps form a functional unit or complex.

| Structure | Measured average density ($g/cm^3$) | Density corrected for shrinkage (Correction factor: 2.78) |
|---|---|---|
| Nuclear euchromatin | 0.46 ± 0.02 | 0.16 ± 0.005 |
| Cytoplasm (region occupied by rough endoplasmic reticulum) | 0.66 ± 0.04 | 0.24 ± 0.01 |
| Nucleolus and associated heterochromatin | 0.94 | 0.34 |
| Red blood cell cytoplasm | 0.94 | 0.34 |
| Mitochondrion | 1.05 | 0.38 |
| Zymogen granule | 1.15 ± 0.20 | 0.41 ± 0.07 |
| Zymogen granule (densest quartile) | 1.37 ± 0.14 | 0.49 ± 0.05 |

**Table 9-1**

Average densities (with and without correction for shrinkage) of various tissue structures, in order of density. For structures on which measurements were made in every image, the standard deviation is given.

*Zymogen granules:*

Our greatest emphasis in this study has been on the measurement and analysis of zymogen granules and their population statistics, and the implications these might have for our understanding of secretory mechanisms. The zymogen granule is visually one of the most distinctive organelles seen in any of the imaging modalities because of its high density and staining intensity. Zymogen granules consistently have a nearly circular profile, with an appreciable range of sizes about their mean diameter. In EM images, the granules appear to have a predominantly uniform density, both within individual granules and between different ones. The majority of granules in XM similarly appear to have a relatively uniform internal density. Frequently however, granules have internal variations of density, suggesting that the intensity of staining in EM may not perfectly reflect the underlying protein density. Furthermore, there is a noticeable range of densities between granules as well. Below we report the population characteristics of zymogen granules, specifically with respect to the parameters diameter and density. The automated image

segmentation methods we developed made possible the compilation of these statistics on a large number of images and zymogen granules.

We analyzed 32 images, 24 of which covered an area of about 100 by 100 μm (enough to include several acini), and 8 of which covered an area of about 36 by 36 μm (centered on a single acinus). Over 75,000 granules in all were encompassed in the imaged areas. Figure 9-8a is a histogram of zymogen granule diameters. The distributions of diameters in the individual images are plotted along with the composite distribution, and are similar in shape to the composite with a mild skew to the right. The differences in height between the distributions for individual images reflect the different image sizes and therefore different numbers of granules encompassed. The average diameter is 0.74 μm with a standard deviation of 0.15 μm. This is very similar to EM measurements of zymogen granule diameter on much smaller numbers of granules, which have produced average values of 0.73 to 0.85 μm (Ermak & Rothman, 1981; Beaudoin *et al.*, 1984). Figure 9-8b is a histogram of the protein density of the zymogen granules. Again, the distributions for the individual images are similar in shape to the composite distribution, having a moderate skew to the left. The average protein density within granules is 0.41 $g/cm^3$ with a standard deviation of 0.07 $g/cm^3$.

We note that this analysis is necessarily affected by the thickness of the sections. The nominal section thickness based on the microtome setting was 0.75 μm, and our measurements place the average thickness at about 0.6 μm (Loo *et al.*, in press), or thinner than the diameter of most of the zymogen granules. As a result, neither the apparent diameter nor the apparent density of any individual granule as judged by its

sectioned appearance is likely to be an accurate measure of its actual diameter or density. One way of assessing the magnitude of sectioning artifact is through the relationship between the apparent diameter and apparent mass of the granules. When there is no sectioning artifact, the granule mass should be proportional to its volume, a cubic function of the diameter. In the limit of infinitely thin sections, the apparent mass is proportional to the area of the section, a square function of the apparent diameter. Figure 9-8c is a log-log plot of apparent mass versus apparent diameter of the zymogen granules. Such a plot should yield a linear function whose slope is equal to the exponent of the relationship between the two parameters. Whether the power is closer to two or three indicates the degree of sectioning artifact that is present. The slope of the regression line through the data is about 2.2, indicating that the effect of sectioning is substantial as might be expected given the small section thickness relative to the mean granule diameter.

Granules that are sufficiently large or sufficiently well centered in the section such that they occupy the full thickness of the section will appear to have their actual density. Granules that only partially fill the thickness of the section will have a lower apparent density. This artifact of sectioning is consistent with the observed tail in the density distribution that extends towards lower densities. A corollary to this is that granules with a higher apparent density are more likely to have been sectioned near their equator. A similar tail to the left might be expected in the distribution of apparent diameters, though it is not readily evident in the data. This might be attributable to a compensatory decrease in the ability to detect partial granules produced by glancing cuts that result in both very small apparent diameter and very low apparent density.

As mentioned above, we might expect granules with a higher apparent density to be more likely to have apparent diameters that reflect their actual diameters. The distribution of apparent diameters of granules above the 75$^{th}$ percentile in apparent density is also plotted in Figure 9-8a. The skew to the right is milder but still present. The average diameter of this group is larger as expected at 0.79 μm, and the standard deviation is unchanged at 0.15 μm. Since this selection criterion might be somewhat biased against the smallest granules, especially those with diameters smaller than the section thickness, we would expect the true average diameter of zymogen granules to lie between 0.74 and 0.79 μm, perhaps closer to the latter. For the purpose of shrinkage correction (see Methods), we used an intermediate value of 0.77 μm.

*Spatial distribution of zymogen granules:*

The ability to process large data sets automatically enables some interesting analyses that would not otherwise be possible. As an example, when reviewing many images of pancreatic acini, we developed the subjective impression that larger granules were more frequently found farther from the central ductal space. We tested the hypothesis that zymogen granule size is positively correlated with the distance from the central duct by analyzing the granules in 23 acini that appeared to be sectioned transversely, or in a plane perpendicular to the axis of the duct. To be selected for inclusion, each acinus had to have a clearly identifiable and approximately centrally located ductal space, with the acinar cells arranged roughly symmetrically about it. Figure 9-9 shows two such acini. The borders of the acini and their duct lumens were manually outlined and stored, and the distances of the enclosed granules from the ducts automatically tabulated.

The sections of the 23 acini contained a total of 6,069 zymogen granules. The apparent diameter of the granules is plotted against their distance from the duct in Figure 9-10a. The correlation between the two parameters is visually somewhat unimpressive at first, and their correlation coefficient is positive but weak at 0.11. However, calculation of the P-value reveals an extremely high statistical significance, as the probability of obtaining a correlation of this magnitude purely by chance when there is no underlying relationship is only about $10^{-16}$. Also plotted in the figure are the averages of distance and diameter of granules within each of the four quartiles of distance from the duct, as well as the upper and lower quartile markers for diameter in each of these four groups. This makes the relationship a bit more apparent, as the average diameter and quartile markers consistently increase from one quartile of distance to the next. Furthermore, when looking at the correlation coefficients between granule size and distance in each of the individual acini, 20 out of 23 are positive, and 3 are negative. Under the null hypothesis (in which positive and negative values would be equally likely) the P-value is only $2.4\times10^{-4}$. Fourteen of the 20 positive individual correlations are statistically significant (P-value less than 0.05), as is one of the 3 negative ones.

A number of factors could obscure the existence or magnitude of a true underlying correlation. One example would be the sectioning artifact, since many of the apparent diameters do not accurately represent the actual ones. We repeated the analysis on the subset of 1,518 zymogen granules in the highest quartile of apparent density from each acinus. As noted above, the part of the population with the highest apparent density should be enriched in granules that are sectioned closer to their equator, and therefore have a more accurate size measurement. The result is plotted in Figure 9-10b. While there

is still a large spread of the points, the trend is substantially more noticeable. Plotting the averages in each quartile of distance again demonstrates the same pattern but with larger increases in average diameter between quartiles. Correspondingly, the correlation coefficient has now more than doubled to 0.23, with a P-value smaller than $10^{-16}$ (the double precision floating point accuracy limit of the computer). Among the correlation coefficients for granules in the individual acini, there are still 20 positive and 3 negative, but 19 of the 23 have increased in positivity (consistent with the trend in the pooled data). The reduced population size however has decreased the number of statistically significant individual positive correlations to 11, and negative to none. Furthermore, if we select only granules at the $90^{th}$ percentile or above in apparent density, the overall correlation coefficient increases again to 0.28, and while the statistical significance is slightly worse because of the reduced population size, the P-value is still extremely low at $4\times10^{-12}$. These results support the hypothesis that a stronger correlation than what is observed may be masked by artifacts such as that introduced by sectioning.

Figure 9-9c is another graphical illustration of the relationship between diameter and distance from the duct. In the two acini, granules in the upper quartile of apparent density are identified by a mark. A dotted line marks the median distance of these granules from the duct lumen. Among these granules, those in the quartile with the largest diameters in each acinus are circled. Even though half of the marked granules fall within the dotted path, only 12 out of the 33 circled granules in one acinus and 4 out of 24 in the other are at the median distance or less. Thus in this image, over two and a half times as many of the largest granules are outside the line as inside it, demonstrating the propensity of larger

granules to be farther from the duct. Again, the same trend can be found in the plots of Figure 9-10.

Other factors that could potentially hide a true correlation are any differences from one acinus to another. The 23 acini in the analysis were selected from 15 images of 12 different tissue sections from 7 different animals, making possible many different sources of variability between acini. Differences in section thickness would be just one example. If such differences were degrading the correlation, we would expect the correlations for individual acini to be higher than that of the pooled data. When all granules are included, 16 of the 23 individual correlations are greater than the pooled correlation, barely allowing the rejection of the null hypothesis (under which individual correlations are equally likely to be above or below the pooled one) with a P-value of 0.047. When only granules in the top quartile of density are included, there is an essentially even split with 11 out of 23 individual correlations greater than the pooled value. Thus any effect of differences between acini on the overall correlation would appear to be relatively small.

Our calculations of the statistical significance of the observed correlations are based on the approximation that under the null hypothesis, the correlation coefficient is distributed normally about zero, with a standard deviation of one over the square root of the sample size. This approximation tends to hold true when the sample size is large, and the distributions of the individual parameters being compared have tails that taper sufficiently quickly (Press *et al.*, 1992). To validate this assumption for our data, we performed a Monte Carlo type simulation. The set of measured values for zymogen granule diameter and distance from the duct were reordered randomly to destroy any underlying correlation between the parameters. The correlation coefficients were

calculated for 10,000 such random orderings. Their histogram, plotted in Figure 9-10c, indeed conforms closely to a normal distribution of the appropriate width, and the maximum magnitude of the simulated coefficients was 0.051, nearly four standard deviations from the mean yet still substantially lower than the observed correlation. The result was similar even when repeated with a much smaller subset of the data, a population of 136 granules from a single acinus, again supporting the assumption of normality.

One point to note is that the seemingly mild increase in average zymogen granule diameter with distance from the duct belies a much more substantial change in the average volume because of the cubic relationship between these parameters. Of the granules represented in Figure 9-10b, those in the quartile closest to the duct have an average diameter of 0.74 μm, while those in the quartile farthest from the duct have an average diameter of 0.85 μm. This 15 percent increase in diameter translates to an impressive 51 percent increase in volume. Meanwhile, the average densities of these two groups are statistically indistinguishable, so this difference in volume represents a corresponding difference in the protein mass of the granules.

**Discussion**

One notable feature of the x-ray micrographs is how qualitatively similar they are at first glance to visible light and electron micrographs of the same tissue. Allowing for obvious differences in resolution between the methods, the major structures reviewed here were easily recognizable in the x-ray images because of their comparable appearance in the other modalities by which they were originally described. The finer

membranous structures such as endoplasmic reticulum and Golgi apparatus are increasingly well defined visually as one switches from visible light (where they are invisible), to x-ray, to electron microscopy.

The mechanism of contrast in x-ray microscopy, based on the underlying protein content of the tissue, is a key distinguishing feature of the method and makes it an important complement to the other forms of microscopy. We have demonstrated that it is possible to answer quantitative questions about the protein content in structures that have long been observed and described by these other methods without the ability to make such measurements. Just as the classic visual characterization of the cellular protein synthesis and transport machinery has contributed greatly to current models of these processes, the new quantitative information should also have important implications for evaluating mechanistic hypotheses.

The classical model of protein transport (Palade, 1975) holds that as soon as protein molecules have begun to be synthesized by the ribosomal complex on the surface of the endoplasmic reticulum, they are sequestered into the cisternal space of the ER. From there they are transported to and processed by the Golgi apparatus, where they advance through its series of cisternae sequentially. They are then packaged into condensing vacuoles which mature into zymogen granules by a process of concentration. Ultimately they are secreted into the ductal system. Movement to and from each of these compartments is accomplished by vesicle transport.

In such a model, one might expect less mature zymogen granules, presumably originating from a more basal region of the cell, to increase in protein density, overall

protein content, or both as they mature and make their way towards the apex of the cell and the ductal space where they ultimately release their contents by exocytosis. Our findings run directly counter to this prediction. The zymogen granules farthest from the duct are about as dense as granules close to the duct, but contain substantially more protein due to their larger volume. This is also inconsistent with another study, based on electron microscopic measurements, that suggested that larger zymogen granules are preferentially discharged during secretion (Beaudoin *et al.*, 1984), since one would expect the granules closest to the duct, which we have found to be smaller, to be discharged first, at least according to the exocytosis model. Our results might however be consistent with an equilibrium type model proposed to explain non-parallel transport between different secretory enzymes stored within the granules (Rothman, 1975), in which the granule contents are transported along their concentration gradients across the granule and cell membranes.

Furthermore, the x-ray images of the structures that likely represent the cisternal spaces of endoplasmic reticulum and Golgi apparatus seem to validate the impression given by electron microscopy that these spaces have a lower protein density than their surroundings. This is somewhat counterintuitive since according to the traditional model, these spaces are supposed to conduct an enormous volume of protein traffic.

Our analysis so far has really only addressed a small number of the quantitative questions that might be answered even by the data we have already collected. In addition, to elucidate mechanisms of protein transport much promise lies in making quantitative measurements of protein distribution in a variety of physiological states, as we have done in the baseline fasted state of the acinar cell. We have already acquired similar data on

tissue after it has been hormonally stimulated to secrete, and will report the results of that analysis in another paper.

One weakness in this study that could be addressed in future experiments was the lack of accurate information about section thickness and how it varied within sections. It was this that required making the assumptions described above, albeit reasonable ones, in the calculation of protein density. While the absolute numerical values presented are impacted by these assumptions, relative comparisons between different cellular compartments can be made without qualification. In any case, as discussed, the values generated appear reasonable despite the uncertainties. We have begun to use atomic force microscopy to characterize more rigorously the thickness and its variation of sections prepared in this way.

## Figure captions

**Figure 9-1a**: Visible light micrograph of plastic embedded and stained pancreatic tissue, demonstrating acinar cells arranged in units called acini. Acinar cells have a distinct polarity, with dense protein containing zymogen granules (zg) near the apex of the cell adjacent to the central duct, and nuclei (N), containing nucleoli (n), at the base of the cell. Cells forming the intercalated duct (ID) extend to the center of the acinus, where they are called centroacinar cells (ca). A prominent blood vessel (BV) containing red blood cells is also seen. From Ross *et al.* (1989), Figure 17.15.

**Figure 9-1b**: High-resolution confocal visible light fluorescence micrograph of a pancreatic acinus, paraffin embedded and hematoxylin-eosin stained. Now the zymogen granules fluoresce intensely, as do the long, rod-shaped mitochondria (m) distributed throughout the cell, otherwise difficult to resolve by conventional visible light microscopy.

**Figure 9-2**: Transmission electron micrograph of a pancreatic acinus, epoxy embedded and thinly sectioned, and stained with heavy metals. The membranous structure of many of the organelles is now apparent. Regions of the cell that appear uniform in VLM are nearly completely occupied by the rough endoplasmic reticulum (rER), which has cisternal spaces of low electron density, and an extracisternal surface studded with dense, particulate ribosomes. The Golgi apparatus (G) appears in this view to consist of membranous stacks enclosing low density cisternal spaces, and tends to occupy a space within the zymogen granule containing portion of the cell near the nucleus. Condensing vacuoles (CV), thought to be precursors to zymogen

granules (Z), are often in close proximity to the Golgi apparatus. From Wheater *et al.* (1987), Figure 15.15.

**Figure 9-3a**: Transmission x-ray micrograph of a pancreatic acinus embedded in plastic. The high contrast is due primarily to the nitrogen content of the tissue in the absence of any stain. All of the structures seen in VLM and EM are readily recognizable in the XM image due to their similar appearance, though there are noticeable differences in resolution between the different imaging modes. The fine membranous structure, clearly visible in EM due to its higher resolution and thinner sections, is suggested in the XM image by fine linear lucencies, mainly in the basal cytoplasm, that probably represent the cisternae of the endoplasmic reticulum (ER). Also apparent are roughly round areas of heterogeneous low density similar to the EM appearance of the Golgi apparatus (G). Several more examples of both follow. The nucleus of a centroacinar cell (ca) is seen in the lumen of the central duct (L). A capillary (C) contains a red blood cell (r).

**Figure 9-3b**: XM image of a pancreatic acinus surrounding an intercalated duct. Several nuclei of ductal cells are apparent (ID).

**Figure 9-3c**: A large field XM micrograph of an area containing several acini, demonstrating the overall organization of the tissue. This montage consists of 400 individual subimages spanning an area approximately 100 by 100 μm.

**Figure 9-4**: XM appearance of nuclei of pancreatic acinar cells. The nuclei contain material of two different densities, the lower density euchromatin consisting of active extended chromatin, and the denser heterochromatin consisting of inactive condensed

chromatin often found at the margin of the nucleus and associated with the nucleolus. Often these cells are binucleated (**e-g**). Figure **9-4f** also demonstrates a pattern of concentric linear lucencies surrounding the nucleus (arrows) probably representing the cisternae of the ER (see Figure **9-6**). Figure **9-4g** shows a rare nuclear division. The nucleus on the left appears to have the condensed chromosomes of late prophase of mitosis.

**Figure 9-5**: XM appearance of mitochondria. These long rod-shaped organelles frequently align along borders between cells (arrows, **a-b**). Sometimes they appear arranged in parallel arrays (**d**) and clusters (**e**).

**Figure 9-6**: XM appearance of endoplasmic reticulum. A pattern of fine concentric linear lucencies (arrows, **a-d**) are frequently seen in the basal cytoplasm surrounding the nucleus, similar in appearance to the EM appearance of the cisternae of the ER. More often, the basal cytoplasm has a finer reticular appearance (**e, f**). At times, the spaces are wider (**g**). Infrequently, some cells, perhaps damaged by hypoxia or preparative trauma, have an obviously striated pattern of density in that region (**h**).

**Figure 9-7**: XM appearance of the Golgi apparatus. Acinar cells often have a roughly round area of heterogeneous density lower than that of its surroundings, located within the zymogen granule containing part of the cell near the nucleus (arrows). Frequently, zymogen granules are also found in the middle of these areas. These regions are similar in location and appearance to those of the Golgi apparatus as seen in EM.

**Figure 9-8**: **a**, the distribution of diameters of the over 70,000 zymogen granules measured in this study. Individual distributions for each image (dotted lines) have a shape similar to that of the whole population (solid line), having a mild skew toward larger diameters. The quartile of granules with the highest apparent density (gray), and possible more accurate diameter estimates (see text), have a slightly higher average diameter (0.79 μm compared to 0.74 μm for the whole population), but a similarly shaped distribution with slightly milder skew. **b**, the distribution of zymogen granule protein density. Again, the individual distributions are similar in shape to that of the composite, with a moderate skew toward lower densities. The mean value is 1.15 g/cm$^3$. The tail is consistent with sectioning artifact. **c**, log-log plot of apparent granule mass versus apparent diameter. The slope of the line, equal to the exponent of the relationship between these parameters, is consistent with a high degree of sectioning artifact (see text).

**Figure 9-9**: **a**, two acini that have been sectioned perpendicular to the axis of the central duct. The acini and their central ducts are outlined, as are the zymogen granules automatically identified by the segmentation algorithm. **b**, zymogen granules in the quartile with the highest apparent density are identified by a square mark. **c**, dotted lines indicate the median distance of the marked granules to the central duct, and thus enclose half of the marked granules. Of these granules, those in the highest quartile of diameter are circled. The number of circled granules outside the dotted lines is significantly more that the number inside (by nearly 3 to 1), indicating a propensity for larger granules to be farther from the duct.

**Figure 9-10**: **a**, a scatter plot of the apparent granule diameter versus distance from the duct for over 6,000 zymogen granules in 23 transversely sectioned acini. A correlation is somewhat difficult to appreciate visually until the average diameter as well as the upper and lower quartile in diameter is plotted for each quartile in distance from the duct. These markers show a progressive increase with distance from the duct. The heights of the central plotting symbols for average diameter include the standard error bars, none of which overlap. The histograms of diameter in the bottom and top quartile of distance from the duct demonstrate a small but significant shift between them. **b**, the same plot of the subset of granules in the top quartile of apparent density, presumably less affected by sectioning artifact (see text). While the spread of points is still wide, the trend is substantially stronger both in magnitude (the correlation coefficient has more than doubled) and statistical significance. **c**, the results of a Monte Carlo type simulation to demonstrate that the assumption of a normal distribution for the correlation coefficient between diameter and distance from the duct under the null hypothesis is valid, permitting an accurate calculation of statistical significance.

**Figures**

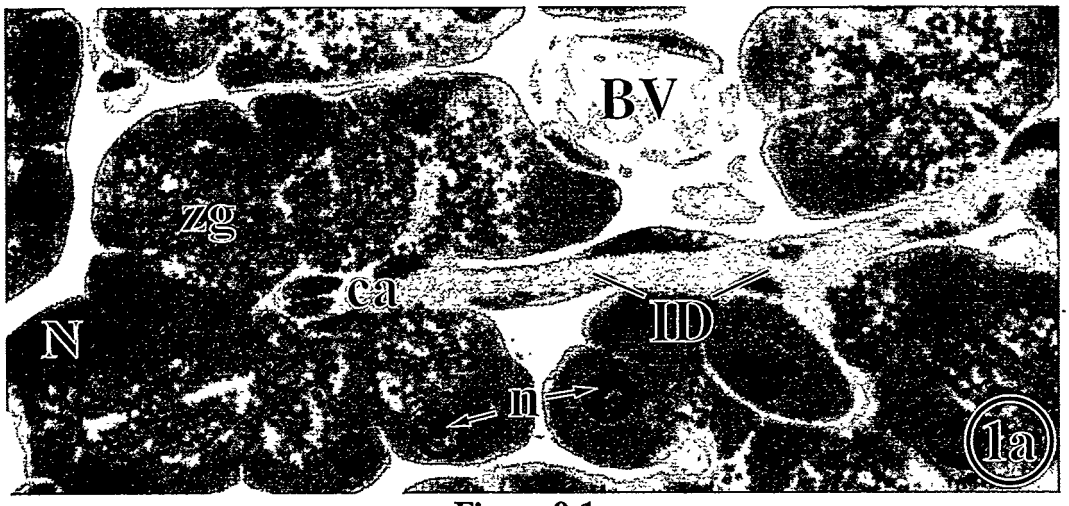


**Figure 9-1a**

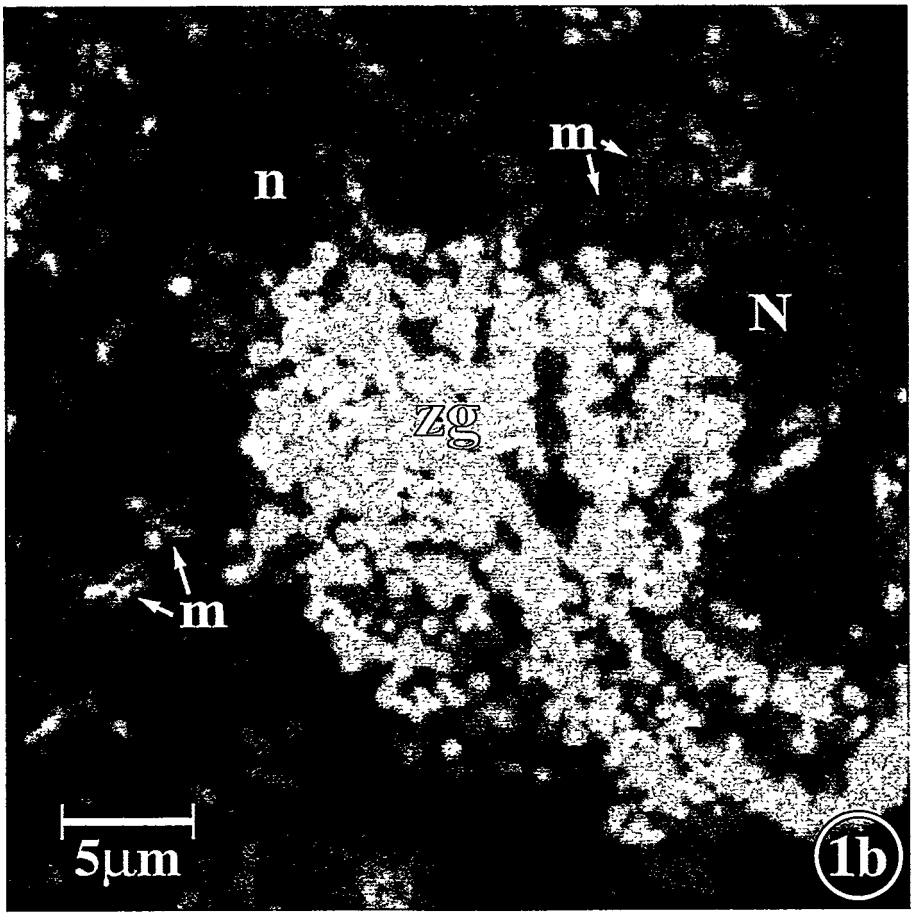


**Figure 9-1b**

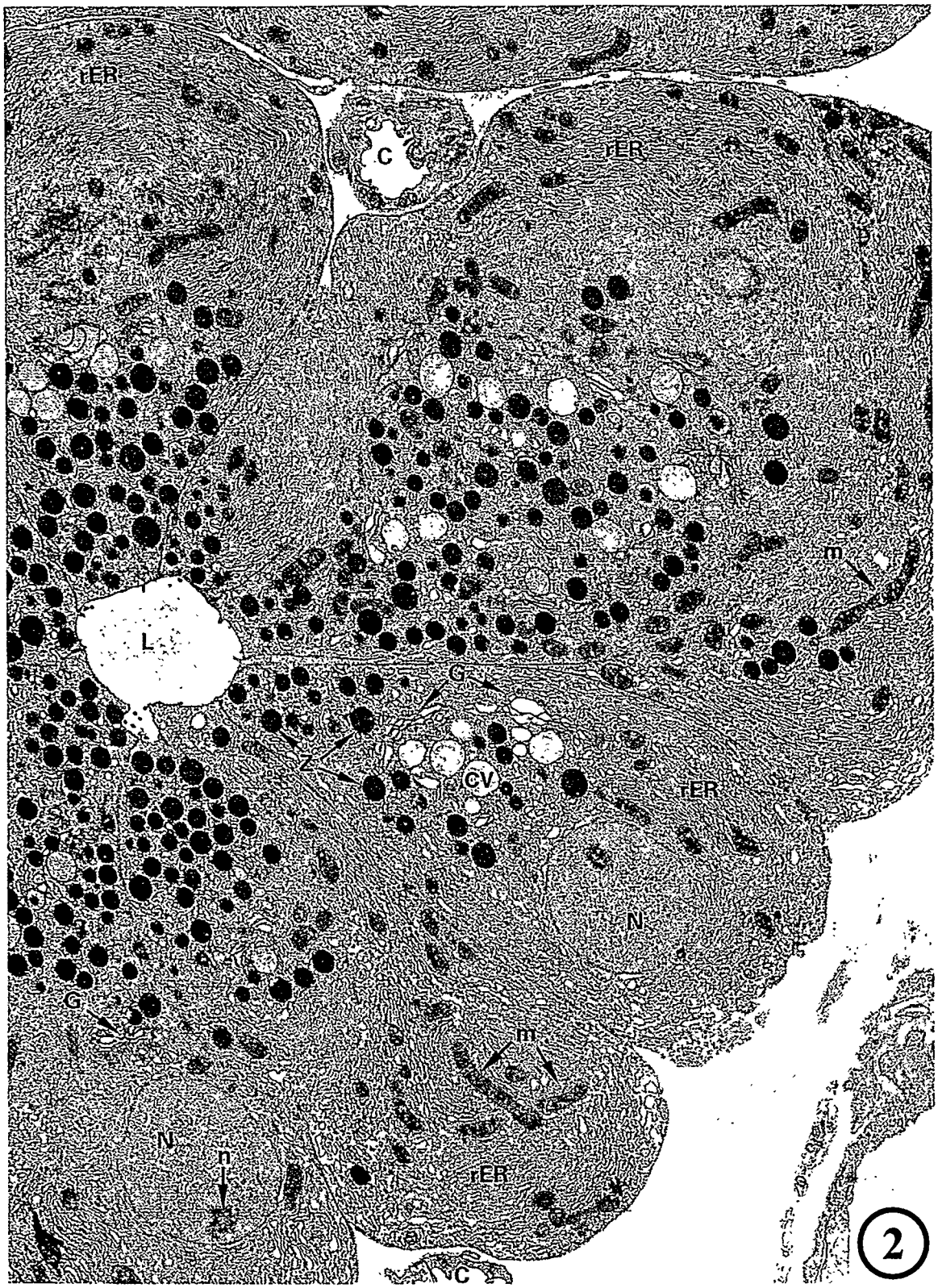


**Figure 9-2**

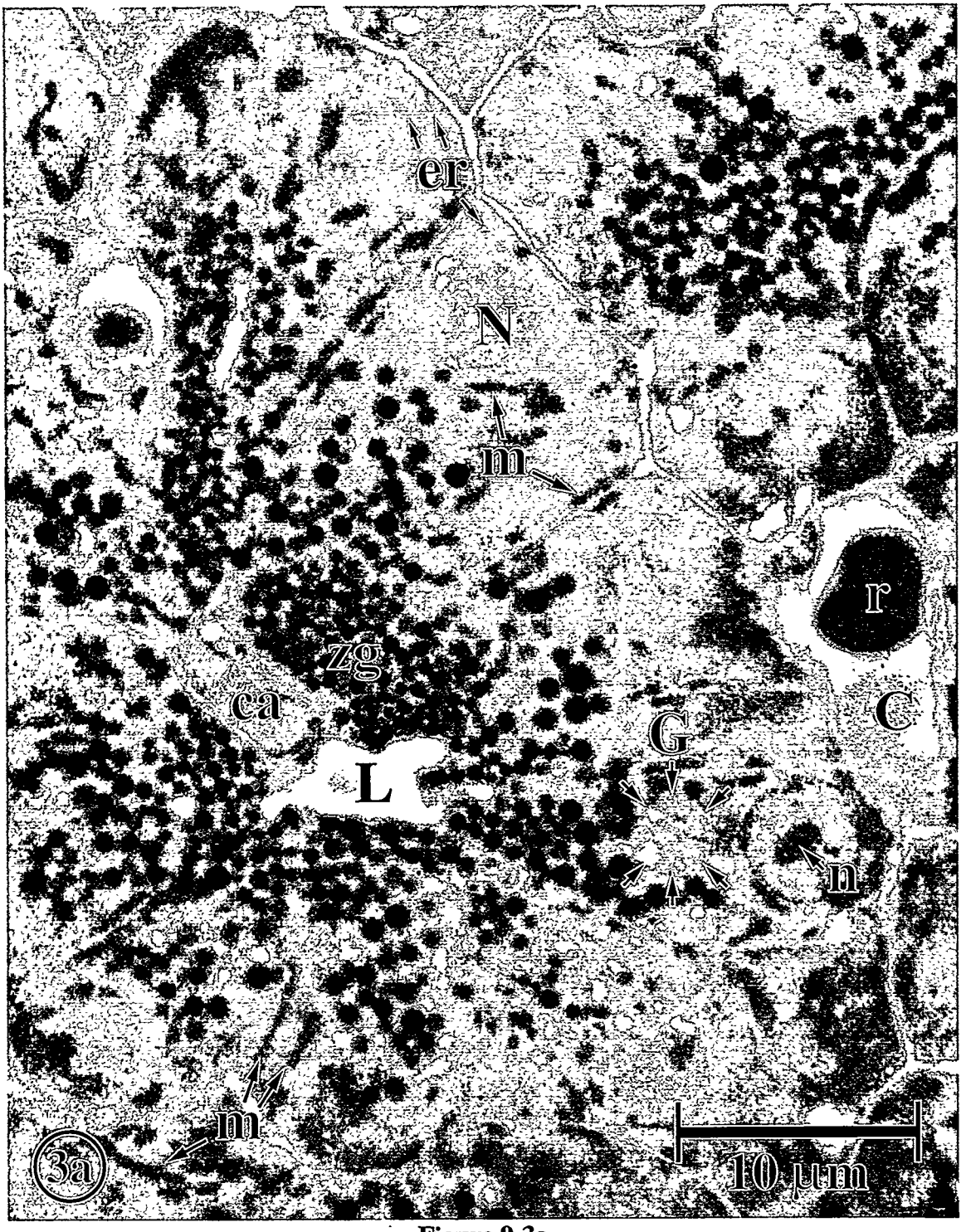


**Figure 9-3a**

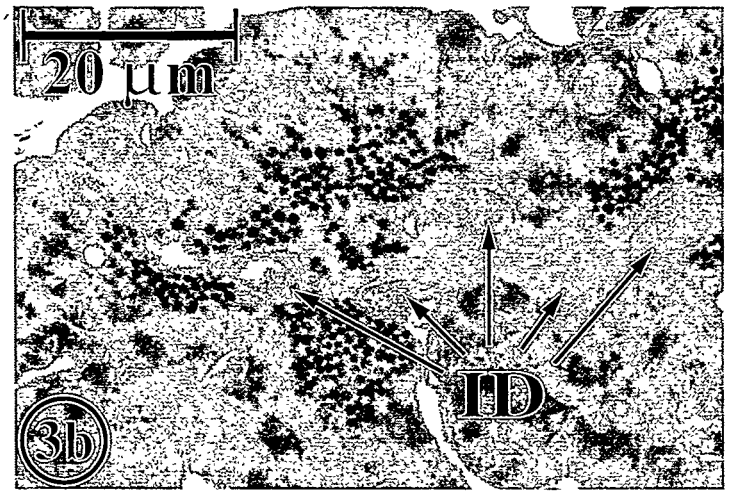


Figure 9-3b

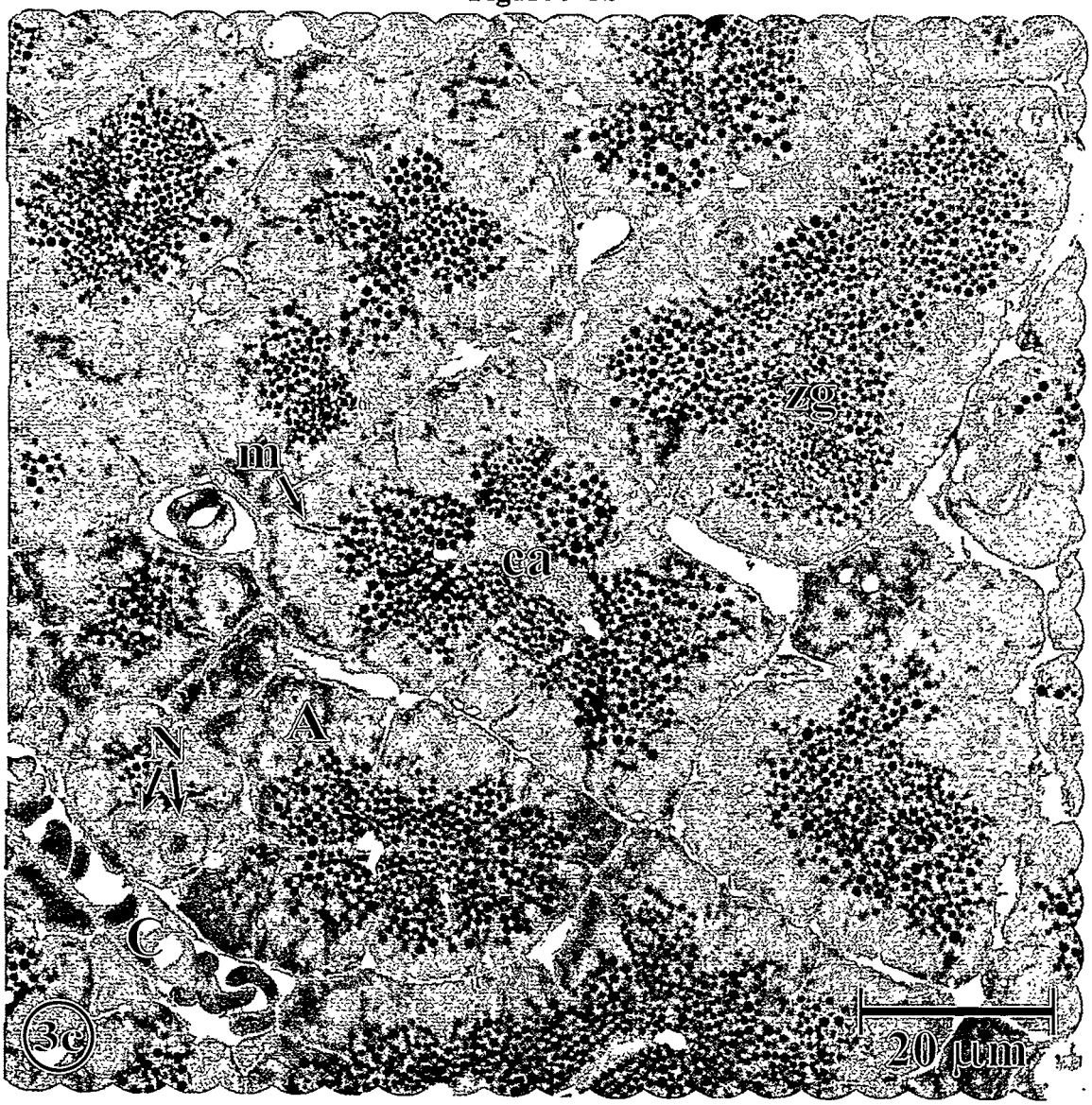


Figure 9-3c

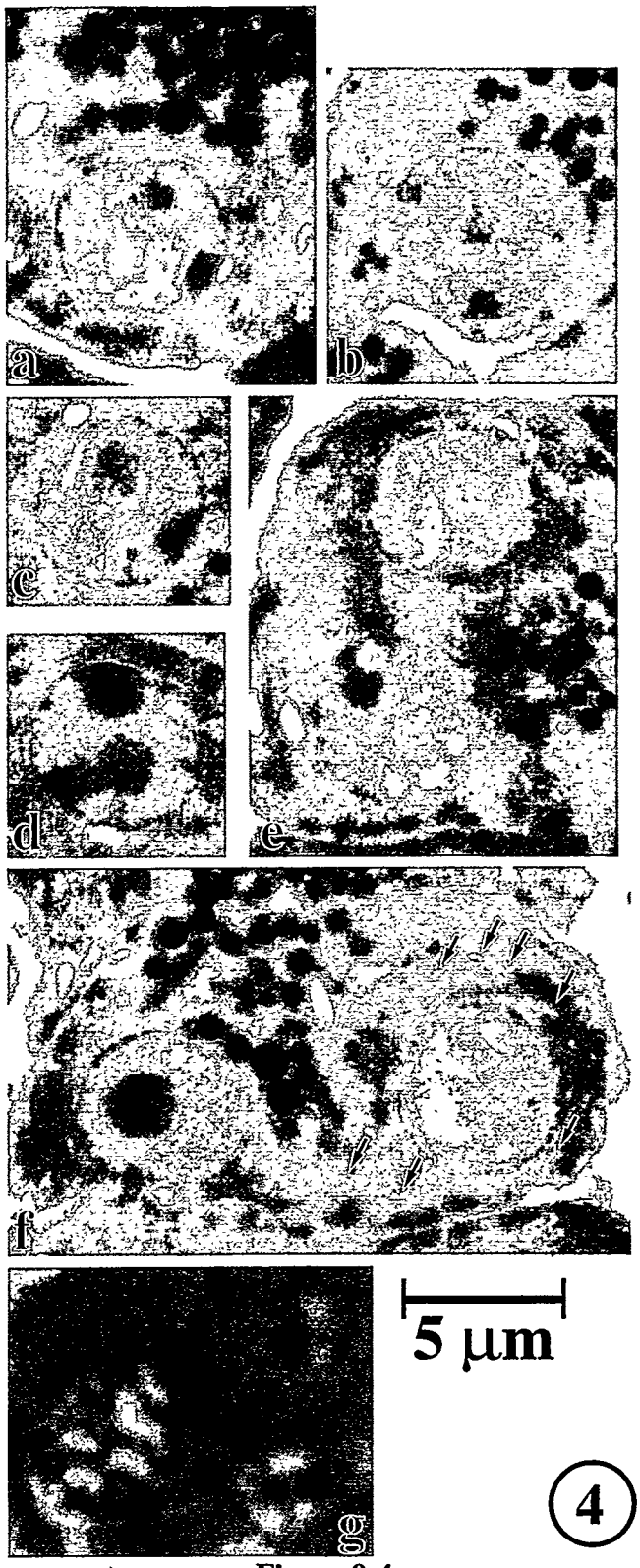


**Figure 9-4**

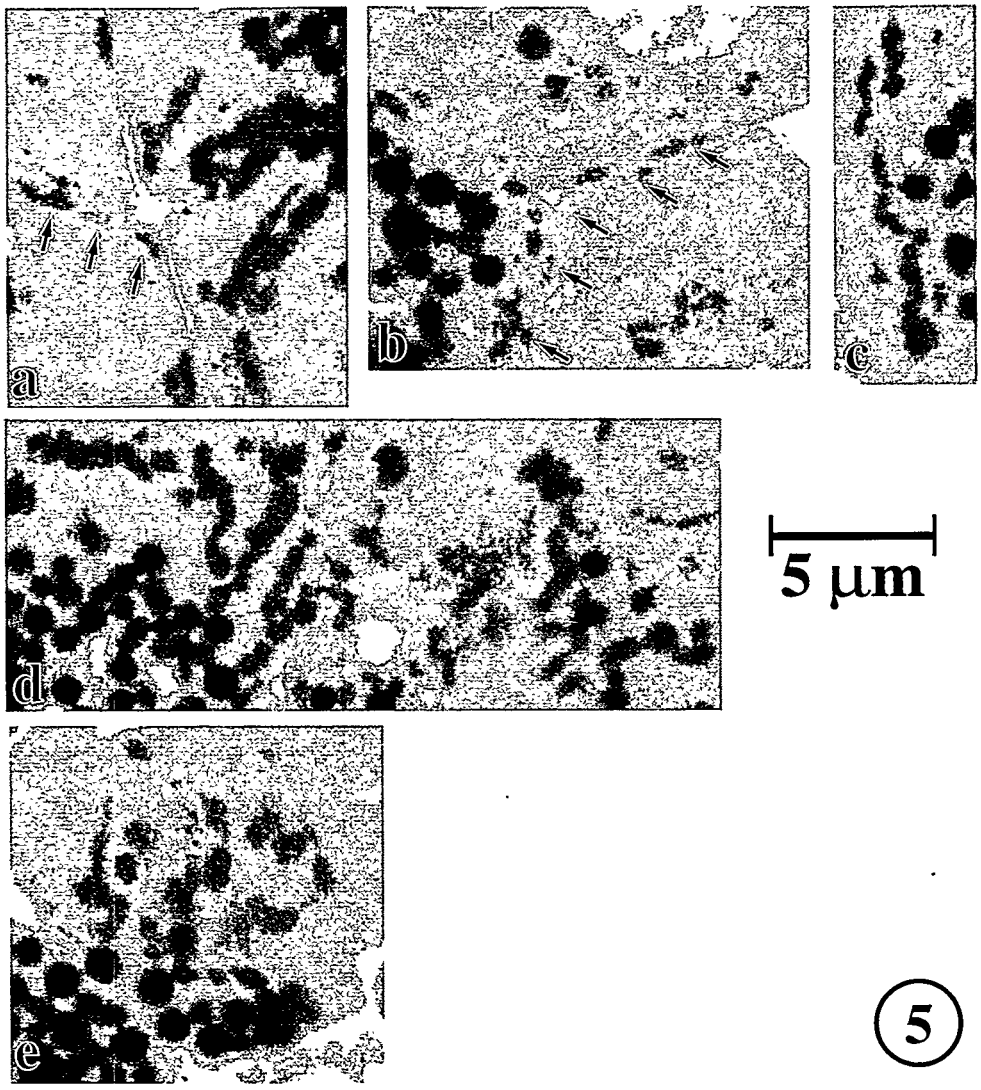


**Figure 9-5**

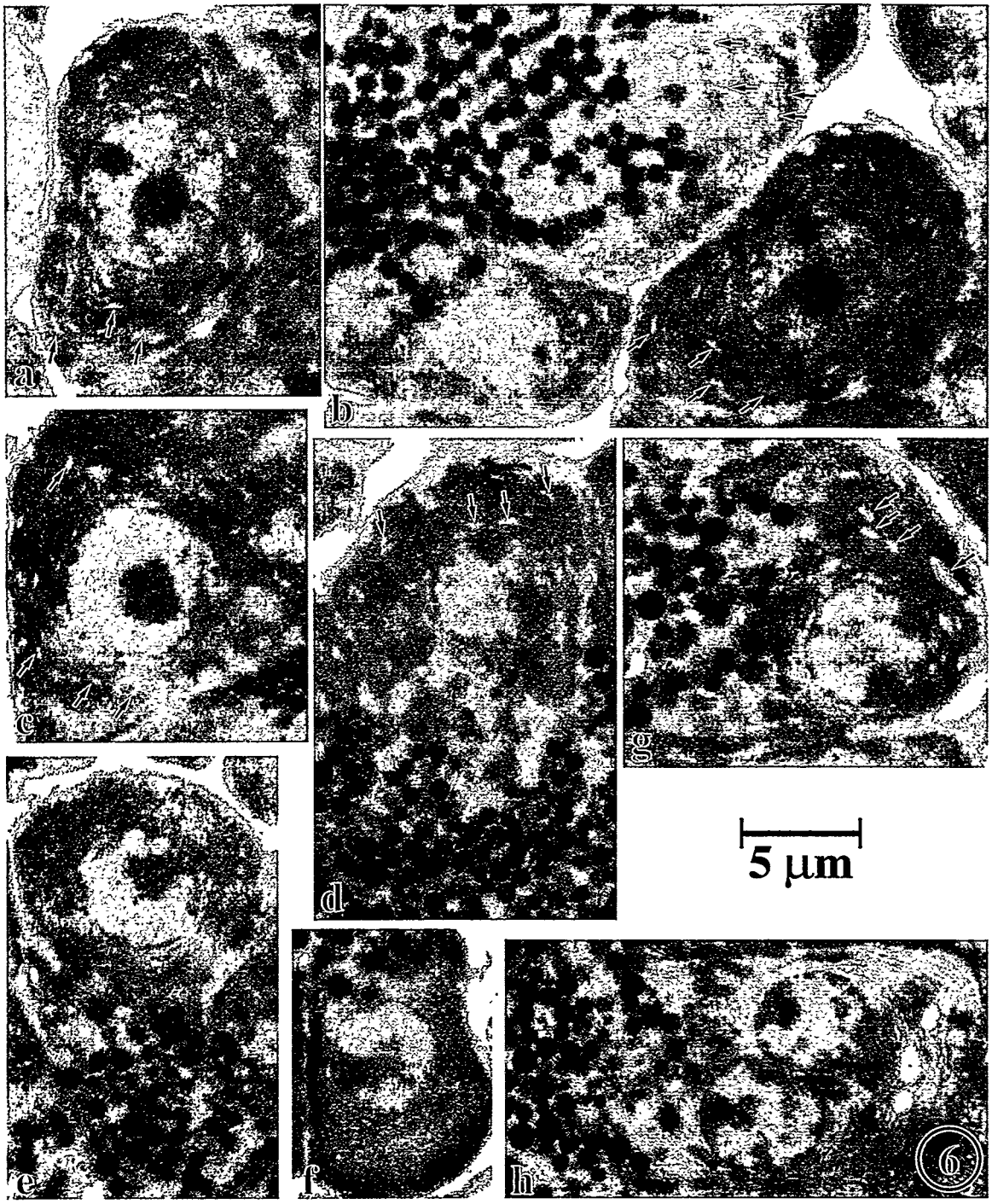


**Figure 9-6**

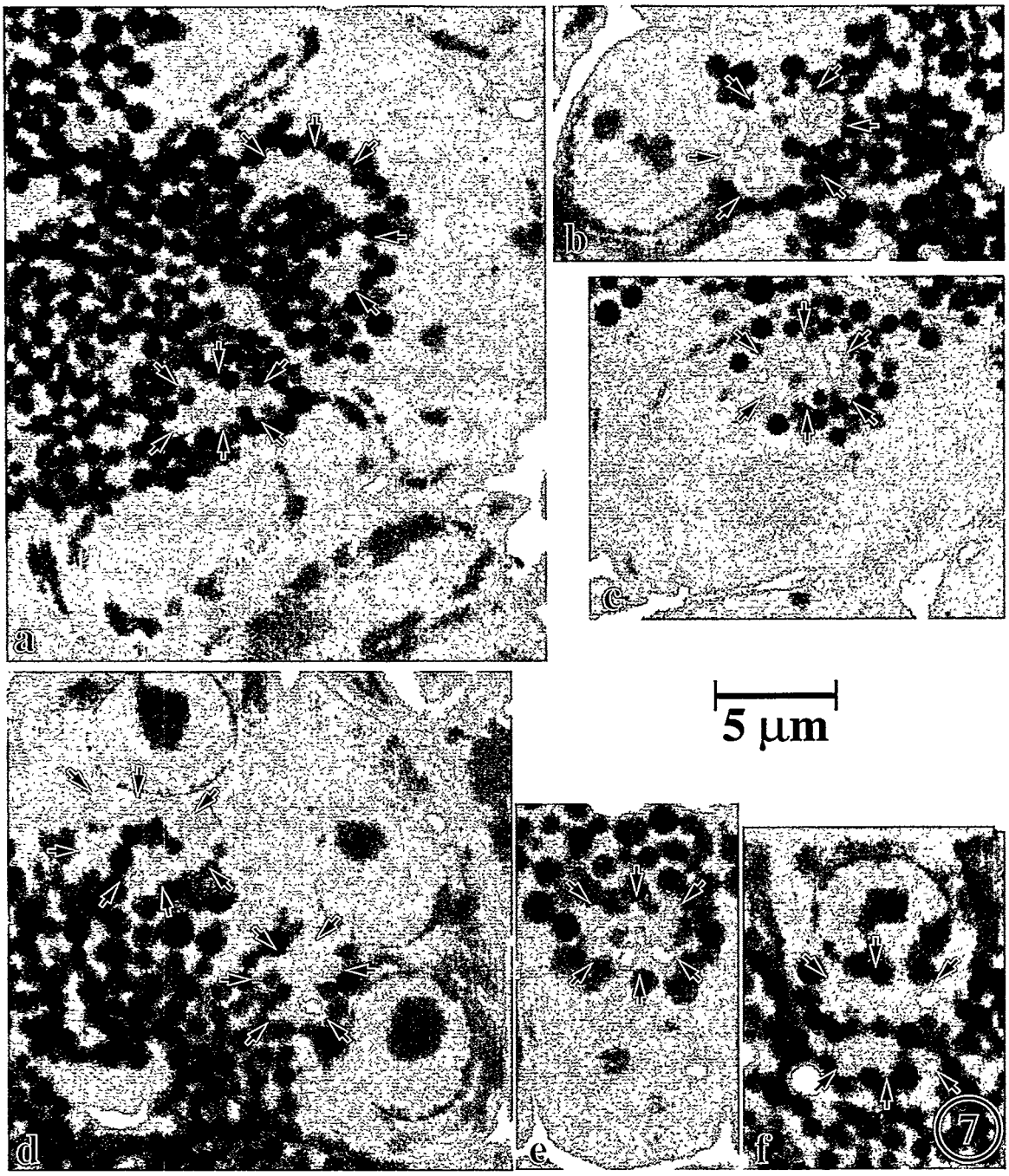


**Figure 9-7**

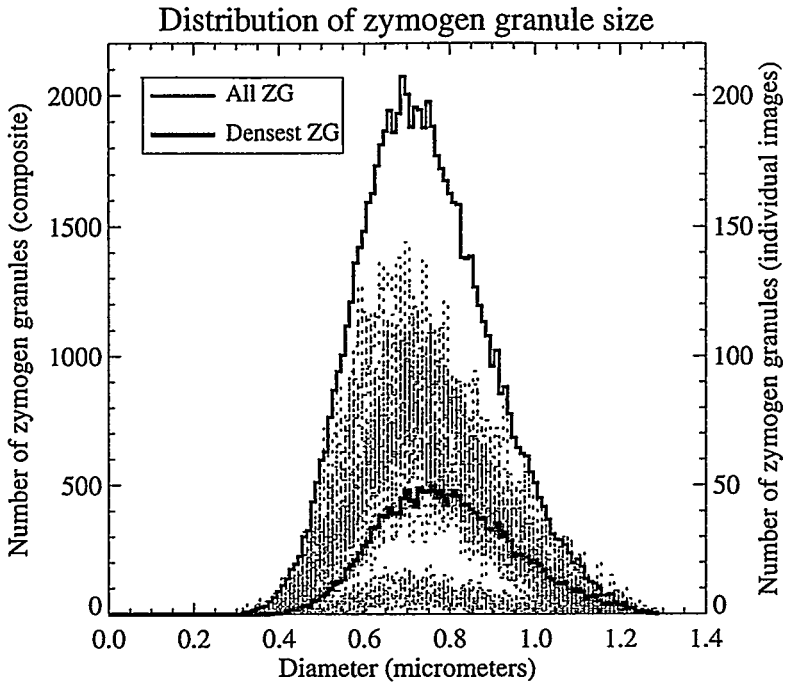


**Figure 9-8a**

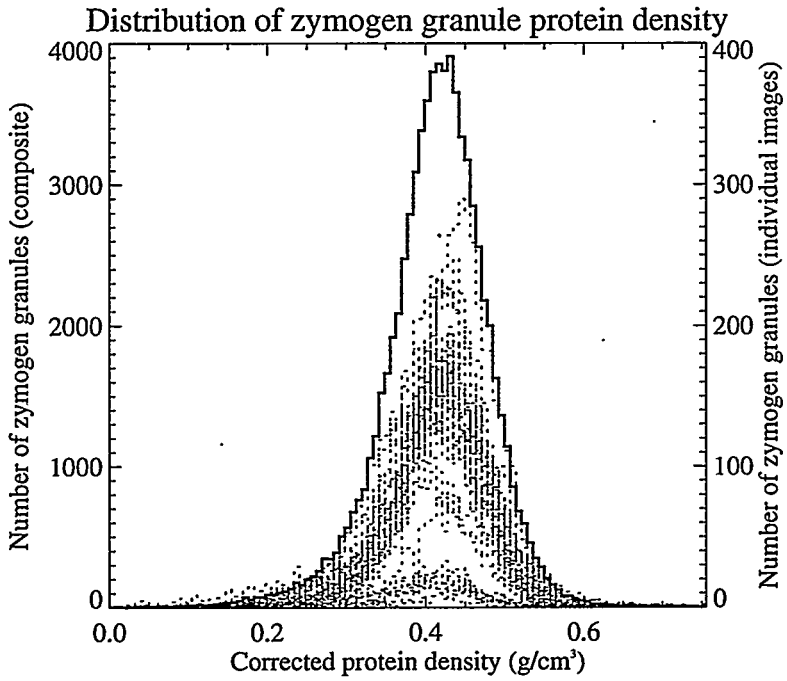


**Figure 9-8b**

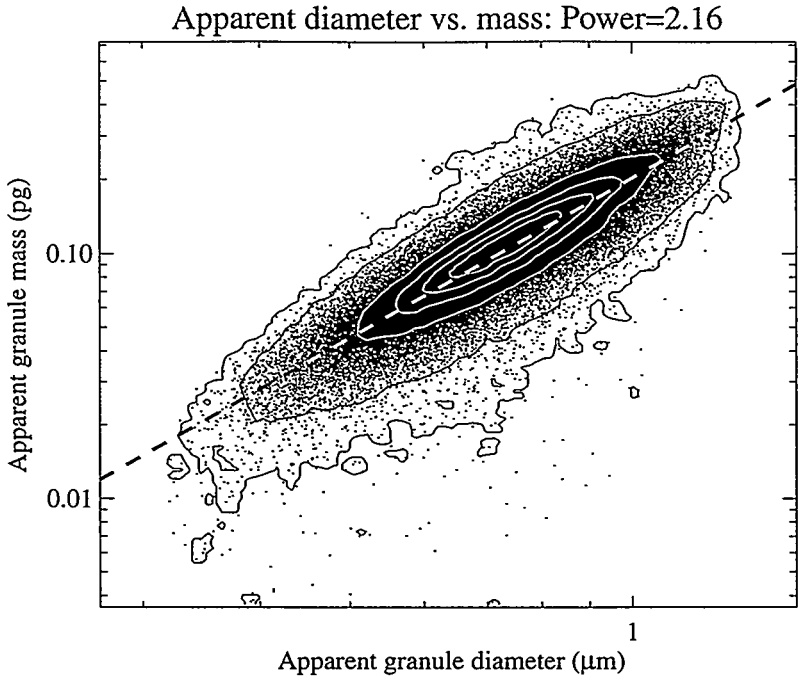


**Figure 9-8c**


**Figure 9-9a**


**Figure 9-9b**


**Figure 9-9c**

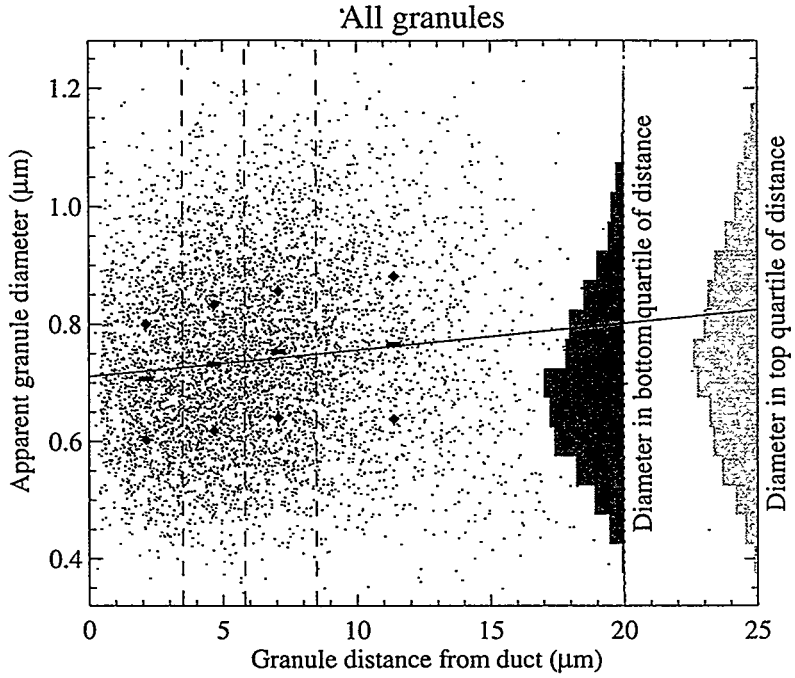


**Figure 9-10a**

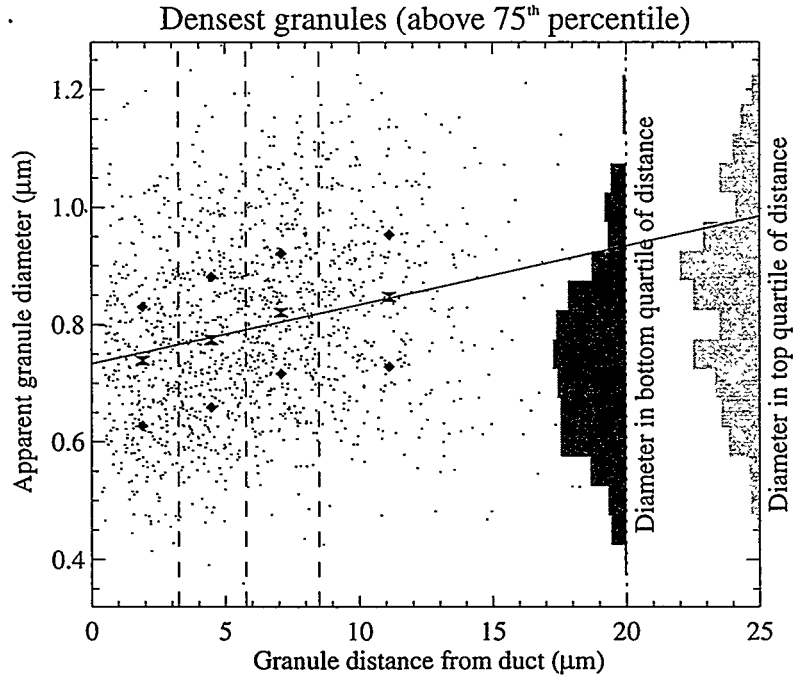


**Figure 9-10b**

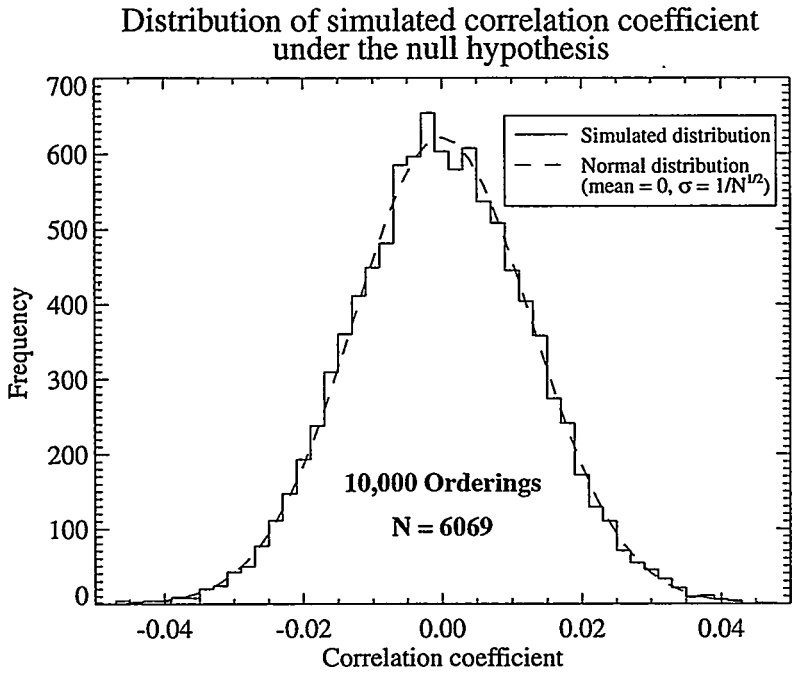
Distribution of simulated correlation coefficient
under the null hypothesis
Simulated distribution
Normal distribution
(mean = 0, σ = 1/N^1/2)
10,000 Orderings
N = 6069
Frequency
Correlation coefficient
700
600
500
400
300
200
100
0
-0.04
-0.02
0.00
0.02
0.04

**Figure 9-10c**

## References


Alberts, B., Bray, D., Lewis, J., Raff, M., Roberts, K. & Watson, J.D. (1989) *Molecular biology of the cell.* 2nd edition. Garland Publishing, Inc., New York.

Beaudoin, A.R., Grondin, G., Filion, M. & Lord, A. (1984) Secretagogues cause a preferential discharge of large size granules in rat pancreas. *Canadian Journal of Biochemistry and Cell Biology.* **62**, 1288-1292.

Ermak, T.H. & Rothman, S.S. (1981) Zymogen granules of pancreas decrease in size in response to feeding. *Cell and Tissue Research.* **214**, 51-66.

Goncz, K.K., Behrsing, R. & Rothman, S.S. (1995) The protein content and morphogenesis of zymogen granules. *Cell and Tissue Research.* **280**, 519-530.

Heck, J.M., Attwood, D.T., Meyer-Ilse, W. & Anderson, E.H. (1999) Resolution determination in x-ray microscopy: an analysis of the effects of partial coherence and illumination spectrum. *Journal of X-Ray Science and Technology.* **8**, 95-104.

Kirz, J., Jacobsen, C. & Howells, M. (1995) Soft x-ray microscopes and their biological applications. *Quarterly Reviews of Biophysics.* **28**, 33-130.

Loo, B.W., Jr., Meyer-Ilse, W. & Rothman, S.S. (2000) Automatic image acquisition, calibration, and montage assembly for biological x-ray microscopy. *Journal of Microscopy.* **197**, 185-201.

Loo, B.W., Jr., Parvin, B. & Rothman, S.S. (1996) Two- and three-dimensional segmentation for measurement of particles in the analysis of microscopic digital images of biological samples. *Three-Dimensional Microscopy: Image Acquisition and Processing III, San Jose, California, January 30 - February 1, 1996.* (ed. by C.J. Cogswell, G.S. Kino, and T. Wilson), Proceedings SPIE Vol. 2655, pp. 209-215.

Loo, B.W., Jr., Sauerwald, I.M., Hitchcock, A.P. & Rothman, S.S. (in press) A new sample preparation method for soft x-ray microscopy: nitrogen-based contrast and

radiation tolerance properties of glycol methacrylate embedded and sectioned tissue. *Journal of Microscopy*.

Meyer-Ilse, W., Denbeaux, G., Johnson, L.E., Bates, W., Lucero, A. & Anderson, E. (in press) The high resolution x-ray microscope, XM-1. *X-Ray Microscopy: Proceedings of the VI International Conference on X-ray Microscopy, Berkeley, August 1-6, 1999*. (ed. by W. Meyer-Ilse, T. Warwick, and D.T. Attwood). American Institute of Physics, College Park.

Palade, G. (1975) Intracellular aspects of the process of protein synthesis. *Science*. **189**, 347-358.

Press, W.H., Teukolsky, S.A., Vetterling, W.T. & Flannery, B.P. (1992) *Numerical Recipes in C: the Art of Scientific Computing*. 2nd edition. Cambridge University Press, Cambridge.

Ross, M.H., Reith, E.J. & Romrell, L.J. (1989) *Histology: a Text and Atlas*. 2nd edition. Williams & Wilkins, Baltimore.

Rothman, S., Anderson, E., Attwood, D., Batson, P., Buckley, C., Goncz, K., Howells, M., Jacobsen, C., Kern, D., Kirz, J., Rarback, H., Rivers, M., Shu, D., Tackaberry, R. & Turek, S. (1990) Soft x-ray microscopy in biology and medicine: status and prospects. *Physica Scripta*. **T31**, 18-22.

Rothman, S.S. (1975) Protein transport by the pancreas. *Science*. **190**, 747-753.

Schmahl, G., Rudolph, D., Niemann, B. & Christ, O. (1980) Zone-plate x-ray microscopy. *Quarterly Reviews of Biophysics*. **13**, 297-315.

Wheater, P.R., Burkitt, H.G. & Daniels, V.G. (1987) *Functional Histology: a Text and Colour Atlas*. 2nd edition. Churchill Livingstone, Edinburgh.